

p-ISSN 1811-1165
e-ISSN 2413-2179

VOLUME 16, No. 1(31), 2019

EURASIAN
PHYSICAL
TECHNICAL

JOURNAL

KARAGANDA STATE UNIVERSITY NAMED AFTER E.A. BUKETOV

KARAGANDA, THE REPUBLIC OF KAZAKHSTAN

EURASIAN PHYSICAL TECHNICAL JOURNAL

p - ISSN 1811-1165
e - ISSN 2413-2179

Volume 16, No. 1(31), 2019

1st issue – March, 2004

Journal Founder:

**KARAGANDA STATE UNIVERSITY
NAMED AFTER E.A. BUKETOV**

**Е.А.БӨКЕТОВ АТЫНДАҒЫ ҚАРАҒАНДЫ
МЕМЛЕКЕТТІК УНИВЕРСИТЕТІ**

**КАРАГАНДИНСКИЙ
ГОСУДАРСТВЕННЫЙ УНИВЕРСИТЕТ
ИМ. Е.А.БУКЕТОВА**

Contact information:

Editorial board of EPhTJ (Build. 2, room 216)
Karaganda State University
named after E.A. Buketov
Universitetskaya Str.28, Karaganda,
Kazakhstan, 100028
Subscription index: 75240
Tel: +7(7212)77-04-03
Fax: +7(7212)77-03-84
E-mail: ephTj@mail.ru

Signed to print on **14.06.2019**.
Format 60x84 1/8. Offset paper.
Volume **20.62 p.sh.** Circulation 300 copies.
Agreed price. Order No. 87.

Басуға **14.06.2019** ж. қол қойылды.
Пішімі 60×84 1/8. Офсеттік қағазы.
Көлемі **20.62** ес.-б.т. Таралымы 300 дана.
Бағасы келісім бойынша. Тапсырыс № 87.

Подписано к печати **14.06.2019**.
Формат 60 × 84 1/8. Офсетная бумага.
Объем **20.62** печ.л. Тираж 300 экз.
Цена договорная. Заказ № 87.

Printed in the Publishing House
of the KarSU named after academician
E.A.Buketov

академик Е.А. Бөкетов атындағы ҚарМУ
баспасының баспаханасында басылып шықты

Отпечатано в Издательстве
КарГУ имени академика Е.А.Букетова

PROJECT MANAGER, RECTOR

Yedrissov A.T., Karaganda State University named after
E.A.Buketov, Karaganda, Kazakhstan

Chief EDITOR

Sakipova S.E., Karaganda State University named after E.A.Buketov,
Karaganda, Kazakhstan

EDITORIAL BOARD

Aringazin A.K., Institute for Basic Research, L.N. Gumilev Eurasian
National University, Astana, Kazakhstan

Dueck J., Erlangen-Nuernberg University, Erlangen, Germany

Dzhumanov S., National University of Uzbekistan named after
M. Ulugbek, Tashkent, Uzbekistan

Ibrayev N.Kh., Institute of Molecular Nanophotonics, Karaganda State
University named after E.A.Buketov, Karaganda, Kazakhstan

Jakovics A., Faculty of Physics and Mathematics, University of Latvia,
Riga, Latvia

Kidibaev M.M., Issyk-kul State University named after K.Tynystanov,
Karakol, Kyrgyzstan

Kucherenko M.G., Director of the Centre of Laser and Information
Biophysics, Orenburg State University, Orenburg, Russia

Kumekov S.E., Kazakh State National Technical University named
after K.Satbaev, Almaty, Kazakhstan

Kuritnyk I.P., Department of Electronics and Automation, High school
in Oswiecim, Poland

Miau J.J., Department of Aeronautics and Astronautics, National
Cheng Kung University, Tainan, Taiwan

Pedrini C., University Claude Bernard Lyon I, France

Potapov A.A., V.A.Kotelnikov Institute of Radio Engineering and
Electronics of RAS, Moscow, Russia

Pribaturin N.A., Institute of Thermal Physics, SB RAS, Novosibirsk,
Russia

Saulebekov A.O Kazakhstan Branch of Lomonosov Moscow State
University, Astana, Kazakhstan

Senyut V.T., Joint Institute of Mechanical Engineering of National
Academy of Sciences of Belarus, Minsk, Belarus

Shrager E.R., National Research Tomsk State University, Tomsk,
Russia

Stoev M., South-West University «Neofit Rilski», Blagoevgrad,
Bulgaria

Trubitsyn A.A., Ryazan State Radio Engineering University, Russia

Zhanabaev Z.Zh., Al-Farabi Kazakh National State University, Almaty,
Kazakhstan

CONSULTANT OF TRANSLATION

Yakhina S.B., Karaganda State University named after E.A. Buketov,
Karaganda, Kazakhstan

TECHNICAL EDITORS

Akhmerova K.E., Kambarova Zh.T. Karaganda State University
named after E.A.Buketov, Karaganda, Kazakhstan

© Karaganda State University, 2019

© Қарағанды мемлекеттік университеті, 2019

Registered by the Ministry of Culture, Information and Public Adjustment of the Republic of Kazakhstan.
Қазақстан Республикасы мәдениет, ақпарат және қоғамдық келісім министрлігімен тіркелді
Registration Certificate No. 4382-Zh, November 7, 2003.

CONTENTS

PREFACE	4
MATERIALS SCIENCE	
Ryaguzov A.P., Kudabayeva M.A., Nemkayeva R.R., Guseinov N.R., Myrzabekova M.M. STUDY OF THE STRUCTURE OF AMORPHOUS CARBON FILMS MODIFIED WITH SILICON OXIDE	6
Astanov S.Kh., Sharipov M.Z., Kasimova G.K. HIPOCHROMIC EFFECT IN RIBOFLAVIN SOLUTIONS.....	12
Yurov V.M., Baltabekov A.S., Laurinas V.Ch., Guchenko S.A. DIMENSIONAL EFFECTS AND SURFACE ENERGY OF FERROELECTRIC CRYSTALS.....	18
Saulebekov A.O., Vénos D., Kambarova Zh.T., Saulebekova D.A., Vassilyeva K.I., Seidualy Kh.B. DEVELOPMENT OF ENERGY ANALYZER OF CHARGED PARTICLES BASED ON THE BASIS NON-UNIFORM ELECTROSTATIC FIELD	24
Kumekov S. E., Saitova N. K. DIFFUSIVE SPECTRA OF ANTISTOKES WING OF PHOTOLUMINESCENCE OF CARBON NANOSTRUCTURES	30
Sharipov M.Z., Mirzhonova N.N., Hayitov D.E., EFFECT OF INHOMOGENEOUS RADIALY DIRECTED MECHANICAL STRESSES ON THE DOMAIN STRUCTURE OF A FeBO ₃ SINGLE CRYSTAL.....	35
Zhumabekov A.Zh., Seliverstova E.V., Ibrayev N.Kh. INVESTIGATION OF PHOTOCATALYTIC ACTIVITY OF TiO ₂ -GO NANOCOMPOSITE.....	42
Agelmenev M.E. INTERMOLECULAR INTERACTION IN LIQUID CRYSTALS.....	47
Zavgorodniy A.V., Aimukhanov A.K., Zeinidenov A.K., Ayubekova A.Ye. THE INFLUENCE OF THE MAGNETIC FIELD ON THE CURRENT-VOLTAGE CHARACTERISTICS OF CUPC NANOSTRUCTURES.....	54
Kopbalina K.B., Mazhenov N.A., Bimbetova G.M. QUANTUM-CHEMICAL CALCULATIONS OF THE STRUCTURE AND ELECTRON TRANSITIONS OF MULTIMOLECULAR FILMS.....	62
ENERGY. THERMOPHYSICS. HYDRODYNAMICS.	
Narimanov R.K., Narimanova G.N. APPLICATION OF A COMPLETE MULTI-NETWORK METHOD FOR SOLVING THE PROBLEM OF FLOWS AROUND SPHERE.....	69
Sabdenov K.O., Sakipov K.Ye. THE CALCULATION OF THE HEAT TRANSFER COEFFICIENT FROM THE WALLS AND PIPES OF THERMAL NETWORKS IN THE ENVIRONMENT.....	73

Yershina A.K., Yershin Sh.A. ABOUT HIGH EFFICIENCY OF TWO-ROTOR WIND POWER UNIT BIDARRIEUS-2.....	82
Sakipova S.E., Tanasheva N.K. MODELING AERODYNAMICS OF THE WIND TURBINE WITH ROTATING CYLINDERS.....	88
Merzadinova G.T., Sakipov K.E., Sharifov D.M., Mirzo A., Bekeshev A. Z. LASER PHOTOACOUSTICS METHOD FOR DETERMINATION OF THE COEFFICIENTS OF THERMAL CONDUCTIVITY AND THERMAL DIFFUSIVITY OF MATERIALS.....	94
ENGINEERING. TECHNIQUE, DEVICES, PHYSICAL METHODS OF EXPERIMENT	
Yurov V.M., Oleshko V.S. THE IMPACT OF THE ENVIRONMENT ON THE CONTACT POTENTIAL DIFFERENCE OF METAL MACHINE PARTS.....	99
Narimanova G.N., Inkina M.A. SYSTEM OF HETEROGENEOUS DATA TRANSMISSION ON THE BASIS OF A SELF-REGULATION NETWORK WITH AN OPTION OF RETRANSMISSION.....	109
ENGINEERING. MODELING OF THE NONLINEAR PHYSICAL AND TECHNICAL PROCESSES	
Yesbayev A.N., Yessenbayeva G.A., Ramazanov M.I. INVESTIGATION OF THE MODEL FOR THE ESSENTIALLY LOADED HEAT EQUATION.....	113
Yessenbaeva G.A., Yesbayeva D.N., Makazhanova T.Kh. ON CALCULATION METHODS FOR THE MODEL OF PLATES BENDING.....	121
Vasenin I.M., Narimanov R.K., Shrager L.A., Perchatkina E.V. MODELING OF A TWO-PHASE FLOW OF LIQUID WITH SMALL-SIZE GAS BUBBLES.....	129
REVIEWS	
Potapov A.A. CREATION AND DEVELOPMENT OF THE FUNDAMENTAL AREA "FRACTAL RADIOPHYSICS AND FRACTAL RADIO ELECTRONICS: DEVELOPMENT OF FRACTAL RADIO SYSTEMS". PART 1. THEORY AND MAIN SCIENTIFIC PROSPECTS.....	137
Potapov A.A. CREATION AND DEVELOPMENT OF THE FUNDAMENTAL AREA "FRACTAL RADIOPHYSICS AND FRACTAL RADIO ELECTRONICS: DEVELOPMENT OF FRACTAL RADIO SYSTEMS". Part 2. SELECTED RESULTS AND PERSPECTIVE TRENDS.....	144
SUMMARIES.....	153
INFORMATION ABOUT AUTHORS.....	161

Dear Authors and Readers!
Honourable colleagues!

At last we are incorporated in the Scopus database!

I am very pleased to inform you that based on the decision of the Content Selection & Advisory Board (CSAB) of May 8, 2019, the Eurasian Physical Technical Journal (Eurasian phys. tech. j.) has been inducted into Scopus in three scientific areas: Energy, Materials Science, Engineering. In an official report, Scopus Title Evaluation experts note that Eurasian phys. tech. j. «meets the standards for acceptance by Scopus»; further - «consistently includes articles that are scientifically sound and relevant to an international academic or professional audience in this field».

Dear authors of articles and honoured editors, this is a rather high appreciation of your work and achievements. We are grateful that you have been with us, and we look forward for further cooperation in the future. The indexing linking process, i.e. adding the content to Scopus.com will begin this year in 2-3 months. The insertion in SCOPUS database is a big responsibility for members of the editorial board, experts and authors of Eurasian phys. tech. j. But, of course, this will improve the quality and extend the information space for Eurasian phys tech. j. materials. and it will be of benefit to the authors.

Since 2008, Eurasian phys. tech. j. has been included on the list of publications recommended by the Control Committee in Education and Science the MES of RK for publication of the main research findings in the area of Physics and Mathematics. The editorial board plans to prepare materials for the inclusion of the journal in the list of publications of the Control Committee in Education and Science of the Republic of Kazakhstan in the field of Engineering sciences, as well as its insertion in other electronic databases.

According to the requirements for international scientific publications, the composition of the editorial board can and should be regularly renewed. This year, the editorial board has introduces two leading scientists who have previously published their papers in the Eurasian phys. tech. j. Let us briefly present the most significant facts from their professional activities to our authors and readers.

One of them is Kucherenko Mikhail Gennadyevich, Doctor of Physics and Mathematics, Professor at the Department of Radio physics and Electronics, Director of the Center for Laser and Information Biophysics of Orenburg State University, Russia. He is a graduate of our Karaganda State University, who graduated with honors. He is the author of over 350 scientific publications in the field of laser physics, molecular optics, nanoelectronics, photonics, and chemical physics.

Kucherenko M.G. is the project manager of the federal program of the Ministry of Education of Russia “Universities of Russia. Fundamental research”. He also directed a number of research projects of the Russian Foundation for Fundamental Research from 1999 to 2017. Under the guidance of Prof. M.G. Kucherenko 9 PhD and a doctoral theses have been passed. Kucherenko M.G. has been a full member of the New York Academy of Sciences since 1996; he was Soros Foundation associate professor (1998). He was awarded the Diploma of the Administration of the Orenburg Region for achievements in scientific activity (1999), the Diploma of the winner of the prize of the Government of the Orenburg region in science and technology in 2007, Diplomas of the Prize of the Governor of the Orenburg Region in Science and Technology in 2011, 2015. He received an official message of thanks from the Federal Agency for Education of the Russian Federation (2006). Professor M. Kucherenko was also awarded the Certificate of appreciation of the Ministry of Education and Science of the Russian Federation (2007), the award pin of the Ministry of Education and Science of Russia “Honored Worker of Higher Professional Education of the Russian Federation” for achievements in the field of education (2009).

The second new editor is Senyut Vladimir Tadeushevich, Candidate of Engineering Sciences, leading research scientist of the laboratory «Nanostructured and superhard materials» of the State Scientific Directorate "Joint Institute of Machine building of the National Academy of Sciences of

Belarus", Minsk. He is the author of more than 350 published works, including 4 monographs, 26 patents and applications for inventions.

Senyut V.T. is the winner of the prize of the Academies of Sciences of Ukraine, Belarus and Moldova for the series of works "New processes for the production of polycrystalline superhard materials, production and use of tools made of them." He was awarded the Bakul certificate of appreciation of the V.N. Bakul Institute of superhard materials of the NAS of Ukraine for the development of research on the synthesis and sintering of cubic boron nitride, as well as the Certificate of appreciation of the NAS of Belarus for his contribution to the development of scientific principles of formation and creation of technologies for the synthesis of new composite nanostructured superhard instrumental materials on the ground of diamonds and diamond-like boron nitride.

Being very pleased that the above-mentioned distinguished scientists agreed to work at our editorial board, we hope that their contribution in the future will make for the expansion and strengthening of international cooperation in the field of applied physics, as well as for improving the image and quality of the Eurasian phys. tech. j.

In this issue of the Eurasian phys. tech. j. we offer you original scientific articles on the physics of nanotechnology, and the solution of current problems of modern applied physics. There are interesting scientific papers on the modeling of complex physical and technical processes of melting, heat and mass transfer, aerodynamics, the study of optical phenomena in solid state physics and the properties of elementary particles. A series of contributions are concerned with the problems of alternative energy, in which the authors suggest ways to improve the environmental ecology. Literally, first-hand useful information can be found in survey papers by Professor A.A. Potapov, which presents the results of a 40-year thematic research in fractal radio electronics, having been conducted at the V.A. Kotelnikov Institute of Radio Electronics of the Russian Academy of Sciences, Moscow. There "... the main areas of the implementation of textures, fractals, fractional operators and methods of nonlinear dynamics into the fundamental problems of radio physics, radiolocation and a wide range of radio engineering to create new information technologies" are considered.

It is known that the Eurasian phys. tech. j. shares information on forthcoming conferences where the latest research results are shared and evaluated, and it publishes some of the most important materials. In this connection, may we remind that on November 22-23, 2019 E.A. Buketov Karaganda State University invites everyone willing to take part in the 11th International Scientific Conference «Chaos and structures in nonlinear systems. Theory and Experiment», dedicated to the 70th anniversary of professor K. Kusainov. Detailed information on the scientific areas of the conference, acceptance of applications for participation and materials submission guidelines can be obtained at the organizing committee address: chaos2019kargu@inbox.ru

Moreover, the following important conferences for the physical and technical community of scientists and young researchers will be held in Moscow. This is the VIII International Conference "Deformation and fracture of materials and nanomaterials" - DFMN-2019, which will be held from 19 to 22 November 2019 at the A.A. Baikov Institute of Metallurgy and Materials Science of the Russian Academy of Sciences, Moscow. The Youth Schooling Conference for students, graduate students and young scientists will be organized within the framework of the conference, where leading scientists will address. The topics of the sections and the materials submission guidelines can be obtained from the website: <http://dfmn.imetran.ru/>.

We are looking forward to see you participating in the announced events and amongst the authors of our future publications.

Respectfully, Chief Editor, Saule E. Sakipova
Karaganda, June, 2019

UDC 538.97; 539.23; 539.216.1.

STUDY OF THE STRUCTURE OF AMORPHOUS CARBON FILMS MODIFIED WITH SILICON OXIDE

Ryaguzov A.P., Kudabayeva M.A., Nemkayeva R.R., Guseinov N.R., Myrzabekova M.M.

National Nanotechnology Laboratory of Open Type,
al-Farabi Kazakh National university, Almaty, Kazakhstan, madina.kudabaeva90@gmail.com

This paper considers amorphous carbon films modified with silicon oxide ($a-C_{1-x}:(SiO)_x$), obtained by the method of magnetron ion-plasma co-sputtering of a combined target in an argon atmosphere. The topography and phase contrast of the film surface were studied by atomic force microscopy. The local structure was studied by Raman spectroscopy. It is shown that an increase in the concentration of silicon leads to an increase in the intensity of photoluminescence. The shift of the G peak to the low-frequency region in $a-C_{1-x}:(SiO)_x$ films indicates an increase in the sp^3 hybridization of carbon bonds.

Keywords: silicon containing amorphous carbon films, atomic force microscopy, Raman spectroscopy, photoluminescence, bond hybridization.

Introduction

Recently, interest in silicon carbide films as a promising material for nanoelectronics and photonics has increased. Moreover, amorphous carbon films modified with silicon and oxygen atoms are of no small interest. Therefore, studies of thin amorphous carbon films modified with structural units of silicon oxide with concentrations up to 20 at. % can reveal new properties.

$a-C_{1-x}:(SiO)_x$ films can have unique properties such as high chemical resistance and high mechanical strength, and resistance to external actions (radiation, temperature, etc.). SiO-doped modified carbon films are classified as wide bandgap semiconductor and may be promising for the development and creation of new semiconductor devices and appliances in the terahertz frequency range. Silicon carbide can form various modifications of the structure, the main of which are 3C (face-centered cubic), 4H and 6H (hexagonal structures) [1]. These structures have individual electronic properties. Therefore, one of the important issues is the possibility of controlling the electronic properties of amorphous carbon films by structural elements of 3C, 4H and 6H groups. The introduction of oxidized structural units into an amorphous carbon matrix should lead to a significant change in the structure and properties of the synthesized carbon films. Knowledge of the effect of synthesis conditions on the formation of a structure with a certain ratio of polymorphic structural units will allow to manage and control electronic processes in thin films of amorphous carbon more effectively. This will make it possible to obtain structurally modified a-C:SiO films with desired properties.

1. Experimental part

Synthesis of nanostructured nanoscale a-C:SiO films was carried out by the method of magnetron ion-plasma co-sputtering of a combined carbon target (99.999 at.%) and high-resistance silicon (100) ($\sim 200 \text{ M}\Omega/\text{cm}^2$) at a direct current in argon atmosphere (99.999 at. %). $a-C_{1-x}:(SiO)_x$ films were simultaneously deposited on quartz, silicon and nickel substrates for 45 minutes with an average growth rate of 3.3 nm/min. The power of the ion-plasma discharge was 14 Watts. The temperature of the synthesized films did not exceed 50°C; the argon pressure was constant and was equal to 0.7 Pa. The thickness of all the films obtained varied from 50 to 100 nm.

The concentration of silicon and oxygen was determined by the method of energy dispersive spectroscopy (EDS) analysis using Quanta 200i 3D scanning electron microscope (FEI Company, USA) in films synthesized on a nickel polished substrate (Fig. 1). Nickel is the only metal the EDS signal of which does not intersect with spectra from carbon, silicon, and oxygen.

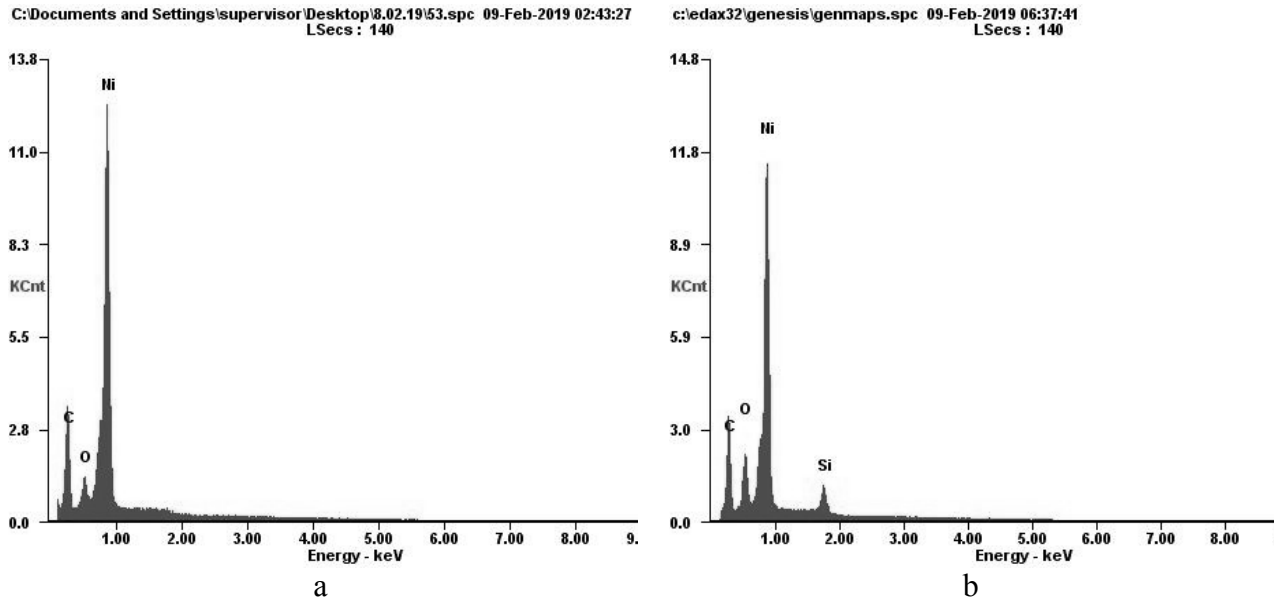


Fig.1. EDS spectra obtained from a) a-C film; b) a-C_{1-x}:(SiO)_x film synthesized on nickel substrate.

In addition, it can be seen that the EDS spectra of other elements were not detected in the synthesized films. The increasing concentration of silicon leads to an increase in oxygen. The thickness of the films was determined on the fresh cleavage of a silicon wafer, as shown in Fig. 2.

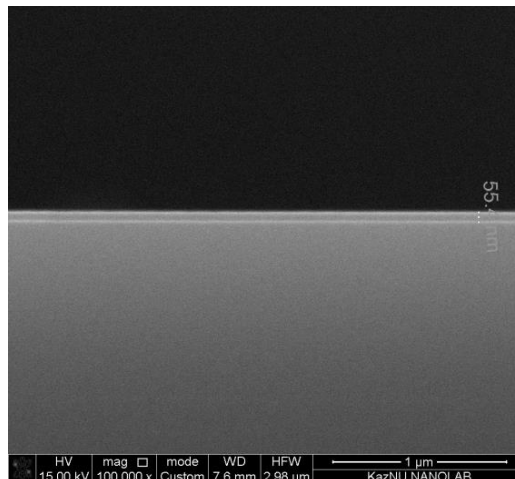


Fig.2. Examples of thickness measurements of a-C_{1-x}:(SiO)_x film

The relative silicon concentration in the amorphous carbon film was calculated without taking into account the oxygen concentration, Table 1. An increase in the EDS peak from oxygen depends both on its presence on the surface of the nickel plate (before the synthesis), and on the surface of the film after taking it out the chamber. In addition, the intensity of the EDS peak of oxygen will be affected by x-rays from nickel atoms. Therefore, taking oxygen into account in calculating the relative concentration would not be correct.

Table 1. The relative silicon concentration in the amorphous carbon film.

Sample Number	1	2	3	4	5	6	7	8	9
$X=X_{Si}/(X_C+X_{Si})$	0	0.04	0.051	0.06	0.07	0.10	0.11	0.12	0.162

Surface topography and phase contrast of the films were studied using atomic-force microscope of Solver Spectrum instrument (NT-MDT, Russia). In addition, the local structure was studied by the Raman spectroscopy method using a NTegra Spectra spectrometer (NT-MDT, Russia).

2. Results and discussions

Topography and phase contrast of the $a-C_{1-x}:(SiO)_x$ films were studied by the method of semi-contact atomic force microscopy. The measurements were carried out using an NSG-01 probe with a radius of less than 10 nm and oscillation frequency of ~ 190 kHz. Fig. 3 (a, c, e) shows the topography of film surface with a relative concentration of silicon in the carbon film being 0, 0.05, 0.16. As can be seen from the figure, the size of the globules forming the film structure increases with increasing concentration of silicon oxide. Figure 3 (b, d, f) shows the phase contrast of the surface; this method of research in atomic-force microscopy shows the existence of regions with different electron density, which would indicate the difference in the phase state of the synthesized films' structure.

Fig. 3 demonstrates that the surface topography patterns of the films with different concentrations of silicon and oxygen are significantly different, but the changes in the phase of probe oscillations are not sufficient (Fig. 3 b, d, f), which can be explained by a change in the surface relief pattern, rather than structural characteristics. Thus, the absence of significant contrast over the entire surface indicates the uniform distribution of electron density over the surface of the synthesized films. Thus, formation of separate structural fragments of silicon and oxygen atoms is absent. The structure primarily forms from carbon and silicon atoms, while oxygen atoms participate as a link between the Si-C and Si-Si structural units.

In confirmation of the above, the local structure of the synthesized films was studied using Raman spectroscopy at an excitation wavelength of 473 nm. Fig. 4 shows a typical Raman spectrum obtained from a-C film. In addition, it can be seen that with increasing concentration of silicon oxide there is an increase in photoluminescence. This is due to the increase in the band gap and concentration of sp^2 C-C bonds [2], which determine the state of the electrons. The π bound and π^* of unbound electron states are responsible for the development of density of allowed states in the top of the valence band and the bottom of the conduction band, respectively. An increase in the formation of sp^2 hybridized bonds and an increase in the energy gap between $\pi - \pi^*$ electron states can involve both silicon and oxygen atoms, which is shown in Fig. 4 as an increase in the slope of the Raman spectrum. As is known [3], it is $\pi - \pi^*$ electronic transitions that are responsible for the appearance of photoluminescence in amorphous carbon, an increase in their concentration results in an increase in photoluminescence. Moreover, an increase in the silicon concentration leads to a shift of the main G peak to the low-frequency region, as shown in Fig. 5.

Figure 5 shows the Raman spectra minus background and photoluminescence. A typical Raman spectrum of amorphous carbon consists of a G peak and a shoulder in the low-frequency region from the main peak; in addition, we observe a second order at a frequency of 3000 cm^{-1} . G peak characterizes stretching of C-C bonds. The appearance of a shoulder in the low-frequency region indicates amorphization of the structure and characterizes the breathing mode of a hexagon molecule of carbon atoms, which is denoted by the D peak [4]. An increase in silicon oxide concentration in a-C film results in disappearance of the shoulder, i.e. D peak.

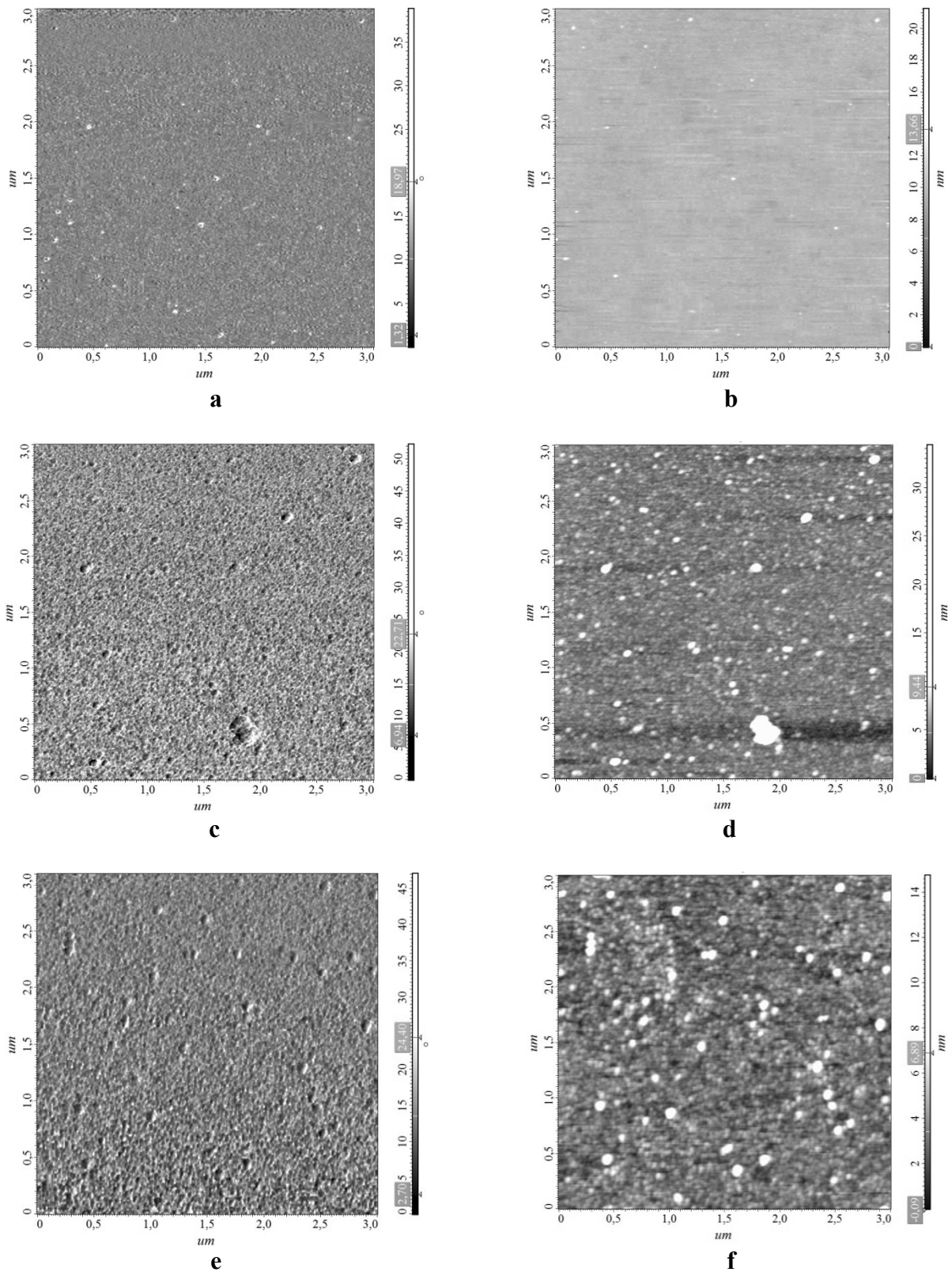


Fig. 3. AFM of a-Canda-C_{1-x}:(SiO)_x films surface with relative silicon concentration in the carbon film 0; 0.051; 0.162:
a, c, e) the surface topography of the films; b, d, f) the phase contrast of the film surface

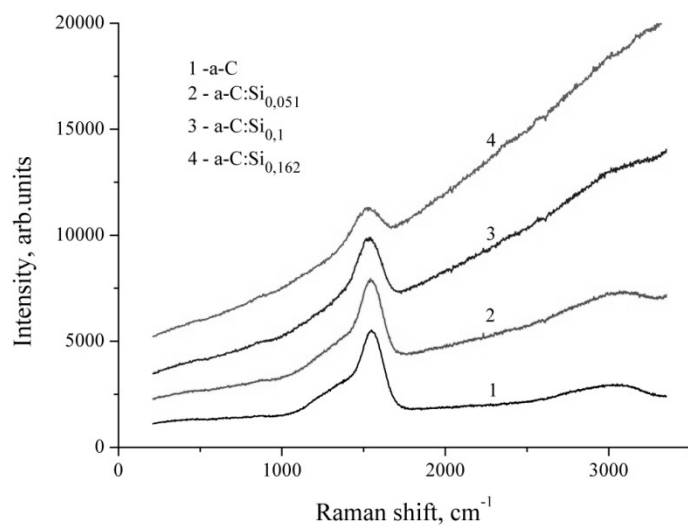


Fig. 4. Raman Spectra from a-C and a-C_x:(SiO)_{1-x} films.

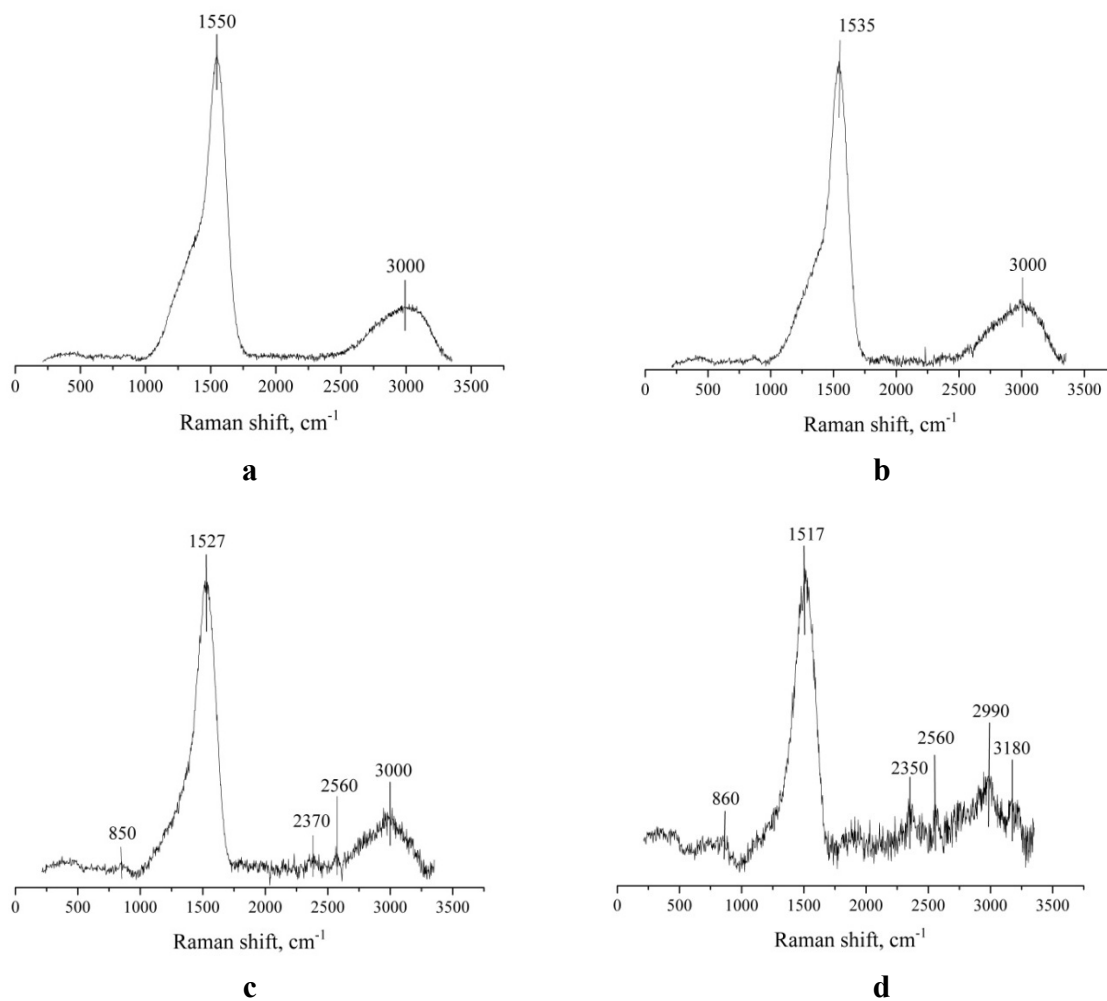


Fig. 5. Raman scattering spectra of a-C_x:(SiO)_{1-x} films: a) X_{Si}=0.0 at.%; b) X_{Si}=0.051 at.%; c) X_{Si}=0.1 at.%; d) X_{Si}=0.162 at.%

This is due to the disappearance of the graphite phase and the transition to a four-coordinated bond of carbon atoms or sp^3 hybridization. At the same time, it should be noted that the appearance of some features within the frequency range of 250 cm^{-1} and 860 cm^{-1} is determined by Si-C bonds and the G peak shift to the low-frequency region of the Raman spectrum also indicates an increase in sp^3 hybridized bonds [5]. As is shown in the work [6], the G band shift to the low-frequency region indicates an increase of sp^3 hybridized bonds in the structure of carbon films. This is apparently due to the occurrence of silicon atoms, which form structures with the carbon atoms of 3C, 4H and 6H. In addition, in the high-frequency region (Fig. 5 c), we observe separation of the second order into a series of frequencies that characterize certain frequencies of bonds with carbon atoms. Apparently, this is due to the presence of silicon atoms in the lattice structure, which in a certain way affect the frequency range of the second-order phonon mode of C-C bonds.

Conclusion

It follows from the above that the surface topography of the synthesized films of amorphous carbon significantly depends on silicon oxide concentration. The study of the films' surface by the phase contrast method in atomic force microscopy had shown a uniform distribution of the structure of C-C, Si-Si, Si-C bonds making up the film. The absence of significant phase contrast indicates the uniform distribution of electron density, and therefore, the absence of the structural SiO_2 units. This means that there is no formation of individual fragments of the silicon and oxygen atoms structure. The structure formation primarily comes from carbon and silicon atoms, while oxygen atoms participate as a link between the structural units of Si-C and Si-Si atoms.

Raman spectroscopy has shown that an increase in the concentration of silicon leads to an increase in photoluminescence. First of all, this is due to the increase in the width of the band gap and concentration of π -electrons.

In addition, it was found that with an increase in the silicon concentration, G peak shifts to the low-frequency region and this indicates an increase in sp^3 carbon atoms. The appearance of carbon atoms in the high-frequency region of second-order peaks is associated with the presence of silicon atoms.

REFERENCES

- 1 Choyke W.J., Pensl G. Physical Properties of SiC. *Material research society Bulletin*, 1997, Vol. 22, Issue 3, pp. 25 - 29.
- 2 Vasiliev V.A., Volkov A.S., Musabekov E., Terukov E.I. Features of photoluminescence of amorphous hydrogenated carbon (a-C:H) films. *Pisma v jurnal tehnikeskoj fiziki*, 1988, Vol. 14, Issue 18, pp. 1675 – 1679.
- 3 Konshina E. A. Absorption and the optical gap of a-C:H films produced from acetylene plasmas. *Semiconductors*, 1999, Vol. 33, Issue 4, pp. 451 – 457.
- 4 Ferrari A.C., Robertson J. Raman spectroscopy of amorphous, nanostructured, diamond-like carbon, and nanodiamond. *Phil. Trans. R. Soc. Lond. A*. 2004, No. 362, pp.2477 – 2512.
- 5 Tomastik J., Ctvrtlik R., Ingr T., Manak J., Opletalova A. Effect of Nitrogen Doping and Temperature on Mechanical Durability of Silicon Carbide Thin Films. *Scientific Reports*, 2018, Vol. 8, No.10428, pp. 1 – 17.
- 6 Ferrari A.C., Robertson J. Interpretation of Raman spectra of disordered and amorphous carbon. *Phys. Rev. B*, 2000, Vol. 61, No. 20, pp. 14095 – 14107.

UDC 535.37; 535.47; 537.635; 543.544.2

HIPOCHROMIC EFFECT IN RIBOFLAVIN SOLUTIONS

Astanov S.Kh., Sharipov M.Z., Kasimova G.K.

Bukhara Engineering-Technological Institute, Bukhara, Uzbekistan, s.h.ostonov@rambler.ru

The process of self-assembly of riboflavin molecules in aqueous and binary mixtures of solvents was investigated by a spectroscopic method. It was shown that the self-assembly of vitamin B2 molecules by the dipole-dipole interaction of van der Waals forces, as a result of which resonant splitting of excited electronic levels of riboflavin occurs. In concentrated solutions and in binary mixtures of solvents, the observed hypochromic effects are due to a decrease in the intensity of the absorption capacity of self-aggregated riboflavin molecules relative to their monomers. The absorption band of self-assembled riboflavin molecules is determined by the obtained linear dichroism spectra in a laminar hydrodynamic flow.

Keywords: Riboflavin, self-aggregation, luminescence, absorption, resonant splitting, electronic levels, hypochromic effect, linear dichroism, dipole-dipole interactions.

Introduction

Recently, interest in silicon carbide films as a promising material for nanoelectronics and Riboflavin (vitamin B₂) is an important and necessary drug for the development and viability of the human body. Vitamin preparation is used in the form of powders, and in the form of aqueous solutions [1, 2]. Self-assembly is a process in which only the components of the final structure are involved [3, 4]. The main condition for the self-assembly of nanoparticles is the formation of a high-molecular local volume [5]. One of the methods for the formation of a local volume with high concentrations is carried out by thermal evaporation of the solvent from a drop of a solution of the dissolved test compound. The authors of [6, 7] obtained ring structures of nanoparticles on the surface of a glass substrate. The assembly of molecules itself can also be carried out in concentrated solutions and in binary mixtures of solvents. The choice of methods for obtaining self-assembled molecules is one of the most pressing issues in this area.

In the process of self-aggregation, depending on the nature of the solvents used, the concentrations of the compounds under study, there is a significant deformation of the electronic spectra of vitamin B₂ and food dyes, in the form of a hypochromic effect [8, 10]. Identifying the nature of the hypochromic effect is one of the urgent problems of condensed matter spectroscopy. The solution of this question may lead to the development of the thermo and photo stability methods of riboflavin depending on the degree of self-aggregation of molecules.

1. The equipment and technique of the experiment.

In the work used powder riboflavin brand "HCH". Electronic absorption spectra were measured on a Specord 50 SA spectrophotometer (Analytik Jena, Germany) allowing measurements in the range of 190-1100 nm. The measurement of fluorescence spectra was carried out on an installation assembled on the basis of two monochromators of the type MDR-76 with photoelectron registration. A FEU-38 (Russia) was used as a photodetector. For the convenience of comparing the absorption and fluorescence spectra, they are normalized to unity. The dispersion of the optical rotation and the linear dichroism spectra were taken on a Jasko-20 dichrograph from an optical set-top box of the double Fresnel parallelepiped used in the visible and UV portions of the spectral region. The following solvents were used: distilled water, ethanol, acetone, chloroform purified according to the procedures, as well as their binary mixtures: ethanol + acetone, ethanol +

chloroform. Binary mixtures were prepared in such a way that the concentration of the test compound remained constant, the ratio of the binary mixture of solvent changed. In the second case, the composition of the binary solvent mixture remained constant, the concentration of riboflavin varied.

2. Results and discussion

2.1. Riboflavin aggregates

In this case, self-assembling of vitamin B2 was carried out by two methods. The first method was that the concentration of the test compound remained constant, the ratios of the binary mixtures changed. In the second case, the compositions of binary mixtures remained constant, but the concentration of vitamin B2 changed.

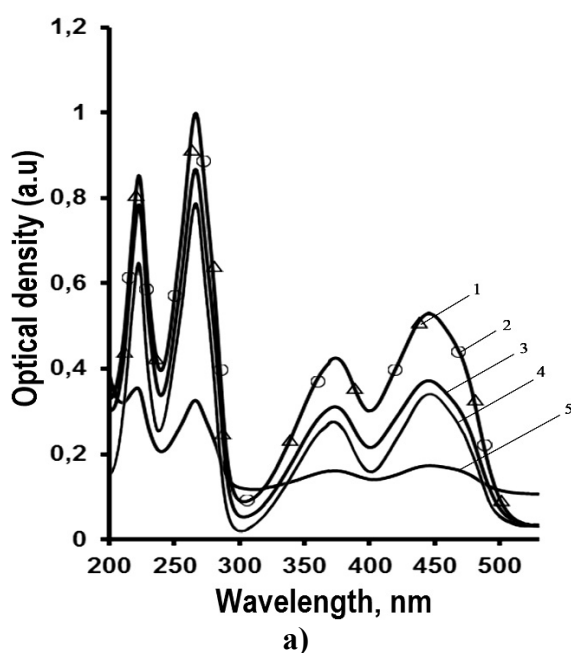


Fig.1a. Absorption spectrum of riboflavin in water (1.2) ($C=2 \cdot 10^{-5}M$) and binary mixtures of alcohol + chloroform (3-5) ($C=4 \cdot 10^{-5}M$) from the share of added chloroform (0-2; 20-3; 40-4; 60-5) in % volume ratio.

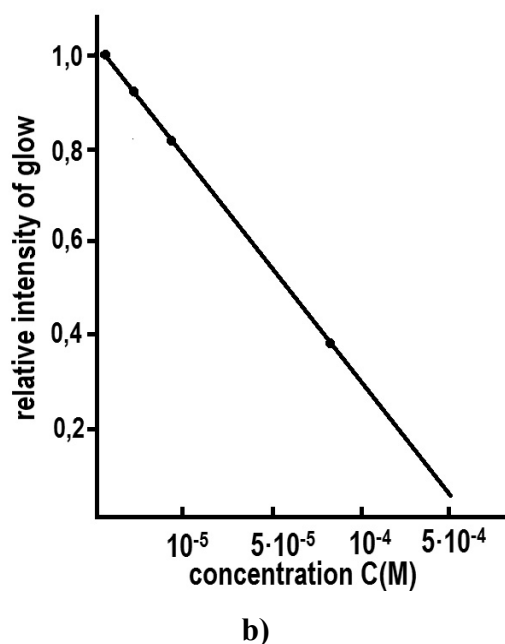


Fig.1b. The dependence of the relative yield of light on the concentration of riboflavin molecules in a binary mixture of solvents alcohol + chloroform (0.35 + 0.65).

Another condition for the use of binary solvents was that they were infinitely dissolved among themselves. As an example, Fig. 1a shows the absorption spectra of riboflavin at a constant concentration ($C = 4 \cdot 10^{-5} M$), the ratios of alcohol and chloroform changed. From figure 1a it can be seen that the absorption spectrum of riboflavin in pure alcohol coincides with the band of vitamin B2 obtained in dilute aqueous solutions. However, as the proportion of chloroform in binary mixtures increases, the integral absorption capacity of riboflavin decreases (curves 3–5, Fig. 1a). In contrast to the absorption spectra, the shape of the fluorescence spectra of the studied molecules with a constant ratio of the binary solvent does not depend on the concentration of the solution and only a decrease in the relative emission yield is observed (Fig. 1b). These phenomena were explained by us the concentration quenching of luminescence. We observed similar concentration quenching of luminescence in binary solvent mixtures for natural dyes. This process is associated with the aggregation of the studied compounds [8-10].

From temperature experiments, the binding energy of self-aggregates of riboflavin molecules was determined. This energy corresponds to the value of 16-20 KJ / mol, which refers to the energy

of the hydrogen bond. On the basis of the experimental results obtained, it can be assumed that a certain binding energy belongs to the alcohol + chloroform system, and riboflavin molecules unite with each other under the action of van der Waals forces. To determine which of the van der Waals forces will lead to the self-aggregation of riboflavin molecules, the distribution of charges on the atoms of vitamin B2 was determined.

2.2. Electronic bands of riboflavin monomers and self-aggregates

On the basis of the results obtained, the dipole moments of the ground (μ) and excited (μ^*), electronic states of the compound under study were calculated [9]. The calculated values of the dipole moments are $\mu=7.222$ Db and $\mu^* = 23.538$ Db, respectively. These values show that riboflavin molecules self-aggregating as results dipole-dipole interaction.

In order to determine the nature of the hypochromic effect in riboflavin solutions, the frequencies ν_{00} were determined at the corresponding intersection point of the normalized absorption and luminescence spectra in the frequency scale for dilute solutions. These values for diluted riboflavin solutions are $\nu_{00} = 20.200$ cm^{-1} (Fig. 2). The most probable transitions to absorption and luminescence for monomeric and self-aggregates of riboflavin molecules were also determined.

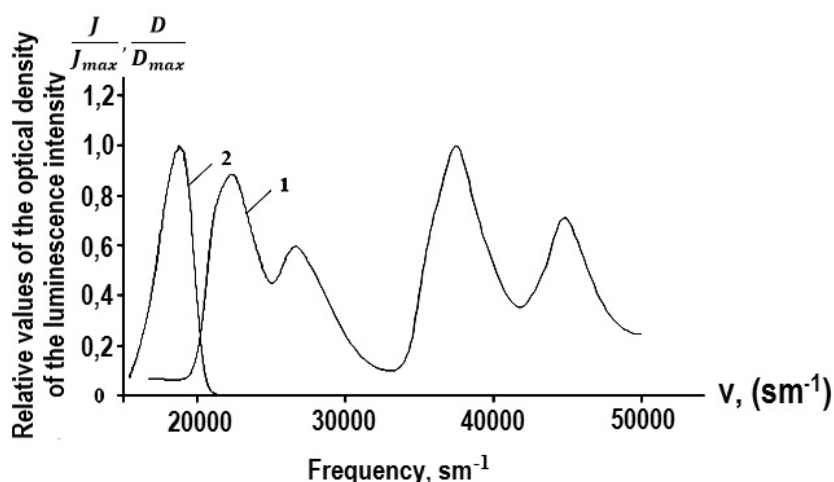


Fig.2. Normalized absorption spectra (1) and fluorescence (2) of dilute solutions of riboflavin ($c = 2 \cdot 10^{-5}$) in water and in alcohol.

The most probable frequency transitions in absorption (ν_p^a) are determined from Fig. 2, for dilute aqueous solutions and binary mixtures of solvents correspond:

$$\nu_p^{a_1}=22300 \text{ cm}^{-1} \text{ and } \sigma_p^{a_1}=4530 \text{ cm}^{-1}; \nu_p^{a_2}=26800 \text{ cm}^{-1} \text{ and } \sigma_p^{a_2}=8580 \text{ cm}^{-1}$$

$$\nu_p^{a_3}=37450 \text{ cm}^{-1} \text{ and } \sigma_p^{a_3}=4660 \text{ cm}^{-1}; \nu_p^{a_4}=44840 \text{ cm}^{-1} \text{ and } \sigma_p^{a_4}=5780 \text{ cm}^{-1},$$

where, σ_p^a is the half-width of the corresponding absorption bands. For a dilute aqueous solution of riboflavin, the maximum of the emission intensity corresponds to the frequency, $\nu_p^f=19050$ cm^{-1} and the half-width of this band has the value $\sigma_p^f=2500$ cm^{-1} .

From fig. 1a, it follows that on the background of the hypochromic effect of absorption and emission bands, the corresponding bands of self-assembled riboflavin molecules do not appear. To obtain the relevant information, we investigated the linear dichroism spectra of the molecules under study. One of these possibilities was realized using the Jasko-20 circular dichrograph with the optical prefix of the double Fresnel parallelepiped. The optical set-top box is designed for studies in the visible and UV part of the spectrum [8, 9].

It was established experimentally that when pumping a solution of self-assembled molecules through a flow cell, they become optically active. Such a flow-through cuvette was developed and

applied to remove the linear dichroism of food dyes and vitamins [11]. Only in this case, the dichrograph registers a different from the zero line of the circular spectrum of linear dichroism. For a clear removal of the linear dichroism spectrum, the rate of solution passage through a flow cell (2mm / hour) was experimentally determined. Such a value of speed was chosen in order to ensure the laminarity of hydrodynamic molasses. In this case, linearly polarized light falls at an angle of 45° on the measuring cell. It has been established experimentally that when pumping solutions of self-assembled molecules through a flow cell, they become optically active.

In fig.3 shows the linear dichroism spectrum of self-collected riboflavin molecules in the frequency scale obtained in a laminar hydrodynamic flow.

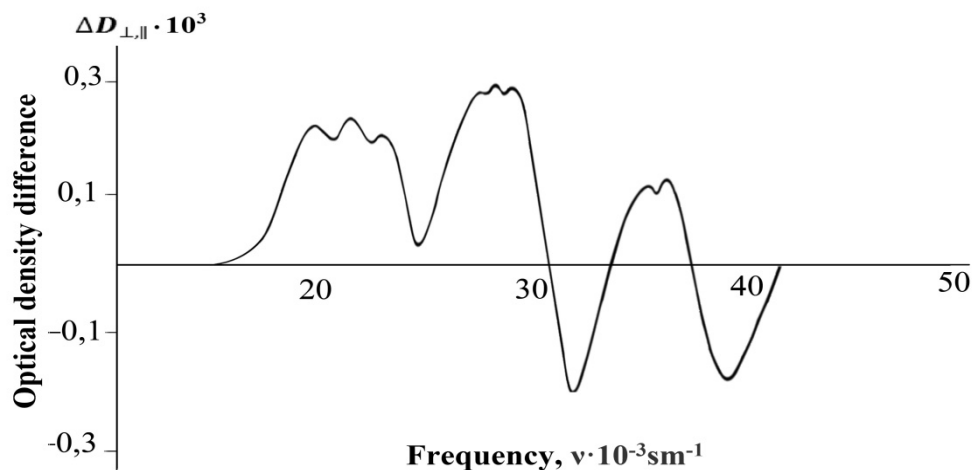


Fig.3. The linear dichroism spectrum of self-collected riboflavin molecules in a laminar hydrodynamic flow.

As can be seen from Fig. 3, the spectrum of linear dichroism is quite informative. The spectral characteristics of the observed bands differ significantly from the absorption spectra of riboflavin monomers obtained in dilute solutions. The parameters of the bands observed in the spectrum of linear dichroism are shown in Table 1.

Using the spectrum of linear dichroism (Fig. 3) and the data presented in Table 1, we can assume that in concentrated solutions, where there is a hypochromic effect, intermolecular interaction (IMI) appears in the form of exciton interaction, which is manifested in concentrated aqueous solutions and binary solvent mixtures of Riboflavin molecules.

Table 1. Energy parameters and optical density differences in linear dichroism of self-assembled riboflavin molecules.

Designations of bands in linear dichroism, ν_c	ν_{max} sm^{-1}	σ_c $\pm 100sm^{-1}$	$\Delta D_{\perp, \parallel} \cdot 10^3 \cdot D$	
			“+”	“-”
ν_{c_1}	21700	1700	0.26	
ν_{c_2}	27800	2000	0.32	
ν_{c_3}	31000	2000		0.22
ν_{c_4}	35000	3400	0.18	
ν_{c_5}	38500	3400		0.16
ν_{c_6}	47800	3800	0,03	

In the Table 1 are used following notations:
 ν_c - numbering of electronic bands;

ν_{\max} -frequency corresponding to the maximum for concentrated solutions of riboflavin;

σ_c is the half-width of the band and

$\Delta D_{\perp\parallel}$ " +", $\Delta D_{\perp\parallel}$ " -" is the difference of the perpendicular and parallel components of optical density with positive and negative values of linear dichroism.

From the analysis of the literature data, it follows that the manifestation of an exciton interaction leads to resonant splitting of the excited electron state [12–13]. Figure 4 shows the scheme of electronic transitions between the normal and excited states of riboflavin in a dilute (m) and concentrated (a) aqueous solution.

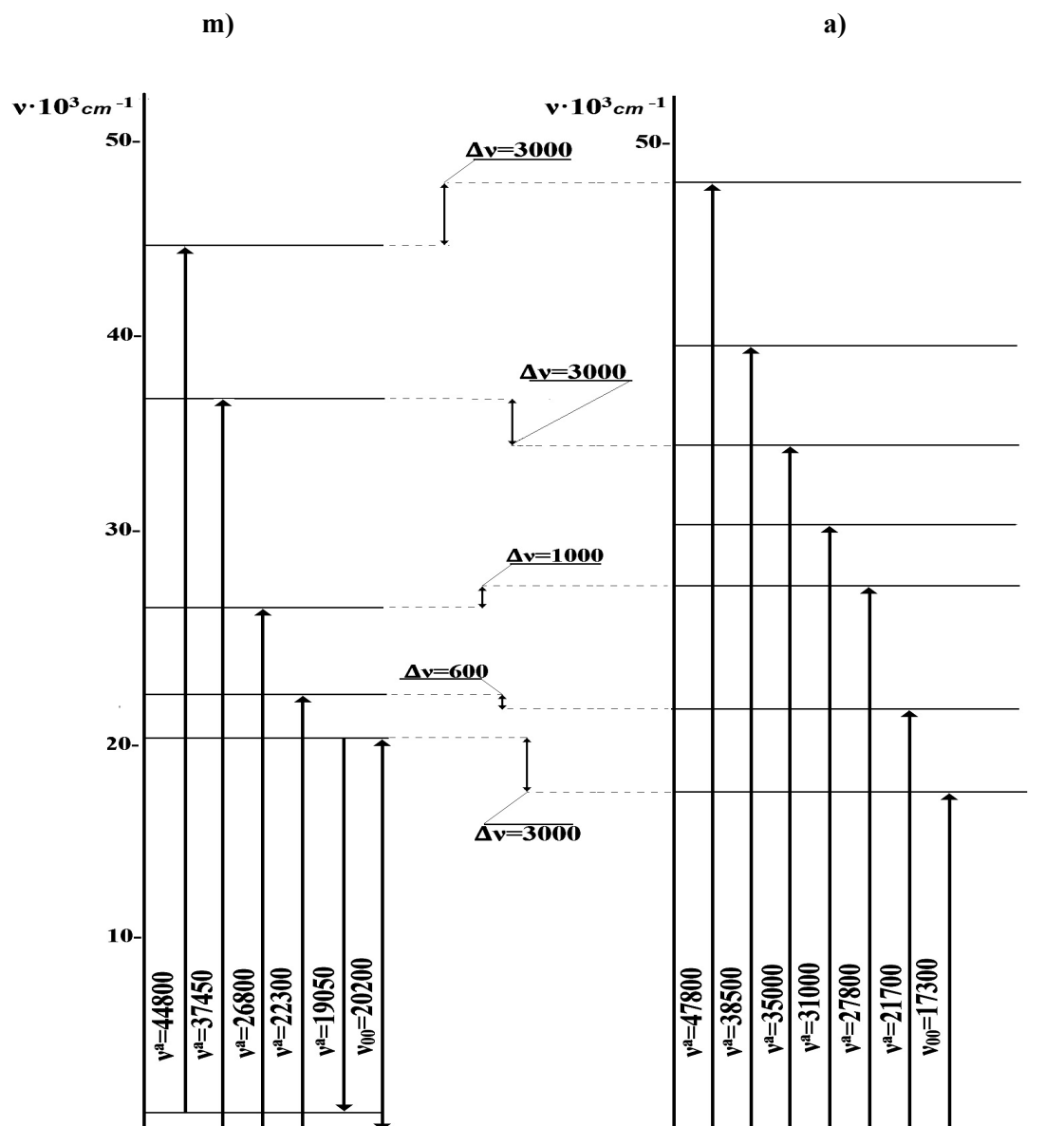


Fig. 4. Diagram of the frequency of electron transitions of monomers (a) and self-aggregates (b) of riboflavin molecules

From fig. 4 it follows that indeed, in concentrated solutions a resonant splitting of the excited electronic state of the vitamin preparation is observed. As can be seen from rice 4, the magnitude of the resonance splitting is $\Delta\nu = 3000 \pm 200 \text{ cm}^{-1}$. In electronic circuits, the thickness of the line indicates electronic transitions that are manifested in the absorption spectrum and linear dichroism.

At the same time, electronic transitions correlate with each other as ratios of optical density values. It also follows from Fig. 4 that, along with the splitting of electronic levels related to the frequency ν_{00} of the transition, splitting is also observed for other electronic levels, the excited states of self-assembled riboflavin molecules.

Conclusion

Thus, it was found that the self-assembly of vitamin B2 molecules is formed by the orientation of monomeric molecules, and they are combined by van der Waals forces. It is shown that as a result of a strong dipole-dipole interaction in a dimeric unit cell, resonant splitting of excited electronic levels occurs, and changes in the probability of electronic transitions in absorption. The first shows that the absorption bands of self-aggregates can be detected in the spectra of linear dichroism of the compounds under study. On the basis of which the nature of the hypochromic effect observed in concentrated solutions of vitamin B2 is explained.

REFERENCES

- 1 Khana S., Rayis M.P., Rizvi A., Alama Md. M., Rizvi M., Naseem I. ROS mediated antibacterial activity of photoilluminated riboflavin: A photodynamic mechanism against nosocomial infections. *Toxicology Reports*. 2019, Vol.6, pp. 136–142.
- 2 Li X., Wu M., Zhang L., Liu H., Zhang L., He J. Riboflavin and ultraviolet A irradiation for the prevention of progressive myopia in a guinea pig model. *Experimental Eye Research*. 2017, Vol.165, pp.1-6.
- 3 Andreeva L.V., Novoselova A.S., Lebedev-Stepanov P.V., Ivanov D.A., Koshkin A.V., Petrov A.N., Alfimov M.V. Patterns of crystallization of solutes from a micro droplet. *Journal of Technical Physics*, 2007, Vol. 77, pp. 22 – 30.
- 4 Roldugin V.I. Self-organization of nanoparticles on interfacial surfaces. *Journal of Chemistry Advances*, 2004, Vol. 73, No. 2, pp. 123 – 156.
- 5 Lebedev-Stepanov P.V. *Introduction to the methods of self-assembly of micro- and nanoparticle ensembles*. Tutorial. Moscow, MEPI, 2012, 280 p.
- 6 Kakhkharov A.M., Bakhramov S.A., Makhmanov U.K., Ismailova O.B., Gafurov Sh.P., Kokharova M.U. The study of the process of self-assembly of fullerene C60 molecules in a binary mixture of ethanol + benzen. *Proceeding of the International Conference*, Samarkand, 2016, September 22-24, pp. 58.
- 7 Kakhkharov A.M., Bakhramov S.A., Makhmanov U.K., Ismailova O.B., Gafurov Sh.P., Kokharova M.U. The study of the process of self-assembly of fullerene C60 molecules in a binary mixture of ethanol + benzen. *Proceeding of the International Conference*, Samarkand, 2016, September 22-24, pp. 59.
- 8 Astanov S.Kh., Sharipov M.Z., Fayzullaev A.R., Kurtaliev E.N., Nizomov N. Thermal destruction of riboflavin in various states of aggregation. *J. Applied spectroscopy*. 2014, Vol. 81, No.1, pp. 37 – 42.
- 9 Astanov S.Kh., Sharipov M.Z., Fayzullaev A.R., Kurtaliev E.N., Nizomov N. Spectroscopic study of photo and thermal destruction of riboflavin. *Journal of Molekular Structure*. 2014, Vol 1071, p. 133 – 138.
- 10 Kurtaliev E.N., Nizomov N, Rahimov Sh.J. The spectral-luminescent and fotochemecal characteristics of several styrylcyanine dyes in solution. *Journal of molecular liquids*. 2011, Vol. 158, pp. 43 – 49.
- 11 Komilov O.S., Turdiev M.R., Kasimova G.K., Muminov A.R., Astanov S.Kh. Structure of Self-Assembled Riboflavin Molecules. *The development of science and technology*. 2018, No. 1, pp. 61 – 69. [in Russian].
- 12 Astanov S.Kh., Kasimova G.K., Turdiev M.R. Spectroscopic manifestations of self-assembly of food dye tartrazine. *Development of science and technology*. 2017, No. 3, pp. 93 – 100. [in Russian].
- 13 Astanov S. *Photonics of molecules of food colorings*. Thesis for the degree of Doctor of Physical and Mathematical Sciences. Tashkent 2003, 53-55p.

UDC 541.18

DIMENSIONAL EFFECTS AND SURFACE ENERGY OF FERROELECTRIC CRYSTALS

Yurov V.M., Baltabekov A.S., Laurinas V.Ch., Guchenko S.A.

E.A. Buketov Karaganda State University, Karaganda, Kazakhstan, exciton@list.ru

To describe the surface tension, a model of the surface layer of atomically smooth ferroelectrics was considered, neglecting the surface roughness. It is believed that a necessary condition for the manifestation of nanostructured properties of a condensed medium is the size dependence of its properties. The surface layer of an atomically smooth crystal consists of two layers, $d(I)$ and $d(II)$. The layer with thickness $h = d$ is called layer (I), and the layer at $h \approx 10d$ is called layer (II) of an atomically smooth crystal. At $h \approx 10d$, the size dependence of the physical properties of the material begins to appear. When $h = d$, a phase transition occurs in the surface layer. It is accompanied by abrupt changes in physical properties, for example, the direct Hall-Petch effect is reversed. It can be concluded that both previous and current results of studies of the surface of condensed media (metals, dielectrics, ferroelectrics, etc.) are due to size effects and the final structures of their existence.

Keywords: surface tension, surface layer, glycine, atomic volume, size dependence.

Introduction

The development of experimental methods of oriented growth of one crystal on the surface of another led to the possibility of obtaining films and superlattices of complex oxides. The structure, size and morphic effects of such heterostructures differ significantly from the structure and properties of bulk single crystals of the same composition [1].

At present, it is also important to create materials, including composite materials, with ferroelectric properties, as well as with multiferroic properties, which can be used, for example, in the manufacture of memory elements or long-term storage media, high-capacity capacitors, microscopic power sources, etc. [2]. Ferroelectric nanocomposite materials as objects whose properties are extremely sensitive to the size effects caused by the increased role of surface effects, which opens up new possibilities for modifying the properties of materials and functional parameters of the devices, special attention is paid [3].

At present, despite a large number of theoretical and experimental studies on the properties of heterogeneous ferroelectric systems, there is no single complete understanding of the laws of modification of the properties of the components of composites [1-3]. It is believed that a necessary condition for the manifestation of nanostructured properties of a condensed medium is the size dependence of its properties [4].

“Normal” size effects are associated with the contribution of surface energy to Gibbs energy. They are called the size effects of the first kind (after Shcherbakov L.M. [5]). Such size effects are characteristic of any systems and are determined by the scattering of quasiparticles (electrons, phonons, etc.) at the boundaries of the system. The phase size effects (size effects of the second kind) are determined by the whole collective of atoms in the system (collective processes). Such size effects are observed only in nanoclusters and nanostructures [6].

In addition to these classical size effects, there are quantum-size effects [7] associated with the quantization of the energy of charge carriers whose motion is limited in one, two, or three directions. The presence of quantum size effects imposes fundamental restrictions on the use of ultra-small nanoelectronic elements [8]. Quantum-size effects are observed when the size of the structure is comparable with the de Broglie wave ($\sim 0.01 - 0.1$ nm).

In this paper, we consider a model of the surface layer of atomically smooth ferroelectrics, neglecting the surface roughness.

1. Surface energy of some ferroelectrics

In [9], the model of the surface layer of atomically smooth metals proposed by us was generalized. Schematically, this model is presented in Fig. 1.

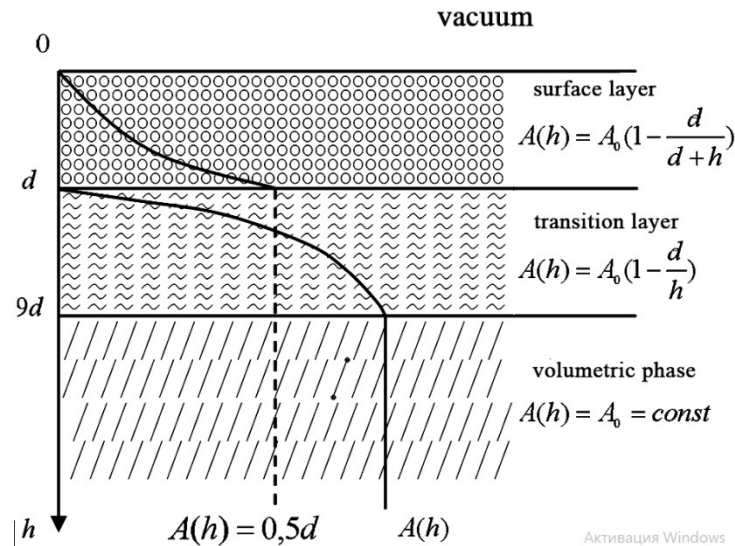


Fig.1. Schematic representation of the surface layer [9].

The surface layer of an atomically smooth metal consists of two layers, d(I) and d(II). The layer with thickness $h=d$ is called layer (I), and the layer at $h \approx 10d$ is called layer (II) of an atomically smooth crystal (Fig. 1). At $h \approx 10d$, the size dependence of the physical properties of the material begins to appear. When $h=d$, a phase transition occurs in the surface layer. It is accompanied by abrupt changes in physical properties, for example, the direct Hall-Petch effect is reversed [10]. The values of the d(I) layer for some metals are given in table 1.

Table 1. The thickness of the surface layer d(I) of some pure metals [9]

Me	d, nm										
Li	0.7	Sr	5.8	Sn	1.4	Cd	1.3	Fe	2.2	Gd	5.3
Na	1.5	Ba	6.2	Pb	1.8	Hg	0.6	Co	2.0	Tb	5.3
K	2.6	Al	1.5	Se	1.3	Cr	2.7	Ni	1.9	Dy	5.3
Rb	2.9	Ga	0.6	Te	2.5	Mo	4.6	Ce	3.8	Ho	5.5
Cs	3.6	In	1.1	Cu	1.6	W	5.8	Pr	4.2	Er	5.5
Be	1.3	Tl	1.9	Ag	2.2	Mn	2.0	Nd	4.5	Tm	5.2
Mg	2.2	Si	3.4	Au	2.3	Tc	3.6	Sm	4.4	Yb	4.6
Ca	4.9	Ge	2.8	Zn	1.1	Re	4.6	Eu	5.8	Lu	5.7

Experimentally, the thickness d (I) can be determined by the method of sliding x-rays. Thus, for gold and silicon, d(I) = 2.4 and 3.4 nm were obtained [11], respectively, which almost coincides with the table. 1.

To determine the thickness of the surface layer of various compounds, we used the dimensional dependence of some physical property $A(r)$:

$$A(r) = A_0 \cdot \left(1 - \frac{d}{r}\right), \quad r \gg d$$

$$A(r) = A_0 \cdot \left(1 - \frac{d}{d+r}\right), \quad r \leq d.$$
(1)

The parameter d is associated with the surface tension σ by the formula:

$$d = \frac{2\sigma v}{RT}.$$
(2)

Here, σ is the surface tension of the bulk sample; v is the volume of one mole; R is the gas constant; T is temperature. In the work [9], and also [12], it was shown that the relation is fulfilled with great accuracy:

$$\sigma = 0.7 \cdot 10^{-3} \cdot T_m,$$
(3)

where T_m is the melting point of the solid (K). The ratio is performed for all metals and for other crystalline compounds. If we substitute it in (2), then at $T = T_m$ we get:

$$d(I) = 0.17 \cdot 10^{-3} v.$$
(4)

Equation (4) shows that the thickness of the surface layer d (I) is determined by one fundamental parameter - the molar (atomic) volume of the element ($v = M/\rho$, M is the molar mass (g/mol), ρ is the density (g/cm³)), which periodically changes in accordance with the table D.I. Mendeleev.

Table 2. Surface tension and thickness of the surface layer of ferroelectrics

Ferroelectric	T_m , K	σ , J/m ²	$d(I)$, nm	$d(II)$, nm
Ba(NbO ₃) ₂	1728 ($T_C = 393$)	1.329	13.1	131
TTC	423 ($T_C = 320$)	0.296	32.5	325
PbTiO ₃	1836 ($T_C = 766$)	1.285	7.1	71
SrTiO ₃	2363 ($T_C = 10$)	1.654	6.1	61
FeTiO ₃	1723 ($T_C < 120$)	1.206	5.2	52
LiNbO ₃	1516 ($T_C \sim 1483$)	1.061	5.4	54
KNbO ₃	1373 ($T_C = 708$)	0.961	6.6	66
BiFeO ₃	1220 ($T_N = 646$)	0.654	7.8	78
PbCu ₃ (VO ₄) ₂ Cl ₂ ¹	743	0.520	24.7	247

In our experiments, we used the size dependence of the dielectric constant [13], magnetic susceptibility [14], and luminescence intensity [15]. In the coordinates $A(r)/A_0 \sim 1/r$, a straight line is obtained in accordance with (1), the tangent of which gives d .

From table 2 it can be seen that the thickness of the surface layer d (I) of ferroelectrics varies from 5 nm for FeTiO_3 to 7.8 nm for BiFeO_3 . Table 2 shows that the surface layer d (II) of some $\text{Ba}(\text{NbO}_3)_2$ and TGS ferroelectrics exceeds 100 nm, which is characteristic of Gleyther nanostructures [16]. But the size dependence of physical properties is also observed in this area. The surface layer d (II) $\approx 10d$ is attributed to the size effects of the first kind. Phase size effects (size effects of type II) are observed in the d (I) region. This area is very different from d (II). The phase transition at $h = d$ can be described in the framework of the Landau mean field theory using the order parameter [17].

The rare mineral $\text{PbCu}_3(\text{VO}_4)_2\text{Cl}_2$, discovered, studied in 1988 and named after the city of Leningrad (now St. Petersburg), has a d (II) surface layer thickness of over 247 nm. This is due, first of all, from equation (4) to a large atomic volume $v = M/\rho$. This means that the thickness of the surface layer depends on the complexity of the structure of the mineral.

2. Discussion of results

In the present work, we consider a model of the surface layer of atomically smooth crystals, neglecting the roughness of the surface, which at the cleavage surface in the vacuum of semiconductors are of the order of 0.05 nm or slightly more. Using the lattice parameter [18], we calculate the number of monolayers R in the d (I) layer of ferroelectrics.

Table 3. How many atoms are from the surface of ferroelectrics?

Ferroelectric	Number of atoms, R	Ferroelectric	Number of atoms, R
$\text{Ba}(\text{NbO}_3)_2$	$a/c = 30/33$	FeTiO_3	$a/c = 10/5$
TTC	$a/b/c = 35/26/57$	LiNbO_3	$a = 10$
PbTiO_3	$a/c = 18/17$	KNbO_3	$a/b/c = 10/14/9$
SrTiO_3	$a = 16$	BiFeO_3	$a/c = 14/6$

An analysis of the rounded data of Table 3 shows that the number of monolayers in the d (I) layer for some $\text{Ba}(\text{NbO}_3)_2$ ferroelectrics and TGS lies in the range of 20-60.

Depending on how the transition from the volume to the surface of a solid body is realized, all surfaces can be divided on the cleavage in vacuum into singular, vicinal and diffusion. On singular surfaces, the transition from the solid to the vapor phase takes place within a single layer, on vicinal surfaces - the transition occurs through several crystallographic planes separated by monoatomic steps, and on diffusion surfaces - the transition from a solid to vapor phase takes place over several atomic layers (Table 3).

The authors of [19] obtained images of the molecular resolution of the TGS polar surface in the contact mode of atomic force microscopy (AFM). According to their estimates, the width and height of the step of the transition layer in the domain wall were ~ 10 nm and ~ 6.9 nm, respectively. It was also suggested that circular protrusions and depressions, whose dimensions differed in the horizontal direction, and the height or depth, as a rule, was 0.6–0.8 nm, appear due to partial dissolution of the TGS surface by adsorbed water molecules, i.e. they are elements of a surface that degrades after splitting a crystal. One of the results of further research was the

observation of the domain structure of ferroelectrics in the nanometer size range in dynamics: during the transition from the ferroelectric phase to the paraphrase and in the process of depolarization in the switching process [20].

Another important result of TGS research is the observation of domain walls with a resolution close to atomic, which made it possible to measure their width [21]. Atomic force microscopy provides unique opportunities for the study of ferroelectric crystals, allowing you to directly visualize domains and record surface distributions of their characteristics, to which a significant number of publications have been devoted in the last decade (see review [22]). According to the results of [22], the height of the step between the TGS domains of a different sign leaves ~ 1 nm and the width of the DS ~ 30 nm (Table 3). The AFM method was used to study a number of ferroelectrics: barium titanate (BaTiO_3), lead titanate (PbTiO_3), ferrite salt ($\text{NaKC}_4\text{H}_4\text{O}_6 \cdot 4\text{H}_2\text{O}$), aluminum guanidinium sulfate (GASH) $\text{C}(\text{NH}_2)_3\text{Al}(\text{SO}_4)_2 \cdot 6\text{H}_2\text{O}$, and guanidinium aluminum sulphate (GASH) $\text{C}(\text{NH}_2)_3\text{Al}(\text{SO}_4)_2 \cdot 6\text{H}_2\text{O}$;) and others. [22]. Even in remote times, X-ray studies performed on BaTiO_3 crystals by Könzig and co-workers [23] showed that in surface layers with a thickness of about 100 (in our case, this is 131 Å, Table 3), the structure is different from the structure of the thickness. In the Curie region (below 120 °C), differences in the structure of the thickness and surface layer are less pronounced, which indicates some tetragonality of the BaTiO_3 surface layers above the Curie point. Könzig suggested that these layers can be interpreted as Shotka-depleted ion layers due to impurities having a concentration of 10^{18} cm^{-3} and creating a field of about $10^5 - 10^6 \text{ V cm}^{-1}$ (which turned out to be wrong in the light of modern research [22]).

Thus, it can be concluded that both previous and current results of studies of the surface of condensed media (metals, dielectrics, ferroelectrics, etc.) are due to the size effects and the final structures of their existence.

Conclusion

From table 2 it can be seen that the thickness of the surface layer $d(I)$ of ferroelectrics varies from 5 nm for FeTiO_3 to 7.8 nm for BiFeO_3 . Table 2 shows that the surface layer $d(II)$ of some $\text{Ba}(\text{NbO}_3)_2$ and TGS ferroelectrics exceeds 100 nm, which is characteristic of Gleyther nanostructures.

It was shown that the relation is fulfilled with great accuracy: where T_m is the melting point of a solid (K). The ratio is performed for all metals and for other crystalline compounds. The resulting equation (4) shows that the thickness of the surface layer $d(I)$ is determined by one fundamental parameter — the atomic volume of the element.

Acknowledgment

The work was performed according to the program of the MES RK. Grants No.0118PK000063 and No. Φ .0780.

REFERENCES

- 1 Anokhin A.S. *Dimensional and morphic effects in epitaxial films of ferroelectrics*. The dissertation of the candidate of physical and mathematical sciences, Rostov-on-Don, SFU, 2015, 136 p.
- 2 Pshenko O.A. *Synthesis, structure and properties of dielectric and ferromagnetic porous glasses and composites with the properties of ferroelectrics and multiferroics based on them*. The dissertation of the candidate of chemical sciences, St. Petersburg, 2017, 212 p.
- 3 Alekseeva O.A. *Dielectric properties and phase transitions in ferroelectric composite materials*. The dissertation of the candidate of physical and mathematical sciences, St. Petersburg, 2018, 133 p.
- 4 Guchenko S.A., Zavatskaya O.N., Yurov V.M., Kasymov S.S., Laurinas V.Ch. Surface energy and the tolman constant of galoganide of alkali metals. *Eurasian Physical Technical Journal*, 2018, Vol.15, No.1(29), pp.48 – 55.

- 5 Shcherbakov L.M. On the statistical evaluation of the excess free energy of small objects in the thermodynamics of microheterogeneous systems. *Reports of the Academy of Sciences of the USSR*. 1966, Vol. 168, No. 2, pp. 388 – 391. [in Russian]
- 6 Uvarov N.F., Boldyrev V.V. Size Effects in the Chemistry of Heterogeneous Systems. *Advances in Chemistry*, 2001, Vol. 70 (4), pp. 307 – 329.
- 7 Tringides M.C., Jatochowski M., Bauer E. Quantum size effects in metallic nanostructures. *Physics Today*. 2007. Vol. 60, No. 4, pp. 50 – 54.
- 8 Arutyunov K.Yu. Quantum Size Effects in Metallic Nanostructures. *DAN Higher School of Sciences, Russian Academy of Sciences*. 2015, No. 3 (28), pp. 7 – 16.
- 9 Yurov V.M., Guchenko S.A., Laurinas V.Ch. Surface layer thickness, surface energy and atomic volume of an element. *Physical and chemical aspects of studying clusters, nanostructures and nanomaterials*, 2018, Vol. 10, pp. 691 – 699.
- 10 Yurov V.M., Laurinas V.Ch., Guchenko S.A. Some questions on the physics of the strength of metallic nanostructures. *Physical and chemical aspects of studying clusters, nanostructures and nanomaterials*, 2013, Vol. 5, pp. 408 – 412.
- 11 Guo J. *X-Rays in Nanoscience: Spectroscopy, Spectromicroscopy, and Scattering Techniques*. Wiley-Vch. Verlag. 2010, 263 p.
- 12 Rekhviashvili S.Sh., Kishtikova E.V., Karmokova R.Yu., Karmokov A.M. To the calculation of the Tolman constant. *Letters to the Journal of Technical Physics*, 2007, Vol. 33, No. 2, pp. 1 – 7.
- 13 Yurov V.M., Portnov V.S., Puzeeva M.P. *Method for measuring surface tension and density of surface states of dielectrics*. Patent RK No. 58155. Publ. 2008, Bull. No.12.
- 14 Yurov V.M., Portnov V.S., Puzeeva M.P. *Method of measuring the surface tension of magnetic materials*. Patent of the Republic of Kazakhstan No. 58158. Publ. 2008, Bull. No.12.
- 15 Yurov V.M. *A method for measuring the surface tension of phosphors*. Patent of the Republic of Kazakhstan No. 23223. Publ. 2010, Bull. No.11.
- 16 Gleiter H. Nanostructured materials: basic concepts and microstructure // *Acta mater*. 2000, Vol. 48, pp. 1 – 29.
- 17 Maritan A., Langie G. and Indekeu J.O. Derivation of Landau theories and lattice mean-field theories for surface and wetting phenomena from semiinfinite ising models. *Physics A*, 1991, Vol. 170, pp. 326 – 354.
- 18 Solntsev Yu.P., Pryakhin E.I. *Materials Science*. SPb. Himizdat, 2007, 783 p. [in Russian]
- 19 Bae M.-K., Horiuchi T., Hara K., Ishibashi Y., Matsushige K. Direct observation of domain structures in Triglicine Sulfate by atomic force microscope. *Jpn. J. Appl.Phys.*, 1994, Vol.33, pp. 1390 – 1395.
- 20 Likodimos V., Labardi M., Allegrini M. Kinetics of ferroelectric domains investigated by scanning force microscopy. *Phys. Rev.*, 2000, Vol. 61, pp. 14440 – 14447.
- 21 Eng L.M., Bammerlin M., Loppacher Ch., Guggisberg M., Bennewitz R., Luthi R., Meyer E., Guntherodt H.-J. Nondestructive imaging and characterization of ferroelectric domains of periodically poled crystals. *Appl. Surf. Sci.*, 1999, Vol. 140, pp. 253 – 258.
- 22 Tolstikhina A.L. *Atomic force microscopy of crystals and films with complex surface morphology*. The dissertation of the doctor of physical and mathematical sciences. Moscow, 2013, 333 p.
- 23 Kentsig V. *Ferroelectrics and antiferroelectrics*. Moscow, 1960, 345 p. [in Russian]

UDK 537.533.34

DEVELOPMENT OF ENERGY ANALYZER OF CHARGED PARTICLES BASED ON THE BASIS NON-UNIFORM ELECTROSTATIC FIELD

Saulebekov A.O.¹, Vénos D.², Kambarova Zh.T.³, Saulebekova D.A.¹,
Vassilyeva K.I.³, Seidualy Kh.B.³

¹Lomonosov Moscow State University, Kazakhstan branch, Nur-Sultan, Kazakhstan

²Nuclear Physics Institute, Czech Academy of Sciences, 250 68 Řež, Czech Republic

³E.A. Buketov Karaganda State University, Karaganda, Kazakhstan, kambarova@bk.ru

The electron-optical characteristics of a mirror energy analyzer based on a non-uniform, hyperbolic decreasing electrostatic field were investigated. In work an approximate-analytical method for calculating the trajectory of charged particles in an electrostatic field, acting in the mirror reflection regime, was used. The equation of motion of charged particles in the integro-differential form is obtained. The scheme of the most optimal variant of the analyzer with a non-uniform field is found.

Keywords: non-uniform field, energy analyzer, mirror reflection regime, electron-optical characteristics, trajectory of charged particles.

Introduction

The great potential of electron spectroscopy, associated with the broad information that the energy spectrum of these particles carries about various physical processes, about the matter structure, stimulates further improvement of the known analysis methods and the development of new directions of electron spectroscopy.

At the initial stage of the development of electron optics, the main research focused on the study of axially symmetric fields with the stigmatic focusing properties of a charged particles beam and the formation of a correct scale-free undistorted image. Electrostatic mirror energy analyzers based on cylindrical, spherical and hyperbolic fields turned out to be the most advanced and widely used devices in the study of small and medium energy electron beams. Among the known classical type fields an electrostatic mirror with a uniform field is the simplest in construction and widely used energy analyzer of charged particle beams.

Further progress in the development of effective methods for studying the solid surface requires a significant modernization of existing or the creation of qualitatively new analyzing systems based on the further development of the theory. The development of high-resolution electron analyzers based on the synthesis of multipoles and a cylindrical field can be attributed to qualitatively new methods [1-10]. To confirm the universality of the obtained results, it is necessary to continue research of analytical systems based on the synthesis of multipoles with other types of classical electrostatic fields. This class of potential fields includes a non-uniform electrostatic field decreasing by a hyperbolic law, which is a superposition of a dipole with a uniform field.

1. Calculation and analysis of the electron-optical properties of an electrostatic non-uniform field

The object of the study is electrostatic non-uniform field acting in the mirror reflection regime, that decreasing by hyperbolic law. The potential is described by the expression

$$U = \frac{U_0}{d} y(1 - Az), \quad (1)$$

where A is dimensionless parameter, at $A=0$ - field (1) is uniform.

The profile of the outer deflecting electrode is determined by calculation the equipotential lines in a non-uniform field. Fig.1 shows a portrait of equipotential lines in an electrostatic non-uniform field at $A = 0.01$.

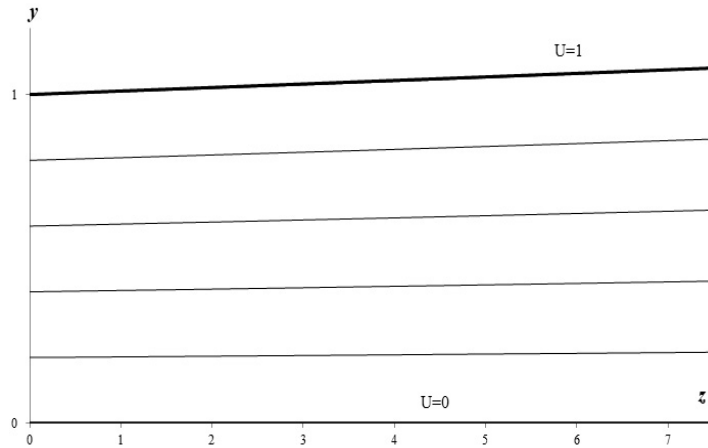


Fig.1. Equipotential lines in a non-uniform field at $A = 0.01$

A field (1) is formed in the space between two electrodes, one of which remains flat and is under the ground potential, the deflecting potential U_0 is supplied to the other electrode, which has a hyperbolic profile (Fig.2).

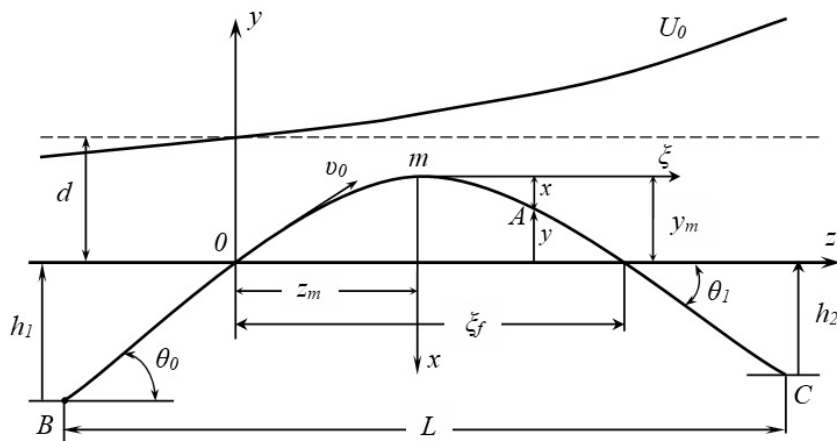


Fig.2. The electrostatic mirror based on non-uniform field.

The dashed line is a flat electrode in the limiting case of a flat mirror (B is source of charged particles; C is electron-optical image of the source)

In the mirror reflection regime a charged particles beam enters field (1) at an angle θ_0 to the z axis, moves along a “return” trajectory having a vertex \mathbf{m} in the electrostatic field region, and returns to the lower electrode at an angle θ_1 . The return trajectory of charged particles consists of right and left branches, asymmetrical about the trajectory vertex \mathbf{m} , therefore, a separate calculation of each of its branches and their subsequent joining is necessary. The condition for joining the right

and left branches of the trajectory is the equality of the functions describing the particles trajectory and their derivatives at the point \mathbf{m} for both branches. For calculate the branches of the return trajectory, let's move to a new coordinate system, the beginning of which is located at the trajectory vertex \mathbf{m} .

According to Fig.2,

$$z = z_m \pm \xi, \quad x = y_m - y. \tag{2}$$

Here, the upper sign in front ξ corresponds to the right branch ($\xi > 0$), the lower sign to the left branch of the trajectory ($\xi < 0$). The distribution of the field (1) in the coordinate system x, ξ has the following form:

$$U(x, \xi) = \omega(1 \pm A'\xi)(y_m - x), \tag{3}$$

where

$$\omega = \frac{U_0(1 - Az_m)}{d}, \quad A' = \frac{A}{1 - Az_m}. \tag{4}$$

According to the law of conservation of energy when moving in an electrostatic potential field, the kinetic energy of a charged particle is determined by the passed potential difference. For a particle moving in the field (3) from point \mathbf{m} to an arbitrary point A , we can write:

$$\frac{m}{2}(\dot{x}^2 + \dot{\xi}^2) - \frac{m v_m^2}{2} = -q(U_m - U) = q\omega G_{1,2}(x, \xi), \tag{5}$$

where

$$G_{1,2}(x, \xi) = x \pm A'\xi(y_m - x). \tag{6}$$

Here and below, the number 1 in the subscript corresponds to the functions for the right branch, the number 2 to the functions of the left branch of the trajectory.

The law of conservation of energy for the longitudinal component of the motion of a charged particle in the field (3), taking into account the condition $v_m^2 = \dot{\xi}_m^2$, because $\dot{x}_m = 0$, as well as the ratio $\frac{d\xi}{dt} = \frac{d\xi}{dx} \frac{dx}{dt} = \xi' \dot{x}$, will be written as follows

$$\frac{m\dot{\xi}^2}{2} - \frac{m v_m^2}{2} = -q \int_0^x \frac{\partial U(x, \xi)}{\partial \xi} \xi' d\xi = \mp q\omega A' \int_0^x (y_m - x) \xi' d\xi, \tag{7}$$

where the derivative ξ' is greater than zero for both branches, as x and ξ are taken in absolute value.

At $x = y_m$, $\frac{m\dot{\xi}^2}{2} = \frac{m v_0^2}{2} \cos^2 \theta_{0,1} = W \cos^2 \theta_{0,1}$, therefore, expression (7) can be rewritten with

respect to $\frac{m v_m^2}{2}$ the following form:

$$\frac{m v_m^2}{2} = q\omega(S' \cos^2 \theta_{0,1} \pm A' f_{m_{1,2}}), \tag{8}$$

where

$$S' = \frac{S}{1 - Az_m}, \quad S = \frac{Wd}{qU_0}, \quad f_{m,2} = \int_0^{y_m} (y_m - x) \xi' dx \quad (9)$$

The value of S has the dimension of length and is some characteristic size of the electron mirror. Solving equations (5), (7) and (8) relatively to ξ' , we come to the integro-differential equation of the trajectory of a charged particle in a non-uniform field (3)

$$\begin{aligned} & \left(\xi'_{1,2} \right)^2 \left[G_{1,2}(x, \xi) \pm A' \int_0^x (y_m - x) \xi'_{1,2} dx \right] = \\ & = S' \cos^2 \theta_{0,1} \pm A' f_{m,2} \mp A' \int_0^x (y_m - x) \xi'_{1,2} dx. \end{aligned} \quad (10)$$

The integral-differential equation (10) has a singular point at $x=0$, since the denominator in this case vanishes, so the solution of the equation is sought as a generalized power series [11]:

$$\xi = \sqrt{x} \sum_{n=0}^{\infty} c_n x^n + \sum_{n=1}^{\infty} a_n x^n. \quad (11)$$

Final results of the calculation of the total projection of the particle trajectory onto the z axis from point source B to its image C are presented below. The equations are obtained in units of the parameter S , which has the dimension of length. According to Fig.2, the total projection of the trajectory from the source to its image is the sum:

$$l = \frac{L}{S} = \frac{1}{S} (H_1 \tan \theta_o + H_2 \tan \theta_1 + \xi_f) = (h_1 \tan \theta_o + h_2 \tan \theta_1 + \xi_f) \quad (12)$$

where in

$$\frac{\xi_f}{S} = 2 \sin 2\theta_o + SA \left(\frac{4}{3} \sin^2 2\theta_o + \frac{8}{3} \sin^4 \theta_o \right) + (SA)^2 \left(\frac{16}{9} \sin^3 2\theta_o + \frac{16}{3} \sin^4 \theta_o \sin 2\theta_o \right), \quad (13)$$

and the inclination angle of the trajectory to the axis at the exit point of the trajectory from the field:

$$\tan \theta_1 = \tan \theta_o + \frac{4}{3} (SA) + \frac{8}{3} (SA)^2 \sin 2\theta_o. \quad (14)$$

Considering the divergence angle $\Delta\theta$ of the beam in the axial plane and the relatively small value of energy spread $\varepsilon = \frac{\Delta W}{W}$ in the beam as small perturbations, one can decompose L into a Taylor series [12]:

$$L = L_o + \frac{\partial L}{\partial \theta} \Delta\theta + \frac{\partial L}{\partial \varepsilon} \Delta\varepsilon + \frac{1}{2!} \left(\frac{\partial^2 L}{\partial \theta^2} (\Delta\theta)^2 + \frac{\partial^2 L}{\partial \varepsilon^2} (\Delta\varepsilon)^2 + \frac{\partial^2 L}{\partial \theta \partial \varepsilon} \Delta\theta \Delta\varepsilon \right) + \dots \quad (15)$$

The second-order angular focusing regime is determined from the condition $\frac{dL}{d\theta} = \frac{d^2L}{d\theta^2} = 0$

$$\cos^2 \theta_o - 3 \sin^2 \theta_o + (SA) \sin 4\theta_o + \frac{4}{3} (SA)^2 \left[\frac{H_2}{S} (\cos^2 \theta_o - 3 \sin^2 \theta_o) + \sin^2 \theta_o (16 \cos^2 \theta_o - 10 \sin^2 \theta_o) \right] = 0. \quad (16)$$

From the analysis of equation (16) it has been established that second-order angular focusing regime can be realized only for the analyzer scheme with parameters $A=0$, $h_1 + h_2 = 0,5$, i.e. for a flat mirror. To search for the parameters of the most optimal variant of analyzer with a non-uniform field decreasing by hyperbolic law, it is necessary to determine the functions $f(\Delta\theta, SA, h_1/h_2) = l(\theta) - l(\theta_o)$ characterizing the longitudinal aberration smearing of the image near the Gaussian focus by the formula (12) for different values of SA and the selected divergence angle $\Delta\theta$ of the analyzed beam.

The aberration smearing functions of electron-optical mirrors with a non-uniform field (Table 1), whose schemes correspond to different values of SA , were calculated and tuned to the second-order angle focusing regime of the flat mirror $h_1 + h_2 = 0,5$, $\theta_o = 30^0$.

Table 1. The aberration smearing functions of electron mirrors with a non-uniform field

SA	θ_1 (deg)	l_θ	$f(\Delta\theta, SA, h_1/h_2)$
0.000	30	2.5981	0.0268
0.005	29.9043	2.6056	0.0154
0.010	29.8082	2.6133	0.0117
0.015	29.7118	2.6210	0.0079
0.020	29.6149	2.6289	0.0063
0.025	29.5178	2.6368	0.0074
0.030	29.4202	2.6449	0.0097
0.035	29.3224	2.6530	0.0125
0.040	29.2242	2.6613	0.0157
0.045	29.1257	2.6697	0.0188
0.050	29.0269	2.6781	0.0220

From the results of calculation the trajectories performed for the angular spread $\Delta\theta = \pm 6^\circ$ of particles at the analyzer entrance, a scheme was found for the most optimal variant of analyzer with a non-uniform field: $h_1 + h_2 = 0,5$, $\theta_o = 30^0$ and $SA = 0.02$. In this case the value of the aberration smearing $f(\Delta\theta, SA, h_1/h_2)$ is 3 times less than the flat mirror ($SA = 0$). This means that in a mirror analyzer built on the basis of a non-uniform electrostatic field that decreasing by a hyperbolic law, which is a superposition of a dipole with a uniform field, the resolution can be improved several times as compared with the case of a flat mirror.

Conclusion

A theoretical study of the electron-optical properties of an analyzing system based on a mirror with a modified electrostatic field has been carried out. Equation of total projection of the particle trajectory on the axis from the source to the image was obtained. The aberration smearing functions of electron mirrors with a non-uniform field were calculated. The optimal variant of the analyzer scheme with a non-uniform field has a higher resolution than a flat mirror.

REFERENCES

- 1 Ashimbaeva B.U., Chokin K.Sh., Saulebekov A.O. Focusing properties of a mirror analyzer with hexapole cylindrical field. *J. of E.Spect. and Rel. Phen.* 2005, 143 (1). pp. 29-32.
- 2 Saulebekov A.O., Assylbekova S.N., Kambarova Zh.T., Tussupbekova A.K. Calculation of the charged particles trajectories in the hexapole cylindrical field. *Eurasian Physical Technical Journal.* 2011, V.8, No.2(16). - pp. 41-49.
- 3 Ashimbaeva B.U., Chokin K.Sh., Saulebekov A.O., Kambarova Zh.T. Modeling of electron-optical scheme of hexapole-cylindrical analyzer. *Applied Physics.* 2012, Issue 2, pp.45-48.
- 4 Assylbekova S.N., Saulebekov A.O., Kambarova Zh.T. Numerical modeling of the electrostatic energy analyzer based on hexapole-cylindrical field with a concave outer electrode. *Eurasian Physical Technical Journal.* 2015, V.12, No 1 (23). pp.25-29.
- 5 Saulebekov A.O., Kambarova Zh.T., Saulebekova D.A. Modeling of electrostatic decapole-cylindrical mirror analyzer. *IOP Conf. Series: Materials Science and Engineering.* 2017, 168, 012078 doi:10.1088/1757-899X/168/1/012078
- 6 Saulebekov A.O., Kambarova Zh.T. Development of mirror energy analyzer based on electrostatic quadrupole-cylindrical field. *Eurasian Physical Technical Journal.* 2017, V.14, No 2 (28), pp.42-47.
- 7 Kambarova Zh.T., Trubitsyn A.A., Saulebekov A.O. Axially symmetric energy analyzer based on the electrostatic decapole-cylindrical field. *Technical Physics.* 2018, Vol. 63, No. 11, pp. 1667–1671.
- 8 Saulebekov A.O., Kambarova Zh.T. Calculation and modeling of the motion of charged particles in the quadrupole-cylindrical field. *Eurasian Physical Technical Journal.* 2018, V.15, No 1 (29), pp.55-60.
- 9 Saulebekov A.O., Trubitsyn A.A., Kambarova Zh.T., Saulebekova D.A. Electrostatic energy analyzer of charged particles on the basis of a quadrupole-cylindrical field in the “ring-axis” focusing regime. *Eurasian Physical Technical Journal.* 2018, V.15, No 2 (30), pp.35-39.
- 10 Wannberg B. An electrostatic mirror spectrometer with coaxial electrodes for multi-detector operation. *Nuclear Instruments and Methods.* 1973, Vol. 107, pp. 549 – 556.
- 11 Zashkvara V.V., Ashimbayeva B.U., Chokin K.SH., Masyagin V.Ye. Raschet trayektoriy zaryazhennykh chastits v elektrosticheskom neodnorodnom pole [Calculation of the trajectories of charged particles in an electrostatic non-uniform field]. *News of the National Academy of Sciences of the Republic of Kazakhstan. Series Physico-Mathematical.* 2000, №2, pp.72-78.[in Russian]
- 12 Gurov V.S., Saulebekov A.O., Trubitsyn A.A. Approximate-Analytical Method of Calculating the Charged Particle Trajectories in Electrostatic Fields (Book Chapter). *Advances in Imaging and Electron Physics.* 2015, V.192, pp. 87-115.

UDC 53.096

DIFFUSIVE SPECTRA OF ANTISTOKES WING OF PHOTOLUMINESCENCE OF CARBON NANOSTRUCTURES

Kumekov S.E., Saitova N.K.

Kazakh National Research Technical University named after K.I. Satpaev, Almaty, Kazakhstan,
skumekov@mail.ru

In paper the photoluminescence radiation with a wavelength shorter than the wavelength of the exciting light that usually have been called anti-Stokes, is studied. These features of photoluminescence were observed previously in such carbon-containing objects as amorphous hydrogenated carbon α -C: H and native biopolymer-collagen. The general structural property of these objects is the presence of carbon hexagons — the nuclei of the benzene ring. A dimer-excimer model of photoluminescence in carbon nanostructures was developed to explain the anti-Stokes wing of the spectra. The temperature dependence of the distribution function of thermally activated pre-excited states in carbon-containing objects is determined. The spectral dependence of the intensity of the anti-Stokes wing taking into account the density of states in the excimer well is calculated.

Keywords: carbon quantum dots, photoluminescence of carbon-containing objects, anti-Stokes radiation, photodissociation, dimeric-excimer model.

INTRODUCTION

Relatively recently [1–6], interesting features of the photoluminescence (PL) of carbon quantum dots (CQD) were discovered: the wide structureless band in the visible spectral region, the half width, the photon energy at the band maximum, and whose shortwave edge depend on the energy of the excitation quantum. Similar features of PL were observed previously in such carbon-containing objects as amorphous hydrogenated α -C: H carbon [7] and native biopolymer-collagen [8]. An additional feature of the PL spectra of α -C: H and collagen was the observation of anti-Stokes radiation (ASR) at temperatures above the temperature of liquid nitrogen. With an increase in the temperature of the samples, the spectral range of the ASR wing expanded to the short wavelength region. Measurements of attenuation kinetics showed the fluorescent character of ASR.

In [7], the observed ASR is explained by the recombination of carriers thermally excited by localized states above the excitation level (Fig. 1). In [8], a qualitative assumption was made about the excimer nature of PL in collagen (Fig. 2).

The general structural property of these objects [1–8] is the presence of carbon hexagons — the nuclei of the benzene ring. The structural feature of the above objects can lead to the formation of sandwich structures [9] representing physical dimers of carbon hexagons-aromatic rings, or their combination, while the term dimer means a physical dimer consisting of two monomers [9].

Dimers can be of different geometry. With a parallel arrangement of monomers, the dimer represents a sandwich structure. It is these dimers that are discussed in this article. In such dimers, monomers are considered as flat graphene-like clusters of different sizes, depending on the number of hexagons forming the cluster.

In the present work, a similar representation of the structure allowed us to develop a dimer-excimer model of radiative processes and explain the main features of the experimental ASR PL spectra in α -C: H and collagen.

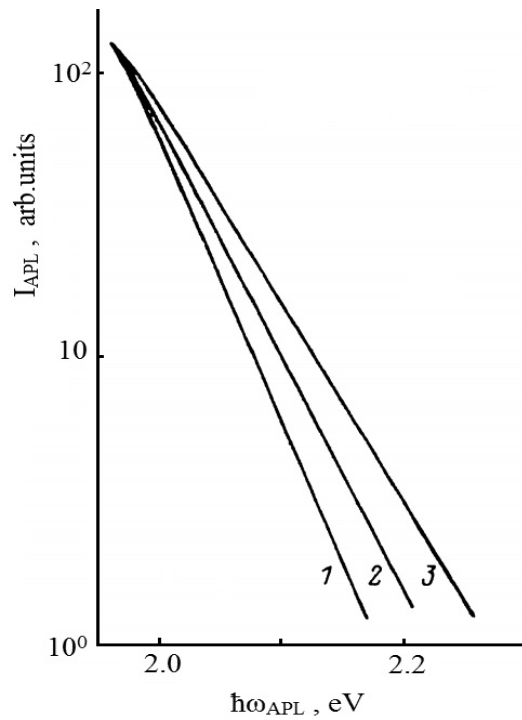


Fig.1. Experimental spectra of ASR in amorphous hydrogenated carbon α -C: H [7]

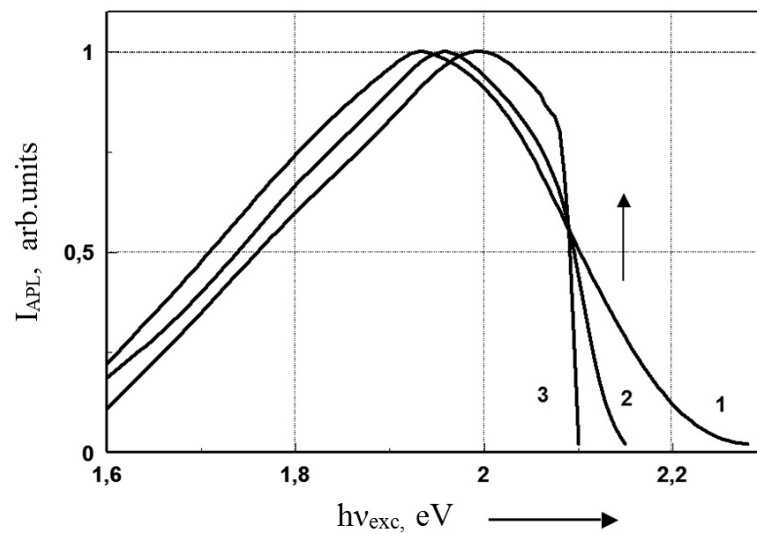


Fig.2. PL spectra of NC, measured at excitation $h\nu_{\text{exc}} = 2.14$ eV. (arrow) and three temperatures: 1-300 K, 2-78 K, 3-4.2 K [8].

1. Model

Figure 3 illustrates the pattern of the origin of the diffuse emission spectrum of an excimer [10]. E_1 and E^* are the electronic terms of the ground and excited states of an excimer; $\hbar\omega_e$ is the energy of a quantum of excitation and resonant fluorescence at transitions 1-1', $\hbar\omega_{\text{APL}}$ is the energy of a quantum of anti-Stokes radiation at transitions 2-2'. The energy interval between states 1 and 1' is ε , and states 2 and 2' is δ . Then $\varepsilon = \hbar\omega_{\text{APL}} - \hbar\omega_e - \delta$.

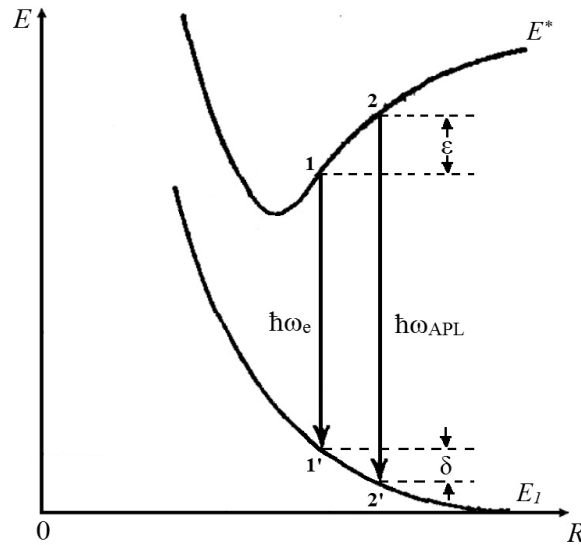


Fig.3. The origin of the diffuse emission spectrum of the excimer [10].
 E_1 and E^* - electronic terms of the ground and excited states

The AS intensity of the PL wing is proportional to the photodissociation cross section σ_{PD} , the concentration of N_{exc} excimer states, and the energy distribution of thermally activated pre-excited states

$$e^{-\varepsilon/kT},$$

where $\varepsilon = \hbar\omega_{APL} - \hbar\omega_e - \delta$.

$$I_{APL} = \sigma_{PD} \cdot N_{exc} \cdot \exp[-(\hbar\omega_{APL} - \hbar\omega_e - \delta)/kT] \tag{1}$$

Photodissociation cross section

$$\sigma_{PD} = \frac{\pi^2 c^2 \hbar^3}{(\hbar\omega)^2 \Delta \tau_{sp}} \tag{2}$$

here c is the speed of light, $\hbar\omega$ is the radiation quantum energy, Δ is the effective width of the emission band, τ_{sp} is the lifetime of the excited state with respect to spontaneous transitions.

In the diffuse model of the origin of PL [10], the width of the emission band is proportional to the amplitude of the monomer oscillations. In the harmonic approximation, we can write the amplitude of monomer oscillations in the form

$$a_v = \sqrt{\frac{2\varepsilon_T}{\mu\omega_0^2}},$$

where ε_T is the oscillator energy, which is generally temperature dependent, μ is the mass, and ω_0 is the natural frequency.

As is known, the average energy of the oscillator's energy, which depends on temperature, has the form

$$\varepsilon_T = \frac{\hbar\omega_0}{2} + \frac{\hbar\omega_0}{\exp\frac{\hbar\omega_0}{kT} - 1}$$

At high temperatures, when $kT \gg \hbar\omega_0$ can be written

$$\varepsilon_T \approx kT$$

Then for the effective width of the spectrum at high temperatures, the expression

$$n\Delta \sim \sqrt{kT}$$

And for the photodissociation cross section of the excimer is true

$$\sigma \sim \frac{1}{\sqrt{kT}}$$

2. The intensity of the anti-Stocks radiation

The intensity of the ASR PL in relative units will be equal to

$$I = \frac{(\hbar\omega_e)^2 \sqrt{\varepsilon_0}}{(\hbar\omega_{APL})^2 \sqrt{\varepsilon_T}} \exp\left(-\frac{\hbar\omega_{APL} - \hbar\omega_e - \delta}{kT}\right)$$

Here $\hbar\omega_{APL} - \hbar\omega_e - \delta$ is the energy of the pre-excited state, counted from state 1. From the last equation, you can find δ values depending on ω_{APL} and temperature T from a comparison with the results of [7] and, accordingly, ε values.

The intensity of radiative transitions involving pre-excited states depends not only on temperature, but also on the density of states in the excimer well. It can be assumed that the electron-oscillation spectrum of states in the excimer well will be close to quasicontinuous at energies above the bottom of this well. Taking this assumption into account, we approximate the density of states by the expression $\rho(\varepsilon) \sim \exp\left(\frac{\varepsilon}{\varkappa_0}\right)$. Then the intensity of the radiative transitions can be written:

$$I_{APL} \sim \exp\left(-\frac{\varepsilon}{kT}\right) \cdot \exp\left(\frac{\varepsilon}{\varkappa_0}\right) \quad (3)$$

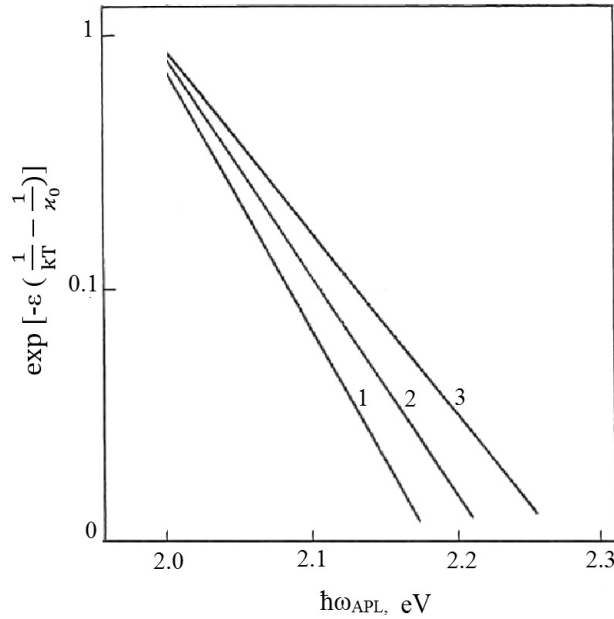


Fig.4. The intensity of radiative transitions in relative units, taking into account the density of energy states.

In Fig. 4, the calculated values of I_{APL} are calculated by formula (3) at different temperatures. The characteristic features of the particle are determined by the characteristic energy \varkappa_0 at various temperatures, the equals 0.023 eV (300 K), 0,026 eV (340 K) and 0.266 eV (370 K). The small increase of the maximal value of \varkappa_0 with the increasing of the temperature can be connected the nonparabolicity of term E^* .

Conclusions

An additional feature of the PL spectra of α -C: H and collagen was the observation of anti-Stokes radiation at temperatures above the temperature of liquid nitrogen. It is proposed the dimer-excimer model of the photoluminescence of carbon quantum dots to explain the features of the spectra. The temperature dependence of the distribution function of thermally activated pre-excited states is calculated. The spectral and temperature dependence of the anti-Stokes photoluminescence wing in amorphous hydrogenated carbon α -C: H and native biopolymer-collagen are explained.

ACKNOWLEDGEMENTS

The research was carried out within the framework of the grant of the Science Foundation of the Republic of Kazakhstan No. №AP05132875.

REFERENCES

- 1 Libin Tang, Rongbin Ji, Xiangke Cao, Jingyu Lin, Hongxing Jiang, Xueming Li, Kar Seng Teng, Chi Man Luk, Songjun Zeng, Jianhua Hao, and Shu Ping Lau. Deep ultraviolet photoluminescence of water-soluble self-passivated graphene quantum dots. *ACS Nano*, 2012, No. 6 (6), pp. 5102 – 5110.
- 2 Juan Peng, Wei Gao, Bipin Kumar Gupta, Zheng Liu, Rebeca Romero-Aburto, Liehui Ge, Li Song, Lawrence B. Alemany, Xiaobo Zhan, Guanhui Gao, Sajna Antony Vithayathil, Benny Abraham Kaiparettu, Angel A. Marti, Takuya Hayashi, Jun-Jie Zhu, and Pulickel M. Ajayan. Graphene quantum dots derived from carbon fibers. *Nano Lett.*, 2012, No. 12 (2), pp. 844–849.
- 3 Mahasin Alam Sk, Arundithi Ananthanarayanan, Lin Huang, Kok Hwa Lim and Peng Chen. Revealing the tunable photoluminescence properties of graphene quantum dots. *J. Mater. Chem.*, 2014, No.2, pp. 6954 – 6960.
- 4 Yonghun Shin, Jintaek Park, Daesun Hyun, Junghee Yang, Jae-Hyeok Lee, Jae-Ho Kim and Hyoyoung Lee. Acid-free and oxone oxidant-assisted solvothermal synthesis of graphene quantum dots using various natural carbon materials as resources. *Proceeding of the Int. Conf. "Electronic Supplementary Material (ESI) for Nanoscale"*, 2015, pp. 5633 – 5637.
- 5 Youfu Wang and Aiguo Hu. Carbon quantum dots: synthesis, properties and applications. *J.Mater.Chem.*, 2014, No. 2, pp. 6921 – 6939.
- 6 Li F., Liu C., Wang Z., Liu W. and Tian F. Mg/N double doping strategy to fabricate extremely high luminescent carbon dots for bioimaging. *RSC Adv.*, 2014, No. 4, pp. 3201 – 3205.
- 7 Vasil'yev V.A., Volkov A.S., Musabekov E., Terukov E.I., Chernyshov S.V. Antistoksovskoye izlucheniye amorfnykh plenok ugleroda a-C:H. *Fiz. Tverd. Tela*, 1990, Vol. 32, No. 3, pp.784 – 788. [in Russian]
- 8 Volkov A.S., Kumekov S.E., Syrgaliev E.O., Chernyshov S.V. Polosa fotolyuminestsentsii i antistoksovo izlucheniye nativnogo kollagena v vidimoy oblasti spektra. *Biofizika (Biophysics)*, 1991, Vol.36, No. 5, pp.770 – 773. [in Russian]
- 9 J. Guillet. *Polymer photophysics and photochemistry*. Cambridge University Press, Cambridge, 1985, 391 p.
- 10 Shpolsky E.V. Diffuse spectra and chemical problems. *UFN*, 1933, No. 8, pp. 325 - 366. [in Russian]

UDC 538.1: 548

EFFECT OF INHOMOGENEOUS RADIALY DIRECTED MECHANICAL STRESSES ON THE DOMAIN STRUCTURE OF A FeBO_3 SINGLE CRYSTAL

Sharipov M.Z., Mirzhonova N.N., Hayitov D.E.

Bukhara Engineering – Technological Institute, Bukhara, Uzbekistan, m.z.sharipov@rambler.ru

The effect of inhomogeneous radially directed mechanical stresses on the domain structure of a FeBO_3 single crystal is studied by a magneto-optical method. It was found that in the magnetic field applied in the FeBO_3 basal plane along the direction of the compressive force, a system of wedge-shaped domains appears in the process of magnetization in the crystal, which exists in a certain temperature-dependent interval of fields in the H_0 range of H_c values. The discussion of the results obtained was carried out within the framework of the thermodynamic theory of the domain structure. It is shown that the theoretical model used well allows one to describe the experimentally observed relative change in d as a function of the magnetic field and temperature.

Keywords: single crystal, domain structure, magnetic field, temperature, thermodynamic theory, magneto-optics, mechanical stresses.

Introduction

Iron borate (FeBO_3) is an easy-plane weak ferromagnet transparent in the visible spectral region, which makes it a convenient object for visual study of the magnetic state and magnetization process of this class of magnetically ordered crystals by the magneto-optical method. For example, in [1, 2], using a polarization microscope using the Faraday method, the domain structure (DS) of FeBO_3 was studied, as well as the influence of compressive mechanical stress and an external magnetic field applied in the basal plane of the crystal. As a result of the studies performed in [1, 2], it was found, in particular, that both the relative orientation of the spontaneous magnetization vector \mathbf{m} in adjacent domains and the direction of domain walls (DW) in FeBO_3 are extremely sensitive to the presence of mechanical stresses in the crystal.

In contrast to [1, 2], where the experiments were carried out under conditions of uniform uniaxial crystal voltage, the results of studies of the effect of heterogeneous mechanical stresses on the FeBO_3 DS are presented below.

1. Samples and experimental technique

A sample of a single crystal of FeBO_3 (space group - D_{3d}^6) used in the experiments was a flat-parallel plate of almost regular hexagonal shape with a thickness of $\sim 45 \mu\text{m}$ with transverse dimensions of 3 mm. The developed faces of the crystal coincided with the plane of easy magnetization (with the basal plane). The crystal surfaces had a sufficiently high optical quality and were not subjected to any additional processing.

DS studies were carried out in the region of maximum transparency of FeBO_3 (in the region of wavelengths of $0.52 \mu\text{m}$) “to the light”. The image of the domains was observed visually in a polarizing microscope and recorded with a digital camera docked with the computer. The magneto-optical contrast of the DS image was due to the difference in the sign of the Faraday effect in the neighboring domains. Since the magnetic structure of FeBO_3 makes it possible to observe the

Faraday effect only at an angle to the optical axis (axis C_3) of the crystal (magneto-optical rotation occurs due to the projection of the vector \mathbf{m} on the direction of light propagation appearing with this crystal orientation) [3, 4], in the experiment the sample was oriented so that the normal to its basal plane (axis C_3) was made with the direction of the incident light angle 10° .¹

The sample was placed in a nitrogen optical cryostat, providing observations in the temperature range of $90 \leq T \leq 290$ K. The magnetization system, consisting of two pairs of Helmholtz coils, made it possible to create in the sample location region along two mutually perpendicular directions a uniform magnetic field of strength $H \leq 50$ Oe (in all experiments the vector \mathbf{H} lies in the plane of the sample).

To reveal the effect of mechanical stresses on the magnetic state of FeBO_3 , all experiments were duplicated on an “unstressed” crystal and a crystal subjected to a non-uniform voltage, and the results were compared with each other.

In the second case, the sample was glued with one of its corners (glue BF - 2) to the copper washer (see below Fig. 1c), which was attached to the cryostat cooler. As the temperature decreased from room temperature, as the temperature cooled, a washer deformed, which was transferred to the sample, causing its non-uniform stress.

2. Experimental results and discussion

At room temperature in the demagnetized state, the sample under study had a two-layer DS with orientation of the domain walls in the basal plane along directions close to the directions of the C_2 axes (the orientation of which was determined by the natural faceting of the crystal), which are the light axes of the intra plane hexagonal anisotropy [5, 6] (Fig. 1a). Such a DS is characteristic of stress-free thin FeBO_3 plates [1, 2]. It is known [1, 2, 6] that in this case the azimuth of the spontaneous magnetization vector \mathbf{m} in adjacent domains in the sample plane differs by approximately 180° , and the boundaries between the domains are Neel-type domain walls (the boundary between the domain layers is the Bloch domain wall, the plane of which parallel to the basal plane of the crystal). As experiments have shown, the DS of the crystal, observed in the case of a “non-stressed” sample, is practically independent of temperature in the entire investigated range of $90 \leq T \leq 290$ K. The DS of the “glued” sample behaves differently: as the temperature decreases, starting at approximately $T = 270$ K, the Neel walls gradually become bent, and the DS turns from a two-layer into through, taking the form of sectors of concentric rings of approximately equal thickness, (fig.1 b).

Referring to fig. 1b, it can be noted that the maximum contrast of the image of the DS is observed in the central part of the sample, with the degree of clarity of the image of the domains practically unchanged throughout the sample area along the vertical Y axis (the orientation of the axes of the selected coordinate system is shown in Fig. 1 c). This non-uniformity of the image contrast is not the result of the defocusing of the microscope optical system, but arises as a result of a change in the azimuthal angle of the vector \mathbf{m} in the basal plane of the crystal.

Indeed, as already noted, the angle of the Faraday rotation at a given point of the sample plane with the x and y coordinates is determined by the projection of the local vector \mathbf{m} to the direction of light propagation, i.e.

$$F \propto m \sin \varphi \sin \theta,$$

where $\varphi = \text{const} \approx 10^\circ$ - angle of light on the sample plane, θ - the azimuth of the vector \mathbf{m} at the point (x, y) about an axis perpendicular to the plane of incidence, and it is considered that \mathbf{m} does not go out of the base plane (the image of the DS, shown in fig. 1b, was obtained when the sample

¹ At large angles of deflection of the direction of light propagation from the optical axis, the influence of natural crystalline birefringence on the polarization of light becomes noticeable, which leads to a decrease in the contrast of the obtained DS images.

was rotated by an angle φ around the Y axis, i.e. θ - azimuth \mathbf{m} relative to the same axis). This shows that the observed change in the magneto-optical contrast is associated with a smooth change in the angle θ along the X axis in the direction from the center of the sample to its periphery (in the Y direction — the $\theta \approx \text{const}$ axis).

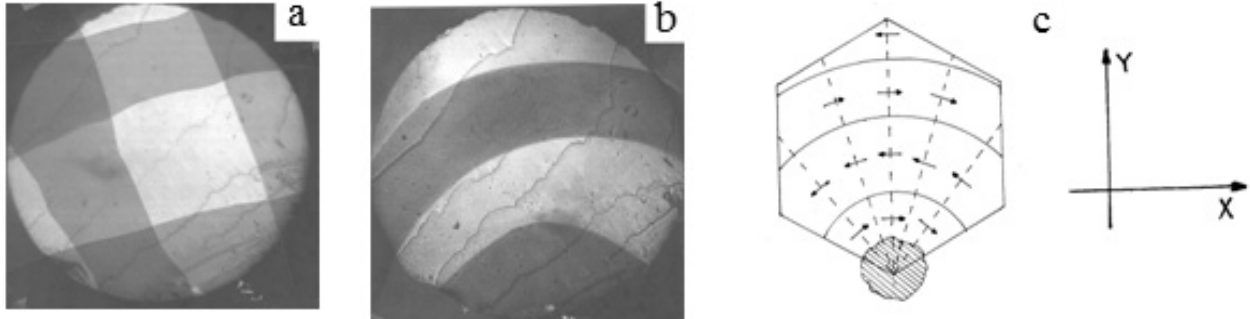


Fig.1. Images of the domain structure of the “glued” FeBO_3 crystal, obtained at $H = 0$: a - $T = 290$ K, b - $T = 90$ K; c is the spatial distribution of the spontaneous magnetization vector (arrows) in the basal plane of a stressed crystal: dashed lines indicate the directions of acting mechanical stresses, the hatched area is a drop of glue that the crystal is glued to the sample holder. On the right - the orientation of the axes of the laboratory coordinate system (the X axis coincides with the direction of one of the three C_2 axes, the Z axis — with the direction of the C_3 axis).

Since the intra plane magnetocrystalline anisotropy in FeBO_3 is not large (at $T = 77\text{K}$, the field of intra plane anisotropy $H_A < 1\text{Oe}$ [7]), according to [1,2,4], in the stressed state of the crystal at $H = 0$, the vector \mathbf{m} is oriented in the basic plane mostly perpendicular to the direction of compression. Obviously, when the mechanical stresses are distributed nonuniformly throughout the crystal, the orientation \mathbf{m} in the basal plane will change from point to point. Based on this, the spatial distribution of the vector \mathbf{m} in the DS of a stressed crystal (shown in Fig. 1b) can be schematically represented as shown in Fig. 1c (it is assumed that \mathbf{m} does not vary in thickness of the crystal). From which it follows that the temperature deformations of the sample holder create in the crystal radially directed non-uniform stresses from the point of its gluing, while the DC of the crystal remains 180-degree.

The process of technical magnetization of a “non-stressed” sample proceeded in the usual way: when a magnetic field is applied along any direction in the basal plane, the area of domains in which \mathbf{m} makes an acute angle with \mathbf{H} increases due to neighboring domains with opposite orientation of magnetization until the crystal passes in monodomain (homogeneous) state. Similarly, a stressed (“glued”) crystal is magnetized upon orientation $H \parallel X$.

Of interest is the evolution of the DS of a stressed crystal, observed at $H \perp X$. In a magnetic field, the DW is under pressure [8]:

$$P = mH(\cos\theta_1 - \cos\theta_2),$$

where θ_1, θ_2 are the angles that the vector \mathbf{m} makes with \mathbf{H} on both sides of the DW. Since the angles θ_1 and θ_2 change along the DB direction (see Fig. 1b, c), the field action in this case leads to the fact that the “dark” domains to the right of the central part of the sample grow due to the “light” domains, and to the left of center — on the contrary, the areas of “light” domains increase (visually “dark” domains are perceived as brown, and “light” - as green).

The process of displacement of the domain walls proceeds most rapidly along the edges of the sample, where the pressure P is maximal (while in its central part along the Y - axis $P = 0$). As a

result, in some field H_0 ($H_0 = 30e$ at $T = 90K$), only two (“bright” and “dark”) so-called counter domains, separated by one zigzag domain wall, remain in the crystal (fig.2 a, b).¹

The resulting domain configuration is obviously determined mainly by the competition between the magnetostatic energy of the E_M crystal and the energy of the DW. From the energy point of view, a flat domain wall having a minimal length is advantageous. However, the maximum will be the magnetostatic energy. Indeed, if on both sides of the DW the vector \mathbf{m} is with the normal to this boundary angles γ_1 and γ_2 , then $E_M \propto m^2 (\cos \gamma_1 - \cos \gamma_2)^2$ [8], i.e. The energy E_M is maximum at perpendicular orientation \mathbf{m} to the plane of the DW. Therefore, in this case, the zigzag DW, reducing the angles γ_1 and γ_2 , ensures a minimum of the free energy of the crystal.

With a further increase in H , the areas of wedge-shaped domains that are separated by DW decrease, but the zigzag shape of DW persists up to the fields of transition of the crystal to a uniform state. Fig. 2 a, b illustrates the change in the DS of a stressed crystal in the process of its magnetization at $H \perp X$, and Fig. 2c shows schematically the resulting spatial distribution of \mathbf{m} in the basal plane of the crystal.

The system of wedge-shaped domains, which occurs in the central part of a stressed crystal when it is magnetized along the Y axis, exists up to some field dependent H_s (at $T = 90K$, $H_c \approx 450e$). It is significant that with the growth of H and/or T the average width of the wedge-shaped domains D and their length L (determined, as shown in Fig. 2c), however, the areas of the “light” and “dark” domains remain equal to each other. At the same time, as the field increases from H_0 to $H \sim 0,8H_c$, a smooth decrease in the contrast of the image of the wedge-shaped domains is observed, after which the system of wedge-shaped domains disappears visually by degrading its image clarity, and at $H = H_c$, the sample surface will evenly colored throughout its area.

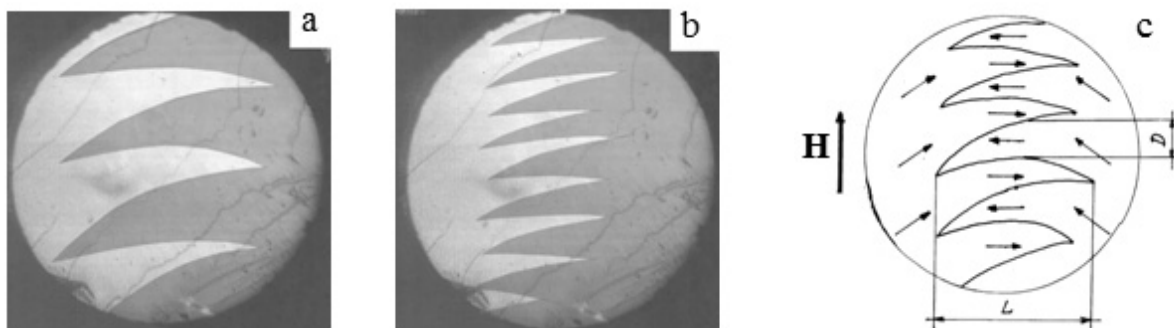


Fig.2. Images of the domain structure of a stressed $FeBO_3$ crystal, observed at $T = 90K$:
 a - $H = 3$ Oe, b - $H = 20$ Oe ($H \perp X$); c - spatial distribution of the spontaneous magnetization vector (arrows inside the circle) in the emerging domain configuration. An arrow outside the circle indicates the direction of the applied field. D - is the average width of the wedge-shaped domain, L - is its length.

Experimental dependences of the average width and length of the wedge-shaped domains on the external magnetic field and temperature are shown in Fig.3 and Fig.4 (the values of D and L were obtained by averaging over the entire number of wedge-shaped domains that exist with the data H and T). Note that, both with the inversion of the direction of magnetization and with the cyclic change of the heating – cooling mode, there was no noticeable hysteresis in the dependences $D(H, T)$ and $L(H, T)$. To interpret the results obtained, we turn to the thermodynamic theory of DS without closure domains. According to [9, 10], the free energy of a crystal per one wedge-shaped domain is represented as

¹ When the temperature changes from 90 to 270 K, the field H_0 decreases by about 1.5 times.

$$E = \frac{\varepsilon L}{D} + NI^2 D, \quad (1)$$

here ε - is the DW energy density, N - is the coefficient determined by the domain configuration and the shape of the domains, I - is the density of the magnetic poles appearing at the end of the domain, L and D are the characteristic size of the domain respectively along and across the direction of the easy axis of magnetization; the first term describes the energy of domain walls of the Neel type, the second one describes the density of the magnetostatic energy (we neglected the Zeeman and magnetoelastic contributions to E , assuming that, in general, the emerging system of wedge-shaped domains is $m \perp H$ and $m \perp \sigma$, where σ - is the longitudinal component of the stress tensor).

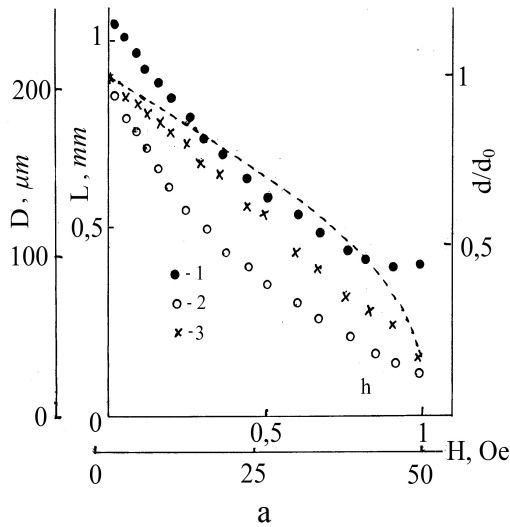


Fig.3. The field dependences of the average width (1) and length (2) of the wedge-shaped domains, as well as the values $d = D/\sqrt{L}$, normalized to their maximum value d_0 (3), obtained at $T = 90\text{K}$. The dashed line is the theoretical dependence $d/d_0(h)$ [9].

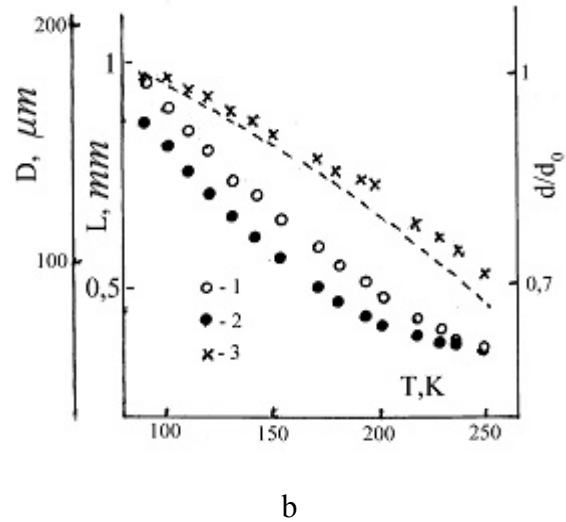


Fig.4. The temperature dependences of the average width (1) and length (2) of the wedge-shaped domains, as well as the values $d = D/\sqrt{L}$, normalized to their maximum value d_0 (3), obtained at $H = 7\text{ Oe}$ ($H \perp X$). The dashed line is the temperature dependence of the ratio d/d_0 , calculated by the formula (5).

In the general case of an arbitrary form of domains, the calculation of the N coefficient is a rather complicated task. At present, such calculations are performed only for the simplest domain configurations. For example, for the simplest regular structure of rectangular domains with $L \gg D$, the coefficient is $N = 1.7$ [9, 10]. Although in our experiments the observed shape of the domains differs noticeably from the rectangular one and the condition $L \gg D$ is fulfilled poorly (in all cases $\frac{L}{D} \sim 5$), for definiteness we take the value N in formula (1) to be 1.7.

In an external magnetic field, the vector m in a strained crystal is deflected from the direction given by the anisotropy induced in the basal plane by stresses. In this case, the direction m is with the direction H ($H \perp X$) angle $\theta = \arccos\left(m \frac{H}{2K}\right) = \arccos(h)$ (K is the magnetic anisotropy constant) [8]. Taking into account that the magnetic poles arise in the process of magnetization inside the crystal (along the zigzag DB), the density of the magnetic poles is defined as:

$$I = \xi m \sin \theta, \quad (2)$$

where $\xi = \frac{2}{(1+\mu)}$ - coefficient taking into account (the so-called μ - correction [8]) magnetic permeability of the medium, which in the field of fields $H_0 \leq H \leq H_c$ has the form [8]:

$$\mu = 1 + \frac{\pi m^2}{K}$$

Since in the calculation of the magnetostatic energy, the distribution of the vector \mathbf{m} in the crystal region near the DB is relevant, by θ in (2) we will understand the angle between the vectors \mathbf{m} and \mathbf{H} averaged over the entire area of the wedge-shaped domain (i.e., we assume that the angle A does not depend on from spatial coordinates). Then, in view of the above, formula (1) can be rewritten in the form:

$$E = \frac{\varepsilon L}{D} + 1,7 \xi m^2 (1-h^2) D. \tag{3}$$

A similar expression for E with $\xi=1$ (i.e., without μ - correction) was used in [11] in interpreting the results of observations of the surface DC of cobalt and magnethoplumbite. A formula describing the change in the energy of a non-Neile-type domain wall in a magnetic field directed perpendicular to its plane was also obtained there. Using the results of [9] and assuming that in our case the vector \mathbf{H} is approximately perpendicular to the DH plane along its entire length, the energy density of the DWs will be represented as:

$$\varepsilon = 8\sqrt{A(K + 2\pi m^2)} \left(\sqrt{1-h^2} - h \arccos(h) \right), \tag{4}$$

where A - is the exchange constant.

Under the condition $\frac{\partial E}{\partial D} = 0$, which determines the minimum of the free energy, from (3) we obtain:

$$D = \frac{1}{m} \sqrt{\frac{\varepsilon L}{1,7 \xi (1-h^2)}}. \tag{5}$$

If we assume that the anisotropy constant in the basal plane of a stressed crystal is $K = -\frac{3}{2} \Lambda \sigma \cos^2(\Psi)$ (Λ - is the magnetostriction constant, Ψ - is the angle between \mathbf{m} and the longitudinal component of the effective voltage tensor $\boldsymbol{\sigma}$), then for $\xi=1$ and $H=0$, the formula (5) coincides with the expression for D , which follows from the theory of equilibrium DS of rhombohedral weak ferromagnets, taking into account the mechanical stresses of the crystal [6].

We note an important consequence of formula (4): according to the calculations performed in [9], for $h \rightarrow 1$, the value of D in (5) tends to some finite limit, and the width of the Neel domain wall goes to infinity. This means that, at $h \rightarrow 1$, the DS disappears by an unlimited increase in the width of the DW. The latter is consistent with the visually observed process of the disappearance of wedge-shaped domains at $H \rightarrow H_c$ as a result of a decrease in the sharpness of their image (see above).

Since the energy density of the DB decreases with increasing h faster than the function $(1-h^2)$ (the dependence $\varepsilon(h)$ calculated by (4) is given in [9]), then, as follows from formula (3), to maintain the energy balance in the process of magnetization at $H \rightarrow H_c$, the value of the ratio

$\frac{L}{D^2}$ should increase, which is observed experimentally. In Fig. 3, the results of the calculation of

the field dependence of $d = \frac{D}{\sqrt{L}}$ normalized to its maximum value d_0 , obtained in [9] on the basis of formulas (4) and (5), are compared with the experimental dependence $\frac{d(H)}{d_0}$. It can be seen that although the form of the calculated and experimental $\frac{d(H)}{d_0}$ dependences is somewhat different, formula (5) allows us to describe the fivefold change in the $\frac{d}{d_0}$ ratio observed in the interval of fields of existence of wedge-shaped domains (But ($H_0 \leq H \leq H_c$)).

Conclusion

From the previous it follows that formula (5) quite well allows us to describe the experimentally observed relative change in the value of $\frac{D}{\sqrt{L}}$ depending on H and T. Thus, despite the relative simplicity of the theoretical model used, on the basis of formulas (4) and (5), it is possible to describe the main features of the DS behavior of a FeBO₃ crystal subjected to heterogeneous radially directed mechanical stresses observed with a change in the external magnetic field and temperature.

Acknowledgments

This work was supported in part by a grant OT-A2-64 Uzbekistan.

REFERENCES

- 1 Lacklison D.E., Chadwick J., Page J.L. Photomagnetic effect in ferric borate. *J. Phys. D: Appl. Phys.* London, 1972, Vol. 5, pp. 810 – 821.
- 2 Scott G.B. Magnetic domain properties of FeBO₃. *J. Phys. D: Appl. Phys.* London, 1974, Vol. 7, No.11, pp. 1574 – 1587.
- 3 Fedorov Yu.M., Leksikov A.A., Aksenov A.E. Magneto-optical phenomena in rhombohedral antiferromagnets with weak ferromagnetism. *Physics of the solid state*. St. Petersburg, 1984, Vol. 26, No. 1, pp. 220 - 226. [in Russian]
- 4 Sokolov B.Yu., Sharipov M.Z. Influence of the biaxial mechanical stress on the domain structure of holmium yttrium garnet ferrite. *Russian Physics Journal*. New York, 2014, Vol. 57, No 8, pp. 1001-1007.
- 5 Sharipov M.Z. The temperature dependence of the Faraday effect in terbium garnet ferrite is investigated near its magnetic – compensation temperature. *Eurasian Physical Technical Journal*. 2017, Vol.14, No. 1(27), pp. 34-40.
- 6 Farztdinov M.M. *Physics of magnetic domains in antiferromagnets and ferrites*. Moscow, Nauka, 1981, 156 p. [in Russian]
- 7 Sharipov M.Z. *Investigation of the effect of mechanical stresses on the magnetic structure of iron borate (FeBO₃)*. The dissertation of the candidate phys.-math. sciences. Tashkent, 2009, 114 p. [in Russian]
- 8 Tikadzumi S. *Physics of ferromagnetism*. Moscow, Mir, 1987, 420 p. [in Russian].
- 9 Privorotsky I.A. Thermodynamic theory of ferromagnetic domains. *UFN*. Moscow, 1972, Vol.108, No.1, pp. 43 – 80.
- 10 Barjahtar V.T., Bogdanov A.N., Yablonsky D.A. *Physics of magnetic domains*. *UFN*. Moscow, 1988, Vol. 156, No. 1, pp. 47 – 92. [in Russian]
- 11 Gemperly R., Zeleny M. Investigation of domain structure of magnetoplumbite. *J. of Physic B: Cond. Mat.* London, 1992, Vol.180 – 181 (pt. B), pp. 581 – 587.

UDC 538.958, 54.057, 541.145

INVESTIGATION OF PHOTOCATALYTIC ACTIVITY OF TiO₂-GO NANOCOMPOSITE

Zhumabekov A.Zh., Seliverstova E.V., Ibrayev N.Kh.

Institute of molecular nanophotonics, E.A. Buketov Karaganda State University,
Karaganda, Kazakhstan, almar89-89@mail.ru

Nanocomposite based on graphene oxide and TiO₂ was synthesized by hydrothermal method. The formation of nanocomposite was confirmed by Raman spectroscopy data. Characteristic peaks of graphene oxide and TiO₂ were recorded. Energy dispersive analysis showed the presence of titanium, carbon and oxygen in the nanocomposite. The specific surface area of TiO₂-GO nanocomposite is 1.16 times more than for pure TiO₂. A study of the photocatalytic activity of synthesized material in electrolytes with different pH was carried out. It is shown that the generation of photocurrent in TiO₂-GO depends on the electrolyte and increases by 2.9, 1.3 and 1.05 times in NaOH, KOH and Na₂SO₄, respectively, compared to the pure TiO₂ films.

Keywords: graphene oxide, TiO₂-GO, nanocomposite material, titanium dioxide, photocatalysis.

Introduction

Photoelectrochemical splitting of water with semiconductors is a "green" and inexpensive way to produce hydrogen fuel. Fujishima and Honda [1] showed for the first time that photoelectrochemical water splitting occurs on the surface of titanium dioxide (TiO₂). This work marked the beginning of the study of semiconductor materials for photocatalysis.

Titanium dioxide is a well-known and most studied functional material in the field of photocatalysis [2-4]. It is widely used in the degradation of environmental pollutants, as well as for the decomposition of organic substances.

Graphene has high electron mobility, large specific surface area and high transparency [5-7]. Earlier it was shown that composites based on TiO₂ and carbon-based materials, including activated carbon, carbon nanotubes and fullerenes, are able to demonstrate higher photocatalytic characteristics than pure TiO₂ [8-10].

Preparation of TiO₂-based composites is an effective way to increase the photocatalytic activity of the material by reducing the charge recombination rate. It is assumed that there is a more efficient separation of charges – photogenerated electrons, are converted into carbon materials, and the holes remain on TiO₂ and thus slow down the recombination of electrons and holes.

At the moment, there are several methods for the synthesis of nanocomposite material based on TiO₂ and graphene oxide. For example, the sol-gel method, the hydrazine reduction method, the hydrothermal method, the solvothermal method and the UV method, and there are 2-step methods for producing a composite [11-15], which directly affect the photocatalytic activity of the obtained materials. In ref. [16-18] it was shown that the electrolyte composition and its pH affect the value of the photogenerated current, as well as the efficiency of water splitting and hydrogen generation H⁺.

In this paper, nanocomposites based on TiO₂ and graphene oxide were synthesized and their structural, optical and photocatalytic properties were investigated. It is shown that the photoactivity of the nanocomposite depends on the electrolyte used.

1. Experiment

Materials

To prepare the TiO₂-GO nanocomposite, graphene oxide (GO, Cheaptubes) and TiO₂ (d>21, anatase, 99.7%, Sigma Aldrich), deionized water (purified by AquaMax water purification system), ethanol (anhydrous) were used. The films were deposited onto the surface of glass substrates coated with a conductive layer FTO (Fluorine doped tin oxide coated glass slide, ~7Ω/sq, Sigma Aldrich). Electrolytes NaOH, KOH, Na₂SO₄ were used to estimate photocatalytic properties. The pH value for them was equal to 13.4, 12.3 and 9.7, respectively. All reagents were analytically grade and used without additional purification.

The preparation and characterization of samples

Nanocomposite based on TiO₂ and graphene oxide was synthesized by hydrothermal method according to the method of [13]. The ratio of GO to TiO₂ was 1%. To measure the photocatalytic activity of the nanocomposite, a paste based on ethanol and TiO₂-GO powder with a concentration of 150 mg/ml was prepared.

The surface morphology of the resulting nanocomposite was studied using a transmission electron microscope (TEM) JEM-1400Plus (Jeol) with an accelerating voltage of 120 kV and a scanning electron microscope (SEM) Tescan Mira-3 (Tescan). The Confotec MR520 microscope (Sol Instruments) with laser excitation at a wavelength of 632.8 nm was used to register Raman spectra.

The porous structure was studied and the specific surface area was measured by the Brunauer–Emmett–Teller (BET) method on the Sorbi–MS (META) measuring complex. Nitrogen was used as an adsorbate. Measurements were carried out at the temperature of liquid nitrogen 77 K.

The photocatalytic activity of the obtained materials was studied by recording the photoinduced current in a standard photoelectrochemical three-electrode cell with a quartz window on a potentiostat-galvanostat P-30J (Elins). Ag/AgCl was used as the reference electrode. The radiation source was a diode lamp with a power of 35 mW/cm². The test samples were spin-coated on the surface of substrates with FTO. Resulting films were connected to the working electrode. A platinum electrode was connected to the negative potential.

2. Results and discussion

TEM and SEM images clearly show titanium dioxide nanoparticles (Fig.1, a and b). At the same time, graphene oxide sheets are barely distinguishable since ratio of GO to TiO₂ is 1:100. Energy dispersive (EDS) analysis of the prepared samples showed that titanium, carbon and oxygen are present in the composition of the nanocomposite (Fig.2, a).

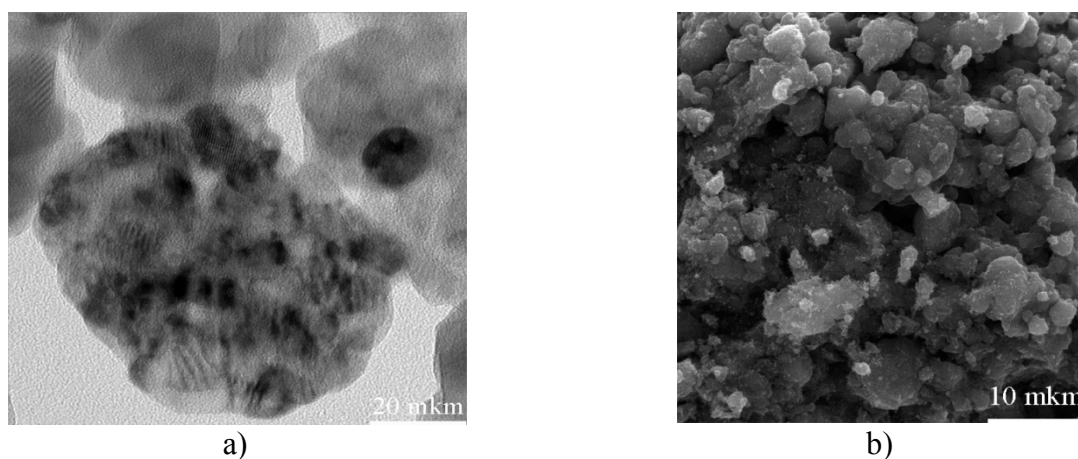


Fig.1. TEM (a) and SEM (b) images Of TiO₂-GO nanocomposite

Raman spectra of the TiO₂-GO nanocomposite of the samples were also recorded (Fig.2, b). The spectra obtained are the combination of individual TiO₂ and GO curves and correlate well with the data obtained in [19, 20] for TiO₂ and graphene oxide in [21]. It was found that in the spectra of nanocomposite material the ratio of the intensities of I_D/I_G bands was increased to 1.2 from 1.05. This indicates that in graphene oxide there is occur an ordering and an increase in the number of aromatic rings in structure during the process of synthesis [21].

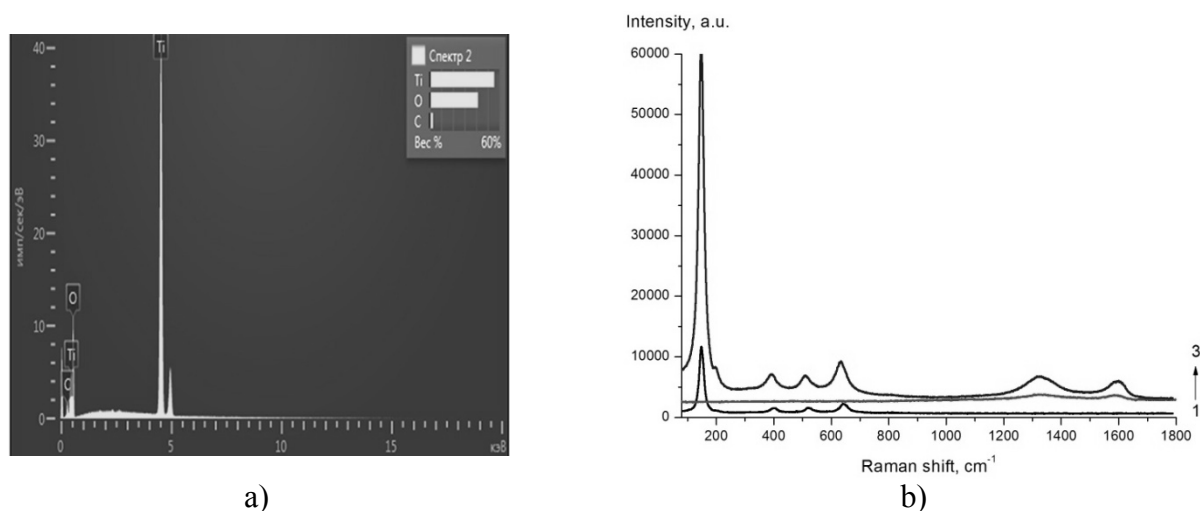


Fig.2. EDS analysis (a) and Raman spectrum (a): 1 – TiO₂, 2 – GO, 3 – TiO₂-GO

Photocatalytic activity of semiconductor materials indirectly depends on its electrotransport properties and specific surface area. In the previous work [22] we investigated electrotransport and optical properties of TiO₂-GO nanocomposite and showed that nanocomposite has higher electrotransport characteristics in comparison with pure TiO₂.

Table 1 shows the specific surface area of the TiO₂-GO nanocomposite films, as well as the titanium dioxide. It is shown the specific surface area of the semiconductor was increased by 16% after the addition of graphene oxide.

Table 1. Specific surface area of TiO₂ and nanocomposite films

Sample	S _{BET} , m ² /g
TiO ₂	67.3
TiO ₂ -GO	78.0

Further, the photocatalytic activity of pure TiO₂ and TiO₂-GO nanocomposite in various electrolytes was studied. The value of the photocurrent of the samples was measured for 20 seconds with cyclic switching on and off the light. To determine the optimal conditions for the generation of electron-hole pairs in pure TiO₂ and in the nanocomposite with GO, the electrolytes of Na₂SO₄, KOH and NaOH, differing in the magnitude of the electrochemical potential, were used.

Fig.3a shows the transient characteristics of the photocurrent for samples based on pure TiO₂. It is seen that for TiO₂ the lowest values of the generated photocurrent were recorded in the electrolyte NaOH. The value of J in other electrolytes is comparable with each other. For the KOH electrolyte, a decrease in the curve profile after 60 s was registered, this indicates on acceleration of the electron recombination process in the TiO₂ film.

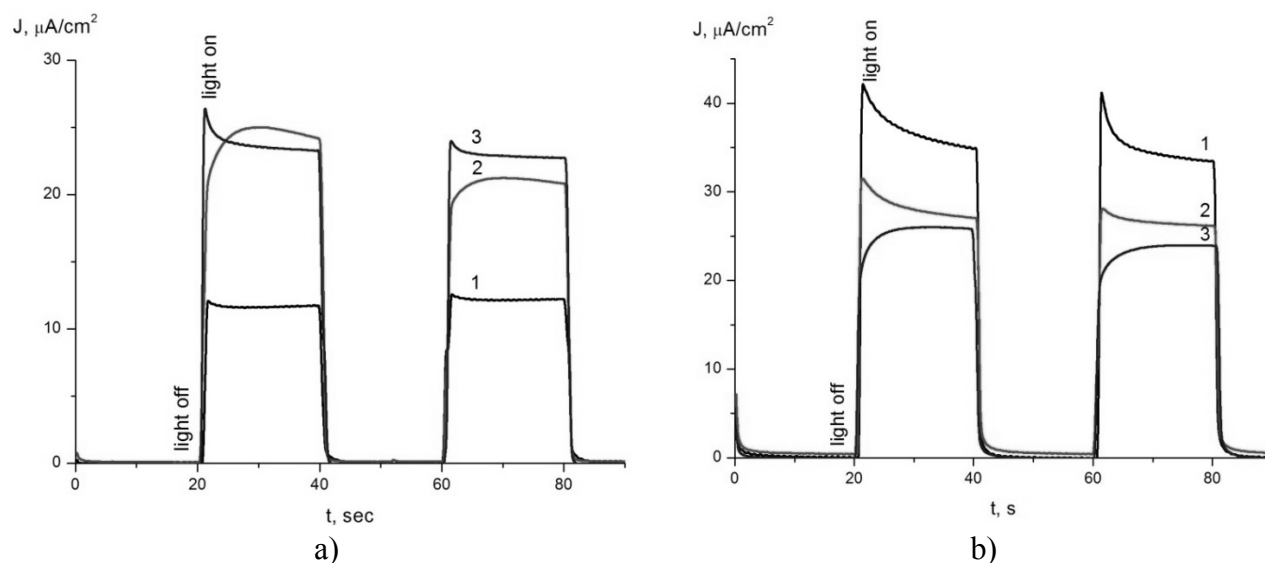


Fig. 3. Transient characteristics of the TiO_2 photocurrent (a) and TiO_2 -GO (b) in the electrolyte: 1 – NaOH, 2 – KOH, 3 – Na_2SO_4 .

Films of TiO_2 in the Na_2SO_4 electrolyte in intensively responds to incident light interval times of 20 s. The subsequent surge in the value of the photocurrent from $t=60$ s shows that the film continues to generate electrons.

Thus, studies of the transient characteristics of the photocurrent showed that TiO_2 generates photocurrents in the Na_2SO_4 electrolyte ($\sim 24 \mu\text{A}/\text{cm}^2$) about 2 and 1.04 times more than in the electrolytes NaOH and KOH, respectively.

Na_2SO_4 is not the most optimal electrolyte for TiO_2 -GO nanocomposite. The most effective electrolyte in this case is NaOH solution. The measurements showed (Fig.3, b) that the value of TiO_2 -GO photocurrent is in 1.25 and 1.4 times better in NaOH than in KOH and Na_2SO_4 . Nevertheless, in all electrolytes under irradiation of TiO_2 -GO nanocomposite there is an increase in the photocurrent by 2.9, 1.3 and 1.05 times (NaOH, KOH and Na_2SO_4 electrolytes) was registered compared to pure TiO_2 .

Conclusion

Thus, studies have shown that hydrothermal synthesis forms a bond between TiO_2 particles and graphene oxide sheets, which indicates the production of nanocomposite. It was confirmed by the data of EDS analysis and Raman spectroscopy.

Studies of the transient characteristics of the photocurrent showed that the most optimal electrolyte for pure TiO_2 is Na_2SO_4 , whereas for the TiO_2 -GO nanocomposite – is NaOH solution. In any case, the photocatalytic activity of the nanocomposite material is in 2.9, 1.3 and 1.05 times greater in NaOH, KOH and Na_2SO_4 solutions, respectively, than in TiO_2 . Since the efficiency of photocatalytic splitting of water into molecular oxygen and hydrogen will depend directly on the magnitude of the photoinduced electrons, it can be assumed that when using the NaOH electrolyte for TiO_2 -GO, hydrogen generation will be higher compared to other electrolytes.

REFERENCES

- 1 Fujishima A., Honda K. Electrochemical photolysis of water at a semiconductor electrode. *Nature*. 1972, Vol.238, pp. 37–38.
- 2 Hoffmann M.R., Martin S.T., Choi W., Bahnemann D.W. Environmental Applications of Semiconductor Photocatalysis. *Chem. Rev.* 1995, Vol. 95, pp. 69–96.
- 3 Fox M.A., Dulay M.T. Heterogenous Photocatalysis. *Chem. Rev.* 1993, Vol. 93, pp. 341–357.

- 4 Kamat P.V. Photochemistry on Nonreactive and Reactive (Semiconductor) Surfaces. *Chem. Rev.* 1993, Vol. 93, pp. 267–300.
- 5 Allen M.J., Tung V.C., Kaner R.B. Honeycomb Carbon: A Review of Graphene. *Chem. Rev.* 2010, Vol. 110, pp. 132–145.
- 6 Bunch J.S., van der Zande A.M., Verbridge S.S., Frank I.W., Tanenbaum D.M., Parpia J.M., Craighead H.G., McEuen P.L. Electronmechanical Resonators from Graphene Sheets. *Science.* 2007, Vol.315, pp. 490–493.
- 7 Stoller M.D., Park S.J., Zhu Y.W., An J.H., Ruoff R.S. Graphene-Based Ultracapacitors. *Nano Lett.* 2008, Vol. 8, pp. 3498 – 3502.
- 8 Woan K., Pyrgiotakis G., Sigmund W. Photocatalytic Carbon-Nanotube-TiO₂ Composites. *Adv. Mater.* 2009, Vol. 21, pp. 2233–2239.
- 9 Xu Y.J., Zhuang, Y.B., Fu X.Z. New Insight for Enhanced Photocatalytic Activity of TiO₂ by Doping Carbon Nanotubes: A Case Study on Degradation of Benzene and Methyl Orange. *J. Phys. Chem.: C* 2010, Vol. 114, pp. 2669–2676.
- 10 Yu Y., Yu J.C., Chan C.Y., Che Y.K., Zhao J.C., Ding L., Ge W.K., Wong P.K. Enhancement of Adsorption and Photocatalytic Activity of TiO₂ by Using Carbon Nanotubes for the Treatment of Azo Dye. *Appl. Catal.: B.* 2005, Vol. 61, pp. 1–11.
- 11 Azizi F. Synthesis and characterization of graphene–N–doped TiO₂ nanocomposites by sol-gel method and investigation of photocatalytic activity. *J. Mater. Sci: Mater. Electron.* 2017. Vol.28, Issues 15, pp.11222–11229.
- 12 Xu T., Zhang L., Cheng H., Zhu Y. Significantly Enhanced Photocatalytic Performance of ZnO via Graphene Hybridization and the Mechanism Study. *Appl. Catal. B: Environ.* 2011, Vol. 101, pp. 382–387.
- 13 Zhang X-Y., Li H-P., Cui X-L., Lin Y. Graphene/TiO₂ nanocomposites: synthesis, characterization and application in hydrogen evolution from water photocatalytic splitting. *J. Mater. Chem.* 2010, Vol. 20, pp. 2801–2806.
- 14 Williams G., Seger B., Kamat P. V. TiO₂-Graphene Nanocomposites. UV-Assisted Photocatalytic Reduction of Graphene Oxide. *ACS Nano* 2008, Vol 2, pp. 1487–1491.
- 15 Zhang Y., Tang Z.-R., Fu X., Xu Y.-J. TiO₂ Graphene Nanocomposites for Gas-Phase Photocatalytic Degradation of Volatile Aromatic Pollutant: Is TiO₂ Graphene Truly Different from Other TiO₂ Carbon Composite Materials?. *ACS Nano.* 2010, Vol. 4, pp. 7303–7314.
- 16 Fa J., Hn L., Nm H., Z. Z., Pandikumar A. Titanium dioxide-reduced graphene oxide thin film for photoelectrochemical water splitting. *Ceramics International.* 2014, Vol. 40, pp. 15159–15165.
- 17 Ni M., Leung K.H., Leung Y.C., Sumathy K. A review and recent developments in photocatalytic water-splitting using TiO₂ for hydrogen production. *Renewable and Sustainable Energy Reviews.* 2007, Vol. 11, pp. 401–425.
- 18 Zhao Y., Hoivik N., Wang K. Recent advance on engineering titanium dioxide nanotubes for photochemical and photoelectrochemical water splitting. *Nano Energy.* 2016. Vol.30, pp.728-744.
- 19 Swamy V., Kuznetsov A., Dubrovinsky L.S., Caruso R.A., Shchukin D.G., Muddle B.C. Finite-size and pressure effects on the Raman spectrum of nanocrystalline anatase TiO₂. *Phys. Rev. B* 2005, Vol. 71, pp. 184302/1–11.
- 20 Ohsaka T., Izumi F., Fujiki Y. Raman spectrum of anatase TiO₂. *J. Raman. Spectroscopy.* 1978, Vol. 7, pp. 321–324.
- 21 Zhang W., Cui J., Tao C-an, Wu Y., Li Z., Ma L. A strategy for producing pure single-layer graphene sheets based on a confined self-assembly approach. *Angew. Chem. International Edition.* 2009, Vol. 48, pp. 5864–5868.
- 22 Zhumabekov A.Zh., Ibrayev N.Kh., Seliverstova E.V., Kamalova G.B. Preparation and study of electrophysical and optical properties of TiO₂-GO nanocomposite material. *Bulletin of the University of Karaganda-Physics.* 2019, Vol. 94. (in Press)

UDK 532.783:541.1:539.21:535.37

INTERMOLECULAR INTERACTION IN LIQUID CRYSTALS

Agelmenev M.E.

E.A.Buketov Karaganda State University, Karaganda, Kazakhstan, amaxut58@gmail.com

The analysis of possible mechanisms for the implementation of orientational ordering in the mesophase of liquid crystals has been carried out. It has been shown that benzene rings in the structure play a major role in the existence of the mesophase. Van-Vleck paramagnetism, due to ring currents in benzene rings, seems to be one of the reasons for such ordering. Apparently, this explains the high degree of order of liquid crystals when exposed to a magnetic field. In this regard, the intermolecular interaction in the case of π -stacking may have a magnetic component. A type of possible intermolecular interaction potential is proposed when simulating the behavior of an ensemble of liquid crystal molecules. It is shown that the ordering of molecules of liquid crystals is associated with the different nature of intermolecular interactions, but having the same order.

Keywords: liquid crystals, aromatic compounds, the potential of intermolecular interaction, modeling

Introduction

Intermolecular interactions in their energy are noticeably weaker than chemical (from tenths to ten kJ/mol, for chemical bonds, of the order of tens and hundreds kJ / mol). Typical dependence of the interaction energy between particles on the distance r , similar to the potential energy curve for diatomic molecules. Some common properties of [1] intermolecular forces acting in different systems are observed:

1. At large distances, these forces are mainly forces of attraction;
2. They decrease faster with distance than Coulomb forces;
3. The repulsive forces are more short-range than the forces of attraction;

The main value, which is trying to calculate theoretically, is the total potential energy of interaction U (g). The exact form of this function determines the success of modeling processes in the molecular system.

Computer simulation using Monte Carlo and molecular dynamics methods is a tool for studying the behavior of systems of condensed matter of varying complexity. The first works on simulating simple atomic liquids were started in 1950. The methods were successfully extended to simulate more complex systems: molecular liquids, polymer and liquid crystal (LC) systems. Computer modeling at the atomistic level is a difficult task, and the size of particles in an ensemble has essentially small values in comparison with other models. As shown in [2], it is reasonable to conduct oscillations of molecular bonds and intramolecular motion at times of 1 fs and 10 fs, respectively; diffusion within the molecular fluid requires simulation of at least 1 ns; growth of orientational order and uniform arrangement of a nematic director for several hundred molecules may require more than 10 ns

The effectiveness of such studies is related to the accuracy of the potential of intermolecular interaction. Understanding the nature of orientational ordering in LCs is a cornerstone in the synthesis of such compounds with desired properties. Therefore, the purpose of this work was to analyze the features of intermolecular interaction in LCs to determine the processes that determine orientational ordering.

1. Features of liquid crystals

Considering a liquid crystal as a continuous medium, one can investigate many physical phenomena - unusual properties in the flow, response to electric and magnetic fields - in NLCs. The foundations of the continuum theory were laid in the late 20s of the 20th century on the basis of a static theory. The formulation of the general conservation laws and the fundamental equations describing the mechanical behavior of the nematic state belong to Eriksen and Leslie [3-4].

In contrast to a normal liquid, a nematic LC (NLC) consists of rod-like molecules, in which the long axes of neighboring molecules are approximately parallel to each other. A vector n , called a director, is introduced to describe the direction of the preferential orientation of molecules in the vicinity of a point. Its orientation in the medium can vary continuously and systematically from point to point (with the exception of singularities). External forces and fields acting on the liquid crystal, can cause the translational movement of the fluid, as well as the orientational movement of the director.

Studies using continual theory on the basis of the balance equations study the behavior of the director during various effects on NLC. Thus, in [5], when considering the Poiseuil flow, the existence of domain structures parallel to the flow, separated by singular lines, was established. The method of numerical simulation established an increase in time as the fixing on the substrate [6] weakened and the texture twist was due to the presence of sycotactic groups [7] when studying the twist-deformation dynamics induced by an electric field. In [8], it was found that the deformation is accompanied by the rotation of the director around an axis perpendicular to the plane of the layer. In [9], the flexo-optic effect for the case of cholesteric LCs with short pitch of a helix, in [10], the fleco-electric effect in NLCs was considered. In [11] the behavior of NLCs depending on the geometry of the electro-optical cell, in [12] the reorientation dynamics of the director in bipolar NLC droplets, in [13] the planar layer of NLC under the action of electric and magnetic fields, in [14] - elastic deformations in NLC using additive potential, in [15] - the microstructural and macrostructural properties of LC polymers with a strong anisotropy of the elastic coefficients are investigated. In [16], a phenomenological theory for axial and biaxial nematic phases using a two-component tensor of degree of order, in [17] the theory of dielectric permeability of NLC molecules with an arbitrarily directed dipole moment, in [18] is a model for describing a pretransition state in antiferroelectric LCs providing the union of the inner layers of the dipole-dipole interaction was developed. In [19], the phase behavior of achiral banana-shaped molecules and in [20] — the behavior of ferroelectric LCs using a quantum-mechanical potential was investigated.

On the basis of the continuum theory, phase diagrams of LCs are investigated using various types of potentials, which are based on the mean field approximation [2-4]. The development of the theory does not require the specification of the exact form of intermolecular forces [4, 21]. However, initially, Mayer and Zaupe suggested that the cause of the stability of the nematic phase is the dipole-dipole component of the anisotropic dispersion forces. It is believed that the rotational motion of molecules is independent of their translational motion.

When the temperature T is less than the temperature of the nematic – isotropic liquid phase transition (T_{NI} bleaching temperature), there is only one minimum in the free energy dependence on the degree of order s , which corresponds to a stable ordered phase. At $T > T_{NI}$, there are two minima, but the minimum at $s = 0$ is the absolute minimum. At $T = T_{NI}$, two minima are again observed: one at $s = 0$, the other at $s = s_c$, but both states have the same free energy, i.e. at this temperature it has a critical transition without a change in volume, but with a sharp change in the order parameter [3-4, 21]. This is defined if the change in volume объема ΔV is known. However, ΔV is usually so small that s_c is 1-2% different. As a result, the theory predicts a universal value $s = 0.44$ for all nematic substances. Although this value is in satisfactory agreement with the data obtained for a number of compounds, there are statistical deviations. Despite this, theoretical studies are being actively carried out on the properties of the compounds themselves, as well as mixtures based on them.

A prerequisite for substantial progress in the management of the mesogenic properties of such compounds is an understanding of the nature of the intermolecular interaction. Numerous studies [21-23] state the importance of the presence of cyclic groups, the need for the length, and rigidity of the structure of LC molecules. The liquid phase does not allow obtaining exact structures from X-ray diffraction studies [21,23]. The difficulty in understanding the general questions of mesogenicity is associated with the diversity of the studied classes of LC [24]. The same structural transformations lead to different results in different classes of LC molecules. So while studying the effect of the structure of nematic LCs based on arylpropargyl ethers of phenols on their electrophysical properties, a number of unexpected results were obtained:

- most of the compounds have a negative sign on the anisotropy of the dielectric constant, despite the expected positive value [6];
- was predicted from geometry studies using molecular mechanics and confirmed experimentally the fact that the sign of this magnitude inverted when attached to the ortho-position of the NO₂ functional group [24]. The cause of the observed inversion is a change in the direction of the dipole moment of the molecules as a result of the rotation of the benzene ring. Such a structural transformation usually leads to the opposite result [25].

The important role of benzene rings in the presence of order in the mesophase is confirmed by their presence in most LC structures [21]. The concepts of the structure of the LC phases are based on a simplified model. In more detailed analysis it is necessary to take into account the conformation of the molecules. As in the molecular crystal, molecules with different conformation, environment, orientation can coexist in the LC phase. One of the most typical complications of the structure of LCs is the formation of dimers and so-called bilayers [22]. The approximation of the mean field, continual theory is not enough to predict mesogenic properties, depending on their structure.

Here are some facts about the benzene rings that exist in the physical chemistry of the liquid crystal:

- rigidity of the benzene ring as a fragment in the structure of LC compounds [21];
- plane-parallelism of rings in the crystalline state [23,26];
- it is known that LC molecules are almost 100% oriented in a magnetic field [27,28];
- benzene rings have a bright anisotropy of magnetic susceptibility [29];
- it was found that with an increase in the number of benzene rings in LC molecules, the anisotropy of magnetic susceptibility increases [30];
- effects with chlorine-containing compounds [31]: the aggregation of chlorine atoms is due to the "chlorophobic" effect - the interaction of benzene rings with each other is energetically more advantageous than their interaction with chlorine; chlorine atoms are pushed out of the interaction region of the benzene rings, which leads to the formation of C1 ... C1-aggregates;
- it is known that aromatic solvents (benzene and its substituted), despite their low dielectric constant, affect many chemical processes as strongly polar liquids. The cause of the "benzene" effect is the large anisotropy of the polarizability of the aromatic rings. As a result, the polarizability significantly depends on the orientation of the solvent molecules to the dipole moments of the molecules of the solute [32].
- π -stacking, non-covalent interaction, determining the self-organization of various molecular systems, including discotic LCs [33-39].

2. Results and discussion

Let's analyze the given data. Indeed, like most organic substances, LCs, as a rule, are diamagnetic. Diamagnetism is due to Larmor precession of electrons. This leads to the appearance of an induced magnetic moment directed opposite to the external field, and therefore the magnitude of the magnetic susceptibility is negative.

Since the atomic susceptibility is isotropic, it can be expected that the anisotropy of the magnetic susceptibility is also small. However, the aromatic systems have a large anisotropy [40]. This can be explained by the fact that the π -electrons of the benzene ring are delocalized and form a "ring current". When the magnetic field is perpendicular to the plane of the ring, one can expect the appearance of a large induced moment directed against the field creating it. In the case of NLC, the susceptibility anisotropy must be positive and proportional to the number of aromatic rings [21]. With each replacement of the benzene ring by cyclohexane, the anisotropy of susceptibility decreases. If there are no aromatic rings in the compound, this value becomes negative. The value of the bridge $-C\equiv C-C\equiv C-$ is especially lowered. Qualitatively, this effect can be associated with ring currents, which in the case of triple bonds can occur in a plane perpendicular to the long axis of the molecule. The presence of a triple bond in the compounds studied by us [24] may be, apparently, one of the reasons for the presence of small values of the anisotropy of the dielectric constant.

It is known that the location of LC molecules in the crystalline state occurs mainly when the antiparallel position of nearby molecules is either head-to-head or overlapped [23]. Therefore, it can be assumed that, given the known "spacing" of the benzene rings of the LC molecules, the far orientational ordering will be determined by the possibility of the formation of interacting parallel pairs of benzene rings of neighboring molecules. Such a mechanism is easy to implement because of its good mobility, due to the small energy barriers of rotation [41]. An increase in temperature in the region of the mesophase leads to a decrease in the degree of order [21], which can be explained by the breaking of bonds between the benzene rings. T_{NI} will increase with increasing binding energy between these rings. The steric factor will play an important role in the orderliness of the molecules and determine the amount of repulsion of other fragments of nearby LC molecules. Apparently, the excess of the energy of such an interaction over the binding energy of the benzene rings makes it impossible for the mesophase to exist in this compound.

As is known [23], in order for a separate crystalline phase to become a precursor of the classical nematic phase, two conditions are required. First of all, it is a parallel or approximately parallel arrangement of molecules. The second condition is the requirement that the forces of intermolecular interaction were not large enough and allowed only translational movement of molecules at such thermal energies, when rotational movement around all three axes is possible.

There are few prerequisites for the existence of ionic and covalent bonds due to non-fulfillment of the second condition. The most frequently considered van der Waals interaction appears to be present, but not dominant. The observed nonfulfillment of the principle of dense packing, which characterizes the isotropy of the van der Waals interaction, in the case of orthorhombic crystalline benzene and its derivatives, is the reason for this statement [42].

As the analysis shows, the unusual properties of benzene rings are due to the anisotropy of the magnetic susceptibility, determined by the existence of ring currents. Apparently, the interaction of the magnetic fields of the benzene rings of neighboring molecules is the main mechanism for the realization of orientational ordering in NLCs. It is easily realized due to the small size of the energy barrier of rotation of the benzene rings, a characteristic arrangement already in the crystalline phase of the LC molecules (head to head or overlapped). This can lead to a parallel arrangement of the benzene rings of neighboring molecules in the presence of a translational motion in the liquid phase. It can be assumed that such a bond can be enhanced by cooperative effects in the direction perpendicular to the long axis of the LC molecules.

In the processes of self-organization of large molecular systems, one of the main factors is the π -stacking process. It is carried out through non-covalent interaction between the aromatic rings of neighboring molecules. However, the nature of these considerations is electrical. Different arrangements of interacting aromatic rings are usually studied (Fig. 1).

Stacking interactions between p systems play a major role in molecular recognition [33-39], in shaping the structure and the functionality of nucleic acids and in determining the tertiary and

quaternary structure of proteins. Vertical stacking between planar molecular systems is favored in polar environment, mainly due to entropic reasons, while electrostatic forces are in general determinant for planar or T-shaped structures in non polar media.

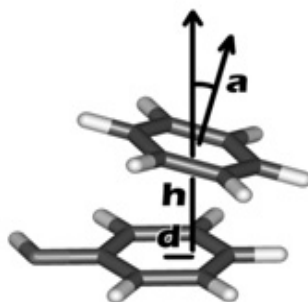


Fig.1. Type of the investigated system of interacting aromatic rings

In this respect, the traditional terminology “p–p” stacking is somewhat misleading since it is suggestive of some kind of special interaction between p molecular orbitals. The calculations presented in [33] revealed that a H_2O molecule accelerates the time of π -stacking formation in a benzene molecular system. The times of stacking formation in the benzene dimer ($n = 2$) and trimer ($n = 3$) cations were calculated to be 594 fs (H_2O) and 922 fs (*no- H_2O*), and 566 fs (H_2O) and 1155 fs (*no- H_2O*), respectively.

Molecular self-assembly and self-organization are Nature’s methods for the creation of dynamic and complex materials necessary for life on earth. These non-covalent interactions include hydrogen bonding, π -stacking, polar-nonpolar interactions, metal coordination, ionic interactions, etc.[34-35]. One particularly interesting example of a selfassembled material is a liquid crystalline phase [36]. The interactions that are crucial for the formation of liquid crystals are very similar to those of biologically relevant interactions: van der Waals forces, π -stacking, dipolar interactions, charge transfer interactions and hydrogen bonding [34-38]. These forces in effect control the properties of liquid crystals. Since these interactions are weak, it allows for partial dissociation to repair disordered units and obtain a uniform and more stable system; this is also known as self-healing. A better understanding of how the structure and morphology of a molecule will affect the self-assembly of supramolecular materials will allow for an efficient and effective design of these building blocks so that their properties can be utilized.

The binding between molecules is in most cases mainly due to van der Waals forces [38-39]. The core–core and tail–tail van der Waals interactions are responsible for the formation of the columnar phase. These packing structures are a function of the symmetry of columns and also intracolumnar van der Waals forces. An introduction to DLCs and the powerful potential it possesses in molecular electronics, as 1D molecular wires due to stacking of its π – π orbitals. The potential of such an interaction in [1] is

$$U = -\frac{A}{r^3} + \frac{B}{r^6}.$$

The non-potential nature of magnetic interaction is a major problem in the development of modeling software. At the same time, the presented potential represents an opportunity to take into account its contribution to some extent. At the same time, there is a possibility that the influence of paramagnetism is manifested not only on such a functional group as aromatic rings [43]. The

potential of intermolecular interaction in the LC should include dispersion, Coulomb and magnetic interactions. The Coulomb is not dominant due to the neutrality of the LC molecules. Therefore, two other interactions are decisive. By the strength of the interaction, they are comparable.

Conclusion

The analysis performed shows the main role of benzene rings in the existence of orientational ordering in nematic liquid crystals. One of the mechanisms that implements this process may be the interaction of the magnetic fields of the ringless rings of neighboring molecules. Van-Vleck paramagnetism, due to ring currents in benzene rings, seems to be one of the reasons for such orderliness. Apparently, this explains the high degree of orderliness of liquid crystals when exposed to a magnetic field. In this regard, the intermolecular interaction in the case of staking may have a magnetic component. A type of possible intermolecular interaction potential is proposed when simulating the behavior of an ensemble of liquid crystal molecules. It is shown that the ordering of molecules of liquid crystals is associated with the different nature of intermolecular interactions, but having the same order.

REFERENCES

- 1 Ibragimov I.M., Kovshov A.N., Nazarov Yu.F. Basics of computer modeling of nanosystems. SPb.: Lan publishing house, 2010, 384 p. [in Russian]
- 2 Mark R. Wilson. Progress in computer simulations of liquid crystals. *Intern. Rev. in Phys. Chem.* 2005, Vol. 24, No. 3-4. pp. 421 – 455.
- 3 P. de Zhen. Physics of liquid crystals, Moscow, Mir, 1977, 400 p. [in Russian]
- 4 Chandrasekar S. Liquid crystals, Moscow, Mir, 1980, 344 p. [in Russian]
- 5 Calderer M. C., Mukherjee B. On Poiseuille flow of liquid crystals. *Liquid Crystals*. 1997, Vol. 22, No.2, pp.121 – 135.
- 6 Derfel G., Gajewska B. Dynamics of the field-induced twist deformation in weakly anchored nematic layers. *Liquid Crystals*. 1997, Vol. 22, No. 3, pp. 297 – 300.
- 7 Frunza O.S., Frunza L., Petrov M., Barbero G. Elastic model for twisted nematic textures in OOBA layers. *Liquid Crystals*. 1998, Vol. 24, No.2, pp.215-218.
- 8 Derfel G., Radomska B. Modelling of the simple shear flow of a flow-aligning nematic. *Liquid Crystals*, 1997, Vol. 23, No. 5, pp. 741 – 748.
- 9 Rudquist P., Carlsson T., Komitov L., Lagerwall S.T. The flexoelectro-optic effect in cholesterics. *Liquid Crystals*, 1997, Vol. 22, No. 4, pp. 445 – 449.
- 10 Billeter J.L., Pelcovits R.A. Molecular shape and flexoelectricity. *Liquid Crystals*, 2000, Vol. 27, No.9, pp. 1151 – 1160.
- 11 Chan P. K. Computer simulation of elongated bipolar nematic droplets II. External field aligned normal to the droplet axis of symmetry. *Liquid Crystals*, 2001, Vol. 28, No. 2, pp. 207 – 215.
- 12 Chan P.K. Computer simulation of elongated bipolar nematic droplets I. External field aligned parallel to the droplet axis of symmetry. *Liquid Crystals*, 1999, Vol. 26, No. 12, pp. 1777 – 1786.
- 13 Kini U.D. Magnetic and electric field induced periodic deformations in planar oriented nematics. *Liquid Crystals*, 1998, Vol. 24, No .2, pp. 177 – 199.
- 14 Le Masurier P.J., Luckhurst G.R., Saielli G. Monte Carlo lattice simulations of the elastic behaviour of nematic liquid crystals. *Liquid Crystals*, 2001, Vol. 28, No. 5, pp. 769 – 778.
- 15 Houjie Tu, Gerhard Goldbeck-Wood, Alan H. Windle. A tensor model of liquid crystalline polymers: application to basic disclination processes. *Liquid Crystals*, 2002, Vol. 29, No. 3, pp. 325-334.
- 16 Mukherjee P.K. Improved analysis of the Landau theory of the uniaxial-biaxial nematic phase transition. *Liquid Crystals*, 1998, Vol. 24, No. 4, pp. 519 – 523.
- 17 Kalmykov Y.P., Coffey W.T. Analytical solutions for rotational diffusion in the mean field potential: application to the theory of dielectric relaxation in nematic liquid crystals. *Liquid Crystals*, 1998, Vol. 25, No. 3, pp. 329 – 339.
- 18 Mottram N.J., Elston S.J. Order parameter theory of the pre-transitional behaviour in antiferroelectric liquid crystals. *Liquid Crystals*, 1999, Vol. 26, No.3, pp. 457 – 464.

- 19 Memmer R. Liquid crystal phases of achiral banana-shaped molecules: a computer simulation study. *Liquid Crystals*, 2002, Vol. 29, No. 4, pp. 483 – 496.
- 20 Glaser M.A., Clark N.A., Walba D.M., Keyes M.P., Radcliffe M.D., Snustad D.C. Mean field theory-based calculation of FLC polarization. *Liquid Crystals*, 2002, Vol. 29, No. 8, pp. 1073 – 1085.
- 21 Sonin A.S. Introduction to Liquid Physics, Moscow, Nauka, 1983, 320 p. [in Russian]
- 22 Pershin V.K., Pershin V.K., Zorkiy P.M. Mesophases - partial order molecular systems: structure, formation mechanisms, polymorphism. *Problems of crystal chemistry*, Moscow, Nauka, 1988, pp. 30 – 82. [in Russian]
- 23 Brayon R.F. Crystal Structure and Liquid Crystal. *Zhurnal strukturnoy khimii - Journal of Structural Chemistry*, 1982, Vol. 23, No. 1, pp. 154 - 174. [in Russian]
- 24 Agel'menev M.Ye. Inversion sign of the anisotropy of the dielectric constant of mesogenic acetylenyl-containing propargyl ethers. *News of The National Academy Of Sciences of The Republic of Kazakhstan, Series Chemistry And Technology*. 2002, No. 5. pp. 20 – 26. [in Russian]
- 25 Grebenkin N. F., Ivashchenko A. V. Liquid crystal materials. Moscow: Chemistry, 1989, 288 p. [in Russian]
- 26 Kitaygorodskiy A.I. Molecular crystals. Moscow, Nauka, 1971, 424 p. [in Russian]
- 27 Asano T., Moriya K., Yano S., Takatani S., Kagabu S. Liquid crystalline phase transitions of the 2-(4-alkoxybiphenyl-4-yl)-5-(4-methylphenyl)pyridines. *Liquid Crystals*, 1998, Vol. 25, No. 2, pp. 263 – 266.
- 28 Filippov S.K., Kolomiets I.P., Sokolova O.S., Antonov E.A., Zorin I.M., Bilibin A.Yu. Preliminary communication - The effect of a substituent in the central ring on the liquid crystalline properties of di (4-alkoxycarbonylphenyl) terephthalates. *Liquid Crystals*, 1998, Vol. 24, No. 5, pp. 787 – 791.
- 29 Van Vleck J.H. *The Theory of Electric and Magnetic Susceptibilities. The International series of monographs on physics*. Oxford: Oxford University Press, 1932, 384 p.
- 30 de Zhe V. *Physical Properties of Liquid Crystal Substances*, Moscow, Mir, 1982, 152 p. [in Russian]
- 31 Grineva O.V., Zorkiy P.M. The energy of intermolecular interaction in crystals of chlorine-containing organic compounds. *Journal of Physical Chemistry*. 1998, Vol. 72, No. 4, pp. 714 - 720. [in Russian]
- 32 Stolov, A.A., Remizov, A.B. Conformational equilibria in aromatic media: the benzene effect. *Journal of Physical Chemistry*, 1995, Vol. 69, No. 3, pp.563-566. [in Russian]
- 33 Hiroto Tachikawa, Ryoshu Iura, Hiroshi Kawabata. Water-accelerated π -Stacking Reaction in Benzene Cluster Cation. *Scientific reports*. 2019, Issue 9, pp. 2377. doi.org/10.1038/s41598-019-39319-7
- 34 Ashwathanarayana Gowda, Sandeep Kumar. Recent Advances in Discotic Liquid Crystal-Assisted Nanoparticles. *Materials*. 2018, Vol.11, pp. 382 – 397. doi:10.3390/ma11030382
- 35 Whitesides G. M.; Grzybowski B., Self-assembly at all scales. *Science*. 2002, 295, pp. 2418 - 2421.
- 36 Goodby J. W., Saez I. M., Cowling S.J., Gasowska J.S., MacDonald R.A., Sia S., Wats P., Toyne K.J., Hird M., Lewis R.A., Lee S.E., Vaschenko V. Molecular complexity and the control of self-organising processes. *Liquid Crystals*. 2009. Vol.36, pp. 567 – 605.
- 37 Kumar S., *Chemistry of discotic liquid crystals: from monomers to polymers*. CRC Press: Boca Raton, 2011, 519p.
- 38 Suhana Mohd Said, Mohamad Syafie Mahmood, Mohammad Noh Daud, Mohd Faizul Mohd Sabri, Nor Asrina Sairi. Structure-electronics relations of discotic liquid crystals from a molecular modelling perspective. *Liquid Crystals*, 2016. doi:10.1080/02678292.2016.1209792.
- 39 Boden N, Bushby RJ, Clements J., et al. Device applications of charge transport in discotic liquid crystals. *J.Mater Chem*. 1999, V9, pp. 2081–2086. doi:10.1039/a903005k.
- 40 Oaro Zh. *Diamagnetic susceptibility and delocalization of electrons. Localization and delocalization in quantum chemistry*, Moscow, Mir, 1978, pp. 306 – 325. [in Russian]
- 41 Dashevskiy V.G. Conformations of organic molecules, Moscow: Khimiya, 1974, 432p. [in Russian]
- 42 Zorkiy P.M., Zorkaya O.N., Lanshina L.V. Orthogonal contacts of benzene cycles: a special type of specific intermolecular interactions. *Journal of Physical Chemistry*, 1995, V.36, №5, pp. 775-789. [in Russian]
- 43 Dorfman Ya.G. Diamagnetism and chemical bonding. Moscow, 1961, 232 p. [in Russian]

UDC 537.632

THE INFLUENCE OF THE MAGNETIC FIELD ON THE CURRENT-VOLTAGE CHARACTERISTICS OF CUPC NANOSTRUCTURES

Zavgorodniy A.V., Aimukhanov A.K., Zeinidenov A.K., Ayubekova A.Ye.

E.A. Buketov Karaganda State, Karaganda, Kazakhstan, AlexZavgorodniy@inbox.ru

The paper presents the results of a study of the role of spin states in the process of charge carrier transfer in copper phthalocyanine (CuPc) nanostructures. It is shown that the film obtained by thermal evaporation has the structure of the α -phase, the CuPc nanowires are in the η -phase. The effect of an external magnetic field on the current-voltage characteristics (IVC) of CuPc nanostructures was studied. It is shown that a decrease in the value of the short-circuit current when an external magnetic field is applied, which is associated with the mechanism of spin polarization in the formation of a bipolaron. It is shown that the effect of "spin blocking" in nanowires is stronger.

Keywords: copper phthalocyanine, nanowires, IVC, charge carrier mobility, magnetic field, spin state.

Introduction

The possibility of using individual molecules and molecular ensembles as active elements of electronics attracts the attention of researchers in various fields of science [1]. The definition of the boundaries of potential and the approach to these boundaries of modern semiconductor technologies is heightened interest in building basic elements of molecular electronics. Further prospects for the development of electronics are associated with the creation of devices using quantum phenomena, in which the count goes on units of photons and electrons. Recently, theoretical and experimental studies of artificially created low-dimensional structures have been widely conducted [2]. At the same time, an active search is underway for materials and mechanisms for spintronics, a field of science that considers the possibilities of controlling information transfer processes using a magnetic field [3].

The high mobility of charge carriers and the efficiency of light energy conversion make it possible to consider metal phthalocyanines as promising materials for photovoltaic cells [4–5]. One of the effective ways to increase the optical sensitivity range and improve the photoelectric characteristics is the formation of nanocomposite structures of metal phthalocyanine complexes. The conductive and magnetic properties of phthalocyanines are of great interest.

This paper presents the results of a study of the influence of a magnetic field on the current-voltage characteristics of a solid CuPc film and CuPc nanowires.

1. Experimental technique

Preparation of substrates for a photosensitive cell was carried out as follows: glass conductive plates (ITO, size 20x20mm, $R_{ITO} = 60 \Omega/\text{cm}$) were placed in an ultrasonic bath and washed for 10 minutes in acetone, in isopropyl alcohol and in deionized water, then dried in drying cabinet for 20 minutes and then subjected to UV treatment for 30 minutes.

A solid film of copper phthalocyanine (Sigma Aldrich, 99%) ~ 140 nm thick was deposited on the surface of a substrate coated with ITO by thermal evaporation in a vacuum using a Carl Zeiss Jena HBA 120/2 installation. The deposition was carried out in a vacuum of 10^{-5} Torr at a rate of 0.5 nm/s.

CuPc nanowires on the surface of a substrate with a conductive ITO coating were obtained using temperature gradient physical vapor deposition (TG-PVD) (fig.1). The substrates were

installed inside a quartz tube in the growth zone. The temperature in the reaction zone was 465°C. The temperature control of the working zone was carried out using the PID controller. The high-purity argon flow rate in the reaction zone was ~150 standard-state cubic centimeter per minute (sccm). The deposition time of nanowires was 6 hours.

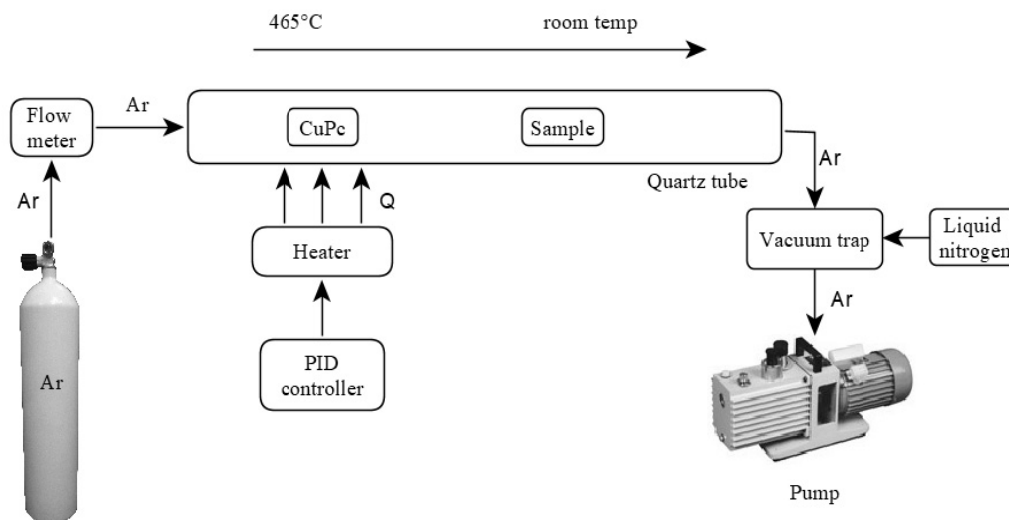


Fig.1. The diagram of the experimental installation TG-PVD

An aluminum electrode with a thickness of ~ 150 nm was deposited on the surface of an organic film by thermal evaporation in a vacuum of 10^{-5} Torr at a rate of 1 nm/s. The choice of ITO as an electrode is due to the fact that this produces the best ohmic contacts with the films and the best values of the electron work function (Figure 2). Aluminum is used as a cathode, since the electron work function for it is - 4.2 eV, which is in good agreement with the LUMO energy for CuPc equal to - 3.5 eV.

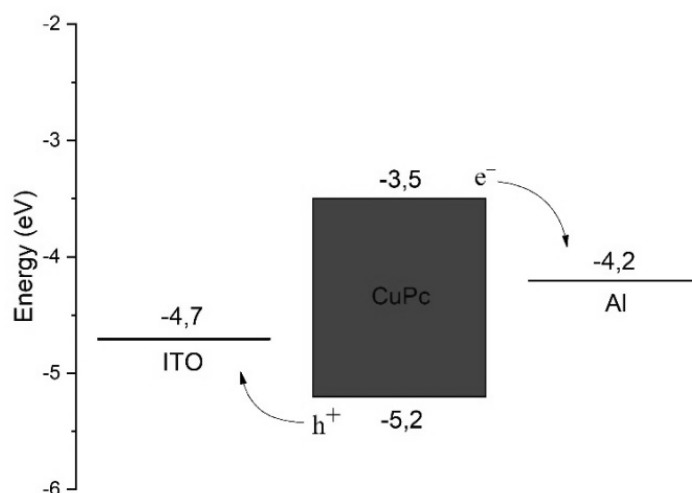


Fig.2. Energy level diagram

The surface morphology of nanostructures (figure 3) was measured using an MIRA 3 LMU electron microscope. The average thickness of the solid film obtained by thermal evaporation was ~ 140 nm.

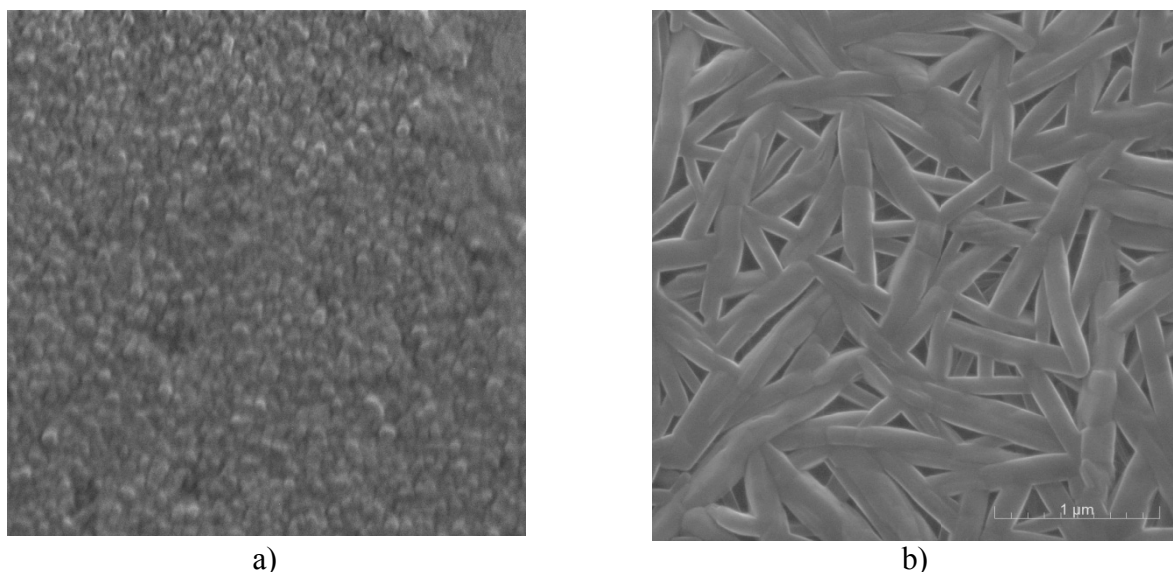


Fig.3. SEM images of the obtained samples:
a) solid CuPc film; b) CuPc nanowires.

The average grain size on the surface of a solid film was ~ 57 nm. The average height of the grown nanowires consisting of stacks of copper phthalocyanine molecules was ~ 137 nm, with an average diameter of ~ 4.5 nm.

2. Results and discussion

The absorption spectrum of copper phthalocyanine was measured on a CM2203 spectrofluorometer (Figure 4). Figure 4 (curve 3) shows the absorption spectrum of CuPc in an alcohol solution. The data obtained show that the absorption spectrum of CuPc has 4 maxima. The first absorption maximum is observed in the ultraviolet region with a wavelength equal to $\lambda = 324$ nm. It is known [6] that copper phthalocyanine molecules can be in one of three crystalline phases: η -CuPc, α -CuPc, β -CuPc. In accordance with this, the observed band with a maximum at 324 nm can be attributed to the Soret band or the B-band. In the B-range, a large absorption peak is observed, which indicates that CuPc has the structure of the metastable α -phase, since during thermal annealing, a sharp decrease in absorption is observed in this range [7]. Also, at wavelengths $\lambda = 604$ nm and $\lambda = 692$ nm, there are second and third absorption maxima in the visible region of the spectrum (Q-band). This spectrum coincides with the studies of the authors [8]. The characteristic splitting of the Q-range into two absorption peaks is a consequence of the crystalline form of phthalocyanine and is called Davydov splitting [9].

The absorption spectrum of a solid film obtained by thermal evaporation (Figure 4, curve 1) has a shift in the long-wavelength region by 2 nm in the Soret region and 14 nm in the Q-band. An increase in the absorption intensity by 1.75 times is also observed. The CuPc molecules in the solid film are in the α -phase.

Figure 4 (curve 2) shows the absorption spectrum of nanowires. As can be seen from the figure, the spectrum has 4 maxima. The maxima in the Q-range at 622 nm and 764 nm indicate that copper phthalocyanine molecules are in the η -phase. The CuPc nanowires in the B-range are characterized by the presence of a wide absorption band up to 540 nm, which is associated with the ordering of the CuPc molecules in the nanowires.

Based on the above data, it can be concluded that the absorption spectrum of copper phthalocyanine nanowires in the region of 400-500 nm is wider compared to the absorption spectrum of CuPc molecules in alcohol and the film obtained by thermal evaporation.

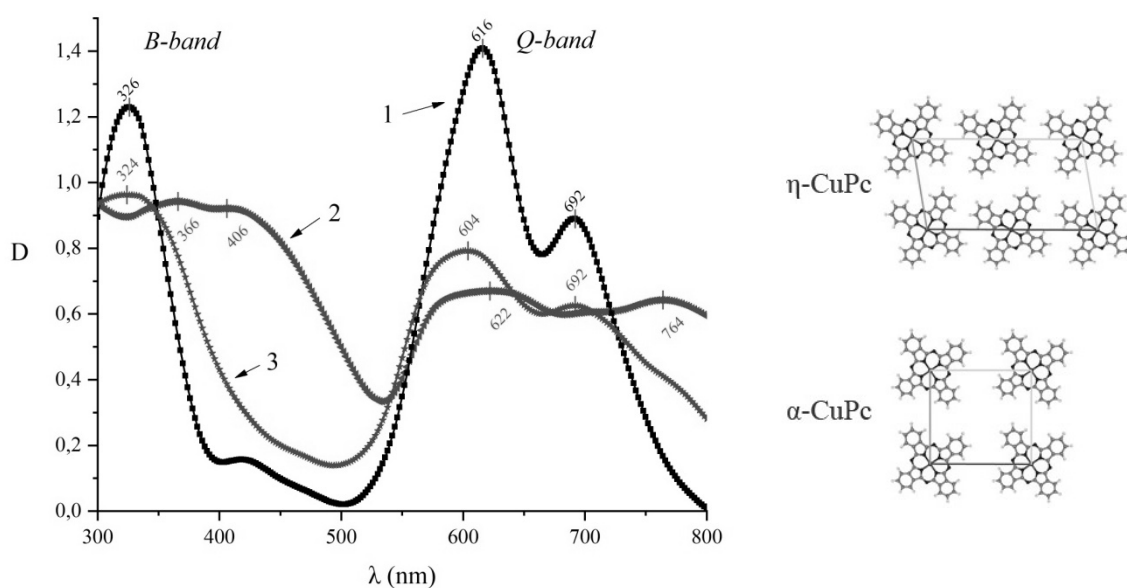


Fig.4. Absorption spectrum of CuPc:

1 – CuPc film obtained by vacuum thermal evaporation; 2 – CuPc nanowires; 3 – CuPc in ethanol

After that, samples of photovoltaic cells were prepared, consisting of several layers: 1 – glass substrate; 2 – a transparent conductive layer of ITO (indium tin oxide), which serves as the anode; 3 – a layer of copper phthalocyanine organic molecules; 4 – aluminum electrode serving as a cathode (Figure 5).

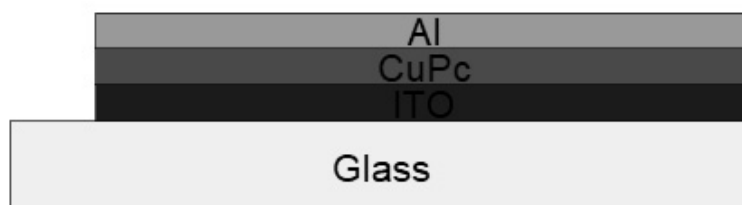


Fig.5. Photovoltaic cell structure

3. The influence of the magnetic field

Measurements of the influence of the magnetic field on the IVC of an organic photosensitive cell were carried out using a P20X potentiostat-galvanostat in the linear sweep mode. The setup diagram is shown in Figure 6. A sample is placed between the poles of a permanent electromagnet. The cell surface was illuminated using a xenon lamp with a power of 100 mW/cm^2 . The IVC of the photosensitive cell was determined by illuminating the sample from the ITO side with a xenon lamp in the wavelength range of 350–750 nm and a power of 100 mW/cm^2 (Figure 6).

Figure 7 shows the IV characteristics of the samples obtained. From figure 6 it is clear that the IVCs are non-linear. The values of idling U_{oc} , short circuit current I_{sc} , filling factor FF and efficiency were determined according to the method [10].

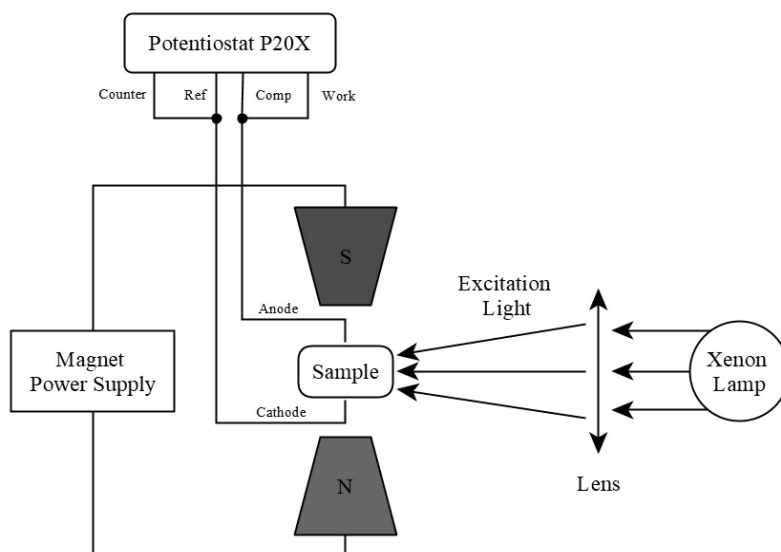


Fig.6. Diagram of the experimental setup for measuring the IVC in an external magnetic field.

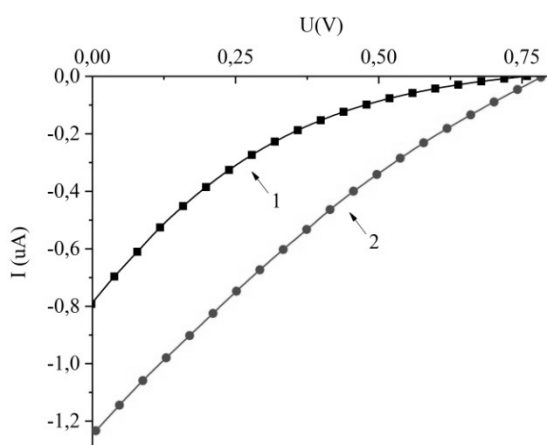


Fig.7. Comparison of current-voltage characteristics:
 1 - IVC of CuPc film obtained by the method of vacuum thermal evaporation;
 2 - IVC CuPc nanowires.

Figure 8 shows the flow patterns of charge carriers in a solid CuPc film obtained by thermal evaporation in vacuum (a) and in CuPc nanowires (b). The solid film obtained by thermal evaporation (Figure 8, a) is amorphous and does not have a clear structure. The presence of an amorphous film structure increases the probability of charge carrier recombination, preventing their movement in the film. This is indicated by the low value of the filling factor and short-circuit current of the IVC cell (Figure 7, curve 1). In nanowires, CuPc molecules have a lamella structure (Figure 8, b). According to [11], the main charge carriers in metal phthalocyanines are positively charged polarons (holes). Due to the imperfection of the film structure, local electronic states are present on the surface of nanowires – electron and hole traps. This is indicated by the observed wide absorption spectrum of nanowires. The traps can capture two polarons, as a result of which a bipolaron will be formed, which subsequently moves along the nanowires, carrying out charge transfer. As the structure becomes more defective, the number of bipolarons will increase, thus increasing the cell current (Figure 7, curve 2).

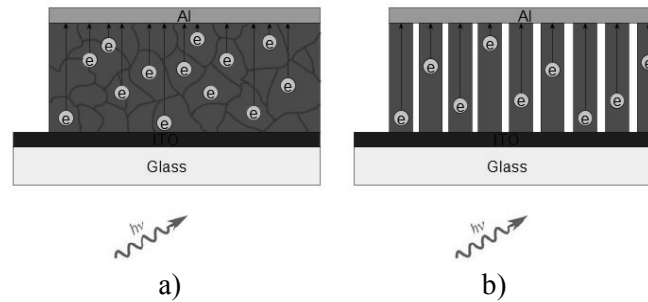


Fig.8. Cell Structure:

a) - CuPc film obtained by vacuum thermal evaporation; b) - CuPc nanowires

The charge carrier mobility of copper phthalocyanine structures was determined according to the procedure [12]. The calculation of the charge carrier mobility was carried out as follows:

$$\mu = \frac{d^2}{V \cdot t_{tr}}, \quad (1)$$

where μ – charge carrier mobility, d – film thickness, V – applied voltage, t_{tr} – transient time.

Transient time is calculated by the formula 4, where τ_{peak} is the time of rise of the peak current from the moment the voltage is applied.

$$\tau_{peak} = 0.786 \cdot t_{tr}, \quad (2)$$

Table 1 shows the parameters of the photoelectric characteristics of copper phthalocyanine nanostructures.

Table 1. Photoelectric characteristics of copper phthalocyanine nanostructures

Sample	$U_{oc}(V)$	$I_{sc}(\mu A)$	$U_{max}(V)$	$I_{max}(\mu A)$	FF	$\eta(\%)$	$\mu(\text{cm}^2/Vs)$
Evaporated	0.75	0.79	0.27	0.28	0.13	7.7E-11	2.6E-3
Nanowires	0.78	1.25	0.35	0.57	0.2	1.95E-10	2.85E-3

To study the effect of a magnetic field on the parameters of the current – voltage characteristics, the samples were placed between the poles of an electromagnet. The effect of the magnetic field (MFE) was determined by changing the value of the short-circuit current of an organic cell when the magnitude of the magnetic field changes from 0 to 0.6 T. MFE was calculated according to [13]:

$$MFE = \frac{I_B - I_0}{I_0} \cdot 100\%, \quad (3)$$

where I_B – short-circuit current in a magnetic field; I_0 – short-circuit current without exposure to a magnetic field.

Figure 9 shows the dependence of the effect of the magnetic field of a cell on the induction value of an external magnetic field. It can be seen from the figure that at the maximum value of the field induction, the short-circuit current of the photosensitive cell based on CuPc nanowires decreases by 61%.

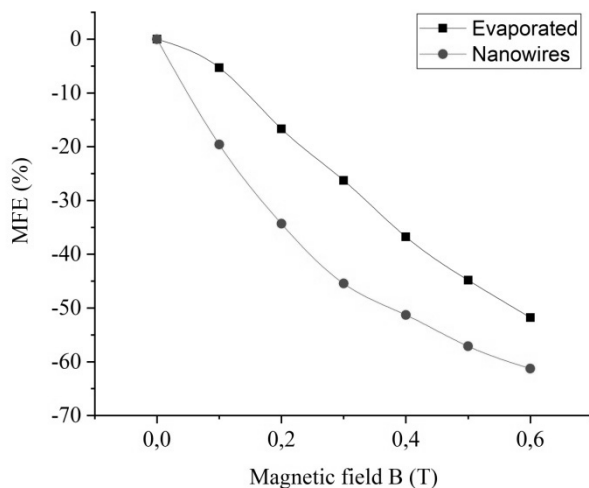


Fig.9. Magnetic Field Effect (MFE)

An external magnetic field affects the spin state of polarons. In the absence of an external magnetic field, two polarons with different spin components can be trapped by a trap, resulting in the formation of a bipolaron - a temporary intermediate quasistationary state (Figure 10, a).

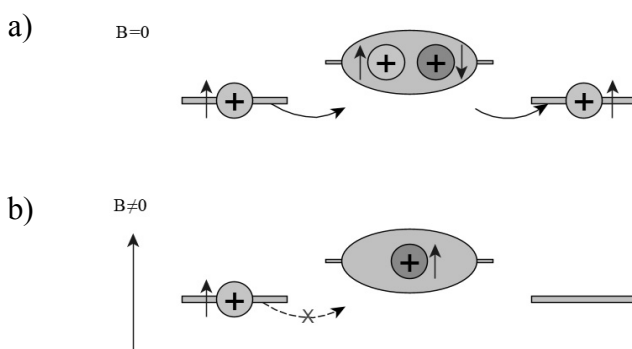


Fig.10. Schematic representation of the formation of a bipolaron at $B = 0$ on the trap of capture (a) and “spin blocking” at $B \neq 0$ (b)

After the collapse of the bipolaron, the hole is able to jump onto the adjacent trap, forming a new bipolaron. Thus, as a result of jumping to nearby defects with the formation of bipolarons, a charge transfer process occurs in the system under study. Due to the hyperfine interaction, the singlet and triplet states of polarons can be mixed [14]. When applying an external magnetic field, the spins of two positively charged polarons are oriented in the same direction (Figure 10, b). The channel of formation of the bipolaron is blocked. This mechanism is called “spin blocking” [15]. As a result, a decrease in the short-circuit current of the photosensitive cell is observed.

The probability of the formation of a bipolaron depends on the rate constant for the repetition of previously uninteracting polarons. In turn, the rate constant of repulsion depends on the dimension of the system in which the reagents are located. With a decrease in the dimension of the system, the rate constant of repulsion increases, which leads to an increase in the probability of the formation of bipolarons. It is obvious that the probability of polaron repulsion in nanowires is higher compared with the film obtained by thermal evaporation. Modulation by an external magnetic field reduces the likelihood of bipolaron formation. Consequently, in nanowires, due to the high probability of polaron repulsion, the effect of “spin blocking” is more pronounced when modulated by an external magnetic field.

Conclusion

Thus, studies have shown that a solid film obtained by thermal evaporation has the structure of the α -phase; CuPc nanowires are in the η -phase. It is shown that the defect structure of the film has a significant effect on the value of the short circuit current of the cell. The effect of a magnetic field on the short-circuit current of the IVC CuPc is investigated. A decrease in the value of the short circuit current is observed when an external magnetic field is applied, which is associated with the mechanism of "spin blocking" in the process of formation of a bipolaron. It has been established that in nanowires, due to the high probability of polaron repetition, the effect of "spin blocking" is more pronounced.

Acknowledgment

This work was supported by the grant of the academician E.A. Buketov Karaganda State University

REFERENCES

- 1 Plotnikov G.S., Zajcev V.B. *Fizicheskie osnovy molekulyarnoj jelektroniki*. Moscow, Fiz. fakul'tet MGU, 2000, 164 p. [in Russian]
- 2 Suzdalev I.P. *Nanotehnologija: fiziko-himija nanoklastero, nanostruktur i nanomaterialov*. Moscow, KomKniga, 2006, 592 p. [in Russian]
- 3 Borisenko V.E., Vorob'eva A.I., Utkina E.A. *Osnovy nanojelektroniki*. Minsk, BGUIR, 2004, 91 p. [in Russian]
- 4 Vidya C., A. Hoskeri Priya, Joseph C.M., Structural and Optical Properties of Vacuum Coated and Annealed Copper Phthalocyanine (CUPC) Thin Films. *Proceeding of the 4th International Conference on Materials Processing and Characterzation (ICMPC) Location: Gokaraju Rangaraju Inst Engin & Technol, Hyderabad, India, 2015*, pp. 1770 – 1775.
- 5 Keeratithiwakorn P., Songkeaw P., Onlaor K. & Tunhoo B., Structural properties of copper phthalocyanine films grown by electrophoretic deposition process. *Materials Today: Proceedings*, 2017, Vol. 4, pp. 6194 – 6199.
- 6 Zou T., Wang X., Ju H., Zhao L., Guo T., Wu W., Wang H., Controllable molecular packing motif and overlap type in organic nanomaterials for advanced optical properties. *Crystals*. 2018, Vol.22, No. 8 (1), pp. 1 – 12.
- 7 Keeratithiwakorn P., Songkeaw P., Onlaor K. & Tunhoo B. Structural properties of copper phthalocyanine films grown by electrophoretic deposition process. *Materials Today: Proceedings*. 2017, Vol. 4. 6194 – 6199.
- 8 Caplins Benjamin W., Mullenbach Tyler K., J. Holmes Russell & Blank David A. Femto second to nanosecond excited state dynamics of vapor deposited copper phthalocyanine thin films. *Phys. Chem. Chem. Phys*, 2016, 18, pp. 11454 – 11459.
- 9 El-Nahass M. M., Bahabri F.S. & Al-Harbi R. Optical Properties of Copper Phthalocyanine (CuPc) Thin Films. *Egypt. J. Sol.*, 2001, Vol. 24, 1, pp. 11-19.
- 10 Khanam Jobeda J., Foo Simon Y. Modeling of High-Efficiency Multi-Junction Polymer and Hybrid Solar Cells to Absorb Infrared Light. *Polymers* , 2019, Vol. 11, Issue 2, No. 383, pp. 2323 – 2325.
- 11 Lixiang C., Yanlian L., Qiaoming Z., Zuhong X., Negative magnetoconductance effects in amorphous copper phthalocyanine thin film: trap-assisted bipolaron formation. *J. Mater. Chem. C*, 2015, Issue 3, pp. 1 – 6.
- 12 Tiwari S., Greenham N.C., Charge mobility measurement techniques in organic semiconductors. *Optical and Quantum Electronics*, 2009, Vol. 41, No. 2, pp. 69 – 89.
- 13 Yan L., Wu Y., Xu Zh., Hu B., Positive and negative magnetic field effects in organic semiconducting materials. *Syntetic Metals*, 2009, Vol. 159, No. 21-22, pp. 2323 – 2325.
- 14 Janssen P., Cox M., Wouters S.H.W., Kemerink M., Wienk M.M. & Koopmans B., Tuning organic magnetoresistance in polymer-fullerene blends by controlling spin reaction pathways, *Nature Communications*, 2013, pp. 1-8.
- 15 Bobbert P. A., Nguyen T. D., F. W. A. van Oost, Koopmans B., and Wohlgenann M. Bipolaron Mechanism for Organic Magnetoresistance. *PRL* 99, 2007, pp. 216801.

UDC 577.322

QUANTUM-CHEMICAL CALCULATIONS OF THE STRUCTURE AND ELECTRON TRANSITIONS OF MULTIMOLECULAR FILMS

Kopbalina K.B.¹, Mazhenov N.A.¹, Bimbetova G.M.²

¹Karaganda State Technical University, Karaganda, Kazakhstan, kopbalina82@mail.ru

²L.N. Gumilyov Eurasian National University, Nur-Sultan, Kazakhstan

Dynamic and static quenching of fluorescence occurs upon contact interaction of oxygen molecules. Of the simplest models of the complex of oxygen and anthracene, a complex consisting of one molecule of oxygen and anthracene molecule is proposed. Quantum-chemical calculations were performed by using the Gaussian 98 software package. Equilibrium geometry of the ground electron state was obtained for a complex of oxygen and anthracene molecules. The electron absorption spectrum is calculated for this complex. It is established that this complex of oxygen and anthracene is not photo-stable.

Keywords: molecular oxygen, anthracene molecule, computer modeling, molecular orbitals, wave function.

Introduction

Molecular oxygen plays an important role in many natural oxidative reactions and technological processes. The establishment of the mechanism of photosensitized oxidative processes involving molecular oxygen is of fundamental interest for photochemistry and photobiology. Collision of the oxygen molecule with the luminophore in the excited state leads to non-radiative energy transfer. The degree of quenching depends on the frequency of collisions, consequently, on the concentration and temperature of the oxygen-containing medium, therefore an oxygen molecule generates a number of interesting photophysical phenomena, the mechanisms of which are not completely clear. In this regard, the study of photoprocesses involving molecular oxygen retains its relevance.

Computer modeling is one of the effective methods for studying complex systems. In recent decades, it is one of the components of almost any research in physics and chemistry. There are many methods of such modeling, oriented on solution various problems and differing both in a strategic approach and in software implementation. Computer modeling is to conduct a series of computational experiments on a computer, the purpose of which is to analyze, interpret and compare the modeling results with the real behavior of the study object and, if necessary, refine the model.

Molecular modeling begins with the formation of a computer model of an object by specifying spatial coordinates. Information on the initial geometry can be obtained by different ways: X-ray structural data bases, search of standard geometries in libraries, construction of structural models by using various software. The next stage of computer modeling of the molecule is the optimization of the geometric structure. Optimization is the search for a structure with minimal energy. There are computational methods for optimizing geometry. Method of molecular mechanics is separately distinguished. In this method atoms in a molecule composition are considered as set material points, which interacting with each other as in the harmonic oscillator model. The other methods (algorithms) of minimization can be divided into two classes: methods based on gradient techniques (method of steepest descent, conjugate gradient method) and methods using the second derivative (Newton-Raphson method and related methods).

1. Quantum-chemical calculations

The calculations were carried out by using the density functional method and the Gaussian 98 software package [1]. Geometry optimization was performed by using the Beke three-parametric hybrid method with gradient-correction correlation of the Lee, Yang and Para functional (B3LYp) and the standard basis set 6-31G (d). The theoretical UV and visible spectra were obtained with considering the time dependence of the density functional method [1–13], where the discrete excitation spectra and the corresponding oscillator strengths were estimated from several dozens of low-energy singlet transitions. The optimized geometries of anthracene and oxygen molecules were calculated. The sequence of energy levels of molecular orbitals (MO) of oxygen is presented in table 1.

Table 1. The sequence of MO energy levels of oxygen.

MO	Energy	MO	Energy
SGG	-1.82017	SGG	-1.69635
SGU	-1.04054	SGU	-0.91208
SGG	-0.78167	SGG	-0.73081
PIU	-0.70022	PIU	-0.54924
PIU	-0.70022	PIU	-0.54924
PIG	-0.49006		
PIG	-0.49006		

Electron spectra for the optimized geometry of anthracene molecules were obtained by using the Gaussian program. The distribution of effective charges on the atoms of the anthracene molecule is obtained. Electron configurations for the S_0 state are constructed based on the molecular orbitals of the anthracene molecule (φ_n -n-number of MO in the ground singlet state) (Table 2). Wave functions of the excited states Φ_i are constructed from these configurations.

Table 2. Energies and wavelengths of electron transitions for S_0 state of the anthracene molecule

Nature of transition	Transition energy, eV	Wave function	Wavelength, nm	Oscillator strength
$S_1(^1\pi \rightarrow \pi^*)$	3.33	${}^1\Phi_1 = -0.16(\varphi_{32} \rightarrow \varphi_{35}) + 0.67(\varphi_{33} \rightarrow \varphi_{34})$	371	0.2224
$T_1(^3\pi \rightarrow \pi^*)$	1.86	${}^3\Phi_1 = 0.24(\varphi_{32A} \rightarrow \varphi_{37A}) + 0.73(\varphi_{34A} \rightarrow \varphi_{35A}) + 0.18(\varphi_{30B} \rightarrow \varphi_{35B}) - 0.57(\varphi_{32B} \rightarrow \varphi_{33B})$	665	0.0047

An analysis of the wave function ${}^1\Phi_1 = -0.16(\varphi_{32} \rightarrow \varphi_{35}) + 0.67(\varphi_{33} \rightarrow \varphi_{34})$ of the excited $S_1(^1\pi \rightarrow \pi^*)$ state shows that absorption at 371 nm with an oscillator strength of 0.2224 occurs when the transition of π -electrons of conjugated bonds to the π^* vacant molecular orbital of the anthracene molecule (Table 2, MO $\varphi_{32} \rightarrow \varphi_{35}, \varphi_{33} \rightarrow \varphi_{34}$), which corresponds to the experimentally observed absorption value of 370 nm. Thus, the calculated electron transition at 371 nm occurs from the S_0 state of the anthracene molecule, which is in the global minimum to the S_1 excited state [9–11]. Molecular orbitals for the S_0 structure of the anthracene molecule are given in Table 3.

Table 3. Molecular orbitals for the S_0 structure of the anthracene molecule

Energy of MO, eV	MO(φ) and contributions AO (χ)
-0,31150	$\varphi_{32} = -0,31\chi_Z^4 - 0,39\chi_Z^{12} - 0,39\chi_Z^{16} - 0,31\chi_Z^{24} - 0,39\chi_Z^{36} - 0,39\chi_Z^{40} + 0,31\chi_Z^{49} + 0,31\chi_Z^{53}$
0,01054	$\varphi_{35} = -0,30\chi_Z^4 + 0,39\chi_Z^{12} - 0,39\chi_Z^{16} + 0,30\chi_Z^{24} + 0,39\chi_Z^{36} - 0,39\chi_Z^{40} + 0,30\chi_Z^{49} - 0,30\chi_Z^{53}$
-0,26840	$\varphi_{33} = -0,23\chi_Z^4 - 0,30\chi_Z^8 + 0,10\chi_Z^{12} - 0,10\chi_Z^{16} + 0,30\chi_Z^{20} + 0,23\chi_Z^{24} + 0,40\chi_Z^{28} - 0,43\chi_Z^{32} - 0,10\chi_Z^{36} + 0,10\chi_Z^{40} + 0,30\chi_Z^{44} - 0,23\chi_Z^{49} + 0,23\chi_Z^{53} + 0,30\chi_Z^{57}$
-0,02679	$\varphi_{34} = 0,23\chi_Z^4 - 0,30\chi_Z^8 + 0,11\chi_Z^{12} - 0,11\chi_Z^{16} - 0,30\chi_Z^{20} + 0,23\chi_Z^{24} + 0,42\chi_Z^{28} + 0,42\chi_Z^{32} - 0,11\chi_Z^{36} - 0,11\chi_Z^{40} - 0,30\chi_Z^{44} + 0,23\chi_Z^{49} + 0,23\chi_Z^{53} - 0,30\chi_Z^{57}$
-0,32152	$\varphi_{32A} = -0,34\chi_Z^4 + 0,34\chi_Z^{12} + 0,34\chi_Z^{16} - 0,34\chi_Z^{24} - 0,34\chi_Z^{36} - 0,34\chi_Z^{40} + 0,34\chi_Z^{49} + 0,34\chi_Z^{53}$
0,02758	$\varphi_{37A} = -0,13\chi_Z^4 + 0,32\chi_Z^8 + 0,30\chi_Z^{12} - 0,30\chi_Z^{16} + 0,32\chi_Z^{20} - 0,13\chi_Z^{24} + 0,24\chi_Z^{28} + 0,24\chi_Z^{32} + 0,30\chi_Z^{36} - 0,30\chi_Z^{40} + 0,32\chi_Z^{44} - 0,13\chi_Z^{49} - 0,13\chi_Z^{53} + 0,32\chi_Z^{57}$
-0,35524	$\varphi_{30B} = 0,13\chi_Z^4 + 0,31\chi_Z^8 + 0,30\chi_Z^{12} - 0,30\chi_Z^{16} - 0,31\chi_Z^{20} - 0,13\chi_Z^{24} + 0,26\chi_Z^{28} - 0,26\chi_Z^{32} + 0,30\chi_Z^{36} + 0,30\chi_Z^{40} + 0,31\chi_Z^{44} + 0,13\chi_Z^{49} - 0,13\chi_Z^{53} - 0,32\chi_Z^{57}$
-0,06187	$\varphi_{33B} = -0,26\chi_Z^4 - 0,24\chi_Z^8 + 0,20\chi_Z^{12} - 0,20\chi_Z^{16} + 0,24\chi_Z^{20} + 0,26\chi_Z^{24} + 0,39\chi_Z^{28} - 0,39\chi_Z^{32} + 0,20\chi_Z^{36} + 0,20\chi_Z^{40} - 0,24\chi_Z^{44} - 0,26\chi_Z^{49} + 0,26\chi_Z^{53} + 0,24\chi_Z^{57}$

According to the definition of academician A.N. Terenin, the photonics of molecules is a combination of photophysical and photochemical processes occurring in them after absorption of a quantum of light [9]. In optically excited electron states, chemical or structural changes can occur. Such processes are called photochemical, in contrast to processes that do not lead to such changes and are called photophysical. After the absorption of a quantum of light in a molecule, several photophysical processes of conversion of the excitation energy can occur [14].

The processes leading to a decrease in the energy of electron excitation, i.e. energy deactivation processes, by their nature, can be radiative (radiation, optical) and non-radiative. A characteristic feature of radiation transitions is the absorption or emission of a quantum of light (photon) by a molecule. The study of the photonics of molecules requires knowledge not only of the energies and wave functions of various electron states, but also of the probabilities of transitions of a molecule from one state to another. The absorption spectrum registered in the experiment most often consists of several bands. The absorption band is characterized by the shape, intensity and position of the absorption maximum, measured in wavelengths or energy units.

When interpreting the absorption spectra, the Frank-Condon principle must be taken into account. It consists in the statement that during the electron transition the electron state of the molecule changes so rapidly that the atomic nuclei do not have time to shift from their equilibrium positions. Since calculations of the excited states are carried out on the basis of the geometry of the ground state of the molecules, according to the Frank – Condon principle, calculated energies of the excited states E_i should be compared with the maximum of the band in the electron absorption spectrum $S_0 \rightarrow S_i$ [11].

Fig.1 presents the electron spectrum $S_0 \rightarrow S_1$ of the anthracene molecule, obtained from the calculation by means of the program “Gaussian-09”. As can be seen, from the fig.1, the maximum of the spectrum is the $\lambda = 371.96$ nm wavelength and corresponds to the transition from the ground state to the first excited singlet state. The oscillator strength is 0.2224. Fig. 2 shows the calculated electron spectrum of the anthracene molecule for the $S_0 \rightarrow T_1$ transition. The maximum of the spectrum is the $\lambda = 665.64$ nm wavelength. The oscillator strength is 0.0047. The obtained data are in agreement with the experimental one [12].

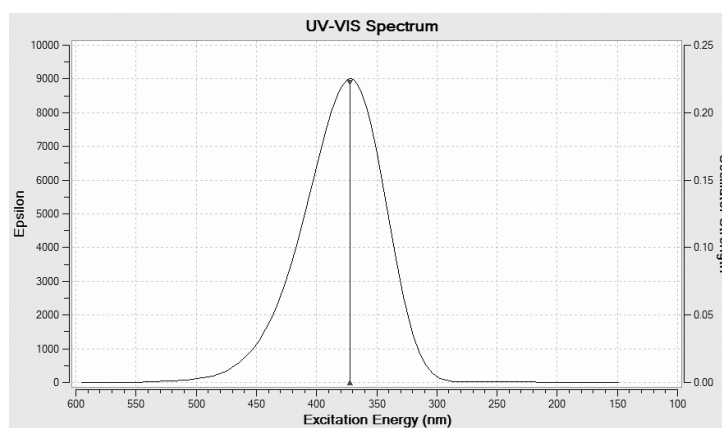


Fig.1. Electron spectrum of anthracene molecule ($S_0 \rightarrow S_1$)

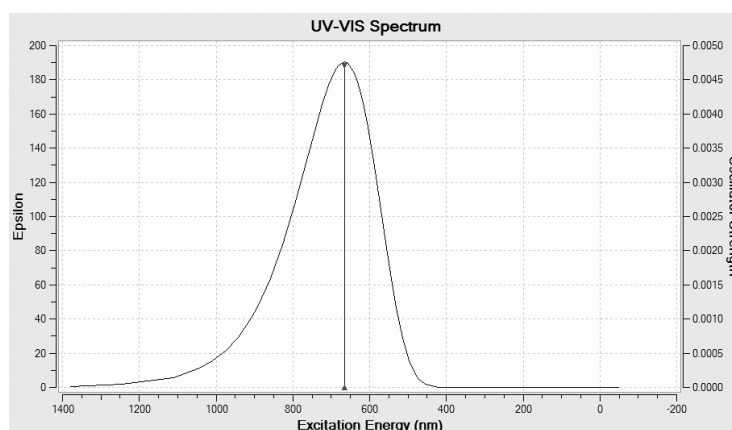


Fig.2. Electron spectrum of anthracene molecule ($S_0 \rightarrow T_1$)

The calculated energies of $S_0 \rightarrow S_1$ and $S_0 \rightarrow S_2$ singlet-singlet transitions, as well as their oscillator strengths (f) of the anthracene molecule are shown in Table 4. Quantum-chemical calculations performed by the ZINDO method for this luminophore give quite good agreement of the spectral characteristics obtained from calculations and experiment. As can be seen from Table 4, the wavelength value ($\lambda=665.64$ nm) of the $S_0 \rightarrow T_1$ transition is close to the experimental one ($\lambda=650$ nm).

If the environment in the film form has a slight effect, then the equilibrium geometry of the ground and the excited electron states can be calculated [13].

Monomer and dimer of anthracene can absorb and fluoresce in the experiment. Therefore, it is necessary to study the spectra of both monomers and dimers of anthracene. At the first stage, it is necessary to determine the geometries of the ground and first excited electron states. Note that in the experiment, an electron vibrational absorption spectrum is observed ($0 \rightarrow 0$, $0 \rightarrow 1$, $0 \rightarrow 2, \dots$).

Monomer and dimer of anthracene can absorb and fluoresce in the experiment. $0 \rightarrow 0$ is pure electron transition, $0 \rightarrow 1$, $0 \rightarrow 2$ is electron oscillatory transition.

2. Results and discussion

We can calculate only pure electron transition. Therefore, it is necessary to first determine the geometry of the ground electron state. The spin of anthracene in the ground state is zero.

Currently, the density functional theory (DFT) method is used to optimize the geometry of large molecules (larger than naphthalene). The most popular is the exchange-correlation functional B3LYP (hybrid functional). Therefore, to solve this problem, the DFT / B3LYP method was chosen. In this case, three exhibitors TZVP were selected. The optimization of the geometry of the ground and excited electron states was carried out in the Gaussian-09 program on the SKIF CYBERIA supercomputer. The equilibrium geometries of the ground and first excited electron states of the anthracene molecule were determined by the DFT / B3LYP / TZVP method.

The truth of the found geometry is confirmed by calculating the oscillation frequencies by the harmonic approximation, all frequencies not imaginary. The geometries of the ground and first excited electron states are significantly different. Therefore, the Stokes shift for the absorption and the fluorescence spectra of anthracene should not be small [14].

To characterize the anthracene electron absorption spectrum, the energy of the first electron transition $S_0 \rightarrow S_1$ and the oscillator strength were calculated by using the temporal dependent density functional theory TDDFT and B3LYP/ TZVP method. In addition, to characterize the fluorescence spectrum, the $S_1 \rightarrow S_0$ transition and the oscillator strength of its were calculated. Calculation results are shown in table 4.

Table 4. Spectra of absorption and fluorescence of anthracene monomers

Absorption Spectrum		
Wavelength, nm		Oscillator strength
$S_0 \rightarrow S_1$	381.84	0.0584
$S_0 \rightarrow S_2$	319.66	0.0002
Fluorescence spectrum		
Wavelength, nm		Oscillator strength
$S_1 \rightarrow S_0$	441.03	0.0607

As shown, modern calculations and experiments, there are 4 types of anthracene. Equilibrium geometries of the ground electron states of anthracene dimers are calculated: slipped-parallel, symmetry C_{2h} , graphite type, symmetry C_i , T-shape, symmetry C_{2v} , Crossed, symmetry D_{2d} . By using the B97D functional the equilibrium geometries of the ground state of 4 anthracene dimers were obtained, the truth of which was confirmed by calculating the frequent oscillations of harmonic approximations (all frequencies not imaginary).

Dynamic and static quenching of fluorescence occurs upon contact interaction of oxygen molecules. Therefore, at the first stage of the study, it is necessary to obtain equilibrium geometry of the complex of oxygen and anthracene. Of the simplest models of the complex of oxygen and anthracene, a complex consisting of one molecule of oxygen and anthracene is proposed. Results of calculations of the electrostatic potential for anthracene molecules show that the surrounding molecules can interact mainly with the central ring. Therefore, it is fair to place the oxygen molecule on the central ring of anthracene (Fig.1).

For such a complex, it is necessary to determine the equilibrium geometry of the ground and first excited electron states. To solve this problem, the B3LYP / TZVP hybrid functional was also

4 Gurinovich G.P. Kislorod, yego lyuminesstentsiya i vliyaniye na lyuminesstentsiyu organicheskikh molekul [Oxygen, its luminescence, and the effect on luminescence of organic molecules]. *Izvestiya Akademii Nauk SSSR, Ser.fiz.* Bulletin of Academy of Sciences of the USSR. Physics series. 1982, Vol. 46, No. 2, pp. 362 – 366. [in Russian]

5 Aymukhanov A.K., Ibrayev N.Kh., Smagulov Zh.K. Polucheniye i spektral'no-kineticheskiye svoystva nanogibridnykh plenok geptadetsilovogo efira bengal'skoy rozy i poliamfolitnogo polimera. [Production and spectral-kinetic properties of nanohybrid films of Bengal rose heptadecyl ether and polyampholytic polymer]. *Bulletin of the Karaganda University. Chemistry series.* 2010, No. 2(58), pp. 112 – 117. [in Russian]

6 Aymukhanov A.K., Ibraev N.Kh., Kucherenko M.G., Chmereva T.M. Kinetika fotoreaktsiy s uchastiyem molekulyarnogo kisloroda v plenkakh lengmyura-blodzhett. [Kinetics of photoreactions involving molecular oxygen in films of Langmuir-Blodgett]. *Optika i spektroskopiya - Optics and Spectroscopy.* 2013, Vol. 114, No. 4, pp. 120 – 126. [in Russian]

7 Aymukhanov A.K., Ibraev N.Kh., Seliverstova E.V. Mezhsloynnyy perenos tripletnoy energii v plenkakh Lengmyura-Blodzhett [Interlayer transfer of triplet energy in Langmuir-Blodgett films]. *Bulletin of the Karaganda University. Physics series.* 2008, No. (51), pp. 20 – 24. [in Russian]

8 Kucherenko M.G. Kinetika staticheskogo nelineynogo samotusheniya lyuminesstentsii v kolloidnykh sistemakh [Kinetics of static nonlinear self-quenching of luminescence in colloidal systems] // - *Kolloid. Zhurnal - Colloid Journal.* - 1998. - Vol.60. No. 3. - pp. 380-388. [in Russian]

9 Rullens F., Divillers M., Laschevsky A. New Regular, Amphiphilic Poly(ampholyte)s: Synthesis and Characterization. *Macromolecular Chemistry and Physics.* 2004, Vol. 205, pp. 1155 – 1166.

10 Terenin A.N. *Fotonika molekul krasiteley - Photonics of dye molecules.* Leningrad: Science, 1967, 616 p. [in Russian]

11 Nurmukhametov R.N. *Pogloshcheniye i lyuminesstentsiya aromaticheskikh soyedineniy. - Absorption and luminescence of aromatic compounds.* M.: Chemistry, 1971. - 216 p. [in Russian]

12 Nurmukhametov R.N., Plotnikov V.G., Shigorin D.N. Priroda vozbuzhdennykh elektronnykh sostoyaniy i lyuminesstentsiya molekul [The nature of the excited electron states and the luminescence of molecules]. *Zhurnal fizicheskoy khimii.* 1966, Vol. 40, No. 5, pp. 1154 – 1157.

13 Birks T.B. *Photophysics of aromatic molecules.* Sidney-London, 1970, 645 p.

14 Mazhenov N.A., Kopbalina K.B., Effect of oxygen on the excited state of complex organic molecules. *Eurasian Physical Technical Journal.* 2012, Vol. 9, No. 2(18), 57 – 60.

APPLICATION OF A COMPLETE MULTI-NETWORK METHOD FOR SOLVING THE PROBLEM OF FLOWS AROUND SPHERE

Narimanov R.K.¹, Narimanova G.N.²

¹ Tomsk State University, Tomsk, Russian Federation

² Tomsk State University of Control Systems and Radioelectronics, Tomsk, Russian Federation,
gufana.n.narimanova@tusur.ru

Using the example of a numerical solution of the classical problem of a viscous flow past a sphere, the efficiency of using the multigrid method was compared with direct calculations. Various difference schemes are considered. It's shown that to go from grid to grid, for a vortex equation, it is necessary to use a 9-point pattern. For different Reynolds numbers the resistance coefficient to friction had been calculated. The limit on the Reynolds number when using the multigrid method is noted.

Keywords: numerical solution, multigrid method, viscosity, flow, sphere, ellipsoid.

Introduction

The increasing complexity of the considered natural and technological problems currently facing humanity increases the requirements for methods of solving such problems. One of the common ways to obtain information is a numerical experiment. Therefore, the development of efficient algorithms was, is and will be a relevant research goal. The development of technology has led to the possibility of using multiprocessor devices and, as a result, to the possibility of using more efficient computing technologies. One of which is the multigrid method that allows parallelizing the numerical algorithm.

As is known, the essence of the full multigrid method (FMM) is based on the sequence of nested grids. Cyclic transitions from one grid to another allow one to effectively suppress the low-frequency components of the residual of the solution when calculating with relaxation difference schemes [1]. The ideology of the method allows the use of parallel computing on multiprocessor technology.

This paper presents the results of a study of the effectiveness of the multigrid method for determining the coefficient of friction resistance with an external stationary flow of an incompressible viscous fluid around a solid sphere. This problem is a classical problem of hydrodynamics, which has solutions obtained by analytical and numerical methods. Therefore, it can serve as a test for approbation of the considered solution method.

The relevance of the chosen class of tasks is undoubted. The movement of multiphase media in a variety of technological and natural processes is of great interest. The solution of the complete problem taking into account the interaction of each particle with the carrier medium is an insoluble problem due to the large number of moving particles. As a rule, they are limited by the phenomenological law of the hydrodynamic resistance of a single spherical or spheroidal particle in a carrier medium. The assumption of spherical particle shape is the most common and quite acceptable.

This approach reasonably led to the fact that most of the efforts to determine the law of resistance was devoted to the study of spherical particles. There are many such works, it is enough to specify [2, 3]. In many cases, a moving particle can more accurately be described as an ellipsoid. And in this regard, of interest are studies devoted to the flow around ellipsoids, in particular, ellipsoids of rotation (spheroids).

In [4-5], the results of analytical calculations for the flow parallel to the main axis of spheroids at small Reynolds numbers are presented. In [6-7], the problem of slow viscous flow of a stationary flow around a triaxial ellipsoid was solved analytically based on the application of a tension-compression transformation, and a simple calculation formula for its resistance was indicated. In [8], this method allowed the solution of a non-stationary problem of determining the resistance force during a slow rotation of an ellipsoid in a viscous fluid.

From the examples of numerical studies, it can be noted [9] where the results of the calculation of the flow around a uniform stationary flow of spheroids of various shapes with the numbers $Re < 100$ in the axisymmetric formulation are presented. The calculated data on the flow around spheroids at Reynolds numbers around 100 are shown [10–13]. The results of numerical and experimental studies allow us to construct correlation dependences used in determining the resistance forces during the motion of particles.

1. Statement of the problem

The peculiarity of the considered problem, which is solved in variables vorticity - current function is the need to solve a system of two interrelated equations. We used the sequential method of solving this system:

- 1) the current function is determined for a given distribution of the vortex function;
- 2) the definition of the vortex function.

The process is repeated iteratively until it is established. Thus, it is necessary to perform a large number of repeated calculations and there is a good reason to assume a significant acceleration of the calculation process when using the multigrid method.

The system of equations describing the stationary flow of a viscous incompressible fluid around a sphere in terms of vorticity – the current function in spherical coordinates is as follows:

$$E^2 \psi = \zeta r \sin \theta$$

$$\frac{R}{2} \left[\frac{\partial \psi}{\partial r} \frac{\partial}{\partial \theta} \left(\frac{\zeta}{r \sin \theta} \right) - \frac{\partial \psi}{\partial \theta} \frac{\partial}{\partial r} \left(\frac{\zeta}{r \sin \theta} \right) \right] \sin \theta = E^2 (\zeta r \sin \theta), \quad (1)$$

where the operator $E^2 = \frac{\partial^2}{\partial r^2} + \frac{\sin \theta}{r^2} \frac{\partial}{\partial \theta} \left(\frac{1}{\sin \theta} \frac{\partial}{\partial \theta} \right)$.

All values are dimensionless as follows:

$$r = \frac{r'}{A}, \quad \psi = \frac{\psi'}{UA^2}, \quad \zeta = \frac{\zeta' A}{U}, \quad R = \frac{2UA}{\nu}. \quad (2)$$

Here A is the radius of the sphere, U is the velocity of the undisturbed flow, and ν is the kinematic viscosity.

The boundary conditions are determined from the assumptions about the absence of perturbations at the remote boundary, the no-slip conditions on the solid sphere, and the axisymmetry of the flow. As the outer boundary, a surface is chosen that is seven radii from the surface of the sphere.

2. Method of solution

In the calculations, difference schemes were used - an explicit Gauss-Seidel scheme, an implicit longitudinal sweep scheme for a variable r . And these schemes were used in the multigrid method. To go from grid to grid, for a vortex equation, it is necessary to use a 9-point pattern, which allows to suppress nonphysical oscillations inherent to difference schemes with increasing Reynolds number [1]. The main characteristic for confirming the reliability of the results obtained

is the coefficient of resistance to friction, which was calculated for different numbers of Re: 0.01, 0.1, 0.5, 2, 5, 10, 20 (Table 1).

The numerical solution of the problem was carried out on a sequence of nested grids 25x25, 50x50, 100x100, 200x200.

3. Results and discussion

The results of numerical calculations were compared with the results of Jenson's research [1] for Reynolds numbers 5, 10, and 20 and with the well-known analytic Stokes dependence for the drag coefficient for friction in the flow at small Reynolds numbers. The data are shown in table 1.

Table 1. Friction drag coefficient

Re	Stoks 16/Re	Jenson	Multigrid explicit scheme	Explicit scheme	Multigrid implicit scheme	Implicit scheme
0.01	1600		1628.3	1683.5	1681	1630.6
0.1	160		163.09	168.23	169.16	163.37
0.5	32		33.77	34.73	33.57	33.94
1	16		17.50	17.63	17.48	17.60
2			10.30	10.54	9.72	10.29
5		5.34			4.98	5.42
10		3.10				3.37
20		1.857			1.94	1.97

Table 2 shows the comparative efficiency data of the multigrid method using different schemes for the direct calculation of the considered scheme. The relations of the time of the "usual" directly calculation on the smallest grid and the calculation time by the multigrid method using the same difference scheme and the same criterion for the termination of iterations in accuracy are given.

Table 2. Comparative effectiveness of the multigrid method.

Re	Multigrid explicit scheme	Multigrid implicit scheme
0.01	1.4	16.3
0.1	1.5	8.3
0.5	1.6	5.7
1	2.2	5
2	2.9	4
5		7.3

As can be seen from the table 2, the combination of the multigrid method and the implicit difference scheme seems to be the most effective. However, it is necessary to recognize that reducing the calculation time by 16 times seems "too" a good result.

The multigrid method has a peculiarity - the calculation on a coarse grid is limited by the stability criterion with respect to the grid Reynolds number. According to the recommendation of

Jenson [1], the grid step cannot exceed the value $4/Re$. Therefore, on the above sequence of grids, it is possible to obtain a solution only for Reynolds numbers less than 5. To calculate the flow field for Reynolds numbers 10 and 20, we used a sequence of grids with dimensions 50x50, 100x100, 200x200.

Conclusion

The high efficiency of the application of the full multigrid method was confirmed by the example of the classical problem of viscous flow around a sphere. The reliability of the calculations is confirmed by comparison with the analytical and numerical results of other authors. The results show that the use of the full multigrid method allows to reduce the time for calculating tasks of this class on average by 4-7 times. There is a limitation on the size of the size of the grid step, affecting the dimension of the nested grids used. These restrictions when applying this procedure on multiprocessor clusters require additional consideration.

REFERENCES

- 1 Fletcher C. *Computational Techniques for Fluid Dynamics*. Moscow, Mir. 1991, Vol. 1, 504 p. [in Russian]
- 2 Jenson V. G. Viscous flow round a sphere at low Reynolds (<40). *Proc. Roy. Soc. London, Ser. A*, 1959, Vol. 249, № 1258, p. 346-366.
- 3 Roache P.J. *Computational hydrodynamics*. Moscow, Mir. 1980, 616 p. [in Russian]
- 4 Lamb G. *Hydrodynamics*. Moscow, Gostekhizdat. 1947, 928 p. [in Russian]
- 5 Happel D., Brenner G. *Hydrodynamics at low Reynolds numbers*. Moscow, Mir. 1976, 630 p. [in Russian]
- 6 Dudin I.V., Narimanov R.K. *Resistance of a triaxial ellipsoid slowly moving in a viscous fluid*. Preprint №37, TSU publishing house, Tomsk, 2000, 11 p. [in Russian]
- 7 Dudin I.V., Narimanov R.K. Resistance in slow movement of the ellipsoid. *Proceedings of the Tomsk Polytechnic University*, Tomsk, 2004, Vol. 307, No.3, pp. 17-21. [In Russian]
- 8 Dudin I.V., Narimanov R.K., Narimanova G.N. Resistance moment at rotation of an ellipsoid in viscous fluid. *Eurasian Physical Technical Journal*. 2018, Vol. 15, No. 2(30), pp. 40-48.
- 9 Zamyshlyayev A. A., Shrager G. R. Fluid Flows past Spheroids at Moderate Reynolds Numbers. *Fluid Dynamics*, Vol. 39, No. 3, 2004, pp. 376-383
- 10 Lipanov A.M., Semakin A.N. Non-spherical particles: resistance and some flow parameters in unlimited volume. *Scientific notes TsAGI*. 2011, Vol. XLII, No. 6, pp. 15 – 22. [in Russian]
- 11 Holser A., Sommerfeld M. New simple correlation formula for the drag coefficient of non-spherical particles. *Powder Technology*. 2008, Vol.184, Issue 3, pp. 361 – 365.
- 12 Loth E. Drag of non-spherical solid particles of regular and irregular shape. *Powder Technology*, 2008, Vol. 182, Issue 3, pp. 342 – 353.
- 13 Clift R., Grace J.R., Weber M. *Bubbles, drops and particles*. New York, Academic press, 1978, 380p.

THE CALCULATION OF THE HEAT TRANSFER COEFFICIENT FROM THE WALLS AND PIPES OF THERMAL NETWORKS IN THE ENVIRONMENT

Sabdenov K.O., Sakipov K.Ye.

L.N. Gumilyov Eurasian National University, Nur-Sultan, Kazakhstan, sakamer2100@gmail.com

A simple semi-analytical method for determining the heat transfer coefficient from cylindrical surfaces is proposed. The idea of the method is based on the representation of the heat wave and the self-similar nature of the process, which allows to obtain an analytical formula. The physical explanation of heat transfer coefficient decrease is given. A comparison of the approximate solution with the numerical solution of the heat propagation problem shows the high accuracy of the analytical formula. The distribution of heat from the pipe into the cold surrounding space at large times with high accuracy can be considered a self-similar process.

Keywords: heat flow, pipeline, heat transfer coefficient, heat wave, self-similarity.

Introduction

When carrying out engineering calculations [1, 2] of heat losses by heat pipes in the environment, the heat transfer coefficient α in Newton's heat transfer law is an uncertain value

$$j = \alpha(T - T_c),$$

where j – the flow of heat; T_w – the surface temperature of the tube wall; T_c – temperature environment.

However, the heat transfer coefficient is assumed to be constant [1], this method can be taken only as an approximation, it gives acceptable results in a limited time interval. But a detailed analysis of the common methods for determining the heat flow j needs a thorough check and justification, since the problem of the distribution of heat from the heated pipe into the surrounding space is not stationary. This means the time variation of the heat transfer coefficient.

In this paper we propose a method for determining the heat transfer coefficient $\alpha(t)$ as a function of time t . For this purpose, the known [3] representation of the heat wave and the assumption of the approximate nature of the self-similar heat propagation are used. Below, a brief explanation of this representation is given by the example of heat propagation from an unbounded flat wall, after which the heat transfer by an infinite length pipe to the surrounding cold environment is analyzed.

1. Heat transfer coefficient between the wall with a constant high temperature and the environment.

Let there be a semi-bounded space (wall) with constant temperature T_w , the wall contacts a semi-bounded medium with low temperature T_0 : $T_w > T_0$. The wall occupies a half-space $x < 0$, the medium is located in the region $x > 0$. The equation of heat propagation in the environment with thermal diffusion coefficient κ is described by the equation

$$\frac{\partial T}{\partial t} = \kappa \frac{\partial^2 T}{\partial x^2}. \quad (1)$$

We will look for the temperature distribution in the form

$$T = T(z), \quad z = \frac{x^2}{4\kappa(t + t_*)},$$

where t_* – is the beginning of the self-similar heat propagation regime, this time must be found from the condition of equality of the heat flow from the exact solution of equation (1) and the heat flow found from the approximate solution of the same equation below.

Calculate the derivatives:

$$\frac{\partial T}{\partial t} = \frac{dT}{dz} \frac{\partial z}{\partial t} = -\frac{z}{t} \frac{dT}{dz}, \quad \frac{\partial T}{\partial x} = \frac{dT}{dz} \frac{\partial z}{\partial x} = \frac{x}{2\kappa} \frac{dT}{dz},$$

$$\frac{\partial^2 T}{\partial x^2} = \frac{1}{\kappa} \left(\frac{1}{2} \frac{dT}{dz} + z \frac{d^2 T}{dz^2} \right).$$

Substituting them into equation (1), we obtain

$$z \frac{d^2 T}{dz^2} + \left(\frac{1}{2} + z \right) \frac{dT}{dz} = 0.$$

Its General solution is

$$T = C_2 + C_1 \int_{z_0}^z \frac{e^{-\zeta}}{\sqrt{\zeta}} d\zeta,$$

where C_1, C_2 - are constant integrations.

Let $z = z_0$ be equal to $T = T_w$, then $C_2 = T_w$. Therefore

$$T = T_w + C_1 \int_{z_0}^z \frac{e^{-\zeta}}{\sqrt{\zeta}} d\zeta,$$

The wall and the environment begin to exchange heat at the initial time $t = 0$, after which the heated heat layer $x_0(t)$, which is a moving wave, "breaks away" from the wall (Fig. 1). To the left of this wave, the temperature $T \approx T_w$, is stored, to the right of the wave front, the temperature is a variable and depends on the x coordinate and time t . Therefore, the requirement used above

$$z = z_0: \quad T \approx T_w,$$

means statement of a boundary condition on the front of this heat wave.

The second boundary condition requires the equality $T = T_0$ for $z \rightarrow \infty$. Fulfilling this condition, we obtain:

$$T_0 = T_w + C_1 \int_{z_0}^{\infty} \frac{e^{-\zeta}}{\sqrt{\zeta}} d\zeta.$$

Denoted

$$\chi = \int_{z_0}^{\infty} \frac{e^{-\zeta}}{\sqrt{\zeta}} d\zeta,$$

Dene the constant C_1 :

$$C_1 = -\frac{T_w - T_0}{\chi}.$$

With this result, you can write

$$T = T_w - \frac{T_w - T_0}{\chi} \int_{z_0}^z \frac{e^{-\zeta}}{\sqrt{\zeta}} d\zeta. \quad (2)$$

The coordinate of the heated layer depends on the time as

$$x_0(t) = \sqrt{4z_0\kappa(t+t_*)}.$$

This shows the existence of arbitrariness in the choice of the constant z_0 . This arbitrariness arose due to the lack of a clear indication of what should be taken as the coordinate of the heat wave.

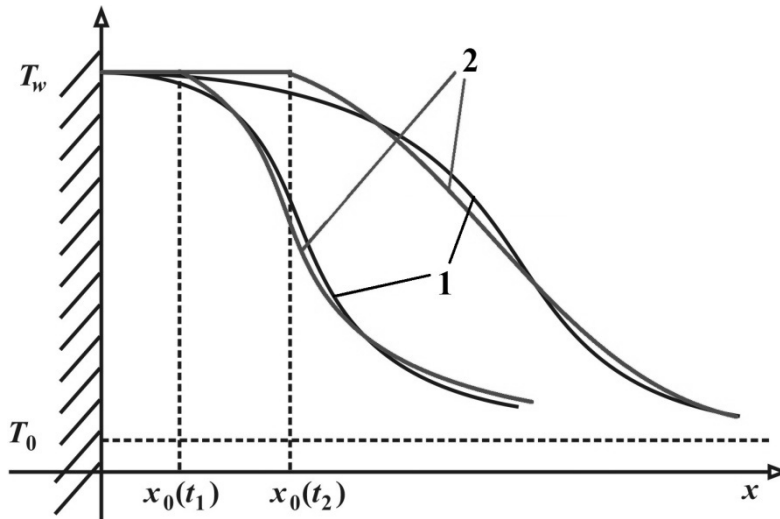


Fig.1. Location of the boundary $x_0(t)$ of the heat wave at two different times t_1 and t_2 ; 1 – real temperature profile; 2 – approximate profile.

But the integral in (2) converges at any (positive) values of z_0 , including $z_0 = 0$. Then it would be logical to choose the lower limit of integration equal to this zero value, and instead of (2) we obtain

$$T = T_w - \frac{T_w - T_0}{\chi} \int_0^z \frac{e^{-\zeta}}{\sqrt{\zeta}} d\zeta, \quad (3)$$

$$\chi = \int_0^\infty \frac{e^{-\zeta}}{\sqrt{\zeta}} d\zeta.$$

Find the heat flow j_w at the boundary of the systems, including on the one hand the wall with the heat wave and the environment on the other hand. This boundary is located at the point $x = x_0(t) = 0$, i.e. the "separation" of the heat wave does not occur. By definition

$$\begin{aligned} j_w &= -\lambda \frac{\partial T}{\partial x} \Big|_{x=x_0(t)} = -\lambda \frac{dT}{dz} \Big|_{z=z_0} \frac{\partial z}{\partial x} \Big|_{x=x_0(t)} = \lambda \frac{T_w - T_0}{\chi} \frac{e^{-z_0}}{\sqrt{z_0}} \frac{x_0(t)}{2\kappa(t+t_*)} = \\ &= \lambda \frac{T_w - T_0}{\chi} \exp(-z_0) \frac{2\sqrt{\kappa(t+t_*)}}{2\kappa(t+t_*)} = \frac{\lambda}{\sqrt{\kappa(t+t_*)}} \frac{e^{-z_0}}{\chi} (T_w - T_0). \end{aligned}$$

As a result, taking into account the equality $z_0 = 0$, the expression is obtained

$$j_w = \frac{T_w - T_0}{\chi} \frac{\lambda}{\sqrt{\kappa(t + t_*)}}.$$

This shows that the heat transfer coefficient α equal

$$\alpha = \frac{1}{\chi} \frac{\lambda}{\sqrt{\kappa(t + t_*)}}.$$

The decrease in the heat transfer coefficient is easy to explain from a physical point of view: as the cold space warms up, it will heat up and accumulate heat, and this is the more the closer to the plate. The plate is covered with a heat shell, and the thickness of this shell gradually increases. As a result, heat transfer through it deteriorates. The outer boundary of this thermal shell is associated with a "heat wave" moving at a speed of dx_0/dt , so the representation of such a wave has a physical justification. The number χ easy to calculate analytically, making the inside of the integral the change of variable $\zeta = s^2$, get

$$\chi = \int_0^{\infty} \frac{e^{-\zeta}}{\sqrt{\zeta}} d\zeta = 2 \int_0^{\infty} e^{-s^2} ds = 2 \frac{\sqrt{\pi}}{2} = \sqrt{\pi}.$$

And the final expression for the heat transfer coefficient will be

$$\alpha = \frac{1}{\sqrt{\pi}} \frac{\lambda}{\sqrt{\kappa(t + t_*)}}.$$

The corresponding formula (3) for temperature can be recorded via the erf error function:

$$T = T_w - (T_w - T_0) \operatorname{erf}(z), \quad \operatorname{erf}(z) = \frac{2}{\sqrt{\pi}} \int_0^z e^{-s^2} ds.$$

If we choose $z_0 \neq 0$, we would get an approximate solution to the problem, and the closer z_0 is to 0, the closer the approximate solution is to the exact solution. The case $z_0 \neq 0$ corresponds to approximate temperature distributions in Fig. 1. It can be seen that in some complex cases (discussed below), when it is not possible to find an exact analytical solution to the problem of thermal conductivity, it is possible to obtain approximate solutions using the idea of "heat wave". One of these cases is the propagation of heat from a cylindrical region into an infinite space, and below we proceed to its detailed analysis.

2. Heat transfer coefficient between a pipe with a constant high temperature and an infinite surrounding cold space.

For cylindrical and spherical problems, the exact self-similar solution cannot be obtained analytically. Therefore, such geometries are of interest for the application of the approximate method, the idea of which is given above. Consider the cylindrical problem below.

Choose a cylindrical coordinate system with the center of symmetry on the pipe axis with radius R , the radial coordinate r is counted from this axis. Along the axis of the pipe, the temperature in it T_p is constant, so for the environment with the initial temperature T_c , the heat equation in the form of

$$\frac{\partial T}{\partial t} = \kappa \frac{1}{r} \frac{\partial}{\partial r} \left(r \frac{\partial T}{\partial r} \right). \quad (4)$$

In mathematical form, initial and boundary conditions are strictly set in the following form:

$$T(t=0, r) = T_c = \text{const},$$

$$T(t, r=R) = T_p, \quad T(t, r=\infty) = T_c.$$

We find an approximate solution to this problem using the idea of a heat wave. Instead of the given boundary conditions, we take other:

$$T(t, r=r_0(t)) = T_p, \quad T(t, r=\infty) = T_c, \quad (5)$$

where $r_0(t)$ – the front of the thermal wave.

Now we are looking for the solution of equation (4) as a function of one self-similar variable containing the characteristic time $t_* = \text{const}$:

$$T = T(z), \quad z = \frac{r^2}{4\kappa(t+t_*)}.$$

Calculate the derivatives:

$$\frac{\partial T}{\partial t} = \frac{dT}{dz} \frac{\partial r}{\partial t} = -\frac{r}{t+t_*} \frac{dT}{dz}, \quad r \frac{\partial T}{\partial r} = \frac{dT}{dz} \frac{\partial z}{\partial r} = \frac{r^2}{2\kappa(t+t_*)} \frac{dT}{dz},$$

$$\frac{\partial}{\partial r} \left(r \frac{\partial T}{\partial r} \right) = \frac{r}{\kappa(t+t_*)} \frac{dT}{dz} + \frac{r^2}{2\kappa(t+t_*)} \frac{d^2T}{dz^2} \frac{\partial z}{\partial r} = \frac{r}{\kappa(t+t_*)} \left(\frac{dT}{dz} + z \frac{d^2T}{dz^2} \right).$$

Taking into account the received expressions the equation (4) turns into the ordinary differential equation

$$z \frac{d^2T}{dz^2} + (1+z) \frac{dT}{dz} = 0.$$

Its General solution contains integration constants C1 and C2:

$$T = C_2 - C_1 \int_{z_0}^z \frac{e^{-\zeta}}{\zeta} d\zeta, \quad \text{here } \frac{dT}{dz} = -C_1 \frac{e^{-z}}{z}. \quad (6)$$

The obtained results can be given the following physical interpretation: the pipe is surrounded by a thermal "shell" and its radius varies according to the law $r_0(t)$ (Fig. 2).

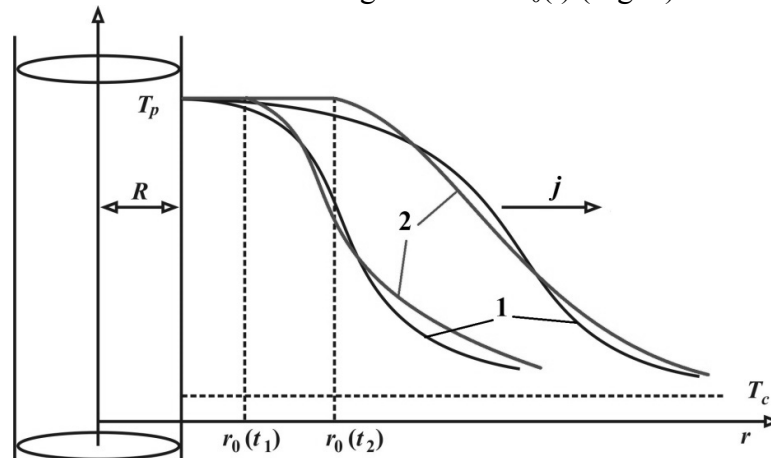


Fig.2. Location of the boundary $r_0(t)$ of the heat wave at two different times t_1 and t_2 :
1 - real temperature profile; 2 - approximate profile.

In the region $r < r_0(t)$ the temperature is constant and equal to T_p , in the region $r > r_0(t)$ the temperature changes according to the first equality in (6). The same figure shows the exact and approximate temperature distributions at different times. Within the shell thickness, the temperature is constant and equal to T_p , this is laid down in the first boundary condition of (5). Therefore, when $z = z_0$, the equality $T = T_p$ must be executed, using the first equality in (6) we find $C_2 = T_p$. The number z_0 remains an indefinite value because of the uncertainty of time t_* , it has the physical meaning of the conditional time when the wave mode of heat propagation begins. But now we can say that the law of changing the thickness of the shell has a specific relationship:

$$r_0(t) = \sqrt{4z_0\kappa(t + t_*)}. \quad (7)$$

The expression for temperature now takes the form

$$T = T_p - C_1 \int_{z_0}^z \frac{e^{-\zeta}}{\zeta} d\zeta. \quad (8)$$

Using the second boundary condition of (5) with this form $T(z)$ we obtain

$$T_0 = T_p - C_1\eta, \quad \eta = \int_{z_0}^{\infty} \frac{e^{-\zeta}}{\zeta} d\zeta,$$

$$\text{or } C_1 = \frac{T_p - T_0}{\eta}.$$

$$\text{Now (8) can be rewritten as } T = T_p - \frac{T_p - T_0}{\eta} \int_{z_0}^z \frac{e^{-\zeta}}{\zeta} d\zeta.$$

Find the heat flow j from the pipe to the environment, this flow must be calculated at the point $r = r_0$:

$$j = -\lambda \frac{\partial T}{\partial r} \Big|_{r=r_0(t)} = -\lambda \frac{\partial T}{\partial z} \Big|_{z=z_0} \frac{\partial z}{\partial r} \Big|_{r=r_0(t)} = \frac{\lambda}{\eta\sqrt{\kappa(t+t_*)}} \frac{\exp(-z_0)}{\eta\sqrt{z_0}} (T_p - T_0).$$

The second equation of (6) is used to calculate the temperature derivative. From here we can see that the heat transfer coefficient for the pipe is

$$\alpha = \frac{\lambda}{\eta\sqrt{\kappa(t+t_*)}} \frac{\exp(-z_0)}{\eta\sqrt{z_0}}. \quad (9)$$

Thus, the formula for the heat transfer coefficient with two uncertain parameters η and t_* is obtained. It cannot be calculated only from the analysis of equations (8) and (9), to determine the η and t_* need an accurate solution to the problem. The exact solution is assumed to be obtained by numerical solution of equation (4) with reduced boundary and initial conditions (5).

3. Comparison of approximate solutions with the results of numerical solution of the problem of heat propagation from a heated pipe to an unlimited cold space.

The following problem was solved numerically to determine the parameters η and t_* and to check the accuracy of the obtained result for the heat transfer coefficient (9)

$$\frac{\partial T}{\partial t} = \kappa \frac{1}{r} \frac{\partial}{\partial r} \left(r \frac{\partial T}{\partial r} \right), \quad (10)$$

Boundary and initial conditions:

$$T|_{r=R} = T_p; \quad \left. \frac{\partial T}{\partial r} \right|_{r \rightarrow \infty} = 0; \quad T|_{t=0} = T_c.$$

Here κ – coefficient of thermal diffusion: $\kappa = \lambda/(c\rho)$, where λ – coefficient of thermal conductivity; c – capacity; ρ – density.

This problem simulates the propagation of heat from a pipe of radius R to an infinite space, in which at the initial time the temperature was T_c , the temperature of the pipe is constant and equal to T_p (Fig. 2). In formula (7), the numerical values of the parameters η and t_* remain undefined. To determine them, it is necessary to compare the heat fluxes determined in the numerical solution and in the approximate way according to the formula (12) below. The condition of maximum proximity of these heat fluxes is used to determine η and t_* . An implicit scheme [4, 5] was used for the numerical solution. In the numerical solution, the heat flux on the pipe surface is determined by the equation

$$j_0 = -\lambda \frac{T_1 - T_0}{h}, \quad (11)$$

where T_1 and $T_0 = T_p$ – are the temperature values at the nodes respectively with numbers $i = 1$ and $i = 0$.

In parallel, together with the definition (11), the calculation of the heat flow is carried out according to the formula

$$j_t = \alpha(T_p - T_c), \quad \alpha = \frac{\lambda}{\sqrt{\kappa(t + t_*)}} \frac{\exp(-z_0)}{\eta \sqrt{z_0}}. \quad (12)$$

Here the numerical values of the parameters η and t_* are chosen so that the heat flux j_t coincides with the calculated flux j_0 by the formula (11).

After finding η and t_* required to carry out the evaluation of the integral

$$\eta = \int_{z_0}^{\infty} \frac{e^{-\zeta}}{\zeta} d\zeta, \quad (13)$$

where the lower limit of integration z_0 must be chosen such that the calculated integral coincides with the previously found value η .

The calculations are performed with the following physical parameters: $R = 0.1$ m, $\lambda = 1.2$ W/(m·K), $\rho = 3000$ kg/m³, $c = 1200$ J/(kg·K), these data give the ratio $\kappa = 3.33 \cdot 10^{-7}$ m²/s. The ambient temperature is $T_c = -5$ °C, the temperature on the pipe surface $T_p = 117$ °C. The values $\eta = 1.828$; $t_* = 50$ s; $z_0 = 0.8 \cdot 10^{-5}$.

For Fig.3 the values of the heat flux from the pipe calculated by the formula (12) and its exact value by the results of the numerical solution of the equation (10) are given. The time on the horizontal axis is given in hours. As shown in Fig. 3 the values of the heat flux in the two methods of calculating the heat flux are very different only at the beginning for a few tens of seconds. In the subsequent time difference is weak.

The change in the radius of the heated zone $r_0(t)$ in time is shown in Fig. 4. Knowledge of $r_0(t)$ does not give much practical use, because we need to know the heat flow to calculate the heat loss from the pipeline. The radius $r_0(t)$ is mainly of theoretical interest.

The temperature distribution $T(t, r)$ is shown in Fig. 5 by results of numerical solution of equation (10). Due to the low coefficient of thermal conductivity, the heating of the surrounding pipeline is slow, more than nine hours the heat wave has shifted by less than 0.8 mm.

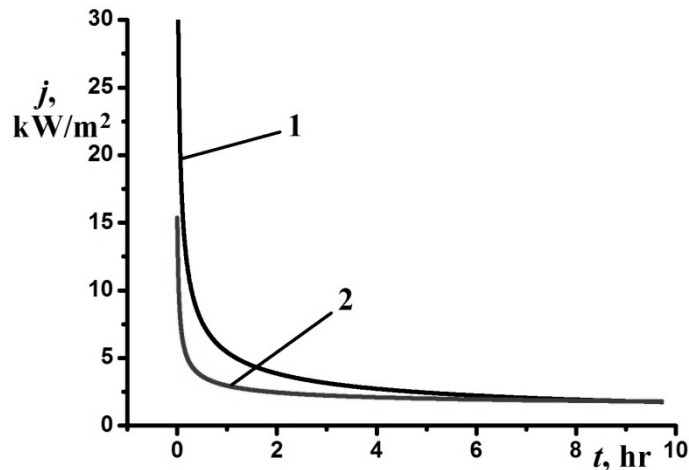


Fig.3. Dynamics of heat flow calculated by the formula (12) - (j_0 , curve 1), and from the result of numerical solution of equation (10) (j_t , curve 2).

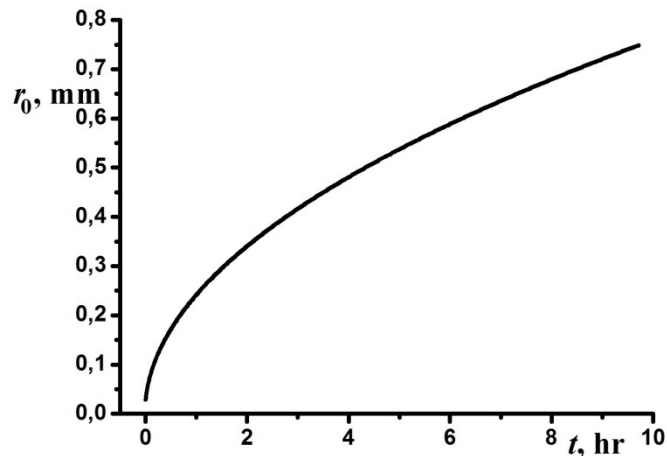


Fig.4. The dependence of the radius $r_0(t)$ on time.

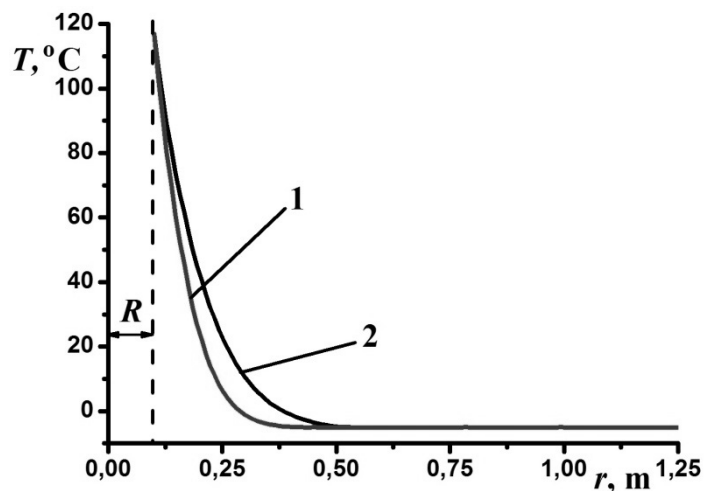


Fig.5. Numerical results of determining the temperature distribution in the vicinity of the pipe at different times: cu. 1 - $t = 4.17$ hours; cu. 2 - $t = 9.72$ hours.

Conclusion

Let us explain the physical nature of the decrease in the heat transfer coefficient: due to the large temperature difference in the pipe and the surrounding space, at the initial time there is a powerful heat transfer, but as the medium warms up near the pipe, a heated layer is gradually formed around it and the layer thickness gradually grows. As a result, around pipe a thermal "cushion" is created, the heat from the pipe must pass through this "cushion" before entering the cold area of the environment. Thus, the increasing heat "cushion" leads to blocking the heat loss from the pipe, which means a decrease in the heat transfer coefficient.

The main result of the study is a simple formula (12), taking into account the variability of the heat transfer coefficient. It is very convenient to use when carrying out engineering calculations of heat loss in thermal networks, and the results obtained on its basis will allow solve more precisely problems of design and optimization of thermal networks.

REFERENCES

- 1 Tkachenko L.A., Repin A.V. *Theory of heat transfer*. Kazan, Kazan University Publishing House, 2017, 151 p. [in Russian].
- 2 Crate F., Black W. *Heat Transfer Basics*. Moscow, World, 1983, 510 p.
- 3 Tikhonov A.N., Samarsky A.A. *Equations of mathematical physics*. Moscow, Science, 1977, 736 p. [in Russian]
- 4 Kalitkin N.N. *Numerical methods. Training allowance*. SPb, BHV-Petersburg, 2011, 512 p. [in Russian]
- 5 Sabdenov K.O., Erzada M. *Mathematical modeling of systems and processes*. Astana, Publishing House of Gumilyov ENU, 2014, 256 p. [in Russian]

UDC: 621.311.24

ABOUT HIGH EFFICIENCY OF TWO-ROTOR WIND POWER UNIT BIDARRIEUS-2

Yershina A.K.¹, Yershin Sh.A.²

¹Kazakh National Women's Teacher Training University, Almaty, Kazakhstan, ainakul82@mail.ru

²al Farabi Kazakh National University, Almaty, Kazakhstan

The article discusses the design features of the wind turbine Bidarrieus-2 with an abnormally high wind power coefficient. The basic design of HBI-rotor of the turbine Bidarrieus-2 is shown. Due to the twin-rotor construction the wind turbine Bidarrieus-2 has much more efficient than all modern wind power devices. In calculating of the power the wind turbine rotational moment has been taken into account. The study results of wind energy that can be converted by the Bidarrieus-2 wind turbine are confirmed it's uniqueness.

Keywords: wind turbine, Darrieus, Bidarrieus-2, HBI-rotor, wind power coefficient

Introduction

Now the propeller-type wind turbines with installed capacity up to several megawatts are widely used. On the basis of many years of experience, the technology of creating a high-power WPU of a propeller-type wind turbine has been mastered [3-8]. But practice shows that the higher the capacity of wind farms, the wider the lifeless territory in these regions (birds, fauna, including the population, leave these places). Also, the gyroscopic effect of a propeller wind turbine can lead to emergency situations [9].

More preferable are the carousel type Darrieus wind turbines, which have the symmetrical wing form NASA and operate on the lifting power of the blades. The overall dimensions of such devices are much less at the same values of the installed power. The material consumption and space occupied by these devices is much less than the propeller ones. At the wind turbine Darrieus the flow is uninterrupted, and as a result, its work is almost noiseless.

It is well known that in the development and creation of any machine an important characteristic of utility (if not the main) is the value of the efficiency factor. In its work, the ratio of the benefits of using this machine to the required costs, such as cost, operating costs, service life, payback, etc., is indicative [1-2]. This also applies to the operation of wind power unit (WPU), for which the efficiency of the unit is determined by the efficiency of wind energy that is named as a power coefficient. The higher the value of this coefficient, the more effective is the economic and commercial value of the WPU [3-11].

At present, there are no serially produced vertically-axial Darrieus, wind turbines of the megawatt capacities on the Kazakhstan, Russian and international markets. Among foreign manufacturers, the low-power production of low-power VA wind turbine can be specified in Finnish company Ropatec, German firms Aseptor, Bekar, Chinese firm Alibaba, etc. Ukrainian, Russian and foreign scientists are interested in vertical axis machines [2, 3, 8]. All these works deal with the study of vertical-axial wind turbines Darrieus, with a single rotation shaft.

For more than 20 years paper authors are conducting research on the development of vertical-axial wind turbine Darrieus type with two coaxially located rotation shafts. Three versions of two-rotor carousel type wind turbines with a high coefficient of wind energy use (CWEU) are proposed [10-11]. All inventions are protected by patents of the Republic of Kazakhstan and the Russian Federation. Let us consider the structural features of the latter construction.

1. Bidarrieus-2 construction

Development and creation of the two first versions of two-rotor wind power units (Bidarrieus-1, HBI-rotor) lead to the possibility of creating the most unique machine that surpasses any modern wind power units by all parameters (from high efficiency to the simplicity of maintenance). It is called a WPU Bidarrieus-2 with HBI-rotor, and in Fig.1 the basic design of HBI-rotor is shown.

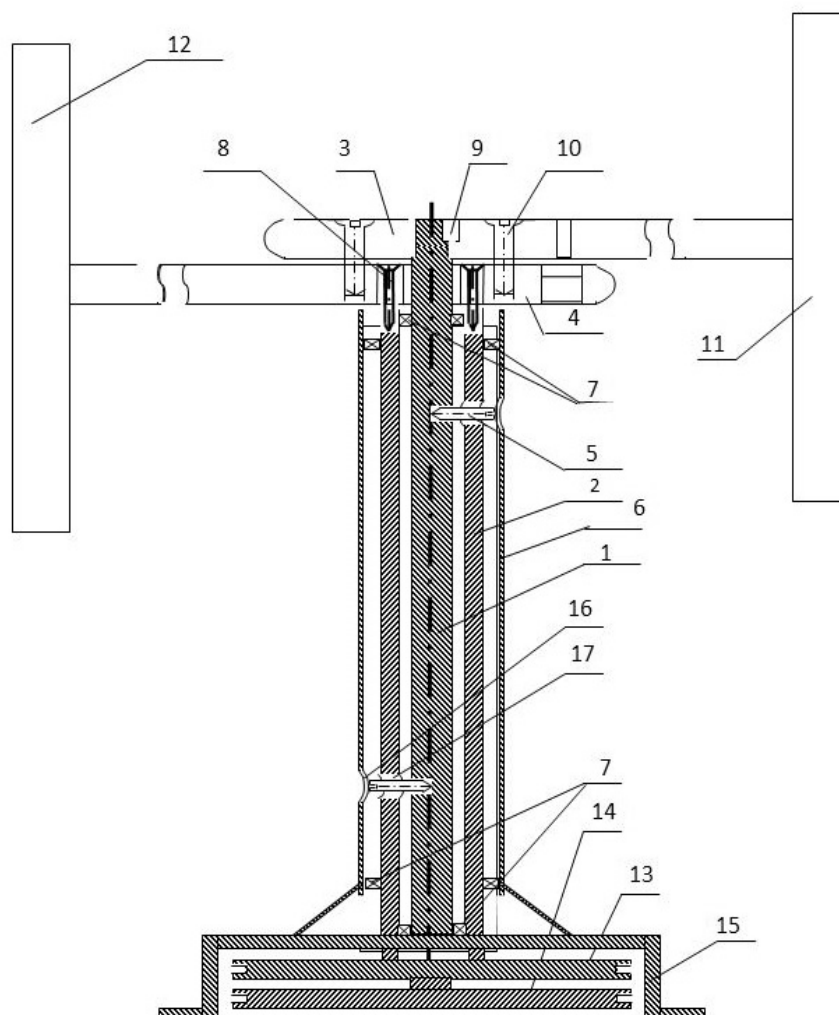


Fig. 1. Basic design of HBI-rotor of the turbine Bidarrieus-2:

1 - central shaft, 2 - external shaft, 3 - top span with cover blade connected with central shaft, 4 - lower span connected with external shaft, 5 - fingers for fixation of an angle between spans, 6 - external stationary case, 7 - bearings, 8 - bolts connecting span 4 with external shaft, 9 - spline, 10 - bolts connecting spans 3 and 4, 11 - blade connected with the top span, 12 - blade connected with the lower span, 13 – pulley connected with external shaft 2, 14 - pulley connected with central shaft 1, a 15 - figured frame for fastening, 16 and 17 - opening for fingers of fixation of an angle between spans 3 and 4.

Unlike the Darrieus design with a single rotation shaft, where a straight run is connected to two working blades, a wind power plant with two coaxially located rotation shafts is proposed. Coaxially installed shafts of rotation are separated from one another by bearing bearings, which makes it possible for them to rotate autonomously: as coordinated in the same direction and in opposite directions. This unit is a two-blade system. The system consists of two semi-spans with one working each blade, one of the semi-spans is jointed with the central rotary shift and the other –

with the external one. As a result, each working blade jointed with this or other semi-spans work independently. Encumbrance on the way of the wind reduces. This principle has been put in a basis of creation of WPP with HBI- rotor and this represents originality and novelty of the offered WPU. The both spans must rotate in one and the same direction with the same angular velocity $\bar{\omega}$. This results in the increase of the area being swept.

Thus, each of the two working blades rotates independently on the area being swept in the form of ring surfaces equal to the diameter of the wind turbine and the width equal to the length of the working blades. The both oppositely arranged blades balance each other and are independent. Correspondingly, the second blade with a semi-span rotates the external shaft and has the area being swept of practically the same kinds as the blade jointed with the central shaft.

Because two-rotor carousel type wind turbine Bidarrieus-2 consists from two autonomous systems or two aerodynamically equidistant nodes that balance each other as a result of a rigid connection through metal bearings. Therefore, it is sufficient to consider one of these units, for example, the work of the central shaft due to the influence of the wind flow on blades 1 and 4 (Fig. 2). This allows determining the technical-economical characteristics of each assembly independently on one another. The results obtained on the first assembly can be adequately transferred to the second wind power assembly. Wind turbine Bidarrieus-2 has 2 coaxial rotational shafts separated from each other by bearings 9, which allows them to rotate autonomously.

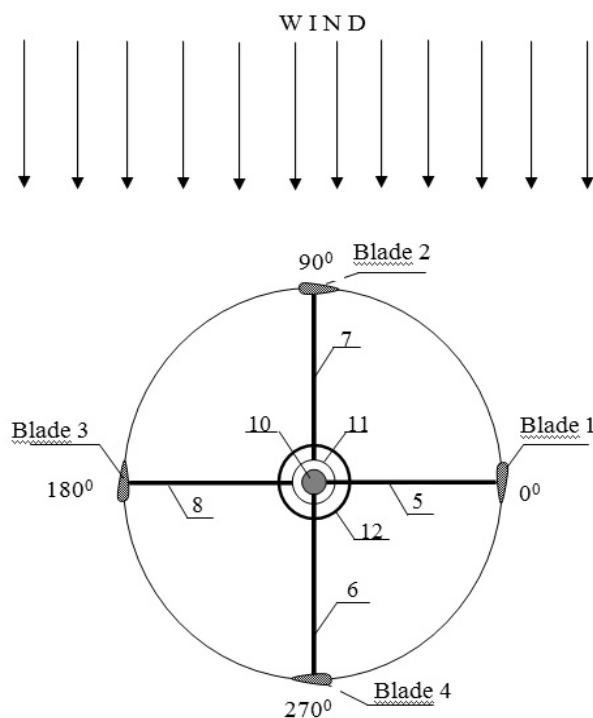


Fig.2. The scheme of positions of both assemblies during rotation of wind turbine Bidarrieus-2 (designations are the same as in Fig. 1)

Fig. 2 schematically shows the joint of semi-spans 5 and 6 and blades 1 and 4 with the central shaft of rotation 10 and joint of semi-spans 7 and 8 and blades 2 and 3 with external shaft 11. The external large circle is a fixed casing 12. Between this casing 12 and external shaft 11 there are bearings, like in our other two-rotor machines. And the second row of bearings is between the central shaft 10 and external shaft 11. The increase in ξ is due to the work of both assemblies. The system with the central shaft of rotation is the first assembly of Bidarrieus-2. A similar assembly consists of semi-spans 7 and 8 with blades 2 and 3 jointed with the external shaft of rotation 11.

Thus, WPU Bidarrieus-2 consists of two assemblies working independently of each other. The assembly has a special constructive form being know-how.

2. Calculation of the Bidarrieus-2 wind turbine power

The power N_t , which is developed by the Darrieus WPU with one rotation shaft, can be determined according to the well-known formula

$$N_t = \xi S \rho \frac{U^3}{2}, \quad (1)$$

where, $S = 2\pi r_0 \ell$ – flowed around area, ρ – air density, U – wind speed, ξ – efficiency of wind power.

The wind turbine capacity can also be determined if the rotary moment of the wind turbine M_{turb} is known

$$N_{turb} = \omega \cdot M_{turb}, \quad (2)$$

where $\vec{\omega}$ – the angular speed of rotation of the turbine shafts.

Rotary moment of the turbine:

$$M_{turb} = r_0 (|\vec{R}_\tau| - |\vec{R}_D|), \quad (3)$$

where \vec{R}_τ – tangential component of the lifting power

$$\vec{R}_\tau = \vec{R}_l \sin \alpha. \quad (4)$$

The lifting power of the blade profile \vec{R}_l is directed perpendicular to the wind attack speed \vec{V} and its volume is determined by [1, 2] formula

$$|\vec{R}_l| = C_y(\alpha) L \rho \frac{V^2}{2}, \quad (5)$$

where $C_y(\alpha) = \sqrt{2\pi} \sin \alpha$ – coefficient of the lifting power, L – length of the blade of symmetric profile with the chord equal to ϵ and V – attack speed.

The force of air resistance to the movement of the blade is registered [12] in the form of the following dependence

$$|\vec{R}_D| = C_x(\alpha) L \rho \frac{V^2}{2} \cos \alpha, \quad (6)$$

where $C_x(\alpha) = 0.014 + \sin^2 \alpha$ – coefficient of resistance of wing profile.

The value of the blade chord which represents wing NASA profile 0021 is determined by the following dependence:

$$b = 1 / r_0$$

r_0 – length of semi-spans of the wind turbine.

Attack speed V is determined [1] by the formula:

$$|\vec{V}| = |\vec{U}| \cdot \sqrt{1 + \chi^2 + 2\chi \cos \theta} = |\vec{U}| \cdot \sqrt{\sin^2 \theta + (\chi + \cos \theta)^2} \quad (7)$$

Equating two ratios (1) and (2) to each other we will write down:

$$\xi \cdot S \cdot \frac{\rho \cdot U^3}{2} = \omega M_t, \quad (8)$$

Substituting values of the wind turbine parameters we will eventually have the following dependence the solution of which allows determining the value χ for Bidarrieus-2.

$$\chi^2 + 2\chi \cos \theta + 1 = \frac{\xi \cdot S \cdot U}{\omega \cdot L \cdot b \cdot r_0 \cdot [C_y(\alpha) \cdot \sin \alpha - C_x(\alpha)]} \quad (9)$$

As the formula turns out bulky, we will enter designation of A

$$A = \frac{\xi \cdot S \cdot U}{\omega \cdot L \cdot b \cdot r_0 \cdot [C_y(\alpha) \cdot \sin \alpha - C_x(\alpha)]} \quad (10)$$

For the purpose of simplification of calculations we will use the value equal to the difference between the dimensionless value A and a unit, denoted B

$$B = 1 - A$$

Then expression (9) is transformed into a simpler form

$$\chi^2 + 2\chi \cos \theta + B = 0 \quad (11)$$

From here tip speed ratio χ for Bidarrieus-2, in $\cos 90^\circ=0$, will be equal to $\chi=15.33$. On the basis of this value the Bidarrieus-2 unit makes 24.41 revolutions per second. Taking into account the volume of removed power (39.4 kW) at one revolution of a regular wind turbine Darrieus it is possible to determine the power removed from a wind flow by Bidarrieus-2 wind turbine, with two shafts of rotation taking into account the number of its rotations (24.41 rps). Taking into account the twice increase in the power removed from a wind flow when using two semi-spans, we have the dependence:

$$39.4 \text{ kW} \times 2 \times 24.41 \text{ rps} = 1924 \text{ kW}.$$

From this, it is concluded that the wind turbine Bidarrieus-2 with the wind wheel diameter of 6 m removes from a wind flow by each unit the power of 1924 kW, and by both units – 3848 kW (see Fig. 2) at the parameters mentioned above. Wind turbine Darrieus removes 394 kW of power from a wind flow.

Thus, it follows that Bidarrieus-2 with both units removes power from the wind flow 10 times more than regular Darrieus unit. Firstly, such high power is related to the, use of peculiar construction of semi-spans which double the power removed from a wind flow. Secondly, it is related to the presence of two independently working units of the device which once again doubles the power of Bidarrieus-2.

Not the last role is played by the high wind speed (30 m/s) which is also taken into account in calculation. The calculation of the power for a simple Darrieus wind turbine with one rotation shaft was carried out at following main parameters: wind power efficiency of $\xi=0.30$, degree of tip speed ratio $\chi=6.2$ [13]. Dimensions of the Darrieus aggregate: the diameter of the wind wheel (the wind turbine span) is 6 m, the length of the working blades is 4 m. The wind speed is 30 m/s. At a given rate of speed χ , a simple Darrieus wind generator, makes 10 rps, this allowing it to operate at high wind speeds, i.e. its service life will be practically unlimited. For the twin-screw Bidarrieus-2 wind turbine, the power consumed by the two DC generators is added together.

Conclusion

The presented two-rotor units are unique, both in terms of design and technical and economical indicators, and have no analogues in the world. Bidarrieus-2 wind turbine is able to occupy a dominant position in wind power, due to the high efficiency of wind energy. The results of the calculations show that for a small installation size (span diameter of about 6-7 meters) Bidarrieus-2 can generate megawatt power from the wind current. According calculations the wind energy utilization factor for the Bidarrieus-2 turbine can reach 0.7. It has been established that high

efficiency of twin-rotor wind turbines is achieved with a wind speed of at least 20 m / s. These findings determine the importance for investment in order to perform full-scale tests of the Bidarrius-2 wind turbine and industrial production in the future not only in Kazakhstan.

REFERENCES

- 1 Bezrukikh P.P. [Ispol'zovanie energii vetra] *Wind power use*. Moscow, 2008, 196 p.[in Russian]
- 2 Yershina A.K., Yershin Sh.A., Zhabbasbayev U.K. *Fundamentals of the theory of the wind turbine Darrieus*. Almaty, Kazakh state ISTI, 2001, 104 p. [in Russian]
- 3 Renewables 2018 Global Status Report (GSR). World Wind Energy Association, June 4, 2018. Available at: <http://wwindea.org/11961-2/>
- 4 Timothy J. McCoy, Dayton A. Griffin. Control of Rotor Geometry and Aerodynamics: Retractable Blades and Advanced Concepts. *Wind Engineering*. 2008, Vol. 32, Issue 1, pp. 13–26.
- 5 Kayan V.P., Kochin V.A., Lebid O.G. Studying the Performance of Vertical Axis Wind Turbine (VAWT) Models with Blade Control Mechanism. *Intern. Journal of Fluid Mechanics Research*, 2009, Vol.36, Issue 2, pp. 154 – 165.
- 6 Horiuchi K., Ushiyama I., Seki K. Straight Wing Vertical Axis Wind Turbines: A Flow Analysis. *Wind Engineering*. 2005, Vol. 29, Issue 3, pp. 243 – 252.
- 7 Yershina A.K., Yershin Sh.A. Vertical-axial compound wind turbine of rotor type. *Proceedings of the ASME-ATI-UIT-2010. Thermal and Environmental in Energy Systems Conference*. Sorrento, Italy, 2010, pp. 621 – 625.
- 8 Yershina A.K., Nursadykova Zh.K., Borybaeva M.A. Analysis of developing wind power apparatus in Kazakhstan. *Eurasian Physical Technical Journal*, 2016, Vol.13, No. 2(26), 99–106.
- 9 Yershina A.K., Yershin Sh.A., Yershin Ch.S., Manatbayev R.K. RK Patent No. 31662 F03D 3/06. Published Nov. 15, 2016.
- 10 Yershina A.K. New perspective version of Bi-Darrieus windturbine. *Journal of International Scientific Publications: Materials, Methods and Technologies*. 2014, Vol.8, pp. 465 - 472.
- 11 Yershina A.K., Yershin Sh.A., Manatbayev R.K., et al. AP Bi-Darrieus wind turbine. *Proceedings of the 15th Intern. Scient. Conference on Renewable energy & innovative technologies* (Bulgaria, 2016), Vol.1, pp. 1 – 8.

UDC: 533.682; 533.6.01; 621.548

MODELING AERODYNAMICS OF THE WIND TURBINE WITH ROTATING CYLINDERS

Sakipova S.E.¹, Tanasheva N.K.²

¹E.A. Buketov Karaganda State University, Karaganda, Kazakhstan, sesaule@mail.ru

²Institute of Applied Mathematics, Karaganda, Kazakhstan, nazgulya_tans@mail.ru

The paper considers the prospects for the development of alternative energy forms in Kazakhstan, in particular, wind energy. The article discusses the possibilities of using computer simulation of the aerodynamics of the flow around a three-bladed wind turbine by the ANSYS FLUENT software package. The system of initial equations and boundary conditions for solving the problem in axisymmetric formulation are presented. The results of the construction of the computational domain and 3-dimensional grid CAD-model of the wind turbine using the subroutine ANSYS MESH are shown. The analysis of the adequacy of the results of the calculation of the aerodynamic drag force for the virtual model of the wind turbine at various velocities of the incident flow is made.

Keywords: wind turbine, aerodynamics, rotating cylinder, drag force, 3-dimensional modeling, Reynolds criterion.

INTRODUCTION

Over recent years, Kazakhstan has been actively developing alternative energy forms, despite the fact that the transition to renewable energy sources for Kazakhstan looks quite difficult due to too cheap coal prices (the country ranks eighth in the world in terms of coal reserves) [1-3]. Indeed, Kazakhstan has significant resources of renewable energy sources (RES), which include water, wind and solar energy. Wind energy is the most relevant direction for the development of renewable energy sources, since wind power plants are among the most environmentally friendly ways to produce energy; they do not require fossil fuels, and do not produce harmful emissions into the environment.

In 2019, the Ministry of Energy of Kazakhstan plans to launch 11 renewable energy source facilities with an overall power of about 400 MW and to generate about 2 billion kWh of electricity [1]. The renewable energy sources market is growing. In 2018, the share of renewable energy in total electricity production was 1.3%, and by 2030 it is planned to reach 10%. Today, intensive work on the design and construction of renewable energy source facilities is in progress region-wise. Favorable conditions are created for the development of renewable energy generating facilities in Kazakhstan, foreign investors are attracted, and auctions are being held to select renewable energy projects [2]. All this necessitates of develop small wind power plants that effectively convert wind energy into electrical or thermal energy.

This paper is concerned with computer simulation of a three-bladed wind turbine with rotating cylinders, which, under certain flow regimes, permits the use of the Magnus effect [4–7]. To determine the most effective parameters, both laboratory and field tests under natural conditions of various wind turbine models were carried out. It is known that the production of mock-ups and the implementation of full-scale and bench tests require significant financial costs and time. At the same time, computing technologies in aerodynamics have reached a high level, which ensures the complementarity of computer simulation and experimental research. The current level of development of software systems, in particular, ANSYS CFX, makes it possible to model a wide class of aerodynamic phenomena from laminar flows to turbulent streams with strong anisotropy of

parameters [8, 9]. For example, the transitional model of turbulence correctly analyzes flow regimes that are close to laminar ones, flows with developed flow separation zone and attached flow region.

1. Formulation of the problem.

System of equations

The problem under study at this stage is solved in an axisymmetric formulation, i.e. the dependence on the azimuthal coordinate φ is not taken into account. Fluid flow is assumed to be laminar and is described by a system of control equations in dimensional formulation [10-11], including:

– total energy conservation equation

$$\frac{\partial(\rho h_{tot})}{\partial t} - \frac{\partial p}{\partial t} + \nabla \cdot (\rho U h_{tot}) = \nabla \cdot (\lambda \nabla T) + \nabla \cdot (U \cdot \tau) + U \cdot (S_{M,rot} + S_{M,buoy}) + S_E \quad (1)$$

– momentum equation

$$\frac{\partial(\rho U)}{\partial t} + \nabla \cdot (\rho U \cdot U) = \nabla p + \nabla \cdot \tau + S_{M,rot} + S_{M,buoy} ; \quad (2)$$

– continuity equation

$$\frac{\partial \rho}{\partial t} + \nabla \cdot (\rho U) = 0 ; \quad (3)$$

The following symbols are used in the equations (1-3):

$h_{tot} = h_{stat} + U^2 / 2 - \omega^2 r^2 / 2$ – total enthalpy in rotary mode;

ω – the angular rotation velocity of fluid; r – radius vector; ρ – fluid density;

λ – heat conductivity coefficient; p – pressure; U – velocity vector;

T – temperature; τ – viscous stress tensor; S_E – energy source;

$S_{M,rot} = -2\rho\omega \times U - \rho\omega \times (\omega \times r)$ – the term taking into account the Coriolis force and the centrifugal force;

$S_{M,buoy} = \rho_{ref} \beta (T - T_{ref}) g$ – impulse source formed by buoyant forces;

β – volumetric expansion coefficient; g – gravitational acceleration vector;

Boundary conditions:

It is assumed that the adhesion condition holds on the side walls and at the bottom without outlet:

$$U_{wall} = 0, \quad (4)$$

At the upper boundary and in the drain region, values of the velocity U and its components along the coordinate axes u_i are given:

$$\left\{ \begin{array}{l} U_{inlet} = u_{axial} \bar{i} + u_{radial} \bar{j} + u_{swirl} \bar{k} \\ u_{axial} = -u_1 \\ u_{radial} = 0 \\ u_{swirl} = 0 \end{array} \right. , \quad \left\{ \begin{array}{l} U_{inlet} = u_{axial} \bar{i} + u_{radial} \bar{j} + u_{swirl} \bar{k} \\ u_{axial} = -u_2 \\ u_{radial} = 0 \\ u_{swirl} = 0 \end{array} \right. \quad (5)$$

The computations based on equations (1-3) with boundary conditions (4-5) were performed in the ANSYS CFX and ANSYS FLUENT software package.

2. Grid model using the ANSYS MESH subroutine

Previously, an unstructured computational grid of the model was generated in the ANSYS MESH subroutine [9]. As main elements of the computational grid tetrahedrons were chosen; those of the walls were prisms. To simulate the flow in the boundary layer, 18 prismatic layers clustered against the walls were developed. Fig. 1 shows a general view of a two-dimensional computational grid. In the procedure, some general recommendations on generating computational grids used to solve other classes of gas-dynamic problems were taken into account, such as: the two neighboring mesh ratios in the region of greatest gradients should not exceed 1.25, the same at interblock boundaries – 2.0 [8, 9]. After the grid had been generated, its quality was checked. As an estimation parameter, the quality parameter was used, the value of which should be at least 0.1.

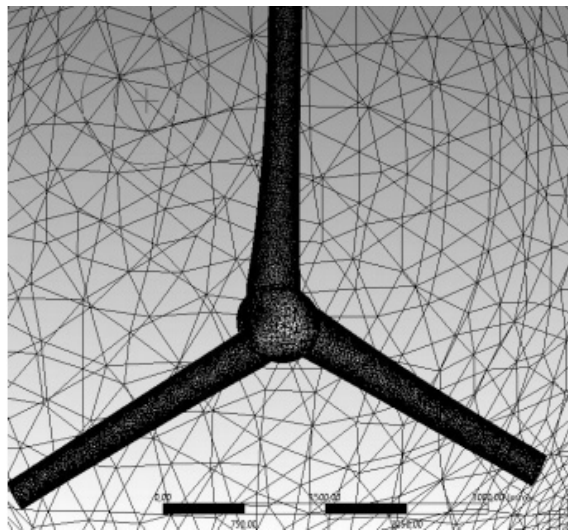


Fig.1. The preliminary 2-dimensional grid model of the wind turbine.

The maximum value of the dimensionless near-wall coordinate Y^+_{\max} for the grid from the first point was 80.29, and for the grid of the second type it was 102.34. Thus, for the computational domain of the 3-dimensional model, a grid with the number of elements of more than 3,000,000 cells was generated, Fig.2.

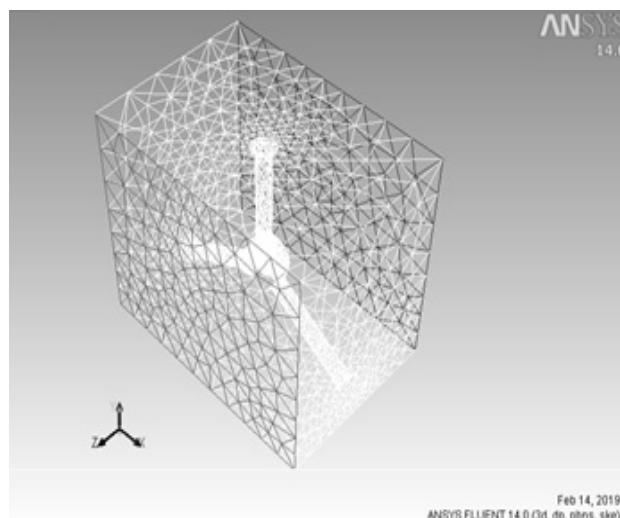


Fig.2. The 3-dimensional grid model of the computational domain around the wind turbine.

Fig. 1 shows that at the initial stage, in the 2-dimensional model the diameter of the cylindrical blades of the wind turbine decreases from their base to the ends, as if they are cut off. As a result of numerous experiments, at the stage of generating 3-dimensional model, the experimenters were able to develop a model of a three-bladed wind turbine with cylindrical blades having flat disks at the ends. Fig.2 most accurately shows the real design [7, see Fig.2]. It can be seen that the diameter of the end bases of the blades is larger than the diameter of the cylindrical blade itself.

Thus, in the ANSYS CFX and ANSYS FLUENT software package, a CAD-model of a wind turbine was developed. That was a wind turbine with blades in the form of rotating cylinders having flat disks at its ends. After that, computational models were developed in DESIGN MODELER. Then, using the mesh generator ANSYS MESH, calculation grids were generated for each element. Next, the computational domains were assembled in the CFX-Pre pre-processor. Figure 3 shows one of the variants of mathematical modeling of a three-bladed wind generator, where the rotation of a cylindrical blade with a flat end is shown.

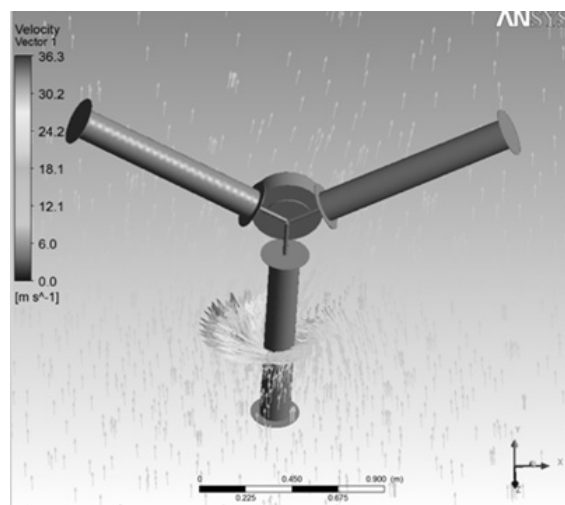


Fig.3. Three-dimensional modeling of the rotation of a wind generator cylindrical blade.

For the numerical implementation of the problem in the described formulation, finite-element software packages ANSYS CFX and ANSYS FLUENT were used. The assumptions about the axial symmetry of the problem and the laminar flow regime permitted to essentially reduce the number of computational nodes and the computation time. In the environment of the same application, the boundary conditions of the problem were set, the accepted assumptions were taken into account and, after completion of the preparation process of objects for modeling, computations could be performed.

3. Discussion of the results

For this particular case, 3.09 million point-elements of the grid model were used in the computations. Computer simulation was made at initial temperature parameters of 288K (15⁰C) and 293K (20⁰C). The results showed that in this range there was no effect of temperature on the values of the drag force. As a result of the calculations, the authors found the values of the drag force and, accordingly, the drag coefficient when the air flow velocity changed, the maximum value of which was 10m/s. The direction of the incident flow was perpendicular to the plane of the wind wheel and did not change.

Fig. 4 shows the change in the drag force value F_d of the virtual model of the wind turbine at different incident flow velocities. The nature of the dynamics, i.e. an increase in the F_d values corresponds to the physical phenomenon, which is confirmed by experimental data [4-6].

The following known formulas were used to calculate the dimensionless parameter [9]. The formula for determining the Reynolds number:

$$Re = \frac{ud}{\nu} \tag{6}$$

where u is the velocity of the air flow, approaching the cylinder; d is the outer diameter of the cylinder under study; ν is the kinematic viscosity of air.

The formula for determining the drag coefficient:

$$C_x = \frac{F_d}{\frac{\rho u^2}{2} S} \tag{7}$$

where F_d is the drag force; u is the air flow velocity; ρ is the air density; S – is s the cross-sectional area of the wind wheel.

The found dependence of the drag coefficient of the virtual model of a wind turbine on Reynolds number practically coincides with the exponential law of variation for the ideal case of a cross flow around a cylinder, Fig.5.

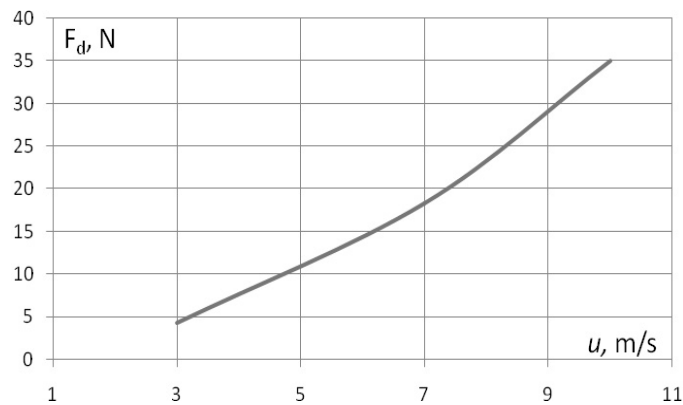


Fig. 4. The dependence of the drag force on the air flow velocity.

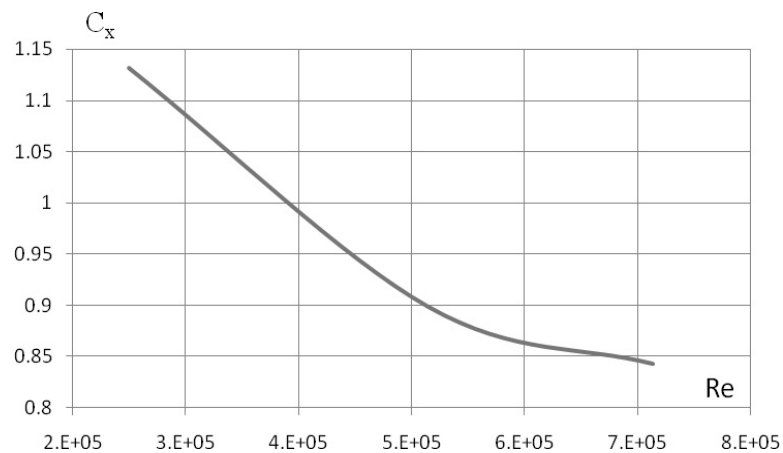


Fig.5. The dependence of the drag coefficient of the wind turbine model on Reynolds number

Thus, the found results of a 3-dimensional modeling of the dynamics of the aerodynamic drag force of a virtual three-bladed model of a wind turbine with rotating cylindrical blades reflect, in a first approximation, the physical flow pattern in the range of air flow variation from 3 to 10 m/s.

Conclusion

At this stage of the simulation, the action of the Magnus effect on the flow aerodynamics has not been studied. Nevertheless, the technique for building a CAD model of a three-bladed wind turbine and simulation of its flow in the ANSYS CFX and ANSYS FLUENT software package has been developed. The ANSYS CFX complex permits to solve complex engineering problems of both internal and external aerodynamics, and to determine the optimal design parameters when exposed to various aerodynamic loads. The calculation of the most efficient flow parameters of the wind turbine will be carried out in ANSYS CFX with corrected graphical parameters of the model in a wider range of boundary conditions.

Acknowledgements

This research was funding by Ministry of Education and Science of the Republic of Kazakhstan of the Program AP051315203 "Development and prototyping wind power plant for alternative power supply using a domestically produced electric generator" for 2018-2020.

REFERENCES

- 1 Ignatieva A. IA Neftegaz.RU, Astana, 11/02/2019. Available at: <https://neftgaz.ru/news/Alternative-energy/194767>
- 2 The development of green energy in Kazakhstan. Available at: www.eenergy.media/2018/09/19/razvitie-zelyonoy-energetiki-v-kazahstane/
- 3 Karatayev M., Clarke M. A review of current energy systems and green energy potential in Kazakhstan. *Renewable and Sustainable Energy Reviews*, Vol. 55, March 2016, pp. 491–504.
- 4 Kussaiynov K., Sakipova S.E., Tanasheva N.K., Kambarova Zh.T., et al. Wind turbine based on the Magnus effect. Innovative patent №30462 of 23.09.2015.
- 5 Sakipova S.E., Tanasheva N.K., Kivrin V.I., Kussaiynova A.K. Study of wind turbine model aerodynamic characteristics with rotating cylinders». *Eurasian Physical Technical Journal*. 2016, Vol.13, No.2 (26), pp.112 – 117.
- 6 Tanasheva N.K., Shrager E.R., Sakipova S.E. et al. Research of aerodynamic characteristics of the wind generator on the basis of Magnus's effect. *Bulletin of the Karaganda University. Physics Series*. 2017, No. 3(87), pp. 60 – 64.
- 7 Sakipova S.E., Shrager E.R., Tanasheva N.K., Botpayev N., Kussaiynova A.K. Study of electro-physical characteristics of wind turbines. *Eurasian Physical Technical Journal*. 2018, Vol.15, No. 2(30), pp.117 – 122.
- 8 ANSYS Fluent software. Available at: <https://www.ansys.com/products/fluids/ansys-fluent>
- 9 Computer modeling of 3D-models of aviation equipment and engineering calculations. Available at: <http://www.ipmce.ru/custom/vsop/themes/3dmodel/>
- 10 Martin O. L. Hansen L. *Aerodynamics of Wind Turbines*. London, Sterling, VA, 2008, 208 p.
- 11 Krasnov N.F. Aerodynamics. Part 2. *Aerodynamical methodology*. Moscow, Higher school, 1980, 416 p.

UDC 536.21

LASER PHOTOACOUSTICS METHOD FOR DETERMINATION OF THE COEFFICIENTS OF THERMAL CONDUCTIVITY AND THERMAL DIFFUSIVITY OF MATERIALS

¹Merzadinova G.T., ¹Sakipov K.E., ¹Sharifov D.M., ²Mirzo A., ³Bekeshev A.Z.

¹L.N. Gumilyov Eurasian National University, Nur-Sultan, Kazakhstan

²Tajik National University, Dushanbe, Tajikistan

³K.Zhubanov Aktobe Regional State University, Kazakhstan

In the article are given results of studies of laser photoacoustic for determination of the thermophysical properties of materials by the microphone detection circuits. It has been shown that the photoacoustic method for determining the thermophysical properties of materials, complementing other existing methods. The characteristic features of the application of the photoacoustic method based on the Rosencweig-Gersho fundamental theory are considered. The mathematical model of the problem for determining the thermal diffusivity of solid-state materials in one-dimensional and three-layer photoacoustic cell is developed. The proposed photoacoustic method can be successfully applied to the study of materials that are complex in structure, such as structurally inhomogeneous, multilayer, composite, powdery, nanomaterials, etc.

Keywords: photoacoustic method, thermal properties, thermal diffusivity and conductivity of materials.

Introduction

The developments of the modern fundamental science and innovative technologies, as a rule, contribute to the emergence of new physical and chemical research method sand to various materials with predetermined properties. In particular, the fundamentals study of the structure of substances at the atomic and quantum levels, laid down in the beginning of the last century, led in the second half to the discovery of optical quantum generators in the optical range: masers in the IR (1954) and lasers (1961) - in the visible radiation region, the authors of which were awarded the Nobel Prize in Physics. Thus, the discovery of lasers, in turn, contributed to the emergence of a number of completely new, research methods of substances, including laser photoacoustic (PA) spectroscopy.

Thermophysical methods for studying the properties of materials, in addition to studies of generally accepted standard thermophysical coefficients (thermal conductivity, heat capacity, thermal expansion, thermal diffusivity, etc.), as well as temperature changes and other related coefficients: optical, mechanical, structural, and many others, are human activities (sciences, technology and production).As noted, despite some progress and the development of theoretical methods for determining the thermophysical properties (TP) of materials (analytical, numerical, computer simulations, etc.), experimental methods still remain the real source for determining and obtaining information [1-2].The correct choice of the method for determining the TP of materials depends on a number of factors that must be considered in their research: on the possibility of the method itself, the physical states and characteristics of the object of study, on the conditions of the experiments set (measurement accuracy, temperature range, source selection, etc.It is known that at present, there are numerous standard equipment and instruments for determining TP materials from different manufacturers.

It may be noted, for example, the German company Netzsch, which offers a sufficient set of thermophysical instruments and equipment, including those based on the laser flash method (LFA) in a wide temperature range. However, despite their high quality indicators, there are a number of

necessary limitations that should be carried out when conducting experimental work. Characteristic features of the considered laser PA methods are: high sensitivity and resolution, versatility, non-contact, high information content, speed, wide areas (practical) applications, sufficient simplicity and inexpensive, available experimental equipment. Due to these qualities, PA methods are successfully applied in almost all areas of scientific research, both fundamental and practical [3-5]. In the framework of this work, we will consider the possibilities of the laser FA method with an indirect (microphone) registration scheme in determining the thermal diffusivity of materials.

1. Mathematical model of the problem.

The theoretical fundamentals of laser photoacoustic methods for determining the thermal characteristics of materials are currently rather well studied, as a rule, at moderate power densities of optical radiation [4-6] and far from the phase transition point.

The main regularities between the values of the PA signal and the desired thermal parameters of the studied substances, with an indirect registration scheme, are described in the framework of the Rosencweig-Gersho (RG) linear theory [8]. Basically, precisely in the linear mode, the results of PA experiments in determining the TPS of various materials and substances are the most preferred and coincide with the literature for known materials [7-11]. We present an analysis of the theory of the laser PA method for determining the thermal diffusivity of solid-state materials, following the condition of [8], i.e. for one-dimensional and three-layer PA chamber consisting of: a transparent gas (air), a sample with an absorption coefficient β and a substrate (Fig.1). The amplitude modulated laser radiation with intensity $I = I_0(1 + \cos \omega t)/2$ and modulation frequency ω falls on the surface of the sample under study. Denote by l_g , l_s and l_b the thickness of the gas layers, the samples and the substrate, respectively.

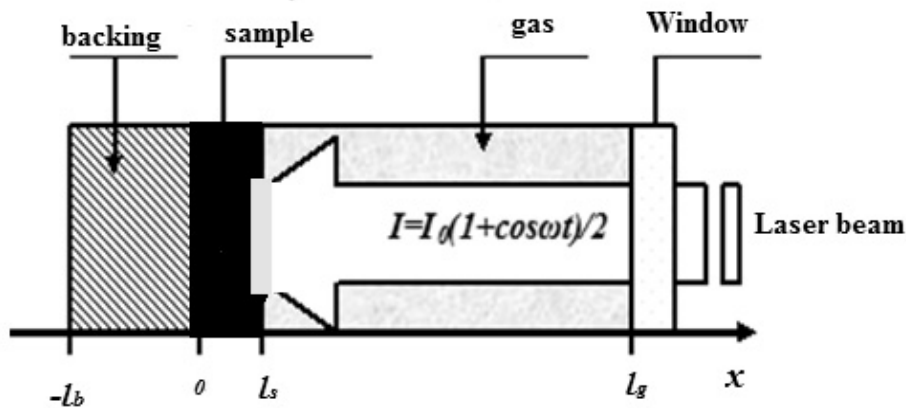


Fig.1. One-dimensional and three-layer PA cell.

It is assumed that the heat released in the sample is transferred to the near-surface layer of gas in the chamber and the substrate, only due to a thermal conductivity, i.e. temperature and heat fluxes at all boundaries are continuous. This layer of gas, thickness is $2\pi\mu_g$, where $\mu_g = \sqrt{2a_g/\omega}$ - the thermal diffusion length, periodically expanding causes an acoustic pressure oscillation in the PA cell. The viscosity and finiteness of the speed of sound in a gaseous medium are neglected, i.e. are met a conditions $l_g \ll \lambda_a$. Under such assumptions, the main task of the PA effect is reduced to determining the periodic component of the temperature field at the sample – substrate interface. It is may be found from the solution of the system of differential heat conduction equations for a gas, a sample and substrate:

$$\frac{\partial^2 T_g}{\partial x^2} = \frac{1}{a_g} \frac{\partial T_g}{\partial t}, \quad 0 \leq x \leq l_g, \quad (1)$$

$$\frac{\partial^2 T_s}{\partial x^2} = \frac{1}{a_s} \frac{\partial T_s}{\partial t} - A[1 + \exp(i\omega t)] \exp(\beta x), \quad -l_s \leq x \leq 0 \quad (2)$$

$$\frac{\partial^2 T_b}{\partial x^2} = \frac{1}{a_b} \frac{\partial T_b}{\partial t}, \quad (-l_s + l_b) \leq x \leq -l_s \quad (3)$$

Here, $T_i(x,t)$ - temperature oscillation, regarding ambient temperature T_0 , for the corresponding layers, k_i , $a_i = \kappa_i / C_{pi}$ - heat conductivity and thermal diffusivity coefficients, $C_{pi} = (\rho c_p)_i$ - specific heat per unit volume, (indices $i = s, b, g$ denote the sample, substrate and the gas filling the PA cell, respectively), $A = \beta I_0 \eta / 2\kappa_s$, η - the efficiency, which the absorbed light is converted into heat through nonradiative transitions.

The necessary boundary conditions for solving the system of equations (1) - (3), follow from the requirement of continuity of temperature and heat fluxes on the substrate – sample and sample – gas boundaries, as well as from the condition of equality of the cell wall temperature with the ambient temperature T_0 :

$$T_g(0, l_g) = T_b(0, -l - l_b) = 0, \quad T_g(0, t) = T_s(0, t), T_b(-l, t) = T_s(-l, t) \quad (4)$$

$$k_g \frac{\partial T_g}{\partial x}(0, t) = k_s \frac{\partial T_s}{\partial x}(0, t), \quad k_b \frac{\partial T_b}{\partial x}(-l, t) = k_s \frac{\partial T_s}{\partial x}(-l, t)$$

Thus, the systems of equation (1) - (3) together with the boundary conditions (4), represent the general thermal part of the mathematical model of the problem [8]. To solve acoustic part of the problem, it is assumed that the generation of acoustic (sound) waves occurs adiabatic (the test sample inside the PA cell is sealed) and the pressure increment can be determined from the adiabatic equation of an ideal gas:

$$\delta P / P_0 = \gamma \delta V / V_0 \quad \text{or} \quad PV^\gamma = const, \quad (5)$$

where, $\gamma = C_p / C_v$ - the ratio of the heat capacities of the gas.

The above mentioned condition is $l_g \ll \lambda_a$, allows to consider the propagation of acoustic waves in the PA cell as a voluminous, and use the ratio $\delta V / V_0 \approx \delta x(t) / l_g$, where are the movements $\delta x(t)$ can be defined as: $\delta x(t) = 2\pi\mu_g \theta(t) / T_0$. For the solving acoustic part of the problem, need to determine the average value of $T_g(x, \omega)$ by thickness $2\pi\mu_g$, determined from the system of equations (1) - (4) for the thermal part of the problem. Therefore, for the acoustic part we have:

$$\delta P_g(t) = \frac{P_0 \gamma 2\pi\mu_g \theta_g(t)}{l_g T_0}. \quad (6)$$

The systems of equation (1) - (4) together with (6) represent a mathematical model of the problem.

3. Analysis of the thermal coefficients

As the analysis shows, the expression for, the dependence of the parameters of the PA signal included in (6) on the optical, thermal, and geometric parameters of the studied media, as well as

the substrate and the buffer gas, is rather complex and ambiguous for the practical application, i.e. analysis of the results of PA experiments. Therefore, for the physically clearer and practical application [8], it is expedient to allocate 6 special cases, for the two most practical important cases:

A) for optically transparent samples, where the inequality is true $l_s < \mu_\beta$, where $\mu_\beta = \beta^{-1}$ the optical absorption length (that is, when the laser radiation is not completely absorbed by the sample and its significant part passes through the medium);

B) for optically opaque samples takes place $l_s > \mu_\beta$, when the sample completely absorbs laser radiation at a distance μ_β significantly smaller than its thickness l_s . The relations between the quantities both μ_g and μ_β on the one hand, μ_β and l_s on the other, make it possible to obtain the six particular cases for A) and B) cases.

In the RG- theory [8], a more detailed analysis is given for each case, the type of dependence of the parameters of the PA signal on the thermal, optical and geothermic characteristics of all the layers of the PA camera and the source of (laser) radiation is determined. Now we are consider some typical special cases of the RG-theory in determining the thermal characteristics of materials

3.1 Optically transparent and translucent samples $l_s < \mu_\beta$

For this case were identified the thermal conductivity and thermal diffusivity coefficients for a number of transparent and translucent nanocomposite polymeric materials [12]. In particular, when the substrate is considered optically thick, i.e. $r_b \gg 1$ and the thermal coupling, between the layers of the PA cell, is taken to be: $b_{gs} \ll 1$ and $b_{bs} \ll 1$, for the complex value of the PA signal, we have:

$$|\delta P_g| \approx \frac{P_0 \mathcal{M}_b I_0}{\sqrt{2} l_g T_0} \frac{\mu_g}{k_b \sigma_b} \left(\frac{4b_{bs}}{\exp(\sigma_s L_s) - \exp(-\sigma_s l_s)} \right) \quad (7)$$

Where, for amplitude and phase of the signal we get:

$$|\delta P_g| \approx A \frac{\mu_g b_{bs}}{k_b \sigma_b} \exp(-\sigma_s l_s), \quad (8)$$

$$\text{and } \varphi = -l_s \sqrt{\frac{\omega}{2a_s}} - \frac{\pi}{2}. \quad (9)$$

Here, $A = \frac{P_0 \mathcal{M}_b I_0}{\sqrt{2} l_g T_0}$. It can be seen that in this case the phase and amplitudes of the PA signal

have frequency dependencies as $\sqrt{\omega}$, ω^{-1} , respectively.

3.2 Analysis of a particular case for optical opaque and thermally thick samples ($\mu_s < l_s < \mu_\beta$)

This corresponds to case 5.2 (b), according to [8]. The characteristic amplitudes of the PA signal and its frequency dependences are as follows:

$$|\delta P_g| \approx \frac{P_0 \mathcal{M}_0}{4l_g T_0} \frac{\mu_g \mu_s r^2}{k_s R^2}, \quad (10)$$

and the frequency is: ω^{-1} . Here r and R , the radii of the laser beam and the PA cell, respectively.

Obviously, with FA experiments the value of $|\delta P_g|$ on the left part of the (10) determined by microphone (i.e. experimentally) and the required thermal characteristics (conductivity, diffusivity) are determined from the corresponding dependences of the quantities in the right-hand side. In particular, determining the coefficient of thermal diffusivity a , can be determined other thermophysical coefficients, as well as, the thermal diffusion length $\mu_i = \sqrt{2a_i/\omega}$ depending on the frequency of modulation of laser radiation or the amount of thermal activity (effusivity): $A = \sqrt{\rho C_p k}$ of the materials. For example, when performing calculations for the coefficient of thermal conductivity of quartz powder (Si – powder), with the values of the parameters [13]:

$$\gamma = 1.402 ; P_0 = 9.9 \times 10^5 Pa ; I_0 = 47.2 mW / cm^2 ; \mu_g = 2.5 \times 10^{-2} cm ;$$

$$l = 1.1 cm ; T_0 = 293 K ; r = 0.27 cm ; R = 0.5 cm \text{ ж } \delta P = 0.034 Pa$$

was received: $\kappa_s = 0.99 J / s \times m \times K$.

Conclusion

Thus, we can conclude that, the PA method for studying the thermal properties of materials has a number of features that substantially differ from other methods. The analysis shows that, despite the numerous methods for determining the thermophysical properties of materials, the PA method with a microphone detection, due to a number of its advantages, can also be successfully used in determining the thermal characteristic of various materials, especially where it is difficult to determine them by other methods. By changing the modulation frequency of the laser radiation, one can determine the length of thermal diffusion and, thus, determine the coefficient of thermal diffusivity of samples to different depths. This allows us to determine the thermophysical parameters, such "inconvenient" for other methods, samples such as multilayer, coated, composite, nanomaterials and others.

REFERENCES

- 1 Fokin V.M., Chernyshov V.N. Theoretical basis for determining the thermal diffusivity of building materials by non-destructive testing. *Bulletin of TSTU*. 2004, Vol. 10, No. 4A, pp. 936 – 945.
- 2 Chernyshov T.I. *Methods and means of non-destructive testing of thermophysical properties of materials*. Moscow, Mashinostroenie, 2001, 240 p [in Russian]
- 3 Zharov V.P., Letokhov V.S. *Laser optical-acoustic spectroscopy*. Moscow, 1984, 320p. [in Russian]
- 4 Mandelis A. *Progress in Photothermal and Photoacoustic Science and Technology*. V. 1. New York, Elsevier. 1992, 542 p.
- 5 Clider D. *Supersensitive laser spectroscopy*. Moscow, Mir. 1986. 520 p. [in Russian]
- 6 Rosencwaig A. *Photoacoustics and Photoacoustic Spectroscopy*, W., New York, 1980, 320p.
- 7 Madvaliev U. *Development of new methods of photoacoustic spectroscopy of condensed matter*. Diss. of the Dr. phys.- math. Sc., Moscow State University, Moscow, 2007, 302 p.
- 8 Rosencwaig A., Gersho A. Theory of the photoacoustic effect with solids. *J. Appl. Phys.* 1976, Vol.47, No. 1, pp. 64 – 69.
- 9 Vinokurov S.A. Determination of the optical and thermophysical characteristics of condensed media by an optoacoustical method. *J. Applied Spectroscopy*, 1985, Vol. 42, No. 1, pp. 1–11.
- 10 Zhuravlev V.E., Morozov A.I. et al. Photothermal determination of the thermophysical characteristics of solid-state objects. *Inzhenerno-Fizicheskii Zhurnal*. 1989, Vol. 56, No. 1, pp. 100 – 105.
- 11 Barros Melo W.L., Faria R.M. Photoacoustic procedure for measuring thermal parameters of transparent solids. *Appl. Phys. Lett.*, 1995, Issue 67 (26), pp. 3892 – 3894.
- 12 Sharifov D.M., Mirzo A., Bekeshev A.Z., et al. Features of photoacoustic methods for studying the thermophysical properties of carbon nanocomposite polymeric materials. *Bulletin of L.N. Gumilyov ENU*, Astana, 2016, No. 6 (115), I - part, pp. 258 – 266.
- 13 Benedetto G., Maringelli M., Spagnolo R. Method for the absolute calibration of photoacoustic cells. *Rev.Sci. Instruments*, 1987, Vol.58, No.6, pp. 977.

UDC 620.1.08

THE IMPACT OF THE ENVIRONMENT ON THE CONTACT POTENTIAL DIFFERENCE OF METAL MACHINE PARTS

Yurov V.M.¹, Oleshko V.S.²

¹ E.A. Buketov Karaganda State University, Karaganda, Republic of Kazakhstan, exciton@list.ru

² Moscow Aviation Institute (National Research University), Moscow, Russia, ovs_mai@mail.ru

In this paper we consider the influence of environmental parameters on the electrons work function and the contact potential difference of metal parts of machines. Experimental studies have been carried out, including measurements of the contact potential difference on samples from Al, Ti and Ni by the Kelvin-Zisman method at different temperatures, pressures and relative humidity, as well as in non-equilibrium and equilibrium environmental conditions. Measurements of the contact potential difference were carried out by the device "Surface-11". Atmospheric parameters were measured by the digital meteorological station HAMA EWS-800. The results of measurements of the contact potential difference of metals were processed by methods of mathematical statistics. The results of experimental studies have shown a direct effect of changes in ambient temperature on the contact potential difference and the electrons work function of metal samples, which has an average correlation. It is found that atmospheric pressure and relative humidity have a weak effect on the contact potential difference and the electrons work function of the metals under study, their influence can be neglected. The effect of equilibrium and non-equilibrium environmental parameters on the contact potential difference and electrons work function of metal samples is studied. The results confirming the reduction of the contact potential difference (increase in the electrons work function) of metals, as well as an increase in the mean square deviation of the measurement results under non-equilibrium environmental conditions are obtained. On the basis of the research it is recommended to measure the contact potential difference of metals in the laboratory.

Keywords: electrons work function, contact potential difference, metal, surface, temperature, pressure, humidity.

Introduction

The method of contact potential difference, which consists in the comparison of the electrons work function of metals, is promising method of nondestructive testing of metal machine parts [1]. The actual task is to ensure the reliability of nondestructive testing of metal parts of machines. Not fully studied is the effect on the method of contact potential difference parameters of the ambient air. Consider the effect on the electrons work function and the contact potential difference of metals such parameters of the atmosphere as temperature, pressure and humidity. Let's start with the analysis of literary sources devoted to this problem.

Temperature dependence of the electrons work function and the contact potential difference of metals. The temperature dependence of the contact potential difference was discovered and studied by A. Volta, his First law States: "On the contact of two different metals, a potential difference arises, which depends on the chemical nature and the temperature of the junctions." A.F. Vladimirov points out [2] that the electrons work function depends on the temperature, which is one of the main thermodynamic parameters of a solid. This dependence is reflected in the concept of temperature coefficients of the electrons work function. However, the experimental data on the temperature coefficients of the electrons work function are contradictory; their sign can be both positive and negative, depending on the experimental conditions [2].

Meanwhile, in [3] it is indicated that at present there is no quantitative theory of temperature dependence of the electrons work function. An example of the temperature dependence of the contact potential difference is the capacitor sensors of temperature measuring devices [4]. The sensor of the device for measuring the contact potential difference of the design scheme Kelvin-Zisman has in its composition a vibrating measuring electrode for comparing the workings of the electrons work function, which when measuring the contact potential difference is applied to the controlled object and forms a dynamic capacitor, one of the plates of which fluctuates. The temperature dependence of the dynamic capacitor is based on the change in its capacitance C due to changes in the relative permittivity between the surface of the metal part and the measuring electrode according to the following formula:

$$C = \frac{\varepsilon_0 \cdot \varepsilon \cdot S}{d}, \quad (1)$$

where $\varepsilon_0 \approx 8.8542 \cdot 10^{-12}$ F/m is the electric constant (vacuum permittivity);

ε is the relative dielectric constant, for dry air $\varepsilon \approx 1.00059$;

S is measuring electrode area, m^2 ;

d is the gap between the measuring electrode and the metal surface, m.

In [4] it is shown that significant changes in the ambient temperature can affect the capacitance of the dynamic capacitor due to changes in the area of the measuring electrode S according to the formula (1) due to the thermal expansion of the metal of the measuring electrode.

In [5] calculations of electrons work function Cu with Ni, Co and Fe coatings at different temperatures are presented. It is shown that with increasing ambient temperature the electrons work function of these systems decreases.

The increase in ambient temperature intensifies physical and chemical processes on the surface of metal parts of machines, for example, such as adsorption, corrosion tribological and others. As a result, the electrons work function of metal parts also changes [6].

In [7] provides details of the calculations of the temperature dependence of the electrons work function of the Al, which show the constancy of the electrons work function in the temperature range from 0 to 420 K. At ambient temperatures of more than 420 K the work function of the electrons begins to decrease.

In [8] it is indicated that the electrons work function of metals, as well as their other properties, depends on temperature, the formula of dependence electrons work function φ on temperature T is given:

$$\varphi = \varphi_0 - \frac{3}{2} k \cdot T, \quad (2)$$

or

$$\varphi = \varphi_0 - \xi \cdot \frac{(k \cdot T)^2}{\varphi_0}, \quad (3)$$

where φ_0 is the electrons work function at absolute zero;

k is Boltzmann constant;

ξ is the coefficient dependent on the crystal structure of the metal ($\xi_{Al}=583$, $\xi_{Fe}=438$, $\xi_{Ag}=478$, $\xi_{Ni}=318$, $\xi_{Cu}=307$).

As can be seen from the formulas (2) and (3) with increasing temperature T electrons work function φ decreases. The authors [8] associate this with the absorption of energy by electrons inside the metal. It is assumed that the increase in the energy of each electron with increasing temperature is $3/2 k \cdot T$. The temperature dependence of electrons work function of 74 metals was analyzed in [9] and it was found that it is insignificant for most metals. In this paper, it is indicated that the determination of the temperature dependence of the electrons work function by measuring the contact potential difference is ineffective.

In [10] it is indicated that the electrons work function changes with temperature. The author of the work [10] connects this fact with the change in the concentration of gases destabilizing the electrons work function, the concentration of which depends heavily on the ambient temperature. In the same work it is noted that the determination of the electron yield according to thermionic emission gives reproducible results only for refractory metals such as W, Mo, Ta. For Fe, Cu, Ni, Ag reliable results of the temperature dependence of the electrons work function at electron thermal emission have not been obtained. In [4] it is shown that the capacitance of the capacitor changes with temperature due to changes in the relative permittivity ϵ (see formula (1)).

1. The effect on the electron work function of contact and difference potential of metal parts of machinery pressure and humidity of the atmosphere.

The operation of the electrons work function depends to a large extent on the conditions of interaction of surfaces with the surrounding atmosphere. Therefore, in order to exclude the atmospheric effect on the value of the measured electrons work function, its laboratory studies are trying to be carried out in a vacuum. However, when determining the electrons work function for technical purposes it is difficult to observe.

The results of experimental studies of the dependence of the contact potential difference between the measuring electrode from Pt and samples from different materials determined at different atmospheric pressures are shown in [11]. The authors point out that at different pressures the contact potential difference of metals varies slightly. Almost always, the contact potential difference at a pressure of $1 \cdot 10^5$ Pa is greater than in vacuum. This is explained by the authors of [11] the difference in the adsorption-desorption processes on the surface of the samples.

The authors of [12] were performed to measure the distribution of the electron work function at the surface of samples of alloy ЭП479 for several months with simultaneous fixation of the temperature, pressure and humidity. The correlation of the change in the values of the electrons work function with the change in air pressure and humidity is established. An increase in humidity by 5 % leads to a corresponding decrease in the electrons work function, by about 20 meV, and Vice versa. The authors of this work believe that the increase in the electrons work function with increasing humidity is associated with an increase in the number of water molecules adsorbed on the surface of metal parts of machines. In the absence of aggressive substances in the air, the electrons work function is stable enough for tens of minutes.

In [6] the results of experimental studies to determine the effect on the measurement of the electrons work function of atmospheric humidity are shown. The electrons work function of Sb, Zn, Cd and their alloys was measured by the contact potential difference method. Studies have shown that the electron yield of these metals and alloys in a humid air atmosphere is greater by a value of 30 to 50 meV than in a dry air atmosphere. The measurement of the electrons work function in the dehydrated air the authors the work was carried out in a special chamber, the entrance to which is set a trap for moisture from the liquid nitrogen, which allowed to reduce the concentration of H_2O in the chamber to a value of 0.005 g/m^3 .

In [13] it is shown that the determination of electrons work function the samples of Al, Zn and W by the method of contact potential difference in a humid atmosphere leads to a decrease in the contact potential difference. The authors of [13] suggest that the reason for this is water vapor in the air, bringing a negative charge, which partially passes into the metal, and then remains on the surface of the metal in the water layer. When measuring the contact potential difference, the water then evaporates in the dry air and the contact potential difference increases (the electrons work function decreases).

With a joint change in the temperature and humidity of the ambient air according to the formula (1) capacitance of the capacitor formed by the metal part and the measuring electrode, the relative permittivity of ϵ_a changes according to the semi-empirical dependence derived by A.R. Volpert [14]:

$$\varepsilon_b = 1 + \frac{p}{T} \left(28 + \frac{\chi \cdot p_H}{p} \cdot \left(\frac{135}{T} - 0.0039 \right) \right), \quad (4)$$

where p is the air pressure, Pa;

T is thermodynamic temperature, K;

p_H is elasticity of saturated water vapor at a given temperature;

$$\lg p_H = 23.19 + \frac{38.16}{T - 46.13} + 2.78;$$

χ is relative humidity, %.

Relative permittivity of air ε can be determined according to the formula [14]:

$$\varepsilon = 1 + \frac{n \cdot \alpha_e}{\varepsilon_0}, \quad (5)$$

where n is the number of gas atoms in 1 m^3 of air;

$\varepsilon_0 \approx 8.8542 \cdot 10^{-12} \text{ f/m}$ is electric constant (permittivity of vacuum);

α_e is electron polarizability of the molecule, $\text{F} \cdot \text{m}^2$.

With

$$n = \frac{p}{k \cdot T}, \quad (6)$$

where p is the air pressure, Pa;

k is Boltzmann constant;

T is the temperature, K.

The relative permittivity of air is very close to the square of refraction of sunlight and increases with the radius of atoms of gases contained in the air [14]. An example of the dependence of the contact potential difference on the atmospheric humidity is the condenser sensors of moisture meters [4]. Recall that the sensor developed by us meter contact potential difference is a dynamic capacitor. The dependence of the dynamic capacitor on humidity is based on the change in capacitance C due to changes in the relative permittivity ε between the surface of the metal part and the measuring electrode according to the formula (1). The dielectric constant generally increases with increasing ambient humidity [4]. Thus, the analysis of literature sources shows the dependence of the electrons work function and the contact potential difference on the environmental parameters.

2. Experimental procedure

The authors conducted experimental studies of the dependence of the contact potential difference of metal samples of pure Al, Ti and Ni on the temperature, pressure and relative humidity of the air atmosphere. The studies were conducted in laboratory conditions.

Parameters of the surrounding atmosphere — pressure, temperature and relative humidity were estimated by the digital weather station HAMA EWS-800 with the declared accuracy of 2 %.

The range of measured environmental parameters in the course of observations was:

- temperatures from 14 to 29 °C with an average temperature of 23 °C;
- atmospheric pressure from 963 to 1022 hPa, with the average value of pressure of 997 hPa;
- relative humidity from 19 to 59 % with an average value of 34 %.

The studied samples of Al, Ti and Ni were previously thoroughly cleaned and dried.

With the help of the device "Surface-11" [15] for several months, more than 300 sessions of measurements of the contact potential difference on the samples were performed. Each measurement session of the contact potential difference consisted of several measurements of the contact potential difference. Statistical methods were used to process the results of measurements of the contact potential difference, the results of calculations are presented in the Table 1. As can be

seen from the table, the greatest stability of the results of measurements of the contact potential difference has Ni, so it is used as a material of measuring electrodes of sensors for measuring the contact potential difference.

Table 1. Statistical characteristics of the investigated contact potential difference

Metal	Estimation of mathematical expectation, mV	Mean square deviation, mV
Al	874	75
Ti	284	70
Ni	208	65

3. Results of the experiment and their discussion.

3.1 Temperature influence.

Figure 1 shows the dependence of the contact potential difference U of the samples from Al, Ti, Ni on temperature t , ceteris paribus: at a pressure of 997 ± 10 hPa and a relative humidity of 34 ± 2 %. The graphs presented in figure 1 are constructed by the least squares method by 14 values of the contact potential difference measured at an air temperature of 14 to 29 °C.

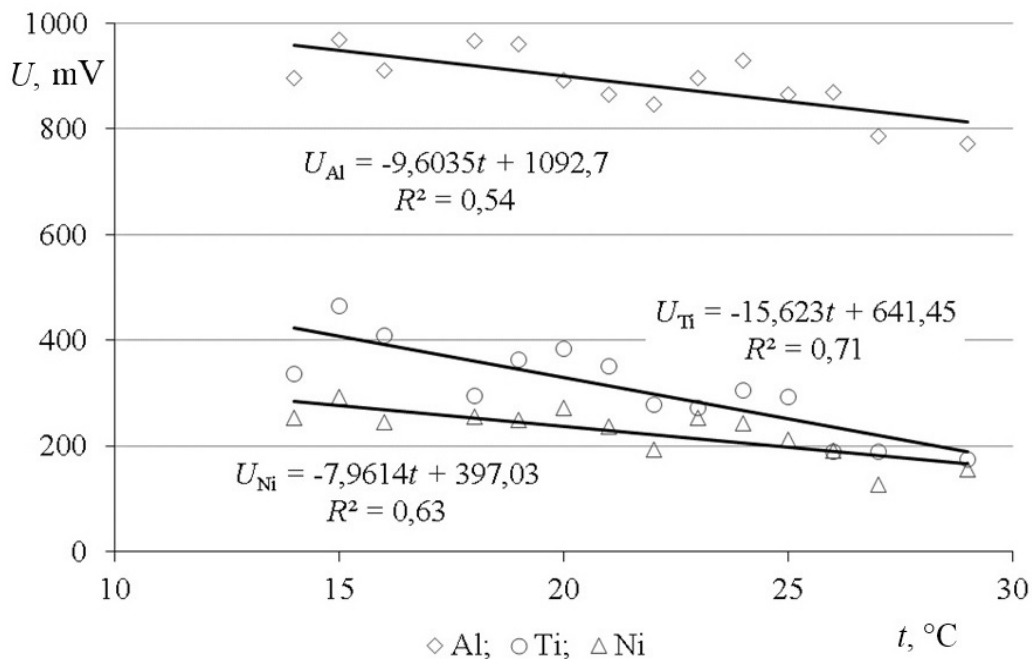


Fig.1. Dependence of the contact potential difference U on the ambient temperature t

Figure 1 also shows the formulas describing this dependence $U(t)$ for Al, Ti and Ni, as well as the value of the determination coefficient R^2 . The reduction of the potential difference U with increasing ambient temperature t can be explained by an increase in the dielectric constant ϵ with increasing temperature according to the formula (1).

As can be seen from figure 1, there is a correlation between the contact potential difference U and ambient temperature t — high for Ni and Ti, and average for Al. The dielectric constant of the air ϵ increases due to the fact that with increasing temperature the air becomes more sparse and

there is a smaller number of n air atoms in 1 m^3 , transmitting an electric current between the measuring electrode and the metal part according to the dependencies (5) and (6).

3.2 Influence of atmospheric pressure.

Figure 2 shows the dependence of the contact potential difference U for samples from Al, Ti and Ni on the air pressure p , ceteris paribus: at an air temperature of $23 \pm 2 \text{ }^\circ\text{C}$ and its humidity of $34 \pm 2 \%$. The graphs presented in figure 2 are constructed by the least squares method using 39 values of the contact potential difference measured at atmospheric pressure from 963 to 1013 hPa. Also in figure 2 formulas describing the dependences $U(p)$ and the determination coefficients R^2 are presented.

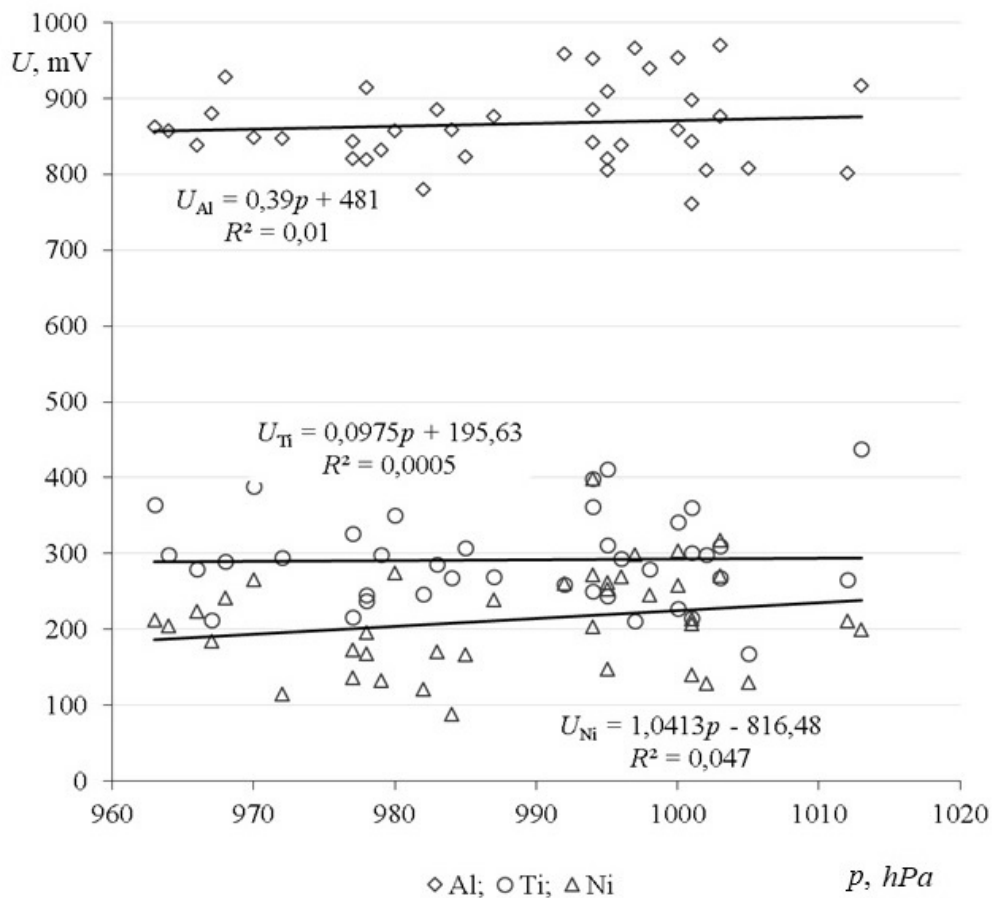


Fig.2. Dependence of contact potential difference U on air pressure p

Figure 2 shows that there is a slight increase in the contact potential difference U with increasing atmospheric pressure p , due to the increase in the number of transmitting electric charges of atoms n according to the formulas (5) and (6), but the correlation between them is small. Under normal atmospheric conditions, the influence of atmospheric pressure on the contact potential difference and the work of the electron yield, apparently, can be neglected.

However, it should be noted that when measuring the contact potential difference at extremely low atmospheric pressure, for example, at high altitude, the contact potential difference may decrease more intensively. Moreover, the factor of influence on the contact potential difference of air pressure should be taken into account when measuring the contact potential difference at artificially reduced (for example, in vacuum) or, on the contrary, at increased (for example, when pumping air) atmospheric pressure.

3.3 Influence of air humidity.

Figure 3 presents the results of analysis of 69 sessions of studies of the dependence of the contact potential difference U on the relative humidity χ all other things being equal: at an air temperature of 23 ± 2 °C and an atmospheric pressure of 997 ± 10 hPa. Also, figure 3 presents the formulas describing the dependence $U(\chi)$, and the coefficients of determination R^2 , characterizing the relationship between the contact potential diversity and air humidity.

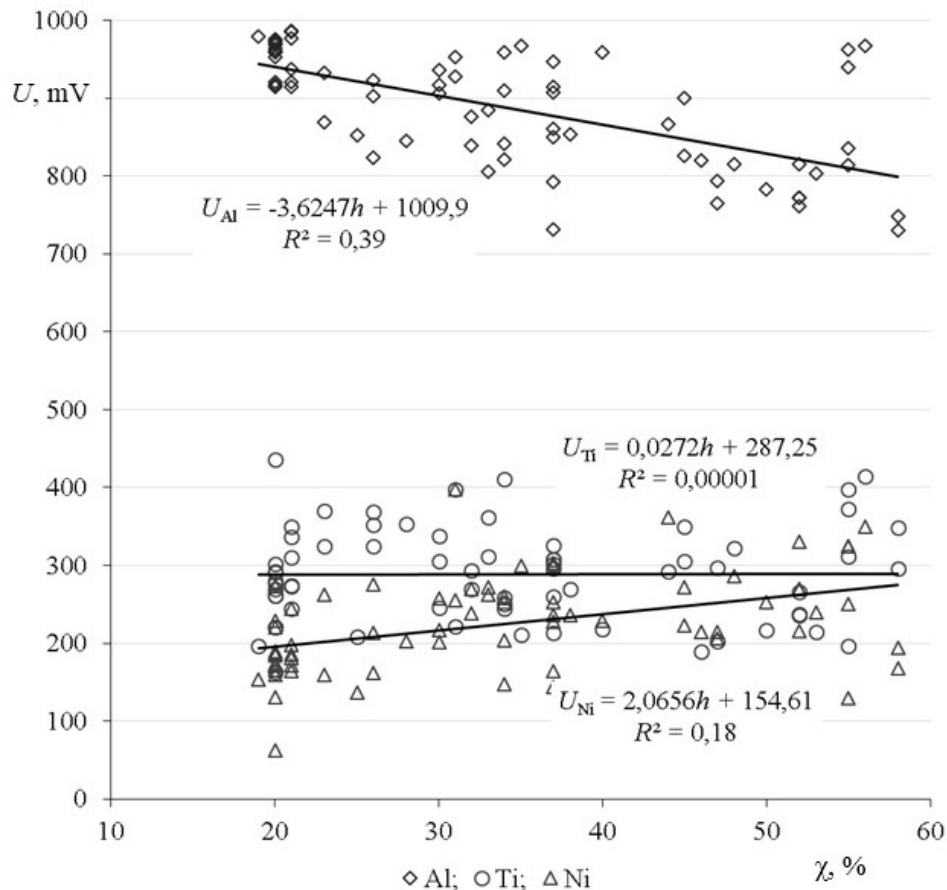


Fig.3. Dependence of the contact potential difference U on the relative humidity χ

Figure 3 shows an ambiguous dependence of the contact potential difference U of different metals on the relative humidity χ — direct for Al and inverse for Ni with low determination coefficients R^2 . On the contact potential difference of the samples from Ti, the change in air humidity χ had virtually no effect ($R^2 \approx 0$).

Different adsorption processes can explain the difference between the dependence of the contact potential difference on the relative humidity of the air— direct for Al and reverse for Ni, on their surface when interacting with water. For samples from Al, this interaction is acceptor (leads to a decrease in the contact potential difference), and for samples from Ni — is donor in nature, resulting in a slight increase in the contact potential difference [6]. However, it should be noted that the measurements of the contact potential difference took place in a relatively dry air atmosphere and it can be assumed that higher humidity can have a greater impact on the contact potential difference.

Thus, the pressure and humidity under normal atmospheric conditions do not significantly affect the value of the contact potential difference, in contrast to the temperature, which slightly changes the relative permittivity ϵ of the gap between the metal part and the measuring electrode, and accordingly to the measured capacitance of the linamic capacitor C according to the formula

(1). However, in the source [4] there are indications of a joint effect of atmospheric parameters — an increase in air humidity further enhances the effect of temperature on the relative permittivity ϵ of air humidity, and, consequently, on the contact potential difference. Therefore, the measurement of the contact potential difference in a humid air atmosphere, in our opinion, is not acceptable.

We carried out measurements contact potential difference in an artificially humidified atmosphere. When measuring the contact potential difference device "Surface-11" at a relative humidity of more than 80 %, the mean square deviation σ of the contact potential difference increased sharply. Reliability of measurements of contact potential difference decreased. This should be taken into account when nondestructive testing of metal parts of machines. Therefore, nondestructive testing by the method of contact potential difference of metal parts of machines is recommended to be carried out in the laboratory with normal and stable air parameters.

3.4 Measurement of contact potential difference in non-equilibrium atmospheric conditions.

In [16] it is shown that in non-equilibrium environmental conditions the electrons work function increases in comparison with the electrons work function measured in equilibrium conditions. The authors carried out experimental measurements of the contact potential difference by the device "Surface-11" [15] on 10 flat samples from pure Al, Ti and Ni. The surface of the samples was pre-cleaned with petroleum ether and dried for 15 minutes. Measurements of the contact potential difference were first carried out in the laboratory under the following environmental parameters: atmospheric pressure 1007 hPa, temperature 24 °C and relative humidity 19 %. Then measurements of the contact potential difference on the same samples from Al, Ti and Ni were carried out in non-equilibrium conditions on the street for 10 minutes, where the atmospheric pressure increased to 1009 hPa, the air temperature decreased to 15 °C (the samples and the surface-11 device were cooled) and the relative humidity increased to 23 %. The parameters of the surrounding air atmosphere were estimated by the digital weather station HAMA EWS-800. At the same time, a decrease in the contact potential difference of the samples measured on the street under non-equilibrium conditions of the surrounding atmosphere was observed. With further stabilization of the new values of temperature and relative humidity (outside), the contact potential difference of the samples increased slightly, although it did not reach the laboratory level.

The arithmetic mean value (estimation of mathematical expectation), dispersion and the mean square deviation of the measured values of the contact potential difference were calculated. The results of measurements of the contact potential difference U and its mean square deviation σ in equilibrium conditions (indoors) and non-equilibrium conditions (outdoors) of 10 samples from Al, Ti and Ni are presented in figures 4 and 5, respectively.

Figures 4 and 5 show that in non-equilibrium atmospheric conditions the contact potential difference decreases and the mean square deviation of the contact potential difference increases. Moreover, this effect of reducing the contact potential difference of metal samples and increasing its mean square deviation is observed when cooling the samples on the street and when they are heated indoors. The values of the contact potential difference measured in equilibrium and non-equilibrium conditions, as seen in figure 4, differ: 80, 29 and 35 mV for Al, Ti and Ni, respectively. The decrease of the contact potential difference (increase of the electrons work function) of metal samples under non-equilibrium conditions is explained by the increase of temperature gradient on the surface and in the depth of the metal, increase of the electrons work function due to the decrease of internal energy of a solid with the stabilization of its energy state.

The increase in the mean square deviation of the contact potential difference for Al in figure 5 was 48 mV, for Ti 43 mV and for Ni 22 mV. The increase in the mean square deviation of the measurement results of the contact potential difference is explained by the intensification of adsorption-desorption processes on the metal surface, as a result of which the electron yield and the surface potential of the metal change.

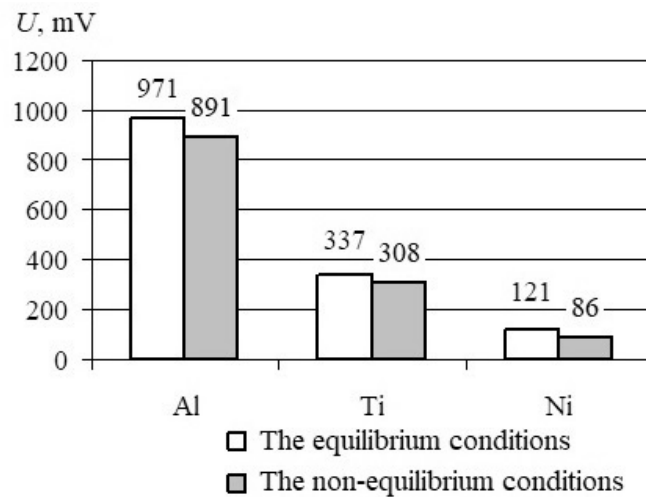


Fig.4. Average values of contact potential difference U of samples from Al, Ti and Ni measured in equilibrium and non-equilibrium atmospheric conditions

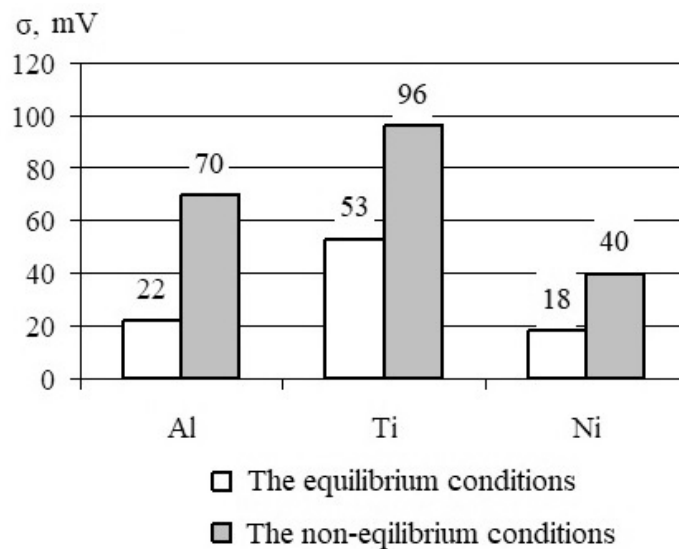


Fig.5. Values of the mean square deviation σ of the contact potential difference of samples from Al, Ti and Ni measured in equilibrium and non-equilibrium atmospheric conditions

Reducing the contact potential difference U and increasing its mean square deviation σ when measured under non-equilibrium conditions according to figures 4 and 5 is a reversible process. In subsequent measurements in the laboratory, the contact potential difference of the samples came to the initial state. In addition, figures 4 and 5 show that the decrease in the contact potential difference U is commensurate with the magnitude of the change in the mean square deviation σ . This indicates a slight influence of non-equilibrium environmental conditions on the reduction of the contact potential difference (increase in the electrons work function).

It should also be noted that the reduction of the electrons work function under non-equilibrium environmental conditions is not strictly. Figure 4 shows the arithmetic mean values of the contact potential difference calculated from 10 samples from each metal. On the surface of metals, new energy States can be formed and with less electrons work function (greater contact potential difference) than under equilibrium conditions [16].

Conclusion

Thus, the determination of the electrons work function of metal parts of machines by the method of contact potential difference, in order to increase the reliability, it is recommended to carry out in the laboratory with constant environmental parameters. This recommendation will make it possible to more accurately obtain the values of the contact potential difference and, accordingly, the electrons work function of structural metal materials, adequately assess the energy state of the surface of metal parts of machines, reduce the economic costs in their manufacture, operation and repair.

REFERENCES

- 1 Oleshko V.S., Yurov, V.M., Fluctuation of the contact potential difference in the determination of the electrons work function from the structural materials of the ionization method. *Proceedings of the 10th Intern. Conf. "Chaos and structures in nonlinear systems. Theory and experiment"*. Almaty, al-Farabi KazNU. 2017, pp. 165 – 169.
- 2 Vladimirov A.F. *Thermodynamic, crystallographic and defect-deformation aspects of changes in the electrons work function*. Diss. ... candidate of phys.-math. scien. Ryazan, Ryazan state agricultural Academy, 2001. 211 p.
- 3 Shebzukhova I.G., Arefev L.P. Anisotropy of electron work function of 3d metal crystals. *Proc. of the Russian Academy of Sciences. Series physical*. 2015, Vol. 79, No. 6, pp. 896 – 899.
- 4 Foreyt I. *Capacitive sensors of non-electric quantities*. Translated from the Czech. V.I. Dmitriev Library on automation. Moscow-Leningrad.: Publish. House "Energy", 1966, 160 p.
- 5 Mamonova M.V., Kozhakhmetov S.Z., Fomin P.A. Calculation of electrons work function from the surface of copper and tungsten during adsorption of monolayer ferromagnetic films. *Bulletin of Omsk University*. 2017, No. 2 (84), pp. 51 – 55.
- 6 Markov A.A. *Electron work function and metal antifriction*. Moscow: Moscow State Institute of Radiotechnics, electronics and automation (Tech. Un-t), 2004, 207 p.
- 7 Babich A.V., Pogosov V.V., Reva V.I. Calculation of the probability of capture of positrons by vacancy, metal vacancy and assessment of contribution to the electrons work function and positrons. *Physics of metals and metallography*. 2016, Vol. 117, No. 3, pp. 215 – 223.
- 8 Rahemi R., Li D. Variation in electron work function with temperature and its effect on the young's modulus of metals. *Scripta Materialia*. 2014, Vol. 99, pp. 41 – 44.
- 9 T. Durakiewicz, A.J. Arko, J.J. Joyce, et al. Thermal work function shifts for polycrystalline metal surfaces. *Surface Science*. 2001, Vol. 478, Issues 1-2, pp. 72 – 82.
- 10 Matosov M.V. *Physics of the electron work function*. Moscow, MAI, 1989, 180 p.
- 11 Surovoy E.P., Titov I.V., Bugerko L.N. Contact potential difference for lead, silver and thallium azides. *Proceedings of Tomsk Polytechnic University*. 2005, Vol. 308, No. 2, pp. 79 – 83.
- 12 Loskutov S.V. Regularities of formation of energy relief of metal surface. *Visnyk Zaporzhia sovereign University*. 1999, No. 1, pp. 138 – 142.
- 13 Babich A.V., Pogosov V.V. The electron work function and the surface tension of a metal surface with a dielectric coating. *Physics of metals and metallography*. 2008, Vol. 106, No. 4, pp.346 – 354.
- 14 Koritsky Yu.V., Pasyukov V.V., Tareev B.M., et al. *Handbook of electrical materials*. Vol.1. Moscow, Energoatomizdat, 1986, 368 p.
- 15 Oleshko V.S., Samoylenko V.M. Application of the device for measuring the contact potential difference "Surface-11" in nondestructive testing of machine parts. *Defense complex — scientific and technical progress of Russia*. 2011, No. 2, pp. 3 – 6.
- 16 Nochovnaya N.A., Nikitin Ya.Yu., Savushkin A.N. Investigation of changes in the surface properties of titanium alloy blades after chemical treatment of carbon-containing contaminants. *Bulletin of the Moscow aviation Institute*. 2019, Vol. 26, No. 1, pp. 236 – 243.
- 17 Betsofen S.Ya., Osintsev O.E., Knyazev M.I., Dolgova M.I., Kabanova Yu.A. Quantitative phase analysis of alloys of the system Al-Cu-Li-Mg. *Bulletin of the Moscow Aviation Institute*. 2016, Vol. 23, No.4, pp. 181 – 188.

UDC 65.011.56

SYSTEM OF HETEROGENEOUS DATA TRANSMISSION ON THE BASIS OF A SELF-REGULATION NETWORK WITH AN OPTION OF RETRANSMISSION

Narimanova G.N.¹, Inkina M.A.²

¹ Tomsk State University of Control Systems and Radioelectronics, Tomsk, Russian Federation, gufana.n.narimanova@tusur.ru

² "EleTeam Limited", Tomsk, Russian Federation, pishchukmariya@mail.ru

The article discusses structural features of wireless data transmission technologies. Based on client-server architecture, a data transmission algorithm has been developed. This algorithm includes the possibility to retransmit with automatic search for the optimal path. A system of heterogeneous data transmission is proposed, which ensures high efficiency of remote data collection and transmission under the conditions of intensive interference. The data transmission system provides automatic selection of the optimal data transmission path.

Keywords: wireless technology, data transmission, heterogeneity, retransmission.

Introduction

Nowadays, wireless data transmission technologies are widespread and today they are experiencing a kind of boom due to the undeniable advantages that they have. At present, for developers of wireless communication technologies, designing and producing a wireless data transmission system suitable for retransmitting and optimizing the data transmission path is an important task, both in terms of providing high technical characteristics and from the standpoint of economic expediency.

The work attempts to create an automated system of heterogeneous data transmission based on an algorithm of a self-regulation network with an option of retransmission, which is competitive at the modern market of wireless technologies.

1. The structure of the developed system and algorithm of its operation

The proposed wireless data transmission system consists of three main elements: 1 — a data collection unit, 2 — a device providing wireless radio data transmission, 3 — a data collection point device (Fig. 1).

In order to ensure the practicality and reliability of the developed algorithm of the self-regulation network with an option of retransmission, the created network was implemented as a wireless mesh topology — a wireless device network built on the mesh principle, in which the devices are connected to each other and are able to play the role of a switch for other devices [1]. That makes possible to use the proposed network under hostile environment conditions or in places where the use of wired technology is very difficult.

From the studied analogs belonging to the WPAN class (Wireless Personal Area Networks), Wireless HART network technology is the closest to the concept of the data transmission algorithm of the developed system. The latter maintains equipment from different manufacturers and uses self-organizing and self-healing mesh architecture.

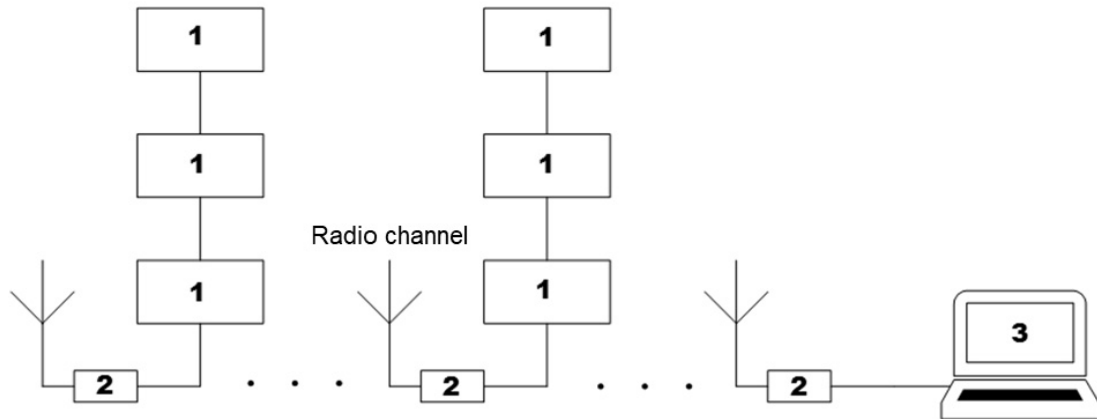


Fig.1. The circuit of the developed system.

The network operation algorithm corresponds to the scheme shown in Figure 2. Here objects 1 ... 4 are wireless data transmission devices. Retransmission assumes data transmission via intermediate devices [2]. In the case when device 1 cannot directly communicate with device 4, their communication will be achieved sequentially through intermediary devices (for example, 2 and 3).

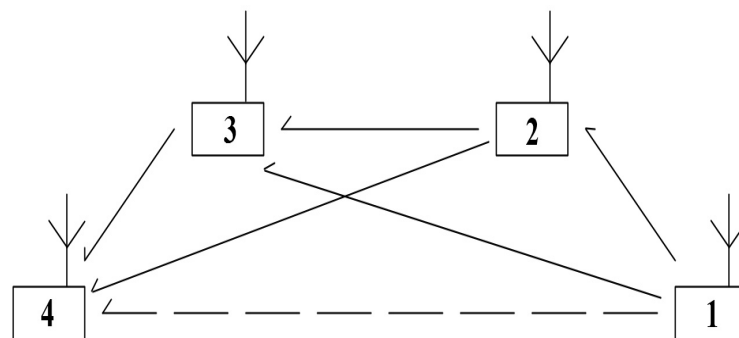


Fig.2. Retransmission circuit.

The Elsimia controller [3], a functional complete product designed for operation in small automation systems with up to 100 I/O signals, serves as the data collection point of the system. If it is necessary to increase the number of signals, the controller makes it possible to connect remote I/O modules of Elsimia and similar to it.

In practice, the considered controller is mainly used in small systems of automatic and automated control of technological processes in such areas as control of climatic equipment, control of small machines and mechanisms, automation of boiler houses, work in systems like “Smart Home” and other facilities. The operation algorithm of the controller is determined by the control program developed by the user in accordance with the requirements for the control system created using the controller.

The system uses such capabilities of the programmable controller as operation with RS-485 interface, Ethernet (local area network) and GSM/GPRS modem. The wireless device interrogator is connected to the controller via RS-485 interface. Then the collected data is transmitted to the operator in one of the ways: using either Ethernet or the built-in GSM/GPRS modem. In case of failure of one of the communication methods, it is possible to use another one.

The developed secondary algorithms for the data collection point significantly expand the functionality of the system. The first algorithm is the initialization of the GPRS module, which is a backup mode for transmitting the collected data and will work in case of a local network failure.

The second algorithm is designed for notification of a communication break in the system at the request of the operator: the operator sends an SMS message with a request about the state of the system and receives an SMS response message with information. This makes for remote monitoring of the system.

To implement the data transmission algorithm, a model of a wireless device was assembled, using which it is possible to gradually develop, test and modify the algorithm. The model includes the following main components: microcontroller, radio module, display module, expansion module.

The system was described using the automaton state. At the stage of data generation, an algorithm for determining the optimal path, based on the calculation of the path rating, comes into operation. In this case, the path optimality is determined by the highest value of the path rating. When calculating the rating, the level of communication between devices and the number of retransmission units are taken into account.

In order to systematize the information and for convenience in operation with the system, a table of commands is created. In the table, the following data is shown: codes of commands executed by the system, their description, address where the command is sent, who sent it, as well as a description of the data that appear when the command is executed. This ensures the completeness and availability of information.

To control the transmitted data, a cyclic redundancy check code (CRC) is used - a checksum algorithm used to check data integrity. CRC is a practical application of error control coding, based on certain mathematical properties of a cyclic code.

Based on the used algorithm schemes, a software code for data transmission was developed, consisting of the following main parts: CRC implementation, data sending by the device, using the Send forwarding method, receiving data by corresponding devices, and an optimal path search algorithm. It should be noted that this system involves two algorithms for receiving data: one is responsible for receiving data by the interrogator device, and the other algorithm is for receiving data by the slave device. A distinctive feature of the latter is the state of execution of commands by the slave in accordance with the table of commands.

2. Results and discussion

The proposed data transfer design is highly competitive with current analogues, both in technical and operational characteristics, as well as in device functionality. At the same time, competitive advantages are offered due to the heterogeneity of the system, the possibility of retransmitting data transmission and self-regulation capability of the network. Heterogeneity provides the possibility of implementing both wireless and wired data transmission, depending on the influencing factors. A distinctive feature of the described data transmission system is the possibility to automatically select the optimal data transmission path.

The optimal operation of the developed system of heterogeneous data transmission is achieved due to the capability of the network to self-regulation, retransmission, as well as the expansion of the functionality of the system under study on the basis of the developed secondary algorithms using the Elsim controller.

The research results indicate that on the basis of the developed software solutions, it is possible to create various analogues of a system with different functionality, as well as to integrate into another product for which such a technical solution is available.

Conclusion

A system of heterogeneous data transmission based at a self-regulation network with an option of retransmission has been developed. The possibility of remote monitoring of the system, as well as the possibility of creating its counterparts with different functionality. The system has a high degree of reliability and efficiency, makes for its competitiveness in the market of wireless technologies.

Acknowledgment

The authors are grateful to Pavel Gennadyevich Nesterenko, the head specialist in EleTeam Limited, for his advice and valuable recommendations.

REFERENCES

- 1 *Mesh topology*. Available at: [https://ru.wikipedia.org/wiki /...](https://ru.wikipedia.org/wiki/...)
- 2 Pischuk M.A. Development of a heterogeneous data transmission system based on a self-regulation network with an option of retransmission. *Collection of materials of the XIII International Conference of Students, Graduate Students and Young Scientists "Innovation 2017"*, eds. A.N. Soldatova, S.L. Minkova. – Tomsk: STT, 2017, pp. 136-139. [in Russian]
- 3 *Programmable logic controller Elsim*. Manual. ZAO EleSi, 2017, pp. 138-146, pp. 78-102. [in Russian]

Article accepted for publication 17.01.2019

INVESTIGATION OF THE MODEL FOR THE ESSENTIALLY LOADED HEAT EQUATION

Yesbayev A.N.¹, Yessenbayeva G.A.², Ramazanov M.I.²

¹L.N. Gumilyov Eurasian National University, Nur-Sultan, Kazakhstan

²E.A. Buketov Karaganda State University, Karaganda, Kazakhstan, esenbaevagulsima@mail.ru

The studied problem for the essentially loaded heat equation is connected with mathematical modeling of thermophysical processes in the electric arc of high-current disconnecting devices. Experimental studies of such phenomena are difficult due to their transience, and in some cases only a mathematical model is able to provide adequate information about their dynamics. The study of the mathematical model is carried out when the order of the derivative in the loaded summand is less than, equal to and greater than the order of the differential part of the heat equation, at a fixed point of the load and in the case when the load point moves at a variable speed. The article is focused mainly on scientific researchers engaged in practical applications of loaded differential equations.

Keywords: thermophysical processes, electric arc, loaded heat equation, boundary value problem, reduction to integral equation

Introduction

The theory of boundary value problems for loaded differential parabolic equations is very relevant for the modeling of physical, technical and applied processes, and also in experimental studies conducted in wide various fields of science. The loaded differential equations are used to model processes of different nature: physical, mechanical, chemical, biological, ecological, economic, etc. Such equations are also widely used in solving various engineering and technical problems.

This information capacity of loaded differential equations is due to the fact that they are based on the fundamental laws of nature, such as, for example, conservation laws. Due to this, processes, completely different in nature, can be described by the same form of equations.

Loaded differential equations arise naturally in the study of nonlinear equations, particles transport equations and optimal control problems, in the numerical solution of integral-differential equations, in the equivalent transformation of boundary value problems, etc. [1]

The modern trend in technology to use super-strong and super-weak currents in many electrical devices leads to the need to study phenomena outside the usual current range. When switching electrical devices or overvoltages an electric arc may appear in the circuit between the current-carrying parts (Fig.1).

Electrical safety has paramount importance for the maintenance of any effective and productive equipment, and one of the most serious threats to security is precisely the electric arc and arc flash. Situations where an electric arc is created in an uncontrolled environment, such as an arc flash, can cause injury, fire, and equipment damage.

In a number of devices the electric arc phenomenon is harmful and especially dangerous. These are, first of all, contact switching devices used in power supply and electric drive: high-voltage switches, circuit breakers, contactors, sectional insulators on the contact network of electrified railways and urban electric transport. When disconnecting the loads of the above mentioned devices, an arc arises between the opening contacts (Fig.2).

Electric arcs can have useful technological purposes when they are used correctly. For example, electric arcs are used in camera flashes, in spotlights for stage lighting, for fluorescent lighting, for arc welding, in arc furnaces (for the production of steel and substances such as calcium

carbide), in plasma cutters (in which compressed air is combined with a powerful arc and is converted into plasma, which has the ability to instantly cut steel), etc.

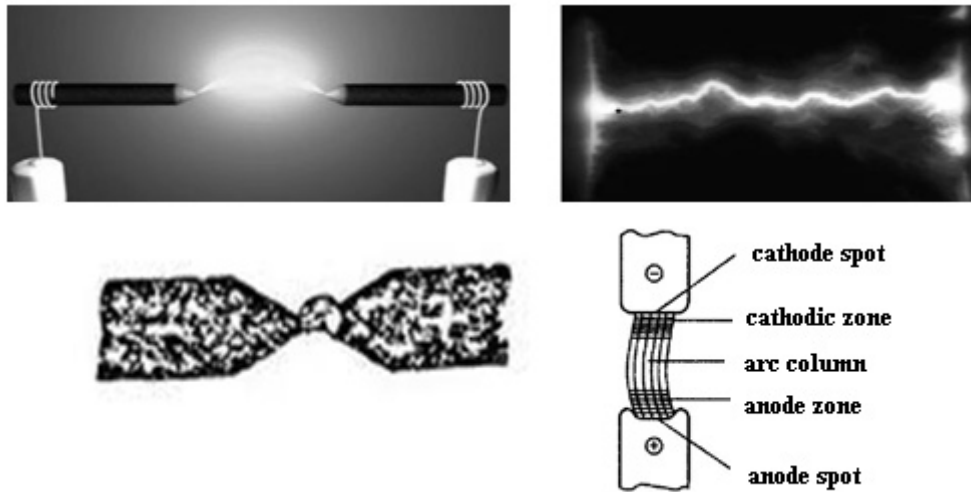


Fig.1. Electric arc

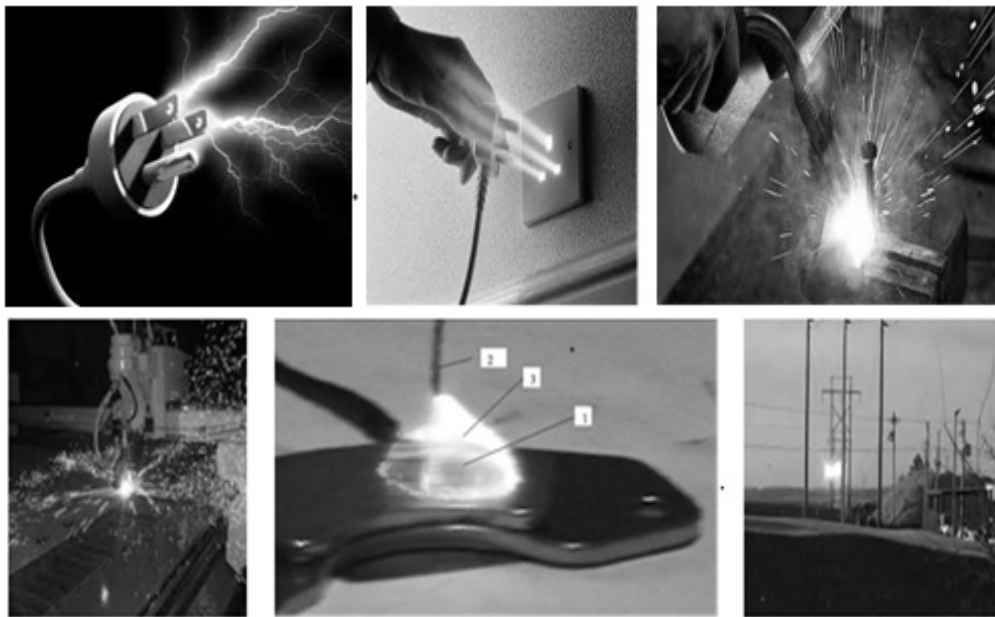


Fig.2. Emergence of electric arc

1. Formulation of the boundary value problem

In the domain $\Omega = \{(x,t) : x \in (0, \infty); t \in (0, \infty)\}$ the essentially loaded heat equation is investigated

$$\frac{\partial u}{\partial t} - \frac{\partial^2 u}{\partial x^2} - \frac{1-2\beta}{x} \cdot \frac{\partial u}{\partial x} - \lambda \cdot \frac{\partial^k u}{\partial x^k} \Big|_{x=\bar{x}(t)} = f(x,t) \quad (1)$$

where $u = u(x,t)$ is an unknown function. β , λ и k are numerical parameters, and $0 < \beta < 1$,

$\lambda \in C$, $k = 0, 1, 2, \dots$ $\lambda \cdot \frac{\partial^k u}{\partial x^k} \Big|_{x=\bar{x}(t)}$ is a loaded summand, $f(x,t)$ is a known function defined in the

domain Ω . The load point moves according to a given law $x = \bar{x}(t)$ for $t \in (0, \infty)$, and the initial condition

$$u(x, 0) = g(x), \quad (2)$$

the boundary condition

$$u(0, t) = h(t) \quad (3)$$

are given. Functions $g(x)$ and $h(t)$ are given at $x \in (0, \infty)$ and $t \in (0, \infty)$ respectively.

As it was noted, when using the basic laws of conservation (energy, mass, etc.), mathematical modeling of various physical processes often leads to the same equations, in particular, to equations of parabolic type. Parabolic equations are most often encountered in the study of problems related to the propagation of heat, both in limited and in unlimited bodies, in the temperature problems of mechanics and physics, in problems of building heat engineering, in the task about the adiabatic filtration of gases and liquids in porous media, etc. Equations of parabolic type are also used in many technical issues, for example, in the study of the influence of the temperature field on the deformation of the railway rail [2]. At the same time, the heat equations are especially frequent.

Thermophysical processes in the electric arc of high-current disconnecting devices (Fig. 2) are described by the physical model, the mathematical interpretation of which is the studied problem (1) - (3). A tool for describing thermal processes in an arc is the heat equation (1).

As previously indicated, when an electrical circuit is disconnected, an electrical discharge occurs in the form of an electric arc. Experimental studies of such phenomena are complex and burdensome due to their temporal short duration, therefore, in many cases, only a mathematical model can give adequate information about their dynamics, so the problem under study is relevant in modern natural science.

2. The solution of the boundary value problem

The solution of the boundary value problem (1) - (3) provided $0 < \beta < 1$ has the form [3]

$$\begin{aligned} u(x, t) = & \frac{1}{2} \cdot \int_0^t \int_0^\infty \left[f(\xi, \tau) + \lambda \cdot \frac{\partial^k u}{\partial \xi^k} \Big|_{\xi=\bar{x}(\tau)} \right] \cdot \frac{x^\beta \cdot \xi^{1-\beta}}{t-\tau} \cdot \exp\left(-\frac{x^2 + \xi^2}{4(t-\tau)}\right) \cdot I_\beta\left(\frac{\xi \cdot x}{2(t-\tau)}\right) \cdot d\xi \cdot d\tau + \\ & + \frac{x^\beta}{2t} \cdot \int_0^\infty g(\xi) \cdot \xi^{1-\beta} \cdot \exp\left(-\frac{x^2 + \xi^2}{2t}\right) \cdot I_\beta\left(\frac{\xi \cdot x}{2t}\right) \cdot d\xi + \\ & + \frac{x^{2\beta}}{2^{2\beta+1} \cdot \Gamma(\beta+1)} \cdot \int_0^t h(\tau) \cdot \exp\left(-\frac{x^2}{4(t-\tau)}\right) \cdot \frac{d\tau}{(t-\tau)^{1+\beta}} \end{aligned} \quad (4)$$

or

$$u(x, t) = \lambda \cdot \int_0^t \int_0^\infty \frac{x^\beta \cdot \xi^{1-\beta}}{2(t-\tau)} \cdot \exp\left(-\frac{x^2 + \xi^2}{4(t-\tau)}\right) \cdot I_\beta\left(\frac{\xi \cdot x}{2(t-\tau)}\right) \cdot \frac{\partial^k u}{\partial \xi^k} \Big|_{\xi=\bar{x}(\tau)} \cdot d\xi \cdot d\tau + \bar{F}(x, t), \quad (5)$$

$$\bar{F}(x, t) = F_1(x, t) + F_2(x, t) + F_3(x, t),$$

$$F_1(x, t) = \frac{1}{2} \cdot \int_0^t \int_0^\infty f(\xi, \tau) \cdot \frac{x^\beta \cdot \xi^{1-\beta}}{t-\tau} \cdot \exp\left(-\frac{x^2 + \xi^2}{4(t-\tau)}\right) \cdot I_\beta\left(\frac{\xi \cdot x}{2(t-\tau)}\right) \cdot d\xi \cdot d\tau,$$

$$F_2(x, t) = \frac{x^\beta}{2t} \cdot \int_0^\infty g(\xi) \cdot \xi^{1-\beta} \cdot \exp\left(-\frac{x^2 + \xi^2}{2t}\right) \cdot I_\beta\left(\frac{\xi \cdot x}{2t}\right) \cdot d\xi,$$

$$F_3(x, t) = \frac{x^{2\beta}}{2^{2\beta+1} \cdot \Gamma(\beta+1)} \cdot \int_0^t h(\tau) \cdot \exp\left(-\frac{x^2}{4(t-\tau)}\right) \cdot \frac{d\tau}{(t-\tau)^{1+\beta}}.$$

3. Reduction of the boundary value problem to the integral equation

The equation (5) can be represented as an integral Volterra equation of the second kind. To do this, the equation (5) can be written as

$$u(x, t) = \lambda \cdot \int_0^t Q(x, t-\tau) \cdot \frac{\partial^k u}{\partial \xi^k} \Big|_{\xi=\bar{x}(\tau)} d\tau + \bar{F}(x, t). \quad (6)$$

$$Q(x, t-\tau) = \frac{x^\beta}{2(t-\tau)} \cdot \exp\left(-\frac{x^2}{4(t-\tau)}\right) \cdot P(x, t-\tau).$$

We differentiate (6) by variable x k times and substitute instead $x = \bar{x}(t)$. As a result, we get

$$\mu(t) - \lambda \cdot \int_0^t K(t, \tau) \cdot \mu(\tau) \cdot d\tau = F(t), \quad (7)$$

$$\mu(t) = \frac{\partial^k u}{\partial x^k} \Big|_{x=\bar{x}(t)}, \quad K(t, \tau) = \frac{\partial^k Q(x, t-\tau)}{\partial x^k} \Big|_{x=\bar{x}(t)}, \quad F(t) = \frac{\partial^k \bar{F}(x, t)}{\partial x^k} \Big|_{x=\bar{x}(t)}. \quad (8)$$

The relation (7) with (8) is a Volterra integral equation of the second kind. Thus, the solving the stated boundary value problem was reduced to the solving the integral equation (7).

4. Properties of the function $Q(x, t-\tau)$

The $Q(x, t-\tau)$ function defines the kernel of the integral equation (7). As it is known, the properties of the kernel play an important role in the question of solvability of the integral equation and dictate the methods of investigation of the integral equation, so a study of the properties of the function $Q(x, t-\tau)$ was carried out, the results of this study are presented in [4].

We list some properties of the function $Q(x, t-\tau)$, necessary for our research.

- 1) The function $Q(x, t-\tau)$, $0 < \tau < t < \infty$, is continuous.
- 2) The function $Q(x, t-\tau) \geq 0$, $0 < \tau < t < \infty$.
- 3) The function $Q(x, t-\tau)$ can be represented as

$$Q(x, t-\tau) = \frac{1}{\Gamma(\beta)} \cdot \gamma\left(\beta, \frac{x^2}{4(t-\tau)}\right), \quad (9)$$

where $\Gamma(\beta)$ is gamma function, $\gamma(\nu, x)$ is incomplete gamma function [5].

- 4) There is a relationship for the function $Q(x, t-\tau)$

$$\int_0^t Q(x, t-\tau) d\tau = \frac{1}{\Gamma(\beta)} \cdot \left[t \cdot \gamma\left(\beta, \frac{x^2}{4t}\right) + \frac{x^2}{4} \cdot \Gamma\left(\beta-1, \frac{x^2}{4t}\right) \right]. \quad (10)$$

4. Solvability of the integral equation

In the case when the load point is fixed: $\bar{x}(t) = x_0$, where $x_0 \in R_+$, we have the following theorem on the solvability of the integral equation (7).

Theorem 1. *If for each fixed value $k = 0, 1, 2, \dots$ with $\bar{x}(t) = x_0$, where $x_0 \in R_+$, and the function $F(t) \in C(0, \infty)$, then the integral equation (7) has a unique continuous solution peuehue [6].*

We investigate the solvability of the integral equation (7) in the case where the load point moves at a variable speed: $\bar{x}(t) = t^\omega$, $\omega \in R$.

Let $k = 0$, then the integral equation (7) takes the form

$$\begin{aligned} \tilde{\mu}_0(t) - \lambda \cdot \int_0^t \tilde{K}_0(t, \tau) \cdot \tilde{\mu}_0(\tau) \cdot d\tau &= \tilde{F}_0(t), \\ \tilde{\mu}_0(t) = u(x, t)|_{x=t^\omega}, \quad \tilde{K}_0(t, \tau) &= Q(x, t - \tau)|_{x=t^\omega}, \quad \tilde{F}_0(t) = \bar{F}(x, t)|_{x=t^\omega}. \end{aligned} \quad (11)$$

When using for the function $Q(x, t - \tau)$ of the representation (9), the kernel of the integral equation (11) is determined by the expression

$$\tilde{K}_0(t, \tau) = \frac{1}{\Gamma(\beta)} \cdot \gamma\left(\beta, \frac{t^{2\omega}}{4(t-\tau)}\right).$$

We calculate the integral

$$\int_0^t \tilde{K}_0(t, \tau) d\tau = \frac{1}{\Gamma(\beta)} \cdot \int_0^t \gamma\left(\beta, \frac{t^{2\omega}}{4(t-\tau)}\right) \cdot d\tau = \frac{1}{\Gamma(\beta)} \cdot \int_0^t d\tau \int_0^{\frac{t^{2\omega}}{4(t-\tau)}} e^{-\xi} \cdot \xi^{\beta-1} d\xi.$$

In the last a ratio producing the replacement of the integration order and the necessary calculations, we obtain the relation

$$\begin{aligned} \int_0^t \tilde{K}_0(t, \tau) d\tau &= \frac{1}{\Gamma(\beta)} \cdot \left[\int_0^{\frac{t^{2\omega-1}}{4}} e^{-\xi} \cdot \xi^{\beta-1} d\xi \int_0^t d\tau + \int_{\frac{t^{2\omega-1}}{4}}^\infty e^{-\xi} \cdot \xi^{\beta-1} d\xi \int_{\frac{t^{2\omega}}{4\xi}}^t d\tau \right] = \\ &= \frac{1}{\Gamma(\beta)} \cdot \left[t \cdot \gamma\left(\beta, \frac{t^{2\omega-1}}{4}\right) + \frac{t^{2\omega}}{4} \cdot \Gamma\left(\beta - 1, \frac{t^{2\omega-1}}{4}\right) \right]. \end{aligned} \quad (12)$$

In (12) the limiting transition as $t \rightarrow 0$ gives that

$$\lim_{t \rightarrow 0} \int_0^t \tilde{K}_0(t, \tau) d\tau = \lim_{t \rightarrow 0} \frac{1}{\Gamma(\beta)} \cdot \left[t \cdot \gamma\left(\beta, \frac{t^{2\omega-1}}{4}\right) + \frac{t^{2\omega}}{4} \cdot \Gamma\left(\beta - 1, \frac{t^{2\omega-1}}{4}\right) \right] =$$

$$= \lim_{t \rightarrow 0} \left[t \cdot \frac{\gamma\left(\beta, \frac{t^{2\omega-1}}{4}\right)}{\Gamma(\beta)} + \frac{t^2}{4} \cdot \frac{\Gamma\left(\beta-1, \frac{t^{2\omega-1}}{4}\right)}{\Gamma(\beta)} \right] = 0. \tag{13}$$

Based on (13) [7], we obtain the following statement about the solvability of the integral equation (11): *if $\tilde{F}_0(t) \in C(0, \infty)$, then the integral equation (11) has a unique continuous solution for any values λ .*

In the case $k = 1$, $\bar{x}(t) = t^\omega$, $\omega \in R$, the integral equation (7) is determined by the expression

$$\begin{aligned} \tilde{\mu}_1(t) - \lambda \cdot \int_0^t \tilde{K}_1(t, \tau) \cdot \tilde{\mu}_1(\tau) \cdot d\tau &= \tilde{F}_1(t), \\ \tilde{\mu}_1(t) &= \frac{\partial u}{\partial x} \Big|_{x=t^\omega}, \quad \tilde{F}_1(t) = \frac{\partial \bar{F}(x, t)}{\partial x} \Big|_{x=t^\omega}, \\ \tilde{K}_1(t, \tau) &= \frac{\partial Q(x, t - \tau)}{\partial x} \Big|_{x=t^\omega} = \frac{1}{\Gamma(\beta) \cdot 2^{2\beta-1}} \cdot \frac{t^{(2\beta-1)\omega}}{(t - \tau)^\beta} \cdot \exp\left(-\frac{t^{2\omega}}{4(t - \tau)}\right). \end{aligned} \tag{14}$$

The kernel $\tilde{K}_1(t, \tau)$ has a singularity of order β , where $0 < \beta < 1$ [7], therefore, we formulate the following statement about the solvability of integral equation (14): *if $\tilde{F}_1(t) \in C(0, \infty)$, then the integral equation (14) has a unique continuous solution for any values λ .*

For $k = 2$, $\bar{x}(t) = t^\omega$, $\omega \in R$, the integral equation (7) is written as follows

$$\begin{aligned} \tilde{\mu}_2(t) - \lambda \cdot \int_0^t \tilde{K}_2(t, \tau) \cdot \tilde{\mu}_2(\tau) \cdot d\tau &= \tilde{F}_2(t), \\ \tilde{\mu}_2(t) &= \frac{\partial^2 u}{\partial x^2} \Big|_{x=t^\omega}, \quad \tilde{K}_2(t, \tau) = \frac{\partial^2 Q(x, t - \tau)}{\partial x^2} \Big|_{x=t^\omega}, \quad \tilde{F}_2(t) = \frac{\partial^2 \bar{F}(x, t)}{\partial x^2} \Big|_{x=t^\omega}. \end{aligned} \tag{15}$$

Taking into account (9) and considering that $x = \bar{x}(t) = t^\omega$ we find the kernel $\tilde{K}_2(t, \tau)$ of the integral equation (15) in the form

$$\begin{aligned} \tilde{K}_2(t, \tau) &= \frac{\partial^2 Q(x, t - \tau)}{\partial x^2} \Big|_{x=t^\omega} = \frac{1}{\Gamma(\beta) \cdot 2^{2\beta-1}} \cdot \left[\frac{(2\beta-1) \cdot t^{(2\beta-2)\omega}}{(t - \tau)^\beta} \cdot \exp\left(-\frac{t^{2\omega}}{4(t - \tau)}\right) - \right. \\ &\quad \left. - \frac{t^{2\beta\omega}}{2(t - \tau)^{\beta+1}} \cdot \exp\left(-\frac{t^{2\omega}}{4(t - \tau)}\right) \right]. \end{aligned}$$

We calculate the integral

$$\int_0^t \tilde{K}_2(t, \tau) d\tau = \frac{2\beta-1}{2 \cdot \Gamma(\beta)} \cdot \Gamma\left(\beta-1, \frac{t^{2\omega-1}}{4}\right) - \frac{1}{\Gamma(\beta)} \cdot \Gamma\left(\beta, \frac{t^{2\omega-1}}{4}\right). \tag{16}$$

Making the limiting transition as $t \rightarrow 0$ in the relation (16), we find that

$$\begin{aligned}
 \lim_{t \rightarrow 0} \int_0^t \tilde{K}_2(t, \tau) d\tau &= \lim_{t \rightarrow 0} \left[\frac{2\beta - 1}{2} \cdot \frac{\Gamma\left(\beta - 1, \frac{t^{2\omega-1}}{4}\right)}{\Gamma(\beta)} - \frac{\Gamma\left(\beta, \frac{t^{2\omega-1}}{4}\right)}{\Gamma(\beta)} \right] = \\
 &= \lim_{t \rightarrow 0} \left[\frac{2\beta - 1}{2(\beta - 1)} \cdot \frac{\Gamma\left(\beta - 1, \frac{t^{2\omega-1}}{4}\right)}{\Gamma(\beta - 1)} - \frac{\Gamma\left(\beta, \frac{t^{2\omega-1}}{4}\right)}{\Gamma(\beta)} \right]. \tag{17}
 \end{aligned}$$

By performing (17) calculations for different values of the parameter ω , we receive

$$\lim_{t \rightarrow 0} \int_0^t \tilde{K}_2(t, \tau) d\tau = \begin{cases} 0, & \omega < \frac{1}{2}, \\ \frac{2\beta - 1}{2 \cdot \Gamma(\beta)} \cdot \Gamma\left(\beta - 1, \frac{1}{4}\right) - \frac{1}{\Gamma(\beta)} \cdot \Gamma\left(\beta, \frac{1}{4}\right), & \omega = \frac{1}{2}, \\ \frac{1}{2(\beta - 1)}, & \omega > \frac{1}{2}. \end{cases}$$

Thus, the kernel $K_2(t, \tau)$ of the integral equation (15) has the property $\lim_{t \rightarrow 0} \int_0^t \tilde{K}_2(t, \tau) d\tau = 0$

only in the case $\omega < \frac{1}{2}$, as we were convinced by the direct calculation, so we formulate a statement similar to the previous: *if $F_2(t) \in C(0, \infty)$ and $\omega < \frac{1}{2}$, then the integral equation (15) has a unique continuous solution for any values λ .*

Since $\lim_{t \rightarrow 0} \int_0^t \tilde{K}_2(t, \tau) d\tau \neq 0$ in the case $\omega \geq \frac{1}{2}$, then the integral equation (15) is a singular integral equation of Volterra. The class of such integral equations is extremely wide and diverse and cannot be unambiguously classified. As a rule, each particular singular integral equation requires a specific study. Methods for studying the solvability and spectral problems of singular integral equations of Volterra are presented in [7].

Based on the statements, we formulate the following theorem.

Theorem 2. *If the function $F(t) \in C(0, \infty)$, $\bar{x}(t) = t^\omega$, where $\omega \in R$, then for $k = 0$ and $k = 1$ with any values of ω , and for $k = 2$ with $\omega < \frac{1}{2}$, the integral equation (7) with (8) has a unique continuous solution for any values λ .*

5. Solvability of the boundary value problem

Since according to Theorem 1 the integral equation (7), to which the boundary value problem (1) - (3) is reduced, has a unique continuous solution, if $F(t) \in C(0, \infty)$, then we have the following solvability theorem for the stated boundary value problem in the case of a fixed point of load.

Theorem 3. If $f \in C_{x,t}^{k-1,1}(\Omega)$, where $\Omega = \{(x,t) : x \in (0,\infty); t \in (0,\infty)\}$, then the boundary value problem (1) – (3) for essentially loaded heat equation has a unique solution $u(x,t) \in C_{x,t}^{k,1}(\Omega)$ in the form (4) when $\bar{x}(t) = x_0$, $x_0 \in R_+$ for each fixed value $k = 0, 1, 2, \dots$ [6].

In the case when the load point moves with a variable speed: $\bar{x}(t) = t^\omega$, $\omega \in R$, from Theorem 2 the following theorem on the solvability of the boundary value problem (1) – (3) is obtained.

Theorem 4. If $f \in C_{x,t}^{k-1,1}(\Omega)$, where $\Omega = \{(x,t) : x \in (0,\infty); t \in (0,\infty)\}$, then the boundary value problem (1) – (3) for essentially loaded heat equation has a unique solution $u(x,t) \in C_{x,t}^{k,1}(\Omega)$ in the form (4) when $\bar{x}(t) = t^\omega$, where $\omega \in R$, for $k = 0$ and $k = 1$ with any values ω , and for $k = 2$ with $\omega < \frac{1}{2}$.

Conclusion

Free-burning arcs are the most intense and high-temperature sources of heat radiation. With an increase in the magnetic field strength and the arc current, the speed of its movement increases and the heat transfer of the arc column with the environment is intensified. This leads to a change in the position of the current-voltage characteristics of the electric arc discharge.

For the studied boundary-value problem (1) - (3), the solvability questions are defined and the solutions are obtained in the form (4) when the order of the derivative in the loaded summand $k = 0, 1, 2, \dots$, that is, is less than, is equal to and greater than the order of the differential part of the heat equation, at a fixed point of load $\bar{x}(t) = x_0$, $x_0 \in R_+$, and in the case when the load point moves with variable speed $\bar{x}(t) = t^\omega$, where $\omega \in R$.

From solution (4) it is clear that the temperature of the arc column is very non-uniform in length and in diameter. Note that the temperature along the cross section of the arc column is also unevenly distributed. It has a maximum on the axis of the column and goes down to its periphery.

REFERENCES

- 1 Dzhenaliev M.T., Ramazanov M.I. *Loaded equations as perturbations of differential equations*. Almaty, Publishing house «Gylym», 2010, 334 p.
- 2 Kostetskaya G.S., Radchenko T.N. *Metody matematicheskoy fiziki. Uravnenie teploprovodnosti* [Methods of mathematical physics. Equation of heat conductivity]. Rostov-on-Don, Electronic textbook, 2016, 47 p. [in Russian]
- 3 Polyanin A.D. *Spravochnik po lineynym uravneniyam matematicheskoy fiziki* [Handbook of linear equations of mathematical physics]. Moscow, Fizmatlit Publ., 2001, 576 p. [in Russian]
- 4 Yesbayev A.N., Yessenbayeva G.A. On the properties of the kernel and the solvability of one integral equation of Volterra. *Bulletin of Karaganda University. Mathematics Series*. 2013, No. 2(70), pp. 65 – 69.
- 5 Prudnikov A.P., Brychkov Yu.A., Marychev O.I. *Integrals and series: in Vol. 2. Special functions*, Moscow: Fizmatlit, 2003, 664 p.
- 6 Yesbayev A.N., Yessenbayeva G.A. On the boundary value problem for a loaded differential heat conduction operator with the stationary point of load. *Bulletin of Karaganda University. Mathematics Series*. 2013, No. 2(70), pp. 59 – 65.
- 7 Polyanin A.D., Manzhirov A.V. *Spravochnik po integral'nyim uravneniyam: Metody resheniya* [Handbook of Integral Equations: Solution Methods]. Moscow, Publishing House “Factorial Press», 2000, 384 p. [in Russian]

UDK 539.384 +004.942+624.73

ON CALCULATION METHODS FOR THE MODEL OF PLATES BENDING

Yessenbayeva G.A.¹, Yesbayeva D.N.², Makazhanova T.Kh.¹¹E.A. Buketov Karaganda State University, Karaganda, Kazakhstan, esenbaevagulsima@mail.ru²«Shanghai Factory-Amigo EC Technology Co., Ltd», Shanghai, China

The article is devoted to the study of plate bending problems, which are of great applied importance and are found everywhere in various branches of science and technology. In this article the structure of the calculation methods is described, their main components are highlighted; the classical approach of calculating rectangular plates hinged supported on two parallel sides and with arbitrary boundary conditions on each of the other two sides is characterized. The mathematical apparatus of the method of trigonometric series is presented in the volume necessary for calculating the plates. Special cases of the calculation for the bending of a rectangular plate by the Levy method are given. This article is focused mainly on mechanics, physicists, engineers and technical specialists.

Keywords: bending of a rectangular plate, plate deflection function, boundary conditions of the plate, equation of S. Germain, Navier solution, Levy solution.

Introduction

Now plates are widely used in various fields of science and technology – in mechanics, physics, chemistry, construction, engineering, instrumentation, aviation, shipbuilding, etc. This is due to the fact that the inherent lightness and forms rationality of thin-walled structures are combined with their high bearing capacity, efficiency and good manufacturability.

The plate can be applied as an independent structure or can be part of the used lamellar system. For example, in the construction plates have all kinds of applications in the form of floorings and wall panels, reinforced concrete slabs to cover industrial and residential buildings, slabs for the foundations of massive structures, etc. Therefore, knowledge of the theory for rectangular plates bending and of classical methods for calculating them is necessary for a modern engineer (Fig. 1).

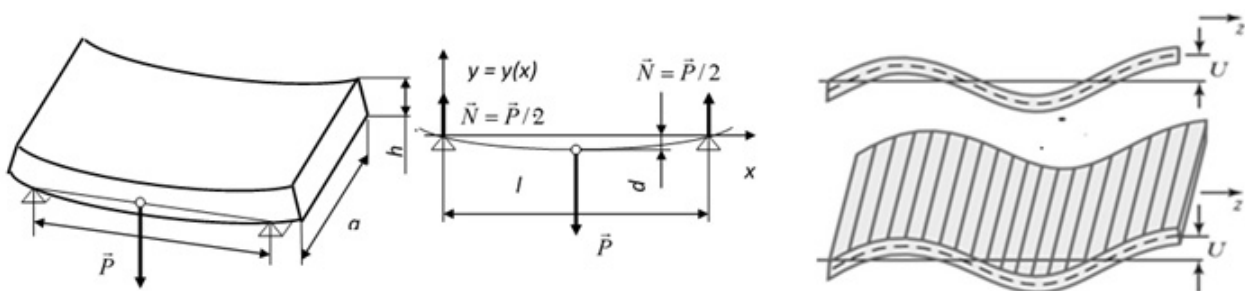


Fig.1. Plate bending. Bending waves

One of the elements of thin-walled spatial systems is a rectangular plate, which has numerous independent applications. An example of a rectangular plate, clamped with one edge, is a vertical panel, and an example of a plate, elastically clamped with three edges, is the wall of a rectangular reservoir. It should be noted that thin plates are a very extensive type of plates and are more often used in many fields of science and technology (Fig. 2).

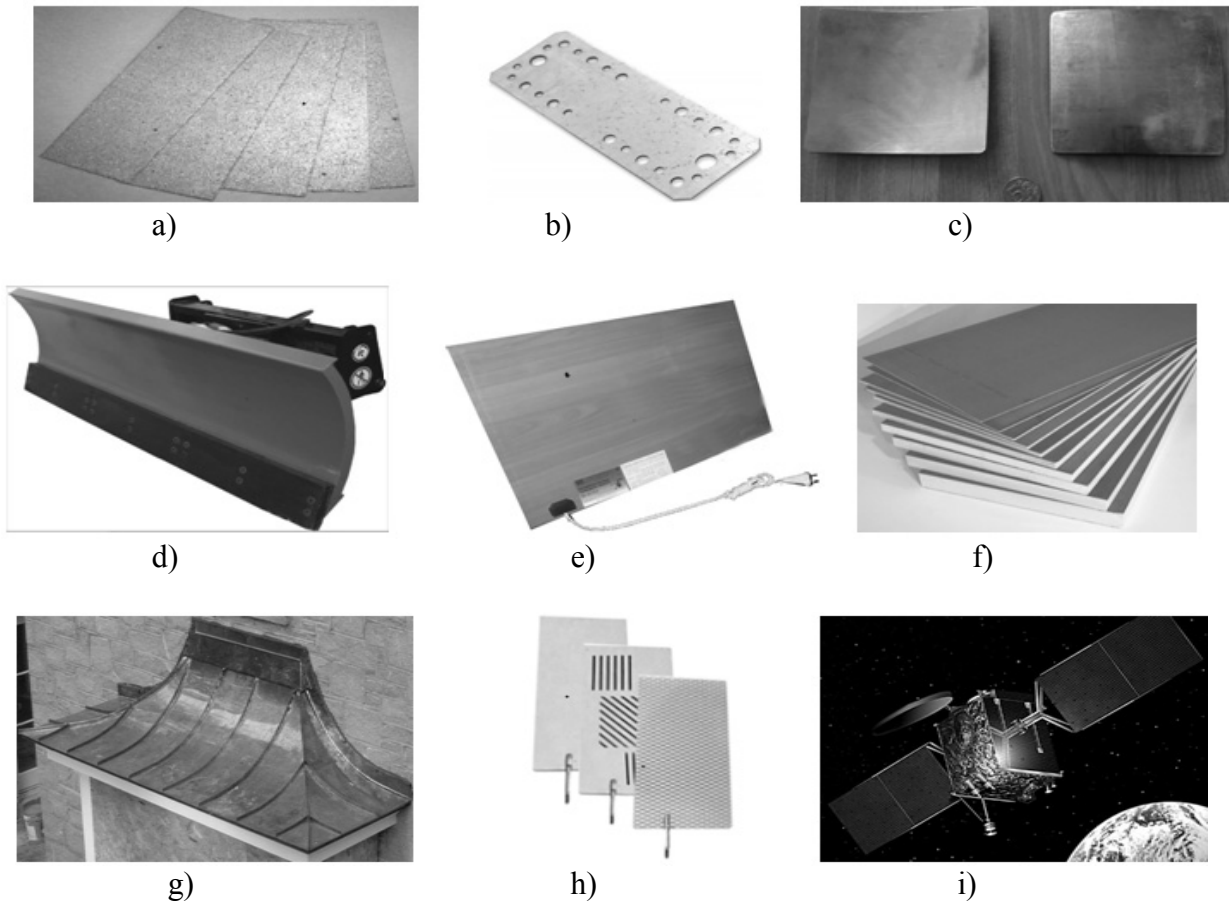


Fig.2. Application of plates:

- a) contact plates; b) mounting plate; c) titanium plates of body armor; d) technical plate for road equipment;
 e) wall-mounted film heater; f) building plates and slabs; g) copper sheets and plates roof;
 h) plates in an alkaline apparatus of water ionization; i) Earth satellite

Many analytical and numerical calculation methods are used to study the problems of plate bending [1- 3]. An exact solution in analytical form for such problems is possible only in some particular cases of the geometrical type of the plate, the load and the conditions for its fixation on the supports, therefore, for engineering practice, approximate, but sufficiently accurate methods for solving the considered boundary value problem are of special importance.

When considering the plate bending problems, the methods of double and single trigonometric series are the most interesting because of connection with their possible numerical implementation in the Maple software package [4].

1. Navier solution

For a rectangular plate ($0 \leq x \leq a$, $0 \leq y \leq b$), hinge supported around the whole contour, we are looking for the desired function $W(x, y)$ of the plate deflections in the form [5]

$$W(x, y) = \sum_{n=1}^{\infty} \sum_{m=1}^{\infty} A_{nm} \sin \omega_n x \cdot \sin \sigma_m y, \quad (1)$$

where A_{nm} are yet unknown coefficients, and $\omega_n = \frac{n\pi}{a}$; $\sigma_m = \frac{m\pi}{b}$.

The solution in the form of (1) is possible because (1) satisfies the boundary conditions of the hinge support on the plate contour. The given load $f(x, y)$ is also decomposed into a similar trigonometric series

$$f(x, y) = \sum_{n=1}^{\infty} \sum_{m=1}^{\infty} f_{nm} \sin \omega_n x \cdot \sin \sigma_m y, \quad (2)$$

where coefficients f_{nm} are determined by the formula

$$f_{nm} = \frac{4}{ab} \int_0^a \int_0^b f(x, y) \sin \omega_n x \cdot \sin \sigma_m y dx dy.$$

In the particular case of a uniformly distributed load of intensity q we obtain

$$f_{nm} = \frac{16}{nm\pi^2} q.$$

Under the action of the concentrated force P , applied at the point of the plate with the coordinates $x = c$, $y = d$, we have

$$f_{nm} = \frac{4}{ab} P \sin \omega_n c \cdot \sin \sigma_m d.$$

Substituting the expressions (1) and (2) into the basic resolving equation of S. Germain

$$D \Delta \Delta W = f(x, y), \quad (3)$$

where D is the cylindrical rigidity of the plate, $\Delta \Delta W$ is the biharmonic operator, we find the values A_{mn} . After substituting the values A_{mn} in (1), we obtain that the plate deflections are determined by the formula

$$W(x, y) = \sum_{n=1}^{\infty} \sum_{m=1}^{\infty} \frac{f_{nm}}{(\omega_n^2 + \sigma_m^2)^2 D} \sin \omega_n x \cdot \sin \sigma_m y.$$

An example of calculating a square plate ($a = b$), loaded with a uniformly distributed load q with Poisson's coefficient $\nu = 0,3$ is given in [6].

2. Levy solution

We consider the case of a plate ($0 \leq x \leq a$, $0 \leq y \leq b$), in which only two opposite edges have a hinge support (for example, $x=0$ and $x=a$) and the other two edges have arbitrary boundary conditions.

We present the desired function of plate deflections $W(x, y)$ in the form [7]

$$W(x, y) = \sum_{n=1}^{\infty} Y_n \sin \omega_n x, \quad (4)$$

where $Y_n = Y_n(y)$ is an unknown function, which is chosen so that expression (4) satisfies the resolving equation S. Germain (3) and boundary conditions on the edges $y = 0$ and $y = b$.

It is obvious that expression (4) satisfies the boundary conditions of hinge support, which are given on the sides $x = 0$, $x = a$ of the plate.

We present the load function $f(x, y)$ in a form of a analogous trigonometric series

$$f(x, y) = \sum_{n=1}^{\infty} f_n(y) \sin \omega_n x, \tag{5}$$

where

$$f_n(y) = \frac{2}{a} \int_0^a f(x, y) \cdot \sin \omega_n x dx. \tag{6}$$

Substituting formulas (4) and (5) into the basic differential equation (3), we obtain

$$Y_n^{IV} - 2\omega_n^2 Y_n'' + \omega_n^4 Y_n = \frac{f_n}{D}. \tag{7}$$

The ordinary differential equation (7) allows us to determine an unknown function Y_n for any number n of expansion. Its general solution can be written as

$$Y_n(y) = A_n \cdot ch \omega_n y + B_n \cdot sh \omega_n y + C_n \cdot y \cdot ch \omega_n y + D_n \cdot y \cdot sh \omega_n y + \varphi_n(y), \tag{8}$$

where A_n, B_n, C_n, D_n is arbitrary integration constants, and φ_n is a partial integral depending on the type f_n and, therefore, on a given external load f .

To determine the four integration constants A_n, B_n, C_n, D_n , the boundary conditions defined at the edges of the plate $y = 0, y = b$ are used, and this boundary conditions, of course, can be different. In the general case, this leads to the solving a system of algebraic equations with respect to unknowns A_n, B_n, C_n, D_n .

After finding the coefficients A_n, B_n, C_n, D_n and determining the function $Y_n(y)$ by the formula (8), the plate deflections can be found by the formula (4) in the form of a series, so bending moments, torque, as well as, transverse forces will be written as

$$\begin{aligned} M_x(x, y) &= -D \sum_{n=1}^{\infty} (\nu Y_n'' - \omega_n^2 Y_n) \sin \omega_n x, & M_y(x, y) &= -D \sum_{n=1}^{\infty} (Y_n'' - \nu \omega_n^2 Y_n) \sin \omega_n x, \\ M_{xy}(x, y) &= -D(1-\nu) \sum_{n=1}^{\infty} \omega_n Y_n' \cos \omega_n x, \\ Q_x(x, y) &= -D \sum_{n=1}^{\infty} \omega_n (Y_n'' - \omega_n^2 Y_n) \cos \omega_n x, & Q_y(x, y) &= -D \sum_{n=1}^{\infty} (Y_n''' - \omega_n^2 Y_n') \sin \omega_n x. \end{aligned} \tag{9}$$

3. The case of uniformly distributed load

Consider the case of a uniformly distributed load of the constant intensity $f = q = const$. Using the formula (5), (6) we obtain

$$q_n = \begin{cases} 0; & n = 2m, \quad m = 1, 2, \dots \\ \frac{4q}{n\pi}; & n = 2m-1, \quad m = 1, 2, \dots \end{cases} \tag{10}$$

Then, taking into account (10), the partial integral of equation (7) can be written as

$$\varphi_n = \begin{cases} 0; & n = 2m, \quad m = 1, 2, \dots \\ \frac{4q}{n\pi\omega_n^4 D}; & n = 2m-1, \quad m = 1, 2, \dots \end{cases} \tag{11}$$

It can be seen from (11) that for even n , the homogeneous differential equation (7) has only trivial solution, so in the case of a uniformly distributed load of constant intensity the deflection function $W(x, y)$ takes the form

$$W(x, y) = \sum_{m=1}^{\infty} [A_{2m-1} ch \omega_{2m-1} y + B_{2m-1} sh \omega_{2m-1} y + y(C_{2m-1} ch \omega_{2m-1} y + D_{2m-1} sh \omega_{2m-1} y) + \frac{4q}{\pi D (2m-1) \omega_{2m-1}^4}] \cdot \sin \omega_{2m-1} x, \quad (12)$$

where the coefficients A_n, B_n, C_n, D_n depend on the given boundary conditions of the plate edges $y = 0$ and $y = b$.

4. Particular cases

As is known, the mathematical model of the plate is completely determined by the deflection function W , and, as shown above, to find the deflection function, it is only necessary to determine the four integration constants A_n, B_n, C_n, D_n , which are found from the boundary conditions. This conditions are given at the edges of the plate $y = 0$ and $y = b$.

Obviously, various approximate methods can be used to find constants A_n, B_n, C_n, D_n . It depends on what degree of accuracy is required in solving a particular practical problem. In addition, it should be borne in mind that the deflection function is defined as an infinite series, finding the sum of which is not always a simple problem. Therefore, it is often necessary to limit ourselves to the finite number of the first members of the series (4) for the deflection function, it also reduces the accuracy of the desired solution.

At the same time, finding analytic expressions for the constants A_n, B_n, C_n, D_n allows us to obtain an analytical expression (formula) for the function of the deflections. And then the function of deflections can be set with the accuracy, which is necessary to solve a particular problem, only limiting the required number of members of the series (4).

We consider finding the integration constants A_n, B_n, C_n, D_n under various boundary conditions on the edges of the plate $y = 0$ and $y = b$ in some particular cases. We show how the coefficients A_n, B_n, C_n, D_n are calculated before analytical expressions are obtained for them.

If we assume that the edges of the plate ($y = 0$ and $y = b$), parallel to the axis x , have a hinge support, then we come to the previously considered Navier solution.

In the case when one of the sides of the plate parallel to the axis x is rigidly pinched and the other side is free, with a uniformly distributed load of constant intensity $f = q$, the integration constants are presented in [7].

Consider this particular case in a more general form, namely, for any kind of external load f . We assume that the side $y = 0$ is free, and the side $y = b$ is rigidly pinched, then the boundary conditions are written as

$$\left(\frac{\partial^2 W}{\partial y^2} + \nu \frac{\partial^2 W}{\partial x^2} \right) \Big|_{y=0} = 0, \quad \left[\frac{\partial^3 W}{\partial y^3} + (2 - \nu) \frac{\partial^3 W}{\partial x^2 \partial y} \right] \Big|_{y=0} = 0; \quad (13)$$

$$W \Big|_{y=b} = 0, \quad \frac{\partial W}{\partial y} \Big|_{y=b} = 0. \quad (14)$$

From the boundary conditions (13), (14) and taking into account (4) and (8) we obtain a system

of algebraic equations for determining the coefficients A_n, B_n, C_n, D_n

$$A_n \left[ch\omega_n b - \frac{1-\nu}{2} \omega_n b sh\omega_n b \right] + B_n \left[\frac{1-\nu}{1+\nu} \omega_n b ch\omega_n b + sh\omega_n b \right] = g_1,$$

$$\frac{A_n}{2} \left[-(1-\nu)\omega_n^2 b ch\omega_n b + (1+\nu)\omega_n sh\omega_n b \right] + \frac{B_n}{1+\nu} \left[2\omega_n ch\omega_n b + (1-\nu)\omega_n^2 b sh\omega_n b \right] = g_2,$$

$$-\frac{1-\nu}{1+\nu} \omega_n \cdot B_n + C_n = g_3,$$

$$\frac{1-\nu}{2} \omega_n \cdot A_n + D_n = g_4,$$

where

$$g_1 = -b \cdot (ch\omega_n b \cdot g_3 + sh\omega_n b \cdot g_4) - \varphi_n(b),$$

$$g_2 = -(ch\omega_n b + b\omega_n sh\omega_n b) \cdot g_3 - (sh\omega_n b + b\omega_n ch\omega_n b) \cdot g_4 - \varphi'_n(b).$$

$$g_3 = \frac{1}{(1+\nu)\omega_n^2} \left[(2-\nu)\omega_n^2 \varphi'_n(0) - \varphi''_n(0) \right],$$

$$g_4 = \frac{1}{2\omega_n} \left[\nu\omega_n^2 \varphi_n(0) - \varphi''_n(0) \right].$$

From the resulting system of equations we find analytical expressions for the coefficients A_n, B_n, C_n, D_n

$$A_n = 2 \frac{[2g_3 - (1-\nu)bg_4]ch\omega_n b + \left[(1-\nu)\omega_n bg_3 - \frac{1+\nu}{\omega_n} g_4 \right]sh\omega_n b}{[4 + (1-\nu)^2 \omega_n^2 b^2]ch^2 \omega_n b - [(1-\nu)^2 \omega_n^2 b^2 + \nu + 1]sh^2 \omega_n b},$$

$$B_n = (1+\nu) \frac{\left[(1-\nu)\omega_n bg_3 + \frac{2}{\omega_n} g_4 \right]ch\omega_n b - [(1+\nu)g_3 + (1-\nu)bg_4]sh\omega_n b}{[4 + (1-\nu)^2 \omega_n^2 b^2]ch^2 \omega_n b - [(1-\nu)^2 \omega_n^2 b^2 + \nu + 1]sh^2 \omega_n b}, \tag{15}$$

$$C_n = g_2 + (1-\nu)\omega_n \frac{\left[(1-\nu)\omega_n bg_3 + \frac{2}{\omega_n} g_4 \right]ch\omega_n b - [(1+\nu)g_3 + (1-\nu)bg_4]sh\omega_n b}{[4 + (1-\nu)^2 \omega_n^2 b^2]ch^2 \omega_n b - [(1-\nu)^2 \omega_n^2 b^2 + \nu + 1]sh^2 \omega_n b},$$

$$D_n = g_1 - (1-\nu)\omega_n \frac{[2g_3 - (1-\nu)bg_4]ch\omega_n b + \left[(1-\nu)\omega_n bg_3 - \frac{1+\nu}{\omega_n} g_4 \right]sh\omega_n b}{[4 + (1-\nu)^2 \omega_n^2 b^2]ch^2 \omega_n b - [(1-\nu)^2 \omega_n^2 b^2 + \nu + 1]sh^2 \omega_n b},$$

Now we consider the case when one of the sides of the plate (for example, a side $y = 0$) parallel to the x axis is supported by an elastic contour, and the other side is rigidly pinched. The elastic contour may be, for example, a beam, bending under the action of pressures applied to it. The boundary conditions on the side $y = 0$ have the form

$$\left(\frac{\partial^2 W}{\partial y^2} + \nu \frac{\partial^2 W}{\partial x^2} \right) \Big|_{y=0} = 0, \quad D \left[\frac{\partial^3 W}{\partial y^3} + (2-\nu) \frac{\partial^3 W}{\partial x^2 \partial y} \right] \Big|_{y=0} = \left(EJ \frac{\partial^4 W}{\partial x^4} \right) \Big|_{y=0},$$

where EJ is the rigidity of the beam.

Analytical expressions for the coefficients A_n, B_n, C_n, D_n are obtained in the same way and have the form

$$A_n = \tilde{g}_1 -$$

$$\begin{aligned}
 & - \frac{2}{(1-\nu)\omega_n} \cdot \frac{D(1-\nu) \left\{ -[2ch\omega_n b + b\omega_n(1-\nu)sh\omega_n b] \tilde{g}_3 + \left[\frac{1+\nu}{\omega_n} sh\omega_n b + b(1-\nu)ch\omega_n b \right] \tilde{g}_4 \right\}}{\left(b\tau\omega_n + \frac{4D}{\omega_n} \right) ch^2\omega_n b + [Db(1-\nu)^2 - \tau] sh\omega_n b \cdot ch\omega_n b - \left[\frac{D}{\omega_n} (1+\nu)^2 + b\tau\omega_n \right] sh^2\omega_n b}, \\
 B_n &= \tilde{g}_2 + \\
 & + \frac{2EJ}{D(1-\nu)^2} \cdot \frac{D(1-\nu) \left\{ -[2ch\omega_n b + b\omega_n(1-\nu)sh\omega_n b] \tilde{g}_3 + \left[\frac{1+\nu}{\omega_n} sh\omega_n b + b(1-\nu)ch\omega_n b \right] \tilde{g}_4 \right\}}{\left(b\tau\omega_n + \frac{4D}{\omega_n} \right) ch^2\omega_n b + [Db(1-\nu)^2 - \tau] sh\omega_n b \cdot ch\omega_n b - \left[\frac{D}{\omega_n} (1+\nu)^2 + b\tau\omega_n \right] sh^2\omega_n b}
 \end{aligned} \tag{16},$$

$$\begin{aligned}
 C_n &= \frac{[\tau\omega_n ch\omega_n b - D(1-\nu^2)sh\omega_n b] \tilde{g}_3 + \left[\frac{2D}{\omega_n} (1-\nu)ch\omega_n b - \tau \cdot sh\omega_n b \right] \tilde{g}_4}{\left(b\tau\omega_n + \frac{4D}{\omega_n} \right) ch^2\omega_n b + [Db(1-\nu)^2 - \tau] sh\omega_n b \cdot ch\omega_n b - \left[\frac{D}{\omega_n} (1+\nu)^2 + b\tau\omega_n \right] sh^2\omega_n b}, \\
 D_n &= \frac{D(1-\nu) \left\{ -[2ch\omega_n b + b\omega_n(1-\nu)sh\omega_n b] \tilde{g}_3 + \left[\frac{1+\nu}{\omega_n} sh\omega_n b + b(1-\nu)ch\omega_n b \right] \tilde{g}_4 \right\}}{\left(b\tau\omega_n + \frac{4D}{\omega_n} \right) ch^2\omega_n b + [Db(1-\nu)^2 - \tau] sh\omega_n b \cdot ch\omega_n b - \left[\frac{D}{\omega_n} (1+\nu)^2 + b\tau\omega_n \right] sh^2\omega_n b},
 \end{aligned}$$

where

$$\begin{aligned}
 \tilde{g}_1 &= \frac{1}{(1-\nu)\omega_n^2} [v\omega_n^2 \varphi_n(0) - \varphi_n''(0)], \\
 \tilde{g}_2 &= -\frac{EJ}{D(1-\nu)^2} \left[v\omega_n \varphi_n(0) - \frac{1}{\omega_n} \varphi_n''(0) \right] + \frac{1}{(1-\nu)\omega_n} \left[\frac{1}{\omega_n^2} \varphi_n'''(0) - (2-\nu)\varphi_n'(0) - \frac{EJ}{D} \omega_n^2 \varphi_n(0) \right], \\
 \tilde{g}_3 &= \left[\frac{EJ}{D(1-\nu)^2} sh\omega_n b - \frac{1}{(1-\nu)\omega_n} ch\omega_n b \right] \cdot \left[v\omega_n \varphi_n(0) - \frac{1}{\omega_n} \varphi_n''(0) \right] - \\
 & - \frac{sh\omega_n b}{(1-\nu)\omega_n} \left[\frac{1}{\omega_n^2} \varphi_n'''(0) - (2-\nu)\varphi_n'(0) - \frac{EJ}{D} \omega_n^2 \varphi_n(0) \right] - \varphi_n(b), \\
 \tilde{g}_4 &= \left[\frac{EJ\omega_n}{D(1-\nu)^2} ch\omega_n b - \frac{1}{1-\nu} sh\omega_n b \right] \cdot \left[v\omega_n \varphi_n(0) - \frac{1}{\omega_n} \varphi_n''(0) \right] - \\
 & - \frac{ch\omega_n b}{1-\nu} \left[\frac{1}{\omega_n^2} \varphi_n'''(0) - (2-\nu)\varphi_n'(0) - \frac{EJ}{D} \omega_n^2 \varphi_n(0) \right] - \varphi_n'(b), \\
 \tau &= 2EJ + bD(1-\nu)^2.
 \end{aligned}$$

Due to the bulkiness of formulas for the determination of the coefficients A_n, B_n, C_n, D_n in the general case, and, consequently, due to the inconvenience and complexity of further use of these formulas, it is recommended that all calculations of the constants A_n, B_n, C_n, D_n be carried out for particular numerical values of a problem in each particular case with given numerical parameters.

Substitution of the found coefficients A_n, B_n, C_n, D_n in (8), (4) and (9) gives the function of plate deflections $W(x, y)$, bending moments and torques, as well as transverse forces in the form of trigonometric series in the each particular case considered above.

In the case of a uniformly distributed load of constant intensity q , the deflection function $W(x, y)$ has the form (12) with coefficients (15) or (16).

Conclusion

Without any difficulty, Levy solution can also be applied to the study for the bending of a plate whose the sides parallel to the axis x have another boundary conditions. Levy solution also extends easily to those cases where the sides of the plate contour, parallel to the axis x , are not quite rigid, but are relatively flexible beams, that bend under the action of the pressures acting on them.

In principle, Levy solution is more accurate than Navier solution, since in it the desired function $W(x, y)$ is approximated by trigonometric functions only in one direction, and in the other direction it is sought precisely from the differential equation (7).

It should be noted that when calculating the plates by analytical methods in the most general formulation: with arbitrary boundary conditions (including elastic), different types of load, complex shapes of plates, with cuts, projections, etc., we have to face with great mathematical difficulties, and in most cases to obtain an analytical solution is not possible. Such a problem can be solved by applying a very efficient finite element method, which is a numerical approximate method for plates, but which gives a sufficiently high accuracy of solutions.

REFERENCES

- 1 Gocelyuk T.B., Matveev K.A., Pel A.N., Pustovoy N.V. *Stroitel'naya mekhanika mashin. Poperechnyy izgib plastin* [Structural mechanics of machines. Transverse bending of plates]. Novosibirsk, Publishing House of NSTU, 2018, 91p. [in Russian]
- 2 Akhanova A.S., Yessenbayeva G.A., Tursyngaliev N.K. On the calculation of plates by the series representation of the deflection function. *Bulletin of the Karaganda University. Mathematics Series*. 2016, №2 (82), pp. 15 - 22.
- 3 Yessenbayeva G.A., Smailova A.A. On the calculation of rectangular plates by the variation method. *Bulletin of the Karaganda University. Mathematics Series*. 2016, 2(82), pp. 56 - 62.
- 4 Kosaurov A.P., Timofeev P.V. *Analiz i osobennosti metodov pri raschete plastin i obolochek na izgib*. [Analysis and features of methods for calculation of plates and shells for bending]. Moscow, Fund «Osnovaniye», 2013, 17 p. [in Russian]
- 5 Zavyalov V.N., Martynov E.A., Romanovsky V.M. *Osnovy stroitel'noy mekhaniki plastin*. [Basics of structural mechanics of plates]. Omsk, SibADI, 2012, 116 p. [in Russian]
- 6 Zhivotov A.G., Yessenbayeva G.A. On the calculation of rectangular plates by the method of trigonometric series. *Bulletin of the Karaganda University. Mathematics Series*. 2015, 3(79), p. 44 – 49.
- 7 Timoshenko S.P., Goodier J. *Teoriya uprugosti* [Theory of elasticity]. Moscow, Nauka, 1979, 560 p. [in Russian]

MODELING OF A TWO-PHASE FLOW OF LIQUID WITH SMALL-SIZE GAS BUBBLES

Vasenin I.M., Narimanov R.K., Shrager L.A., Perchatkina E.V.

Tomsk State University, Tomsk, Russia, ring_0@mail.ru

The model of the motion of a gas-liquid medium with small-size bubbles in a gravity field following free and forced convection was proposed. The model automatically takes into account the processes causing free convection in gravity field in the presence of heterogeneous concentration of bubbles. Compared to the model of interpenetration continuums to describe a two-phase medium, this model does not contain small parameters for derivatives. The two-phase flow in context of the problems similar to the water ozonation problem in contact tanks is considered. The analogy to compressible gas models allows obtaining the solution using well-established numerical solution schemes.

Keywords: two-phase flow, gas-liquid medium, small-size bubbles, heterogeneous, water ozonation

Introduction

The movement of gas-liquid mixtures is wide-spread in nature and various technological processes. The diversity of these phenomena is determined by the proceeding physicochemical reactions, external conditions, the object dimensions, the magnitude of gas phase bubbles, etc. One of the actual technological processes of increasing interest is the disinfection of water in water-supply systems through its ozonation [1-4]. This is due to the high activity of ozone, which allows you effectively affect many types of pollution, both natural and artificial origin. The other purifying methods, for example, electropulse water machining [5], are also of some interest.

The complex motion of multiphase media stimulates the development of methods for sensor monitoring of the gas-liquid mixture behavior [6]. From the great number of the works devoted to the experimental study of ascending gas-liquid flows, we should take note of the following [7-9]. The works devoted to the numerical simulation of two-phase bubble motion are very numerous and are mainly held by the Euler continual approach of representing polydisperse flows [10-13]. The authors in their works [12-13] suggest the promising method for computing the bubble velocities by solving transport equations. Equations of water-air mixtures in context of various problems are periodically considered in the scientific literature. However, the mixture flow in gravity field, taking into account combined action of free and forced convection, has not been practically studied.

Thus, the urgency of the development of the gas-liquid mixture models is undeniable. The purpose of this work is to develop a physico-mathematical model of a two-phase flow of water with small-size bubbles in context of the problems similar to the problem of water ozonation in contact tanks.

1. Physical task description

In this approach, the movement of bubbles in water is considered as the movement of small particles with a density much lower than the density of water. The physical basis of this convection is very simple. By means of the Archimedes buoyant force a lighter mixture containing a larger amount of gas floats in a heavier fluid in the same way as light warm air floats in a cold environment. The mathematical model for small-size bubbles is simpler than the equations of two-phase fluid flow with arbitrary size bubbles and allows us to significantly simplify the problem.

We will call air bubbles small if for their sizes the following conditions are satisfied: the constancy of the bubble shape; the equality of the temperature of the bubble to the ambient

temperature; the short bubble velocity setting time. Moving in water bubbles retain their spherical shape by virtue of the action of surface tension force, so that the movement of each bubble can be considered as the movement of a spherical particle. To satisfy this requirement bubbles, floating up in water under the action of Archimedes buoyant force, should have a size smaller than $2 - 3 \times 10^{-3} m$ [14]. The estimates [15] show that for air bubbles with a diameter less than $2.5 \cdot 10^{-3} m$ the relaxation time of the air and water temperature difference does not exceed $0.1 s$. Since the time of small-size bubble staying in the water mass of a contact tank is assumed to be quite long, the temperature difference between bubbles and water can be neglected. The transient time of the velocity of bubbles floating up in water should be negligible compared with the characteristic time of their motion in the whole region. Since this requirement is essential for further simplifications, we will address this issue in more detail.

Consider the equation of the gravitational small-size bubble floating-up in a liquid medium.

$$\frac{d\mathbf{U}_s}{dt} = \frac{C_R}{m} (\mathbf{U} - \mathbf{U}_s) + \mathbf{g} \left(1 - \frac{\rho_b^0}{\rho_s^0}\right), \quad (1)$$

where \mathbf{U}_s , ρ_s^0 – bubble velocity and the density of gaseous phase; \mathbf{U} , ρ_b^0 – the velocity and density of water, t – time, m – bubble mass, C_R – the resistance coefficient of moving bubble. In general, the C_R variable is: $C_R = \frac{1}{2} C_D \rho_b^0 S |\mathbf{U} - \mathbf{U}_s|$, where C_D – resistance coefficient depending on the Reynolds number, S – bubble mid-section area.

Taking into account the added masses, the equation of particle motion is written as

$$\left(\frac{1}{2} + \frac{\rho_s}{\rho_e}\right) \frac{\tau^*}{T_0} \frac{d(\bar{u} - \bar{u}_s)}{d\bar{t}} = \left(\frac{1}{2} + \frac{\rho_s}{\rho_e}\right) \frac{\tau^*}{T_0} \frac{d(\bar{u})}{d\bar{t}} - f_R(|\bar{u} - \bar{u}_s|) (\bar{u} - \bar{u}_s) - \tau^* \bar{g} \left(1 - \frac{\rho_s}{\rho_e}\right)$$

where $\tau^* = \frac{m}{C_R}$ – the relaxation time of bubble velocity, i.e. $\tau^* = \frac{d_s^2 \rho_s^0}{18\mu}$, T_0 – the characteristic time of bubble floating-up in ozonator; $\bar{t} = \frac{t}{T_0}$; μ – dynamic coefficient of viscosity for water, $f_R(|\bar{u} - \bar{u}_s|) = (1 + 0,15 \text{Re}^{0,682})$.

External decomposition of the solution is sought by the method of successive approximations as $\bar{u} - \bar{u}_s = \bar{y}_0(\bar{t}) + \frac{\tau^*}{T_0} \bar{y}_1(\bar{t})$. This takes into account that outside the initial boundary layer, $t > \frac{\tau^*}{T_0}$, the variable $\frac{d\bar{u}_s}{d\bar{t}}$ has the order $\frac{|\bar{u}_s|}{|1|} \approx 0,2 m/s$, while the product is $gT_0 \approx 200 m/s$. Writing the equation in the projections, we obtain the system of equations:

$$\left(\frac{1}{2} + \frac{\rho_s}{\rho_e}\right) \frac{\tau^*}{T_0} \frac{d\left(y_{0x} + \frac{\tau^*}{T_0} y_{1x}\right)}{d\bar{t}} - \left(\frac{1}{2} + \frac{\rho_s}{\rho_e}\right) \frac{\tau^*}{T_0} \frac{du_x}{d\bar{t}} + f_R(|\bar{u} - \bar{u}_s|) \left(y_{0x} + \frac{\tau^*}{T_0} y_{1x}\right) = \tau^* g \left(1 - \frac{\rho_s}{\rho_e}\right)$$

$$\left(\frac{1}{2} + \frac{\rho_s}{\rho_e}\right) \frac{\tau^*}{T_0} \frac{d\left(y_{0y} + \frac{\tau^*}{T_0} y_{1y}\right)}{d\bar{t}} - \left(\frac{1}{2} + \frac{\rho_s}{\rho_e}\right) \frac{\tau^*}{T_0} \frac{du_y}{d\bar{t}} + f_R(|\bar{u} - \bar{u}_s|) \left(y_{0y} + \frac{\tau^*}{T_0} y_{1y}\right) = 0$$

where $|\bar{u} - \bar{u}_s| = \sqrt{(u_x - u_{xs})^2 + (u_y - u_{ys})^2}$.

From the second equation of the system, taking into account that $f_R(|\vec{u} - \vec{u}_s|) \neq 0$ and, rejecting the terms of the order $\frac{\tau^*}{T_0}$, we can obtain that $y_{0,y} = 0$ and therefore in this approximation

$f_R(|\vec{u} - \vec{u}_s|) = f_R(|u_x - u_{sx}|)$. Rejecting in the first equation the summands of order $\frac{\tau^*}{T_0}$ and taking into account the remark about the value of the right-hand side, we obtain that in this approximation the term characterizing the resistance force takes the form. In the first equation rejecting the summands of the order $\frac{\tau^*}{T_0}$ and taking into account the remark about the value of the equation right-hand side, we obtain that in this approximation the term characterizing the resistance force takes the following form $f_R(|y_{0,x}|(y_{0,x})) = (1 - \frac{\rho_s}{\rho_g})\tau g$.

Assuming that the air density $\rho_s^0 = 1.29 \text{ kg/m}^3$, the dynamic coefficient of viscosity for water $\mu = 10^{-3} \text{ kg/m}\cdot\text{s}$ and the diameter of bubbles $d_s = 2 \times 10^{-3} \text{ m}$ for the Stokes resistance law, we can obtain that $\tau^* = \frac{d_s^2 \rho_s^0}{18\mu} \approx 3 \times 10^{-4} \text{ s}$. However, when evaluating it is necessary to take into account the added mass of water, which is several times the mass of air in a bubble. Hence instead of $\tau^* = 3 \cdot 10^{-4} \text{ s}$, we obtain the value $\tau^* = 1.2 \cdot 10^{-1} \text{ s}$. This time is two orders of magnitude shorter than the time T_0 (which is 10-30 s) of bubble floating-up in the 4 m high ozonator. Thus, the relaxation time of the velocity of bubbles with a diameter of $\sim 2 \times 10^{-3} \text{ m}$ is far less than the characteristic time of the process under consideration, so to simplify the solution we can apply the asymptotic expansion in the small parameter $\tau = \tau^*/T_0$. As obtained above we introduce

$$\mathbf{F} = \mathbf{g} \left(1 - \frac{\rho_B^0}{\rho_S^0} \right).$$

In the agreed notation, the equation (1) is written in the following form

$$\frac{d\mathbf{U}_s}{dt} = \frac{1}{\tau} \mathbf{U} - \frac{1}{\tau} \mathbf{U}_s + \mathbf{F}. \quad (2)$$

From this equation, the bubble velocity \vec{U}_s can be expressed analytically and we can obtain an integral equation having the form

$$\mathbf{U}_s = e^{-\int_0^t \frac{dt}{\tau}} \left[\mathbf{U}_{s0} + \int_0^t \left(\frac{1}{\tau} \mathbf{U} + \mathbf{F} \right) e^{\int_0^t \frac{dt}{\tau}} dt \right]. \quad (3)$$

Integrating by parts and leaving only the first order terms on τ , we will obtain

$$\mathbf{U}_s = \mathbf{U} + \tau \mathbf{F} - \tau \frac{d\mathbf{U}}{dt} + e^{-\int_0^t \frac{dt}{\tau}} \left[\mathbf{U}_{s0} - (\mathbf{U} + \tau \mathbf{F})_0 + \tau \frac{d\mathbf{U}}{dt} \Big|_0 \right] + \theta(\tau^2), \quad (4)$$

where index "0" is for the initial values and the value $\theta(\tau^2)$ denotes second-order terms of smallness.

2. The mathematical modeling of a two-phase flow with small-size bubbles of gas mixture

Note that in formula (4) the time derivative is taken along the bubble trajectory, that is

$$\frac{d\mathbf{U}}{dt} = \frac{\partial \mathbf{U}}{\partial t} + \mathbf{U}_s \nabla \mathbf{U}.$$

Further, mindful that the relaxation time of bubble velocity τ is small, in (4) we dismiss the terms of the second order in τ . As follows from (4), after the relaxation time expires, the initial conditions can also be ignored. As a result of simple transformations over the remaining terms of the equation, we obtain

$$m \left(\frac{\partial \mathbf{U}}{\partial t} + \mathbf{U}_s \nabla \mathbf{U} \right) \approx \frac{1}{2} C_D S \rho_b^0 |\mathbf{U} - \mathbf{U}_s| (\mathbf{U} - \mathbf{U}_s) + m \mathbf{g} \left(1 - \frac{\rho_b^0}{\rho_s^0} \right). \quad (5)$$

Being rewritten this equation assumes the form of

$$m \left(\frac{\partial \mathbf{U}}{\partial t} + [\mathbf{U} + (\mathbf{U}_s - \mathbf{U})] \nabla \mathbf{U} \right) \approx \frac{1}{2} C_D S \rho_b^0 |\mathbf{U} - \mathbf{U}_s| (\mathbf{U} - \mathbf{U}_s) + m \mathbf{g} \left(1 - \frac{\rho_b^0}{\rho_s^0} \right), \quad (6)$$

It can be easily discerned that from (6) for a given fluid velocity field all the projections of the vector $(\mathbf{U} - \mathbf{U}_s)$ for the bubble velocity lag can be calculated by solving a system of algebraic equations.

When deriving the equations of two-phase convection in water with small-size bubbles, for the sake of simplicity we assume that the two-phase convective flow is two-dimensional and laminar. The axis OY is vertically guided in the direction opposite to the direction of gravity. In particular, in the case of the Stokes resistance law ($C_D = 24/Re$) for a two-dimensional flow in x, y plane with velocities $\mathbf{U} = (u, v)$, $\mathbf{U}_s = (u_s, v_s)$, approximately for small τ to within the terms of the order τ^2 , we get

$$u - u_s \approx \tau \frac{\partial u}{\partial t}, \quad (7)$$

$$v - v_s \approx \tau \left[\frac{\partial v}{\partial t} - g \left(1 - \frac{\rho_b^0}{\rho_s^0} \right) \right]. \quad (8)$$

where $\tau = \frac{d_s^2 \rho_s^0}{18 \mu T_0}$ – the relaxation time; d_s – bubble diameter; μ – liquid viscosity coefficient.

Let us denote the bubble velocity vector as $\mathbf{U}_s = (u_s, v_s)$ and the water velocity vector as $\mathbf{U} = (u, v)$. Let $\rho_l = \rho_b^0 (1 - \rho_s / \rho_s^0)$ denote the mass of liquid in a unit volume, ρ_s – the mass of the bubbles in a unit volume, p – pressure. Taking into account the conditions made, we write down the projections of the two-phase mixture motion equations on the x and y axes.

$$\rho_l \left(\frac{\partial u}{\partial t} + \mathbf{U} \nabla u \right) + \rho_s \left(\frac{\partial u_s}{\partial t} + \mathbf{U}_s \nabla u_s \right) + \frac{\partial p}{\partial x} = \mu \Delta u, \quad (9)$$

$$\rho_l \left(\frac{\partial v}{\partial t} + \mathbf{U} \nabla v \right) + \rho_s \left(\frac{\partial v_s}{\partial t} + \mathbf{U}_s \nabla v_s \right) + \frac{\partial p}{\partial y} = \mu \Delta v - g (\rho_l + \rho_s),$$

Introduce new variables $\delta u_s = u_s - u$, $\delta v_s = v_s - v$ and vector $\mathbf{W} = (\delta u_s, \delta v_s)$. The system of equations (9) can be rewritten with the new variables

$$\begin{aligned}
 (\rho_l + \rho_s) \left(\frac{\partial u}{\partial t} + \mathbf{U} \nabla u \right) + \rho_s \left(\frac{\partial \delta u_s}{\partial t} + \mathbf{W}_s \nabla u + \mathbf{U}_s \nabla \delta u_s \right) + \frac{\partial p}{\partial x} &= \mu \Delta u, \\
 (\rho_l + \rho_s) \left(\frac{\partial v}{\partial t} + \mathbf{U} \nabla v \right) + \rho_s \left(\frac{\partial \delta v_s}{\partial t} + \mathbf{W}_s \nabla v + \mathbf{U}_s \nabla \delta v_s \right) + \frac{\partial p}{\partial y} &= \mu \Delta v - g(\rho_l + \rho_s).
 \end{aligned} \tag{10}$$

Assume that

$$\begin{aligned}
 \bar{u} = \frac{u}{V}, \quad \bar{v} = \frac{v}{V}, \quad \bar{u}_s = \frac{u_s}{V}, \quad \bar{v}_s = \frac{v_s}{V}, \quad \bar{\mathbf{U}} = \left(\frac{u}{V}, \frac{v}{V} \right), \quad \bar{\mathbf{W}}_s = \left(\frac{\delta u_s}{\delta V}, \frac{\delta v_s}{\delta V} \right), \quad \bar{\delta u}_s = \frac{\delta u_s}{\delta V}, \quad \bar{\delta v}_s = \frac{\delta v_s}{\delta V}, \\
 \bar{\mathbf{U}}_s = (\bar{u}_s, \bar{v}_s), \quad \bar{\rho}_l = \frac{\rho_l}{\rho_l^0}, \quad \bar{\rho}_s = \frac{\rho_s}{\rho_l^0}, \quad \bar{p} = \frac{p}{\rho_l^0 V^2}, \quad \bar{x} = \frac{x}{L}, \quad \bar{y} = \frac{y}{L}, \quad \bar{t} = \frac{t}{(L/V)},
 \end{aligned}$$

where L – the length scale, V – the velocity scale, δV – the scale of bubble velocity lag.

The equations (10) can be transformed to the non-dimensional form

$$\begin{aligned}
 \left(\frac{\partial \bar{u}}{\partial t} + \bar{\mathbf{U}} \nabla \bar{u} \right) + \frac{\bar{\rho}_s}{\rho_l + \rho_s} \frac{\delta V}{V} \left(\frac{\partial \bar{\delta u}_s}{\partial t} + \bar{\mathbf{W}}_s \nabla \bar{u} + \bar{\mathbf{U}} \nabla \bar{\delta u}_s \right) + \frac{1}{\rho_l + \rho_s} \frac{\partial \bar{p}}{\partial x} &= \frac{1}{\text{Re}} \Delta \bar{u}, \\
 \left(\frac{\partial \bar{v}}{\partial t} + \bar{\mathbf{U}} \nabla \bar{v} \right) + \frac{\bar{\rho}_s}{\rho_l + \rho_s} \frac{\delta V}{V} \left(\frac{\partial \bar{\delta v}_s}{\partial t} + \bar{\mathbf{W}}_s \nabla \bar{v} + \bar{\mathbf{U}} \nabla \bar{\delta v}_s \right) + \frac{1}{\rho_l + \rho_s} \frac{\partial \bar{p}}{\partial z} &= \frac{1}{\text{Re}} \Delta \bar{v} - \frac{1}{\text{Fr}}.
 \end{aligned} \tag{11}$$

Here $\text{Re} = \frac{(\rho_l + \rho_s)VL}{\mu}$ – Reynolds number, $\text{Fr} = \frac{V^2}{gL}$ – Froude number.

From equations (11) it can be seen that in the region of large Reynolds numbers when the inequality (12) is satisfied

$$\frac{\bar{\rho}_s}{\rho_l + \rho_s} \frac{\delta V}{V} \ll 1, \tag{12}$$

we can neglect the second terms as compared with the first ones in the left part of these equations, and solve the following system

$$\begin{aligned}
 \frac{\partial \bar{u}}{\partial t} + \bar{\mathbf{U}} \nabla \bar{u} + \frac{1}{\rho_l + \rho_s} \frac{\partial \bar{p}}{\partial x} &= \frac{1}{\text{Re}} \Delta \bar{u}, \\
 \frac{\partial \bar{v}}{\partial t} + \bar{\mathbf{U}} \nabla \bar{v} + \frac{1}{\rho_l + \rho_s} \frac{\partial \bar{p}}{\partial y} &= \frac{1}{\text{Re}} \Delta \bar{v} - \frac{1}{\text{Fr}}.
 \end{aligned} \tag{13}$$

Near the solid boundaries, due to the no-slip condition, the velocity of liquid along with inertial terms tends to zero. Meanwhile under the influence of Archimedes force bubbles continue to float up. Consequently, in the equations (11) near the solid walls, due to the presence of terms of the form $\bar{\mathbf{W}}_s \nabla \bar{u}$ and $\bar{\mathbf{W}}_s \nabla \bar{v}$, corrections to the inertial terms can become comparable.

In these cases, when fluid moves, viscous force begins to play a defining role. Therefore, the value of the terms in equations (11) should be evaluated in comparison with the viscous terms. It is easy to see that in the region of small Re numbers, the terms dropped above will be small if the inequality (14) is satisfied.

$$\frac{\bar{\rho}_s}{\rho_l + \rho_s} \frac{\delta V}{V} \ll \frac{1}{\text{Re}} = \frac{\mu}{(\rho_l + \rho_s)VL}. \tag{14}$$

With simultaneous satisfaction of the inequalities (12) and (14), equations (13) can be used in the entire flow region. Both inequalities coincide in form, if for the length scale in (14) we choose the distance L , on which the Reynolds number is equal to 1 near the solid boundary. However, the

sense of these inequalities is completely different and they are satisfied for the different scales. In the inequality (12), parameters V and L refer to the flow region with the large Reynolds numbers, and the inequality (14) includes the scales characterizing the flow region for the small Reynolds numbers. To close the system of equations (13), we should add the mass conservation equation for the two-phase mixture, the bubble mass conservation equation, the energy equation, and the equation of state.

3. Equation of state of a two-phase mixture containing water and gas bubbles

Let $\rho = \rho_l + \rho_s$ denote the mixture mass density, z - water mass fraction in the mixture, $z = \frac{\rho_l}{\rho}$. Then $\frac{\rho_s}{\rho} = (1-z)$. The mass unit of the mixture, which occupies specific volume $\frac{1}{\rho}$, contains z kg of water, which occupies the volume $\frac{z}{\rho_b^0}$, and $(1-z)$ kg of gas, which occupies the volume $\frac{1-z}{\rho_s^0}$. Owing to the additivity of the volumes, we can write

$$\frac{1}{\rho} = \frac{z}{\rho_b^0} + \frac{(1-z)}{\rho_s^0}. \quad (15)$$

Express from (15) the value $\frac{1}{\rho_s^0}$ and substitute it into the ideal gas equation of state

$\frac{P}{\rho_s^0} = \frac{RT}{\mu_s}$, where μ_s - the molar mass of gas. As a result we obtain

$$P \left(\frac{1}{\rho} - \frac{z}{\rho_b^0} \right) = (1-z) \frac{R}{\mu_s} T. \quad (16)$$

At the pressure up to 10^8 Pa, the dependence of water density on pressure is described by the experimentally obtained linear law [15]

$$\rho_b^0 = \rho^* \left(1 + \frac{P}{k} \right), \quad (17)$$

where ρ^* and k is the medium parameters.

Substituting (17) into (16) and defining a variable $\bar{R} = \frac{(1-z)R}{\mu_s}$ we obtain the mixture equation of state (18)

$$P \left[\frac{1}{\rho} - \frac{z}{\rho^* \left(1 + \frac{P}{k} \right)} \right] = \bar{R} T. \quad (18)$$

4. Energy equation for a two-phase mixture containing water and small-size bubbles

Since the temperature of water and small-size bubbles can be considered equal, the amount of heat that is contained in the mixture with a constant volume is

$$\bar{C}_v \rho T = z \rho C_b T + (1-z) \rho C_v T, \quad (19)$$

where C_b - heat capacity of water, C_v - heat capacity of gas at constant volume.

From here it follows that the heat capacity of the mixture \bar{C}_V is

$$\bar{C}_V = zC_B + (1-z)C_V. \quad (20)$$

Similarly, for the heat capacity of the mixture at constant pressure, we can find that

$$\bar{C}_P = zC_B + (1-z)C_P. \quad (21)$$

Ratio of specific heat of this mixture is

$$\bar{k} = \frac{\bar{C}_P}{\bar{C}_V} = \frac{zC_B + (1-z)C_P}{zC_B + (1-z)C_V}. \quad (22)$$

Thus, a two-phase mixture of water and small-size bubbles can be considered as a "gas" with the heat capacities (20), (21), ratio of specific heat (22), and the equation (18). Let us calculate the entropy of this "gas". Firstly, it should be noted that the equation of state (18) resembles the Van der Waals equation of state, if in the latter we neglect molecular collisions.

According to [16] the entropy of this gas written in the above terms is

$$\bar{S} = C_V \ln T + \left(\frac{1}{\rho} - \frac{z}{\rho^* \left(1 + \frac{P}{k}\right)} \right) \bar{R}, \quad (23)$$

in the adiabatic process remains constant.

Therefore, from (23) setting $\frac{\bar{S}}{\bar{R}}$ equal to some constant value we can get

$$\left[\frac{1}{\rho} - \frac{z}{\rho^* \left(1 + \frac{P}{k}\right)} \right] T^{\frac{\bar{C}_V}{\bar{R}}} = \left[\frac{1}{\rho_0} - \frac{z}{\rho^* \left(1 + \frac{P_0}{k}\right)} \right] T_0^{\frac{\bar{C}_V}{\bar{R}}}.$$

Hence, using the equation of state (18) and taking into consideration the equality $\bar{C}_P - \bar{C}_V = \bar{R}$ we find

$$\frac{T}{T_0} = \left(\frac{P}{P_0} \right)^{\frac{\bar{k}-1}{\bar{k}}}. \quad (24)$$

We use equation (24) to evaluate the variation of the adiabatic temperature of a two-phase medium upon changing pressure. Put the case that the mass fraction of bubbles z in the contact tank does not exceed 10^{-4} . Taking this estimate as a basis, we find that the mass fraction of water is $(1-z) \sim 0.9999$. Assuming that the heat capacity of water $C_B = 4.180 \frac{kJ}{kg \cdot K}$, we get $\bar{k} = 1.000007$.

Substituting pressure ratio $\frac{P}{P_0} = 2$ into the formula (24), we find that with this pressure change,

the temperature of the two-phase medium in the tank changes by 0.0005%. It follows as a logical consequence that the two-phase medium consisting of water and gas bubbles will have an almost constant temperature while moving in a tank. Also knowing that the temperature of the phases according to the above almost coincides, further it is possible to consider them identical and equal to a certain value T_0 . This value, equal to the temperature of the incoming water, will be used instead of the energy equations of a two-phase mixture and bubbles.

Conclusion

The mathematical model formulated above, unlike the model of interpenetrating continua for a two-phase medium, does not contain small parameters for derivatives and is much simpler from the point of view of numerical solution. By virtue of the consideration of the medium compressibility and the dependence of the density on the concentration of bubbles, this model automatically takes into account the processes causing free convection in the gravity field in the presence of the heterogeneous concentration of bubbles. This kind of convection, when the supply of gas mixture is not uniform in space, significantly affects the duration of stay of the bubbles in the reactor and, consequently, the completeness of the reactions that occur. An additional advantage of the proposed mathematical model is its analogy with compressible gas models. Going forward this analogy makes it possible to use well-developed numerical schemes for solving equations of gas dynamics.

Notwithstanding the fact that for simplicity the above conditions were presented on the example of two-dimensional equations for a two-phase mixture, they remain valid in the case of three-dimensional flows.

REFERENCES

- 1 Kuzubova L.I., Kobrina V.N. *Chemical methods of water preparation. Chlorination, ozonation, fluoridation*. Novosibirsk, 1996, 132 p. [in Russian]
- 2 Kozhinov V.F., Kozhinov I.V. *Water ozonation*. Moscow, Stroiizdat, 1974, 496 p. [in Russian]
- 3 Orlov V.A. *Water ozonation*. Moscow, Stroiizdat, 1984, 88 p. [in Russian]
- 4 Dankverts P.V. *Gas-liquid reactions*. Moscow, Himia, 1973. [in Russian]
- 5 Shaimerdenova K.M., Aitpaeva Z.K., Hasenov A.K., Kutum B.B., Bulkairova G.A. Changes in the structure of the electrodes and their destruction during the electric pulse water treatment. *Eurasian Physical Technical Journal*. 2017, Vol. 14, No. 1(27), pp. 103 – 108.
- 6 Pribaturin N.A., Meledin V.G. Multi-informative methods of experimental study of the structure and evolution of two-phase flows. *Eurasian Physical Technical Journal*. 2013, Vol. 10, No. 2(20), pp. 3 – 10.
- 7 Burdukov A.P., Valukina N.V., Nakoryakov V.E. Features of the flow of a gas-liquid bubble mixture at low Reynolds numbers. *Prikladnaya Mekhanika & Tehnicheskaya Fizika - Journal of Applied Mechanics and Technical Physics*. 1975, No. 4, pp. 137-141. [in Russian]
- 8 Hibiki T., Coda H., Kim S. et al. Structure of Vertical Downward Bubbly Flow. *Int. J. Heat Mass Transfer*. 2004, Vol. 47, pp. 1847 – 1862.
- 9 Kashinski O.N., Randin V.V., Lobanov P.D., Bogoslovtssev G.V. Influence of the gas phase dispersion on the characteristics of a bubbly flow. *Teplofizika & Aeromehanika*. 2005, Vol. 12, No. 4, pp.637 – 643. [in Russian]
- 10 Ramkrishna D. *Population Balances. Theory and Applications to Particulate Systems in Engineering*. N.Y., Acad. Press, 2000, 355 p.
- 11 Marchisio D.L., Fox R.O. *Computational Models for Polydisperse Particulate and Multiphase Systems*. Cambridge, Cambridge University Press, 2013? 508 p.
- 12 Terekhov V.I., Pahomov M.A. Influence of bubbles on the flow structure and friction in a descending turbulent gas-liquid flow. *Teplofizika & Aeromehanika*. 2008, Vol. 15, No. 4, pp. 629 – 642. [in Russian]
- 13 Pahomov M.A., Terekhov V.I. Simulation of a turbulent flow structure in an ascending polydisperse gas-liquid flow. *Izvestiya RAN. Mekhanika zhidksoti i gaza*. 2015, No. 2, pp. 57 – 69. [in Russian]
- 14 Kraiko A.N., Nigmatulin R.I., Starkov L.E., Sternin L.E. et al. Mechanics of multiphase media. Results of science and technology. *Hydromechanics*. Moscow, 1972, Vol. 6, pp. 94. [in Russian]
- 15 Parkin B.R., Gilmor F.R., Broud G.L. *Shock waves in water with air bubbles*. In the coll. *Underwater and underground explosions*. Moscow, Mir, 1974, pp. 152 – 258. [in Russian]
- 16 Landau L.D., Lifshitz E.M. *Statistical physics*. Part. 1. Moscow, Nauka, 1976, 584 p. [in Russian]

UDC: 530.17: 537.86 + 621.396.96

**CREATION AND DEVELOPMENT OF THE FUNDAMENTAL AREA
"FRACTAL RADIOPHYSICS AND FRACTAL RADIO ELECTRONICS:
DEVELOPMENT OF FRACTAL RADIO SYSTEMS".
PART 1. THEORY AND MAIN SCIENTIFIC PROSPECTS.**

A.A. Potapov

V.A. Kotelnikov Institute of Radio Technologies and Electronics of the RAS, Moscow, Russia,
Joint Chinese-Russian Laboratory of Information Technologies and Fractal Processing of Signals,
Jinan University, Guangzhou, China, potapov@cplire.ru

In the first part of the article, scientific prospects in new information technologies based on textures, fractals, fractional operators and nonlinear dynamics methods created and developed by the author during 40 years are presented. The study is being conducted in the framework of the fundamental scientific area "Fractal Radio physics and Fractal Radio electronics: Designing Fractal Radio Systems", initiated and developed by the author in the V. A. Kotelnikov IRTE of the RAS from 1979 until the present day.

Keywords: radio physics; radiolocation; nonlinear dynamics; dimension theory; textures; fractals; scaling; fractional operators.

INTRODUCTION

The article discusses the main trends for the introduction of textures, fractals, fractional operators, non-Gaussian statistics and non-linear dynamics methods [1-10] into the fundamental problems of radio physics, radiolocation and a wide range of radio engineering to create new information technologies. The investigation is being conducted within the framework of the research area "Fractal Radio physics and Fractal Radio electronics: Designing Fractal Radio Systems", initiated and developed by the author in the V. A. Kotelnikov IRTE of the RAS from 1979 until the present day [11-28].

1. Main research areas

The main scientific areas developed by the author with students from 1979 until the present day can be classified as follows [11–28]:

1. Development of new information technologies for modern airborne and ground integrated radio engineering systems for remote sounding and monitoring of the environment, radiolocation, radio vision and navigation, operating in the ranges of optical, millimeter and centimeter waves (MMW and SHF band). Theoretical and experimental studies of the physical bases of scattering and propagation of radio waves, taking into account the spatially inhomogeneous characteristics of the medium being sounded.

2. Fundamental research in the area of textural and fractal approaches to the problems of radio physics, radio engineering, radiolocation, electrodynamics, electronics, control, and a wide range of related scientific and technical prospects. Empirical and theoretical modeling of the corresponding hereditary non-local real stochastic processes.

3. Application of correlation-extremal methods for solving problems of information search, detection, measurement of characteristics and tracking of dynamic fractal and non-fractal objects in stochastic images. Such tasks arise in radiolocation, natural resources survey, remote sounding, navigation, meteorology, information processing from unmanned aerial vehicles (UAVs) and synthetic aperture radars (SAR), medicine, biology, in the automation of scientific research, etc.

4. Development of the theory and experimental studies of broadband (BB) and ultrabroadband (UBB) signals and processes. Development of fractal and nonlinear BB and UBB signals, including fundamentally new types of signals (N-signals).

5. Development and elaboration of mathematical, including textural and fractal, methods for processing optical and radar images in information systems for various purposes (radiolocation, medicine, materials science, nanotechnology, scanning probe microscopes, astronomy, etc.).

6. Development and design of radio-electronic devices for the implementation of mathematical fractal methods for detecting super-weak multidimensional signals against the background of high-intensity non-Gaussian noise for new generation information systems.

7. Physics of the basic radiolocation equation for sounding fractal objects and randomly inhomogeneous media. Fractal-scaling or scale-invariant radiolocation, fractal multi-frequency MIMO-systems.

8. Theory of wave diffraction on a fractal multiscale surface. Multiple scattering of waves in fractal discrete randomly inhomogeneous media with relation to the radiolocation of self-similar multiple group targets. Waves in disordered large fractal systems (radiolocation, nanosystems, clusters of unmanned aerial vehicles and small spacecraft, space debris, etc.).

9. Application of the fractal theory in adaptive population methods for forming dynamic groups of UAVs with the organization of "distributed intelligence", the collective interaction of UAVs in a group and in the processing of incoming information in regards to the theory of their effective application. Development of solutions within the context of the concept of a distributed measuring environment, when each point of a certain dynamic environment is capable of performing sensory, measuring and informational functions, as well as based on a fractal-graph approach that makes for studying the growth of complex networks and the method for manipulating with such networks at the global level without a detailed description.

10. Formulation of the foundations of the fractal paradigm and the global fractal-scaling method. Elaboration and development of the functional principle "Maximum topology with minimum energy" for the received signal, that makes for more efficient use of the advantages of fractal-scaling processing of incoming information.

Fractal geometry is great and brilliant achievement of B. Mandelbrot (1924-2010). But its radiophysical / radiotechnical and practical implementation is the achievement of the world-famous Russian scientific school of fractal methods under the guidance of Prof. A.A. Potapov (V. A. Kotelnikov IRTE, RAS). In a metaphorical sense, it can be said that fractals represented a thin coating of amalgam on the powerful backbone of science at the end of the 20th century. Up to date, the attempts to diminish their significance and rely only on classical knowledge have suffered an intellectual fiasco. In December 2005 in the USA B. Mandelbrot (1924-2010) personally approved the developed classification of fractals, Fig.1. The numerous results obtained by the author on the above mentioned scientific areas have been concretized and illustrated in [18–20].

2. Theoretical foundations of the created fractal-scaling methods

In the fractal-scaling approach proposed and having been developed in the V.A. Kotelnikov IRTE of the RAS for 40 years, description and processing of signals and fields is carried out exclusively in fractional measure space using scaling hypotheses, heavy-tailed non-Gaussian stable distributions [1] and, as far as possible, using the apparatus of fractional integral derivatives [3-9, 11, 13, 14] . Note that if an equation includes a time fractional derivative, it is interpreted so as there is memory or, in the case of a stochastic process, non-Markovism.

The main property of fractals is the non-integral value of their dimension D . Development of the dimension theory started from the works of Poincare, Lebesgue, Brauer, Uryson and Menger. In various areas of mathematics, there occur sets that are negligible in one sense or another and are indistinguishable in terms of Lebesgue measure. To distinguish between such sets with a hugely complicated topological structure, it is necessary to involve nontraditional characteristics of

smallness, for example, capacity, potential, measures, and Hausdorff dimension, etc. The use of the Hausdorff fractional dimension, closely related to the concepts of entropy, fractals and strange attractors in the theory of dynamical systems, turned to be the most optimal [2, 4, 11, 13].



Fig.1. Meeting with B. Mandelbrot at his home in New York on 16.12.2005

The concept of a measure and Hausdorff dimension is defined by a p -dimensional measure with an arbitrary real positive number p introduced by Hausdorff in 1919. The concepts introduced by Hausdorff are based on the Carathéodory construct (1914). The Hausdorff dimension $\dim_H A$ is defined in terms of the Hausdorff α -measure of the set $mes_{H,\alpha}$ as

$$mes_{H,\alpha} = \liminf_{\varepsilon \rightarrow 0} \sum_{\Gamma(A)} [d(U)]^\alpha, \quad (1)$$

where the lower bound \inf is taken with respect to finite or counting coverings Γ of the set A by balls U , the diameters of which are $d(U) < \varepsilon$.

The dimension $\dim_H A$ is defined as such α_0 number that measure (1) is equal to zero for $\alpha > \alpha_0$, and for $\alpha < \alpha_0$ it is equal to infinity. In the general case, the concept of measure is not connected with either the metric or the topology. However, the Hausdorff measure can be developed in an arbitrary metric space based on its metric, and the Hausdorff dimension itself is connected with the topological dimension.

The basics of the modern theory of probability are the limit theorems on the convergence of distributions of sums of independent random variables to the so-called stable distributions: Gaussian or non-Gaussian. The former ones base on the central limit theorem, and the latter (non-Gaussian) ones base on the limit theorem proved by B.V. Gnedenko (1939) and V. Döblin (1940) [1]. In this case, the limit theorem imposes restrictions on the form of non-Gaussian distributions. In order for the distribution law $F(x)$ to belong to the domain of attraction of a stable law with a characteristic exponent α ($0 < \alpha < 2$), different from the Gaussian one, it is necessary and sufficient that

$$1) \quad \frac{F(-x)}{1-F(x)} \rightarrow \frac{c_1}{c_2} \quad \text{for } x \rightarrow \infty, \quad (2)$$

2) for each constant $k > 0$

$$\frac{1 - F(x) + F(-x)}{1 - F(kx) + F(-kx)} \rightarrow k^\alpha \quad \text{for } x \rightarrow \infty, \tag{3}$$

where the coefficients $c_1 \geq 0$, $c_2 \geq 0$, $c_1 + c_2 > 0$, $0 < \alpha < 2$.

To prove (2) and (3) it is necessary and sufficient that with a certain selection of B_n constants, the following conditions were met [1, p. 189]:

$$\begin{aligned} nF(B_n x) &\rightarrow \frac{c_1}{|x|^\alpha} && (x < 0), \\ n[1 - F(B_n x)] &\rightarrow \frac{c_2}{x^\alpha} && (x > 0), \end{aligned} \tag{4}$$

$$\lim_{\varepsilon \rightarrow 0} \overline{\lim}_{n \rightarrow \infty} n \left\{ \int_{|x| < \varepsilon} x^2 dF(B_n x) - \left[\int_{|x| < \varepsilon} x dF(B_n x) \right]^2 \right\} = 0.$$

The smaller the α value, the longer the distribution tail and the more it differs from the Gaussian distribution. For $1 < \alpha < 2$, stable laws have a mathematical expectation; for $0 < \alpha \leq 1$, stable laws have neither dispersions nor mathematical expectations. Conditions (2)-(4) determine the so-called *non-Gaussian statistics*.

In ordinary statistics, fluctuations tend to zero when the sample size or the number of N terms increases. This guarantees the asymptotically exact repeatability of averages and is the source of the traditional successes of classical statistical methods in radiolocation. For Levy statistics, the situation may differ radically. With an increase in the sample size, the accuracy of statistical estimations does not improve! The standard form of the central limit theorem predicts disappearing fluctuations for large N , and from the generalized central limit theorem (for $\alpha < 1$) it follows that the fluctuations are significant for arbitrarily large N . At the same time, for $\alpha < 1$, a case of global non-ergodicity of processes is observed.

Note one more fact. Non-integral values of the α index in the range of $1 < \alpha \leq 2$ correspond to the generalized Brownian motion with long-term correlations and statistical self-similarity, i.e. fractal process. Self-similarity is mathematically expressed by power laws. The fractal dimension of the probability space of the time series is equal to α index:

$$\alpha = 1/H. \tag{5}$$

where H is the Hurst exponent. It is necessary to distinguish the “ordinary” fractal dimension D of the signal or image under study and the fractal dimension determined by the α index. If D characterizes the “curvedness” of objects, then α characterizes the tail thickness of probability distributions [4, 11, 13].

In V.A. Kotelnikov IRTE of the RAS, various original methods for measuring the fractal dimension D have been developed; including the dispersion method, the method taking into account singularities, functionals, triad, based on the Hausdorff metric, sample subtraction, based on the operation "Exclusive OR", etc. [11, 13, 16]. The local dispersion method for measuring the fractal dimension D is based on measuring the dispersion of the intensity / brightness σ_i^2 of optical or radar image fragments by two spatial scales δ_i^2 :

$$D \approx \frac{\ln \sigma_2^2 - \ln \sigma_1^2}{\ln \delta_2 - \ln \delta_1}, \quad i = 1 \text{ or } 2. \tag{6}$$

In the Gaussian case, the dispersive dimension of a random sequence converges to the Hausdorff dimension of the corresponding stochastic process. The principal difficulty is that any numerical method involves discretization (or discrete approximation) of the process or object being analyzed; and discretization destroys fractal properties. To resolve this conflict, it is necessary to develop a special theory based on the methods of fractal interpolation and approximation.

The fractal dimension D or its signature $D(t, f, \bar{r})$ in different parts of the surface image is a texture measure. Fractal methods can function at all signal levels: amplitude, frequency, phase and polarization. Fractional mathematical analysis has a long history and extremely rich content [5, 14]. Ideas about fractional integro-differentiation interested many prominent scientists: Leibniz, Euler, Liouville, and others. Interest in fractional mathematical analysis arose almost simultaneously with the origin of classical analysis (as early as in 1695 G. Leibniz mentioned this fact in letters to G. L'opital when considering differentials and derivatives of $1/2$ order). Note the set of papers by the associate member of the Petersburg Academy of Sciences (1884) A.V. Letnikov, who, during his 20 years of scientific work, developed a complete theory of differentiation with an arbitrary index [14].

At present, the expression for the fractional derivative D_{at}^α in the form proposed by Riemann and Liouville (${}_{RL}D_{at}^\alpha$) is most frequently used.

The operator of integro-differentiation in the sense of Riemann-Liouville of the fractional order $\alpha \in R$ originated at the point a is defined as follows [3-7, 9, 11, 13, 14]:

$${}_{RL}D_{at}^\alpha f(t) = \frac{\text{sign}(t-a)}{\Gamma(-\alpha)} \int_a^t \frac{f(\tau)}{|t-\tau|^{\alpha+1}} d\tau, \quad \alpha < 0, \quad (7)$$

$${}_{RL}D_{at}^\alpha = f(t), \quad \alpha = 0, \quad (8)$$

$${}_{RL}D_{at}^\alpha = \text{sign}^n(t-a) \frac{d^n}{dt^n} D_{at}^{\alpha-n} f(t) = \frac{1}{\Gamma(n-\alpha)} \frac{d^n}{dt^n} \int_a^t (t-\tau)^{n-\alpha-1} f(\tau) d\tau, \quad (9)$$

where $n-1 < \alpha \leq n$, $n \in N$; $\text{sign}(z)$ is determined by the equalities $\text{sign} 0 = 0$, $\text{sign} z = z/|z|$, ($z \neq 0$); $\Gamma(\alpha)$ is a gamma function.

For functions differentiable on the interval $[a, b]$, the definitions of fractional derivatives according to Riemann-Liouville and Letnikov are equivalent. Currently, the Caputo formula [6, 7, 14] is widely used:

$${}_C D_{at}^\alpha f(t) = \text{sign}^n(t-a) {}_{RL} D_{at}^{\alpha-n} f^{(n)}(t), \quad n-1 < \alpha \leq n, \quad n \in N. \quad (10)$$

The Riemann-Liouville and Caputo derivatives are associated by the formula [11]

$${}_C D_{at}^\alpha f(t) = {}_{RL} D_{at}^\alpha f(t) - \sum_{k=0}^{n-1} \frac{f^{(k)}(\tau)}{\Gamma(k-\alpha+1)} |\tau-t|^{k-\alpha}, \quad n-1 < \alpha \leq n, \quad n \in N. \quad (11)$$

In the case $\alpha = n$ we get

$${}_{RL} D_{at}^n f(t) = {}_C D_{at}^n f(t) = \text{sign}^n(t-a) \frac{d^n}{dt^n} f(t), \quad n \in N. \quad (12)$$

The Caputo derivative has the same physical interpretation as the Riemann-Liouville derivative. In particular, for $f(0) = 0$ and $0 < \alpha < 1$ there is the exact equality

$${}_C D_{0t}^\alpha f(t) = {}_{RL} D_{0t}^\alpha f(t). \quad (13)$$

When comparing these derivatives, pay attention to the fact that in order to compute the Riemann-Liouville derivative it is necessary to know the function values, and as for the Caputo derivative, one should know the derivative values, which is much more complicated. Some advantage of the Caputo derivative is that it is zero for a constant function, which is more usual for a researcher.

Conclusion

For the first time, the problem in the title of the work began to be studied by the author exactly 40 years ago at the IRE of the Academy of Sciences of the USSR when carrying out a fundamental research cycle related to the development of new breakthrough radio physical technologies for radiolocation. The main objective was to detect various low-contrast objects against the background of heavy clutter from the ground surface on the base of one-dimensional (signal) and multi-dimensional (optical and radar images) sample.

First, the *complete* families of textural features were studied (for the first time ever), then the transition to fractal features started (again first-ever). Later on, the author united these families of features in a common cluster of features. Huge data arrays obtained by the author in optics and on millimeter waves in long-term joint field experiments with leading enterprises of the USSR served as the source material. Up to the beginning of 2019, the author's priority in the above-mentioned scientific fields is confirmed by more than 1,000 scientific works and 37 domestic and foreign monographs and individual chapters in them in Russian and English [28].

Acknowledgments

The work was performed within the framework of a state task and was partially supported by the International Scientific and Technical Center (project No. 0847.2, 2000–2005, USA), the Russian Foundation for Basic Research (projects of the Russian Foundation for Basic Research No. 05-07-90349, 07-07-07005, 07-07-12054, 07-08-00637, 11-07-00203, 18-08-01356-a), as well as the “Leading Talents” project (project No. 00201502, 2016–2020) at Jinan University (Guangzhou, China).

REFERENCES

- 1 Gnedenko B.V., Kolmogorov A.N. *Limit distributions for sums of independent random variables*. Moscow-Leningrad, 1949, 264 p. [in Russian]
- 2 Rogers C.A. *Hausdorff Measures*. London: Cambridge Univ. Press, 1970, 197 p.
- 3 Oldham K.B., Spanier J. *The Fractional Calculus*. New York, Acad. Press, 1974, 225 p.
- 4 Mandelbrot B. *The Fractal Geometry of Nature*. New York, Freeman and Company, 1982, 470 p.
- 5 Samko S.G., Kilbas A.A., Marichev O.I. *Integrals and derivatives of fractional order and some of their applications*. Minsk, Science and Technology, 1987, 688 p. [in Russian]
- 6 Nakhshuev A.M. *Fractional calculus and its application*. Moscow, Fizmatlit, 2003, 272 p. [in Russian]
- 7 Pskhu A.V. *Partial fractional derivative equations*. Moscow, Science, 2005, 199 p. [in Russian]
- 8 Volterra V. *The theory of functionals, integral and integro-differential equations*. Moscow, Nauka, 1982, 304 p.
- 9 Uchaykin V.V. *The method of fractional derivatives*. Ulyanovsk, Artichoke, 2008, 512 p. [in Russian]
- 10 Skolnik M.I. *Radar Handbook*. 3rd ed. New York, McGraw Hill, 2008, 1200 p.
- 11 Potapov A.A. *Fractals in radio physics and radiolocation*. Moscow, Logos, 2002, 664 p.
- 12 Bunkin B.V., Reutov A.P., Potapov A.A. et al. *Issues of advanced radiolocation*. Moscow, Radio Engineering, 2003, 512 p. [in Russian]
- 13 Potapov A.A. *Fractals in radio physics and radiolocation: sampling topology*. Moscow, University Book, 2005, 848 p.
- 14 Potapov A.A., Chernykh V.A. *Fractional calculus of A.V. Letnikov in fractal physics*. Saarbrücken: LAMBERT Academic Publ., 2012, 688p.
- 15 Potapov A.A. *Fractals and chaos as the basis of new breakthrough technologies in modern radio systems*. In the book: R. Kronover. *Fractals and chaos in dynamical systems*. Moscow, Technosphere, 2006, pp. 374-479.
- 16 Potapov A.A., Gulyaev Yu.V., Nikitov S.A. et al. *The latest techniques of image processing*. Moscow, Fizmatlit, 2008, 496 p.
- 17 Potapov A.A. *The fractal method and the fractal paradigm in modern natural science*. Voronezh, PPC “Scientific book”, 2012, 108 p.

- 18 Potapov A.A. On the Fractal Theory Application in Adaptive Population Methods of Formation of Dynamical Groups of Unmanned Aerial Vehicles and in Processing of Incoming Information in Respect to its Effective Application Theory. *Eurasian Physical Technical Journal*. 2017, Vol. 14, No. 1(27), pp. 6–17.
- 19 Potapov A.A. On the Issues of Fractal Radio Electronics. Part 1. Processing of Multidimensional Signals, Radiolocation, Nanotechnology, Radio Engineering Elements and Sensors. *Eurasian Physical Technical Journal*. 2018, Vol. 15, No. 2(30), pp. 5 – 15.
- 20 Potapov A.A. On the Issues of Fractal Radio Electronics. Part 2. Distribution and Scattering of Radio Waves, Radio Heat Effects, New Models, Large Fractal Systems. *Eurasian Physical Technical Journal*. 2018, Vol. 15, No. 2(30), pp. 16 – 23.
- 21 Potapov Alexander A. *Chaos Theory, Fractals and Scaling in the Radar: A Look from 2015*. Chapter 12 in the book: *The Foundations of Chaos Revisited: From Poincaré to Recent Advancements*. Switzerland, Basel, Springer Int. Publ., 2016, pp. 195 – 218.
- 22 Potapov Alexander A. *On the Indicatrixes of Waves Scattering from the Random Fractal Anisotropic Surface*. Chapter 9 in the book: *Fractal Analysis - Applications in Physics, Engineering and Technology*. Rijeka, InTech, 2017, pp. 187 – 248.
- 23 Potapov Alexander A. *Postulate “The Topology Maximum at the Energy Minimum” for Textural and Fractal-and-Scaling Processing of Multidimensional Super Weak Signals against a Background of Noises*. Chapter 3 in the book: *Nonlinearity: Problems, Solutions and Applications*. Vol. 2. New York, Nova Science Publ., 2017, pp. 35 – 94.
- 24 Alisultanov Z.Z., Agalarov A.M., Potapov A.A., Ragimkhanov G.B. *Some Applications of Fractional Derivatives in Many - Particle Disordered Large Systems*. Chapter 7 in the book: *Fractional Dynamics, Anomalous Transport and Plasma Science*. Switzerland: Springer Int. Publ., 2018, pp. 125 – 154.
- 25 Potapov A.A. *Multiple scattering of waves on a fractal ensemble of particles and in large disordered fractal systems*. In the book: *"Turbulence, Atmospheric and Climate Dynamics"*. Moscow, Fizmatkniga, 2018, pp. 564-573.
- 26 Potapov A.A. Fractal-scaling or scale-invariant radiolocation and fractal signal and image processing. *Collection of scientific papers on the 65th anniversary of the foundation of V. A. Kotelnikov IRTE of the RAS and the 110th anniversary of the birth of Academician V. A. Kotelnikov*. Moscow, V. A. Kotelnikov IRTE of the RAS, 2018, pp. 99-104.
- 27 Potapov A.A. Wave scattering on a stochastic fractal surface. *Collection of scientific papers on the 65th anniversary of the foundation of V. A. Kotelnikov IRTE of the RAS and the 110th anniversary of the birth of Academician V. A. Kotelnikov*. Moscow, 2018, pp. 155-159.
- 28 *Professor Alexander Alekseevich Potapov*. Biography and Bibliography Reference. Ed. by Academician Yu. V. Gulyaev. Moscow, 2019, 169 p.

UDC: 530.17: 537.86 + 621.396.96

**CREATION AND DEVELOPMENT OF THE FUNDAMENTAL AREA
"FRACTAL RADIOPHYSICS AND FRACTAL RADIO ELECTRONICS:
DEVELOPMENT OF FRACTAL RADIO SYSTEMS".
Part 2. SELECTED RESULTS AND PERSPECTIVE TRENDS.**

Potapov A.A.

V.A. Kotelnikov Institute of Radio Technologies and Electronics of the RAS, Moscow, Russia,
Joint Chinese-Russian Laboratory of Information Technologies and Fractal Processing of Signals,
Jinan University, Guangzhou, China, potapov@cplire.ru

In the second part of the article, the main results on the creation of new information technologies based on textures, fractals, fractional operators and nonlinear dynamics methods obtained over 40 years by the author and the team under his leadership are presented. The investigation has been conducted within the framework of the research area "Fractal Radio physics and Fractal Radio electronics: Designing Fractal Radio Systems", initiated and developed by the author in the V. A. Kotelnikov Institute of Radio Technologies and Electronics of the Russian Academy of Sciences from 1979 until the present day. Introduction of the above-mentioned radiolocation terms to the scientific use enabled the author for the first time in the world to propose and then apply new dimensional and topological (but not energy!) features or invariants that are combined under the generalized concept of "sampling topology" ~ "fractal signature".

Keywords: radio physics; radiolocation; nonlinear dynamics; dimension theory; textures; fractals; scaling; fractional operators.

INTRODUCTION

The paper discusses the main areas of the implementation of textures, fractals, fractional operators and methods of nonlinear dynamics into the fundamental problems of radio physics, radiolocation and a wide range of radio engineering to create new information technologies. The investigation is conducted within the framework of the research area "Fractal Radio physics and Fractal Radio electronics: Designing Fractal Radio Systems", initiated and developed by the author in the V. A. Kotelnikov IRTE of the Russian Academy of Sciences from 1979 until the present day [1-50].

1. Main results

As a result of joint long-term natural experiments with leading industry research institutes and design departments of the USSR and Russia, a statistical analysis of large amounts of new data on the spatiotemporal dispersion characteristics of land covers within MMW and SHF ranges was carried out. It took into account their seasonal and angular variations in various weather conditions in order to define the boundaries of radar contrasts, the distribution laws of the specific RCS, the spectral width, the time and the fluctuation correlation interval of the intensity of reflected simple and complex phase-shift keyed signals within MMW range and the structure of the reflected pulse signals that made it possible to consider the terrain features when developing various imaging systems.

A theory of millimeter radio waves scattering by chaotic covers was developed. It used the first introduced functionals of stochastic backscattered fields and frequency coherence functions with regard to the antenna directivity diagram and the correlation of unevenness slopes. The results of

this theory make it possible to determine the coherence zones of space-time radio channels with variable parameters for optimal selection of the sounding signal bandwidth, frequency spacing in multi-frequency systems and values of complex sounding signal base, reflected signal characteristics, generalized uncertainty functions, potential accuracy of aircraft over flight height estimates, characteristic dimension of unevenness. Theoretical and experimental results were used in preparation of reference digital radar maps.

For the first time, a new class of informative features, based on the fine structure of the reflected radar signals of millimeter range radio waves has been proposed. It makes for improving the identification of land covers.

For the first time, *complete* assemblies of textural and spatial spectral-correlation features of optical and radar images of real land covers have been studied, followed by clustering and determination of the most informative features for certain texture classes. It has been proved that the existence domain of textural features of radar images within the MMW range is completely determined by the corresponding domains of optical image features. The performed experiments demonstrated the effectiveness and generality of the proposed approach in the problems of land cover classification when integrating images on optical and millimeter waves. The integration of images increases the efficiency of detection, identification and classification based on an extended vector of informative and stable features. The results of image processing are detailed digital radar maps. Such maps make it possible to present radar information in a form suitable for further use in the radio navigation of aircraft and the identification of various types of ground objects. [Note that these studies had no analogues, neither in the USSR nor in Russia, and have not lost their relevance at the present time].

For the first time, the author has developed a number of textural methods for detecting various objects and their contours in real optical and radar images of the ground surface at small signal / background ratios. A relationship between the dimensions of the object and the analyzed fragment of optical and radar images of a wide class of land covers in the case of optimal detection has been established.

The possibility of stochastic autoregressive synthesis of optical and radar images of land covers with transformation of intensity bar graphs has been theoretically substantiated and experimentally confirmed. The optimal dimensions of the intensity domain and the order of the autoregressive series involved in the forecasting for adequate image synthesis have been determined. With an increase in the correlation order, the domain for determining the textural features of the synthesized images is narrowed. When comparing parts of the original optical or radar image with a synthesized reference standard, it is shown that the resulting two-dimensional binary field of cross-correlation coefficients directly detects the location of the object in the original image. It makes for obtaining a circulation a map and dynamics of the detected object. Using various combination algorithms (classical correlation, the method of pair functions, and the method of absolute difference) it has been established that the physical accuracy of stochastic autoregressive synthesis reaches 90%

On the base of the above mentioned radio physical studies, a system approach to developing an axiomatic information model of radar maps of non-uniform terrain has been developed and implemented. A generalized radio physical model for generating radar maps of non-uniform terrain has been developed. It involves both methods of stochastic autoregressive image synthesis and the information about the field of specific RCS of land covers. The characteristic gradation number of the specific RCS of the ground surface has been defined. Based on the analysis of the system architecture for obtaining the reference standard, an algorithm for synthesizing in the radio range of contour and halftone radar maps of non-uniform terrain is implemented. It is shown that the destruction of the correlation maximum takes place for a contour radar map of the terrain at a wavelength of 8.6 mm at an angle of relative turn of $5^0 \dots 7^0$, and for a halftone radar map – at an angle of $14^0 \dots 17^0$. Then, the fractal parameters have been first introduced into the generalized radio

physical model for developing radar maps of non-uniform terrain. This fact has increased the information content of the synthesis.

The existence of a strange attractor controlling radar scattering from vegetation covers was predicted. Later on, the effect was experimentally detected at a wavelength of 2.2 mm (2002). The obtained results confirmed the theoretical ideas about the existence of chaos in a dynamic system that described the nature of the scattering of electromagnetic waves by vegetation covers. The reconstruction of the attractor made it possible to determine its fractal dimension D , the maximum Lyapunov exponent, embedding dimension, the prediction interval (time). The experimental characteristics of the strange attractor formed the basis of a fundamentally new non-Gaussian model of radar scattering of MMW by vegetation cover based on the theory of dynamical systems and stable distributions. It was shown that the interval (time) of predicting the intensity of the reflected radar signal is approximately by an order of magnitude longer than the classical correlation time. This made it possible to introduce into the theory of radiolocation a new essential characteristic, namely, the interval (time) of prediction, which extended the techniques and circuitry of radio locators.

A reliable physical substantiation of the practical application of fractal methods in modern branches of radio physics, radio electronics, and information control systems was established. In the mid 80s of the XX century an operating model of coherent compact digital solid-state radar (DSR) on parametrons with a sounding wavelength of 8.6 mm with a complex signal base $> 10^6$ and processing an input sub-noise signal on a carrier frequency was made jointly with “Almaz” Central Design Bureau. While optimal processing, the energy potential of the DSR increased by 50 dB. Then, a DSR on two sounding frequencies in MMW and SHF ranges with a fractal slot antenna (the first in the USSR) was made. For the synthesis of images Radon transformation was used. In 1997, methods of fractal modulation and fractal signals were developed for the first time. They included H-signals, first introduced by the author.

The efficiency and perceptiveness of application of the fractional measurement and scaling ratios theory (for textures and fractals) in the case of detection and identification (general filtering) of one-dimensional and multidimensional radar signals from low-contrast targets against the background of intense non-Gaussian interference of various kinds were found and proved for the first time. Thus, that was *fundamentally new* radio engineering.

It is proved that when collecting, transforming and storing information in modern complex monitoring systems of remote and mobile objects under conditions of intense interference, the latest methods for processing information flows and multidimensional signals proposed by the author are of great importance. Typically, the characteristics of such complex systems are demonstrated on different space-time scales. The most adequate valuation of states of the system under study and the dynamics of the state change of its subsystems are realized when using the theory of fractals and processing multidimensional signals in a fractional dimension space with the necessary consideration of scaling effects, which was first proposed and developed by the author in V.A. Kotelnikov Institute of Radio Technologies and Electronics of the RAS.

A new method for measuring fractal dimension and the corresponding fractal signatures of signals, images and wave fields, called by the authors a “local- dispersive” one, was proposed and established. This method, as well as its effectiveness, was confirmed in practice by numerous examples of corresponding digital processing of optical and radar natural and synthesized images, including those with low contrast objects. Textural and fractal digital methods make it possible to partially overcome a priori uncertainty in radar problems using *geometry* or a *sample topology* — both one-dimensional and multidimensional. In this case, topological features of the sample, rather than averaged implementations, which are often of a different nature, are of great importance.

Methods of fractal classification, clustering and identification of many types of natural and artificial objects were studied for the first time on great arrays of experimental data in the form of optical and radar images of real land covers with surface and subsurface objects. The number of

areas around which fractal dimension values are grouped depends on the parameters of the algorithm and the measurement technique. For example, with a small size of the measuring window, we have a large number of groups; increasing its size, we obtain a fixed number of groups or clusters; and, finally, with a very large window size, there 2-3 groups remain (fractal objects – non-fractal objects – exception objects).

Investigation of the type or sampling topology of a one-dimensional (multidimensional) signal for tasks, such as artificial intelligence, for the first time has made for compiling fractal features dictionaries based on fractal primitives that are elements of a fractal language with fractal grammar. The obtained data have been introduced into the synthesis of reference and current radar maps of non-uniform terrain, as well as into developing non-energy radar detectors.

The results (UAV, SAR, medicine, etc.) show that fractal processing methods result in an increase in the quality, object and target details in passive and active modes by several times. These methods can be successfully applied to information processing from space and aviation complexes, stealth high-altitude pseudo-satellites (HAPS) or detecting HAPS and UAV clusters, synthesized clusters of space antennas and space debris. The fractal characteristics of elves, jets and sprites, the most interesting types of recently discovered altitude discharges in the ionosphere, have been investigated. The algorithms for extraction of a moving remote object of unknown shape (fractal or non-fractal) in a low-contrast image formed in optical-electronic systems have been synthesized with co-authors. Experimental results in images obtained in natural conditions, confirm the effectiveness of the proposed processing methods. The possibility of synthesizing new fractal functions and fractal functionals based on the theory of fuzzy sets has been proved for the first time. The construction of new classes of fractal and multifractal subsets on fuzzy sets has been formalized. As test functions, any classical non-differentiable functions can be used.

It has been shown for the first time that the physical content of the diffraction theory involving multiscale surfaces becomes more distinct with the fractal approach and regard of the fractal dimension D or the fractal signature as a parameter. Consideration of fractality significantly brings together theoretical and experimental characteristics of scattering patterns of land covers, which is important for radar and remote sounding tasks. For the first time ever, a long list of characteristic types of more than 70 fractal surfaces based on Weierstrass functions, as well as more than 70 three-dimensional scattering patterns and their cross sections calculated for $\lambda = 2.2$ mm, $\lambda = 8.6$ mm and $\lambda = 3.0$ cm wavelengths at different values of the fractal dimension D and changing scattering geometry has been studied and presented.

Analogs of Maxwell's equations with Caputo fractional derivatives have been deduced. Gauge invariance has been considered and the diffusion-wave equation for scalar and vector potentials has been deduced. A particular solution of the diffusion-wave equation has been found and analyzed. A rigorous electrodynamic calculation of numerous types of fractal antennas, the design principles of which form the basis of fractal frequency-selective surfaces and volumes (fractal “sandwiches”) has been made.

Based on the topology of fractal labyrinths, a series of tiny broadband fractal antennas has been synthesized. The author has proposed to synthesize large stochastic robust antenna arrays using the properties of fractal labyrinths. Combination of several fractal labyrinth clusters with different fractal dimensions makes it possible to develop adaptive broadband fractal antennas. For the first time, a model of a “fractal” capacitor as a fractal impedance has been proposed and implemented. Fractal-scaling methods for the tasks of radiolocation and the formation of the fundamentals of a fractal element base, fractal sensors and fractal radio systems have been developed, substantiated and applied. A physical approach to modeling a fractal capacitor and fractal impedances has been developed. Promising elements of fractal radio electronics are functional elements, the fractal impedances of which are implemented on the basis of the fractal geometry of conductors on the surface (fractal nanostructures) and in space (fractal antennas), the fractal geometry of the material microrelief surface, etc. Advanced approaches can be extended to a wide class of electrodynamic

problems in the study of fractal magnonic crystals, fractal resonators, fractal screens and barriers, as well as other fractal frequency-selective surfaces and volumes.

A new type and a new method of modern radiolocation (namely, fractal-scaling or scale-invariant radiolocation) has been discovered, proposed and established. The efficiency of the functionals, which are determined by topology, fractional dimension and the texture of a received multidimensional signal for the synthesis of fundamentally new non-energy detectors of low-contrast objects against the background of interference has been proved. An increase in the sensitivity of the radio system (that is equivalent to an increase in the range of action) when using fractal and texture features in topological detectors, has been confirmed. This leads to fundamental changes in the very structure of theoretical radiolocation, as well as in its mathematical apparatus.

Fractal radiolocation can describe and adequately explain a much greater class of radiolocation phenomena. The basis of the scientific area created for the first time in Russia and in the world, is the concept of fractal radio systems and fractal radio elements, sampling topology and the global fractal-scaling method proposed and developed by the author in the V. A. Kotelnikov IRTE of the RAS. The theoretical radiolocation-related research makes it possible to solve effectively the problem of detecting signals in conditions of intense interference and develop new fractal multi-frequency MIMO systems.

The following postulates of fractal radiolocation have been developed:

1 – intelligent signal / image processing based on the theory of fractional measure and scaling effects for calculating the field of fractal dimensions;

2 – sampling a received signal in noise can be classified as stable non-Gaussian probability distribution of a D signal;

3 – topology maximum with a minimum of the input random signal energy (i.e. maximum “escape” from the received signal energy).

These postulates open up new possibilities for ensuring stable operation at a small signal / (noise + interference) relationship or an increase in the radar range.

The theoretical issues of fractal non-inertial relativistic radiolocation and quantum cosmology in a curved space-time of negative fractal dimension have been substantially developed together with colleagues from Russia and Israel (Haifa, Technion). *Example:* Based on the Schrödinger equation with the fractional calculus operator with respect to spatial coordinates, the Feynman path integral for the generalized Lagrangian with the fractional differentiation operator with respect to time has been calculated. Note that at present in the United States, this fundamental scientific trend acquired an imposing name of “*Fractal Cosmology*”.

The results of experimental and theoretical studies obtained by the author have been implemented by leading industry research institutes and design departments of the USSR and Russia and used in developing radio systems for various purposes, in interpreting data of remote radio physical studies of the environment and in other applied tasks in which optical and radar images of the ground surface serve as information materials.

Based on multi-year research, new theoretical trends were formulated and developed in the theory of statistical solutions, statistical radio engineering and statistical radio physics, for example, “The Statistical Theory of Fractal Radiolocation”, “Statistical Fractal Radio Engineering”, “Theoretical Foundations of Fractal Radiolocation”, etc. The results listed above formed the basis of the fractal paradigm and the unitary global idea of fractal natural science.

And one more thing:

In the book of I. I. Guay On the little-known hypothesis of Tsiolkovsky / Prefaced and ed. by Doctor of Technical Sciences P.K. Oschepkova. – Kaluga: Kaluga Book Publishing House, 1959. – 248 p. (pp. 24-25) one can find the following words:

“New scientific hypotheses almost always require new and unusual arguments because these hypotheses deal with the new, not the expected, and the necessary regularities that this hypothesis promises to create in the future are not obvious at first sight. This is the main vulnerability of new

hypotheses, whereas well-established theories confirmed by practice often seem to be unshakable. But not even the best hypothesis can be considered complete and absolutely motionless and, as Leonardo da Vinci said, a scientist following traces will never get ahead.”

2. On promising trends of research on fractals and textures

On the basis of the above mentioned author's works, let us try to bring into focus the most promising trends of fractal research in the field of progress in modern fundamental and applied sciences:

1. Investigation of the capabilities of textural (spatial and spectral), fractal and entropy features for radar detection tasks.
2. Synthesis of new models of radar signals scattering by land covers based on the theory of deterministic chaos, strange attractors and fractal probability distributions – stable distributions.
3. Investigation of wave phenomena (propagation and scattering of waves, diffusion processes) in fractal inhomogeneous media based on fractional integrodifferential operators. Further development of fractal electrodynamics.
4. Synthesis of channel models of radar and telecommunication system based on spatial fractal generalized correlators and fractal frequency coherence functions.
5. Investigation of the possibilities of identification of target shape or contours using fractal, textural and entropic features. Work on the singularities of the input function.
6. Investigation of the potential possibilities and limitations of fractal methods for processing radar and communication signals, including fractal modulation and demodulation, fractal coding and data compression, fractal image synthesis, fractal filters. Transition to fractal radio systems. Fractals in acoustic electronics.
7. Investigation of adaptive space-time signal processing based on fractional dimension and fractional operators.
8. Search and study of new combined methods for detecting and identification of low contrast target classes in high-intensity non-Gaussian noise.
9. Investigation of the possibilities of developing new media for transmitting information, multiple-band fractal absorbing materials, constructing fractal antennas and fractal frequency selective surfaces and volumes. Further development of the theory and technology of fractal impedances.
10. Synthesis of new classes of fractals and multifractals with a generalization of the concept of set measure.
11. Study of the type or sampling topology of a one-dimensional (multidimensional) signal, for example, for tasks of artificial intelligence in order to compile dictionaries of fractal features based on fractal primitives that are elements of the fractal language with fractal grammar, i.e. investigation of the *problem of “dimensional sclerosis”* of physical signals and signatures. These concepts, introduced by the author, suggest the study of the topological features of each specific individual sampling, but not average implementations, which are often of different nature.
12. The forecast of the formation mechanisms and roughness characteristics in order to control the geometrical parameters of the microrelief to obtain the desired physicochemical and operational properties of products with modern non-equilibrium processing technologies of their surface layer. Fractals in nanotechnology. (In 2008, the author proposed a new concept, namely, “Scaling of a rough fractal layer and nanotechnology”).
13. The development of fractal non-inertial relativistic radiolocation in curved space-time of connected structures, i.e. fractal geometry of space-time of deterministic structures. At present, in the USA this fundamental scientific trend has acquired an imposing name of “*Fractal Cosmology*”. Our works with co-authors are listed in publications on this theoretical trend (arXiv: Cornell University, USA).

Conclusion

The performed investigations are priority in the world and serve as the basis for further development and substantiation of the practical application of fractal-scaling and texture methods in modern radio physics, radiolocation and nanotechnology, as well as in development of fundamentally new and more accurate fractal-texture (topological) methods for detecting and measuring parameters of radio signals in the spatiotemporal radar channel of the propagation of electromagnetic waves with scattering. The crucial distinction of the proposed textural-fractal methods from the classical ones is due to a fundamentally different approach to the main components of the signal and field. This made it possible to get to a new level of information structure of real non-Markov signals and fields. Thus, this is fundamentally *new radio engineering*. The introduction of fractals, scaling effects and fractional operators gives "impetus" to modern electronics as well, since all foregoing and present-day electronics is based exclusively (and only!) on the basis of the theory of integral functions.

The results and conclusions made by the author together with his students also have great innovative potential, the realization of which, in their opinion, will provide a solution to a number of problems of modern radio physics, radio engineering, radiolocation, communication and control. They will ensure new quality of detection and identification systems, development of new information technologies and competitiveness enhancement of domestic radio electronics products.

The author has named only the most important issues related to the use of fractals, textures and scaling effects in radio physics and radiolocation. In the development of fractal trends, many important stages have already been passed, including the stage of formation of this field of science. However, many problems still remain to be solved. Not results, not specific decisions are of the greatest value, but namely, *the method of solution*, the approach to it. That is global fractal-scaling method created and developed by professor A.A. Potapov. B. Mandelbrot (1924-2010) deserves full credit for formulation of the theory of fractal geometry. But its radio physical / radio technical and practical implementation is the achievement of the world-famous Russian scientific school of fractal methods headed and led by the author of the article.

Acknowledgments

The work was performed within the framework of a state task and was partially supported by the International Scientific and Technical Center (project No. 0847.2, 2000–2005, USA), the Russian Foundation for Basic Research (projects of the Russian Foundation for Basic Research No. 05-07-90349, 07-07-07005, 07-07- 12054, 07-08-00637, 11-07-00203, 18-08-01356-a), as well as the "Leading Talents" project (project No. 00201502, 2016–2020) at Jinan University (Guangzhou, China).

REFERENCES

- 1 Andreev G. A., Potapov A. A., Khokhlov G. I. Statistical characteristics of millimeter waves reflected by vegetation. *Radio Engineering and Electronics*, 1982, Vol.27, No.10, pp. 1863-1868.
- 2 Andreev G. A., Potapov A. A. The effect of chaotic surface irregularities on the reflected pulsed signal of millimeter waves. *Radio Engineering and Electronics*, 1986, Vol. 31, No. 7, pp.1405-1414.
- 3 Potapov A. A., Galkina T. V., Orlova T. I., Khlyavich Ya. L. The dispersion method for detecting deterministic objects in texture optical and radar images of the land surface. *Radio Engineering and Electronics*, 1990, Vol. 35, No. 11, pp. 2295-2301.
- 4 Potapov A. A. Investigation of the effect of vegetation cover on the backscattered field of millimeter waves. *Radio Engineering and Electronics*, 1991, Vol. 36, No. 2, pp. 239-246.
- 5 Potapov A. A., Galkina T. V., Orlova T. I., Khlyavich Ya. L. A method for extracting contours of extended deterministic objects in stochastic fields. *Radio Engineering and Electronics*, 1991, Vol. 36, No.11, pp. 2240-2242.
- 6 Potapov A. A., Kolesnikov A. I. Correlation characteristics of ground surface images. *Radio engineering and electronics*. 1993 Vol. 38, No. 7, pp. 1270 – 1279.

- 7 Potapov A.A., Kolesnikov A.I. Spectral characteristics of ground surface images. *Radio engineering and electronics*. 1993 Vol. 38, No. 10, pp. 1851 – 1852.
- 8 Paveliev V. A., Potapov A. A. The effect of the ground surface on the structure of a pulsed signal in the range of millimeter waves. *Radio engineering and electronics*. 1994 Vol. 39, No. 4, pp. 573 – 582.
- 9 Potapov A. A. A generalized correlator of fields scattered by rough surfaces. *Radio engineering and electronics*. 1996 Vol. 41, No. 7, pp. 816 – 823.
- 10 Potapov A. A., Sokolov A. V. Frequency coherence function of the wave field scattered by a rough surface with a large Rayleigh parameter. *Radio engineering and electronics*. 1996 Vol. 41, No. 9, pp. 1071-1076.
- 11 Potapov A. A., German V. A. Application of fractal methods for processing optical and radar images of the ground surface. *Radio engineering and electronics*. 2000, Vol. 45, No.8, pp. 946 – 953.
- 12 Potapov A. A. Fractals in radio physics and radiolocation. Elements of the fractal theory. *Radio engineering and electronics*. 2000, Vol. 45, No. 11, pp. 1285 – 1292.
- 13 Opalenov Yu. V., Potapov A. A. Stochastic signals and the Radon transformation at raster radar imaging by a microwave digital radar with fractal information processing. *Radio engineering and electronics*. 2000, Vol. 45, No. 12, pp. 1447 – 1458.
- 14 Potapov A. A. Fractals in radio physics and radiolocation. Fractal signal analysis. *Radio engineering and electronics*. 2001 Vol. 46, No. 3, pp. 261-270.
- 15 Potapov A. A., German V. A. Effects of deterministic chaos and a strange attractor at radiolocation of a dynamic system of vegetation cover type. *Letters to the Technical Physics Journal*, 2002, Vol. 28, No.14, pp. 19 – 25.
- 16 Potapov A. A. Fractals in radio physics and radiolocation. Fundamentals of the theory of wave scattering by fractal surface. *Radio engineering and electronics*. 2002 Vol. 47, No. 5, pp. 517 – 544.
- 17 Potapov A. A. New information technologies based on probabilistic textural and fractal features in radar detection of low contrast targets. *Radio engineering and electronics*. 2003 Vol. 48, No. 9, pp. 1101-1119.
- 18 Potapov A. A., German V. A. On the methods for measuring fractal dimension and fractal signatures of multidimensional stochastic signals. *Radio engineering and electronics*. 2004 Vol. 49, No. 12, pp. 1468 -1491.
- 19 Potapov A. A., Bulavkin V. V., German V. A., Vyacheslavova O. F. Investigation of a processed surface microrelief using fractal signature methods. *Journal of Technical Physics*, 2005, Vol. 75, No. 5, pp.28 – 45.
- 20 Gulyaev Yu. V., Nikitov S. A., Potapov A. A., Davydov A. G. On the development of fractal radio systems. Numerical analysis of electrodynamic properties of Sierpinski fractal antenna. *Radio engineering and electronics*. 2005 Vol. 50, No. 9, pp. 1070-1076 .
- 21 Gulyaev Yu. V., Nikitov S. A., Potapov A. A., German V. A. Ideas of scaling and fractional dimension in the scheme of the fractal radio signal detector. *Radio engineering and electronics*. 2006 Vol. 51, No. 8, pp. 968-975.
- 22 Potapov A. A., German V. A. Methods for fractal processing of weak signals and low contrast images. *Autometry*, 2006, Vol. 42, No. 5, pp. 3-25.
- 23 Potapov A. A., Potapov A. A. (jun.), Potapov V. A. Fractal capacitor, fractional operators and fractal impedances. *Nonlinear World*, 2006, Vol. 4, No, 4-5, pp. 172-187.
- 24 Potapov A. A. On the theory of functionals of stochastic backscatter fields. *Radio engineering and electronics*. 2007 Vol. 52, No. 3, pp. 261-310.
- 25 Potapov A. A., Gilmutdinov A. Kh., Ushakov P. A. System principles and the element base of fractal radioelectronics. Part I. Stages of formation and state. *Radio engineering and electronics*. 2008 Vol. 53, No. 9, pp. 1033-1080.
- 26 Potapov A. A., Gilmutdinov A. Kh., Ushakov P. A. Systemic principles and element base of fractal radio electronics. Part II. Synthesis methods, models and prospects of application. *Radio engineering and electronics*. 2008 Vol. 53, No.11, pp. 1347-1394.
- 27 Bogolyubov A.N., Potapov A.A., Rekhviashvili S. Sh. A method for introducing fractional integrodifferentiation in classical electrodynamics. *Bulletin of Moscow University. Ser. 3. Physics. Astronomy*, 2009, No. 4, pp. 9-12.
- 28 Bogolyubov A. N., Potapov A. A., Rekhviashvili S. Sh. Interpretation of the diffusion wave equation solution using fractional integro-differentiation. *Bulletin of Moscow University. Ser. 3. Physics. Astronomy*, 2010, No. 3, pp. 54-55.
- 29 Potapov A. A., Matveev E. N. Fractal electrodynamics, scaling of fractal antennas based on ring structures and multi-scale frequency-selective 3D media or fractal “sandwiches”: transition to fractal nanostructures. *Radio engineering and electronics*. 2010 Vol. 55, No.10, pp. 1157-1177.
- 30 Gulyaev Yu. V., Panasenko S. V., Potapov A. A., Chernogor L. F. Optimal detection and optimal parameterization of the envelope soliton. *Reports of the Academy of Sciences*, 2011, Vol. 436, No. 5, pp. 606-610.
- 31 Rekhviashvili S. Sh., Potapov A. A. A memristor and the integral quantum Hall effect. *Radio engineering and electronics*. 2012 Vol. 57, No.2, pp. 207-210.

32 Panasenko S. V., Potapov A. A., Chernogor L. F. Results of the application of algorithms of the optimal detection and estimation theory for the envelope soliton analysis. *Radio engineering and electronics*. 2012 Vol. 57, No.3, pp. 330-338.

33 Potapov A. A. The fractal method, fractal paradigm and the method of fractional derivatives in natural science. *Bulletin of N. I. Lobachevsky Nizhny Novgorod University. Series: Mathematical Modeling. Optimal control*. 2012, No. 5(2), pp. 172-180.

34 Malyshev K. V., Potapov A. A., Chernyshev S. L. Shaped superlattices in the classical problem of signal filtering against the background noise based on a meshed nonlinear network. *Radio engineering and electronics*. 2013, Vol. 58, No.4, pp. 367-374.

35 Potapov A. A., Shifrin Ya. S., Kuzeev R. R. Genetic and self-affinity methods for fractal antennas development. *Antennas*, 2014, No. 3 (202), pp. 25-48.

36 Leonov K. N., Potapov A. A., Ushakov P. A. Applying invariant properties of chaotic signals in the synthesis of new noise-resistant broadband information transmission systems. *Radio engineering and electronics*. 2014, Vol. 59, No.12, pp. 1209-1229.

37 Potapov A. A. The origins of fractal-scaling or scale-invariant radiolocation (1980-2015). *Radio Engineering*, 2015, No. 8, pp. 95-108.

38 Potapov A. A., Laktyunkin A. V. Frequency coherence function of spatial temporal radar channel of imaging of anisotropic fractal surface and fractal objects. *Radio engineering and electronics*. 2015, Vol. 60, No.9, pp. 906-913.

39 Potapov A. A. Fractal and topological sustainable methods of overcoming expected uncertainty in the radiolocation of low-contrast targets and in the processing of weak multi-dimensional signals on the background of high-intensity noise: A new direction in the statistical decision theory. *IOP Conf. Ser.: J. Physics*, 2017, Vol. 918, No 012015, 19 p.

40 Potapov A.A. On strategic trends in the synthesis of new types of radar textural and fractal detectors of low contrast objects with the extracting their contours and the localization of coordinates against the heavy clutter background from the surface of the ground, sea and precipitation. *Proc. IV All-Russian STC "RTI Systems of ASD-2016"*, Moscow, N.E. Bauman MSTU Publishing House, 2017, pp. 438-448.

41 Potapov A. A., Potapov Alexey A., Potapov V. A. Fractal Radioelement's, Devices and Fractal Systems for Radar and Telecommunications. *Proc. 14th Sino - Russia Symposium on Advanced Materials and Technologies. Ed. Mingxing Jia. Beijing: Metallurgical Industry Press*, 2017, pp. 499 – 506.

42 Potapov A. A. Textural and fractal-scaling methods for detecting, processing and identification of weak radar signals and low-contrast images against the heavy clutter background. *Bulletin of aerospace defense*, 2018, No. 2 (18), pp. 15-26.

43 Potapov, A. A. Fractals, Scaling, Textures, Fractional Operators and Deterministic Chaos as the Physical and Mathematical Components of the New Conceptions and Methods in Radar and Radio Physics. *Proc. IET Int. Radar Conf. 2018 (China, Nanjing, 17-19 October, 2018). Beijing: The Institution of Engineering and Technology (IET)*, 2018, No F0275, 6 p.

44 Potapov A. A. Waves in disordered large fractal systems: radiolocation, nanosystems, clusters of unmanned aerial vehicles and small spacecraft. *Radio engineering and electronics*. 2018, Vol. 63, No.9, pp. 915-934.

45 Bagmanov V. Kh., Potapov A. A., Sultanov A. Kh., Wei Zhang. Fractal filters for signal detection in the processing of remote sounding data. *Radio engineering and electronics*. 2018, Vol. 63, No.10, pp. 1062-1068.

46 Potapov A. A. Fractal-scaling or scale-invariant radiolocation and fractal signal and image processing. *Collection of scientific papers on the 65th anniversary of the foundation of V. A. Kotelnikov IRTE of the RAS and the 110th anniversary of the birth of Academician V. A. Kotelnikov*. Moscow, V.A.Kotelnikov IRTE of the RAS, 2018, pp. 99-104.

47 Potapov A. A. Wave scattering on a stochastic fractal surface. *Collection of scientific papers on the 65th anniversary of the foundation of V. A. Kotelnikov IRTE of the RAS and the 110th anniversary of the birth of Academician V. A. Kotelnikov*. Moscow, V.A. Kotelnikov IRTE of the RAS, 2018, pp. 155-159.

48 Potapov A.A. Fractal electrodynamics. Numerical simulation of small fractal antenna devices and fractal 3D microstrip resonators for modern ultra-wideband or multi-band radio engineering systems. *Radio engineering and electronics*. 2019, Vol. 64, No. 7, pp. 735.

49 Gulyaev Yu.V., Potapov A.A. Application of the theory of fractals, fractional operators, textures, scaling effects and nonlinear dynamics methods in the synthesis of new information technologies for the tasks of radio electronics (in particular, radiolocation). *Radio engineering and electronics*. 2019, Vol. 64, No.8, pp. (in the press)

50 Professor Alexander Alekseevich Potapov. Biography and Bibliography reference. Ed. by Academician Yu. V. Gulyaev. Moscow, 2019, 169 p.

SUMMARIES

ТҮСІНІКТЕМЕЛЕР

АННОТАЦИИ

Рягузов А.П., Кудабаяева М.А., Гусейнов Н.Р., Немкаева Р.Р., Мырзабекова М.М.

Кремний оксидімен модификацияланған аморфты көміртекті қабыршақтарының құрылымын зерттеу.

Бұл жұмыста магнетронды ионды-плазмалық тозаңдату әдісімен аргон атмосферасында аралас нысанада алынған кремний оксидімен ($a-C_{1-x}:(SiO)_x$) модификацияланған аморфты көміртекті қабыршақтар қарастырылған. Қабыршақ бетінің топографиясы мен фазалық контрасты атомдық-күштік микроскопта зерттелді. Локалдық құрылымы Рамандық спектроскопиямен зерттелді. Кремний концентрациясының артуы фотолуминесценцияның өсуіне әкелетіні көрсетілген. $a-C_{1-x}:(SiO)_x$ қабыршақтарында көміртегі гибридіті sp^3 байланыстарының артуынан G пиктің төмен жиілікті аймаққа ығысуы анықталған.

Рягузов А.П., Кудабаяева М.А., Гусейнов Н.Р., Немкаева Р.Р., Мырзабекова М.М.

Исследование структуры пленок аморфного углерода, модифицированных оксидом кремния.

В данной работе рассматриваются пленки аморфного углерода, модифицированные оксидом кремния ($a-C_{1-x}:(SiO)_x$), полученные методом магнетронного ионно-плазменного со-распыления комбинированной мишени в атмосфере аргона. Исследованы топография и фазовый контраст поверхности пленок методом атомно-силовой микроскопии. Изучена локальная структура методом рамановской спектроскопии. Показано, что увеличение концентрации кремния приводит к росту фотолуминесценции. Смещение G пика в низкочастотную область в пленках $a-C_{1-x}:(SiO)_x$ указывает на увеличение sp^3 гибридизации связей углерода.

Астанов С.Х., Шарипов М.З., Касимова Г.К.

Рибофлавин ерітіндісіндегі гипохромдық әсер.

Еріткіштердің сулы және бинарлы қоспаларында рибофлавин молекулаларының өздігінен жиналу процесі спектроскопиялық әдіспен зерттелді. В2 витамин молекулаларының өздігінен жиналу Ван-дер-Ваальс күштерінің диполь-дипольдық өзара әрекеттесуімен жүретіні, нәтижесінде рибофлавин молекулаларының қозған электрондық деңгейлерінің резонанстық ыдырауы байқалатыны көрсетілген. Қойылтылған ерітінділерде және еріткіштердің бинарлы қоспаларында байқалатын гипохромдық әсерлер рибофлавиннің өзі агрегацияланған молекулаларының олардың мономерлеріне қатысты жұтылу қабілетінің азаюына байланысты. Рибофлавиннің өздігінен агрегацияланған молекулаларын жұтылу жолағы ламинарлы гидродинамикалық ағында алынған сызықтық дихроизм спектрімен анықталған.

Астанов С.Х., Шарипов М.З., Касимова Г.К.

Гипохромный эффект в растворах рибофлавина.

Спектроскопическим методом исследован процесс самосборки молекул рибофлавина в водных и бинарных смесях растворителей. Показано, что самосборка молекул витамина В₂ происходит диполь-дипольным взаимодействием Ван-дер-Ваальсовых сил в результате которого происходит резонансное расщепление возбужденных электронных уровней молекул рибофлавина. В концентрированных растворах и в бинарных смесях растворителей наблюдаемые гипохромные эффекты обусловлены уменьшением интенсивности поглощательной способности самоагрегированных молекул рибофлавина по отношению их мономеров. Полоса поглощения самоагрегированных молекул рибофлавина определены полученными спектрами линейного дихроизма в ламинарном гидродинамическом потоке.

Юров В.М., Балтабеков А.С., Лауринас В.Ч., Гученко С.А.

Сегнетоэлектрлік кристалдардың өлшемдік эффектілері және беттік энергиясы.

Беттік керілуді сипаттау үшін бетінің кедір-бұдырлығын ескермей, атомдық тегіс сегнетоэлектриктердің беттік қабатының моделі қарастырылған. Конденсирленген ортаның нанокұрылымдық қасиеттерін анықтаудағы қажетті шарт оның қасиеттерінің өлшемге тәуелділігі болып саналады. Атомдық тегіс кристалдың беткі қабаты $d(I)$ және $d(II)$ екі қабаттан тұрады. Қалыңдығы $h = d$ болатын қабат - атомды тегіс кристалдың (I) қабаты, ал $h \approx 10d$ қабаты - (II) қабат деп аталады. $h \approx 10d$ кезінде материалдың физикалық қасиеттерінің өлшемге тәуелділігі байқала бастайды. $h = d$ болғанда беттік қабатта фазалық ауысу жүреді. Ол физикалық қасиеттердің күрт өзгеруімен қатар жүреді, мысалы Холлдың тура әсері кері түріне өзгереді. Конденсирленген ортаның (металдар, диэлектриктер, сегнетоэлектриктер және т.б.) бетін зерттеудің бұрынғы және заманауи нәтижелері өлшемдік әсермен және олардың соңғы құрылымдарымен шартталған деген қорытынды жасауға болады.

Юров В.М., Балтабеков А.С., Лауринас В.Ч., Гученко С.А.

Размерные эффекты и поверхностная энергия сегнетоэлектрических кристаллов.

Для описания поверхностного натяжения рассмотрена модель поверхностного слоя атомарно-гладких сегнетоэлектриков, пренебрегая шероховатостью поверхности. Считается, что необходимым условием для проявления наноструктурных свойств конденсированной среды является размерная зависимость ее свойств.

Поверхностный слой атомарно-гладкого кристалла состоит из двух слоев – d(I) и d(II). Слой толщиной $h=d$ назван слоем (I), а слой при $h \approx 10d$ – слоем (II) атомарно-гладкого кристалла. При $h \approx 10d$ начинает проявляться размерная зависимость физических свойств материала. При $h=d$ в поверхностном слое происходит фазовый переход. Он сопровождается резкими изменениями физических свойств, например, прямой эффект Холла-Петча меняется на обратный. Можно заключить вывод, что и прежние и современные результаты исследований поверхности конденсированных сред (металлов, диэлектриков, сегнетоэлектриков и т.д.) обусловлены размерными эффектами и конечными структурами их существования.

Саулебеков А.О., Венос Д., Камбарова Ж.Т., Саулебекова Д.А., Васильева К.И., Сейдуалы Х.Б.

Біртекті емес электрстатикалық өріс негізінде зарядталған бөлшектердің энергия талдағышын құру.

Гиперболалық заң бойынша кемитін біртекті емес электрстатикалық өріс негізіндегі айналы энергия талдағыштың электрондық-оптикалық сипаттамалары зерттелген. Жұмыста айналы шағылу режимінде жұмыс істейтін электрстатикалық өрісте зарядталған бөлшектердің траекториясын есептеудің жуық-аналитикалық әдісі қолданылды. Интегралдифференциалды түрде зарядталған бөлшектердің қозғалыс теңдеуі алынды. Біртекті емес өрісі бар талдағыштың ең оптималды нұсқасының сұлбасы анықталды.

Саулебеков А.О., Венос Д., Камбарова Ж.Т., Саулебекова Д.А., Васильева К.И., Сейдуалы Х.Б.

Разработка энергоанализатора заряженных частиц на основе неоднородного электростатического поля.

Исследованы электронно-оптические характеристики зеркального энергоанализатора на основе неоднородного, спадающего по гиперболическому закону, электростатического поля. В работе применялся приближенно-аналитический метод расчета траектории заряженных частиц в электростатическом поле, действующем в режиме зеркального отражения. Получено уравнение движения заряженных частиц в интегралдифференциальной форме. Найдена схема наиболее оптимального варианта анализатора с неоднородным полем.

Көмеков С.Е., Саитова Н.К.

Көміртегі нанокұрылымдардың фотолюминесценциясында антистокс қанатының диффузды спектрлері.

Мақалада толқын ұзындығы қоздыратын жарық толқын ұзындығынан қысқа болатын фотолюминесценттік сәулелену - анти-Стокс деп аталатын сәулелену зерттеледі. Фотолюминесценцияның бұл ерекшеліктері құрамында көміртегі бар аморфты сутектендірілген көміртегі α -C: N және табиғи биополимер-коллаген сияқты заттарда бұрын байқалды. Бұл объектілерді біріктіретін ортақ құрылымдық қасиет – құрамында көміртегілік алтыбұрыштардың - бензол сақинасы ядросының болуы. Құрамында көміртегі бар нанокұрылымдардағы фотолюминесценцияның димер-эксимерлік моделі спектрдің анти-стокс қанатын түсіндіру үшін жасалған. Құрамында көміртегі бар объектілерде термиялық белсендірілген алдын-ала қоздырылған күйлерді үлестіру функциясының температуралық тәуелділігі анықталды. Анти-стокс қанатының қарқындылығының спектрлік тәуелділіктері эксимер шұңқырлардағы күйлердің тығыздығын ескеруімен есептелген.

Күмеков С.Е., Саитова Н.К.

Диффузные спектры антистоксова крыла фотолюминесценции в углеродных наноструктурах.

В статье исследуется фотолюминесцентное излучение с длиной волны, меньшей длины волны возбуждающего света, которую обычно называют антистоксовой. Эти особенности фотолюминесценции ранее наблюдались в таких углеродсодержащих объектах, как аморфный гидрогенизированный углерод α -C: N и нативный биополимер-коллаген. Общим структурным свойством этих объектов является наличие углеродных гексагонов – ядер бензольного кольца. Димер-эксимерная модель фотолюминесценции в углеродных наноструктурах была разработана для объяснения антистоксового крыла спектров. Определены температурные зависимости функции распределения термически активированных предварительно возбужденных состояний в углеродсодержащих объектах. Рассчитаны спектральные зависимости интенсивности антистоксова крыла с учетом плотности состояний в эксимерной яме.

Шарипов М.З., Миржоновна Н.Н., Найитов Д.Е.

FeVO₃ монокристаллының домендік құрылымына біртекті радиалды-бағытталған механикалық кернеулердің әсері.

Магнитооптикалық әдіспен FeVO₃ монокристаллының домендік құрылымына біртекті радиалды бағытталған механикалық кернеулердің әсері зерттелді. Бұл жағдайда сығу күшінің бағыты бойымен FeVO₃ базистік жазықтығына әсер ететін магнит өрісінде кристалдағы магнителу процесінің нәтижесінде сына тәрізді домендер жүйесі пайда болады, олар температурадан тәуелді H_c шамаларының H_0 диапазонындағы өрістер интервалында бар болады. Алынған нәтижелер домендік құрылымның термодинамикалық теориясы аясында жүргізілді. Қолданылатын теориялық модель экспериментте байқалатын d шамасының салыстырмалы өзгеруін магнит өріс пен температураға байланысты сипаттауға жақсы мүмкіндік беретіні көрсетілген.

Шарипов М.З., Миржоновна Н.Н., Найитов Д.Е.

Влияние неоднородных радиально-направленных механических напряжений на доменную структуру монокристалла FeVO_3 .

Магнитооптическим методом исследовано влияние неоднородных радиально направленных механических напряжений на доменную структуру монокристалла FeVO_3 . Обнаружено, что в магнитном поле, приложенном в базисной плоскости FeVO_3 вдоль направления сжимающей силы, в процессе намагничивания в кристалле возникает система клиновидных доменов, существующая в некотором зависящем от температуры интервале полей в диапазоне H_0 величин H_c . Обсуждение полученных результатов проведено в рамках термодинамической теории доменной структуры. Показано, что используемая теоретическая модель хорошо позволяет описать экспериментально наблюдаемое относительное изменение величины d в зависимости от магнитного поля и температуры.

Жумабеков А.Ж., Селиверстова Е.В., Ибраев Н.Х.

TiO_2 -GO нанокompозитінің фотокаталитикалық белсенділігін зерттеу.

Гидротермальдік әдістің көмегімен графен оксиді және TiO_2 негізінде нанокompозит синтезделген. Нанокompозиттің құрылуы Раман-спектроскопия мәліметтерімен дәлелденген. Раман-спектрлерінде графен оксиді мен TiO_2 –нің сипаттамалық максимумдары тіркелді. ЭДС талдау мәліметтері нанокompозитте титан, көміртек және оттегінің бар болуын көрсетті. TiO_2 -GO нанокompозитінің беттік меншікті ауданы TiO_2 –мен салыстырғанда 1,16 есе үлкен. Әр түрлі рН деңгейлі электролиттерде синтезделген материалдың фотокаталитикалық белсенділігінің зерттеуі жүргізілген. TiO_2 -GO-да фототоқтың генерациясы электролитке тәуелді болатыны және NaOH, KOH және Na_2SO_4 -де таза TiO_2 қабыршақтарымен салыстырғанда сәйкесінше 2,9, 1,3 және 1,05 есе артатындығы көрсетілген.

Жумабеков А.Ж., Селиверстова Е.В., Ибраев Н.Х.

Исследование фотокаталитической активности нанокompозита TiO_2 -GO.

Гидротермальным методом синтезирован нанокompозит на основе оксида графена и TiO_2 . Образование нанокompозита было подтверждено данными Раман-спектроскопии. В Раман-спектрах зарегистрированы характерные пики оксида графена и TiO_2 . ЭДС анализ показал присутствие титана, углерода и кислорода в нанокompозите. Удельная площадь поверхности нанокompозита TiO_2 -GO в 1,16 раз больше, чем для TiO_2 . Проведено исследование фотокаталитической активности синтезированного материала в электролитах с различным уровнем pH. Показано, что генерация фототока в TiO_2 -GO зависит от электролита и возрастает в 2,9, 1,3 и 1,05 раза в NaOH, KOH и Na_2SO_4 , соответственно, по сравнению с пленками чистого TiO_2 .

Агельменев М.Е.

Сұйық кристалдардағы молекулааралық өзараәрекеттесулер.

Сұйық кристалдардың мезофазасындағы бағдарлы реттілікті жүзеге асырудың ықтималды механизмдеріне талдау жүргізілген. Құрылымдағы бензол сақиналар мезофазаның бар болуында негізгі рөл атқаратыны көрсетілді. Бензол сақиналардағы сақиналық тоқпен шартталған Фан-Флековский парамагнетизмі мұндай реттіліктің бір себебі болуы мүмкін. Бұл магнит өрісінің әсері кезіндегі сұйық кристалдарда реттіліктің жоғары дәрежесін түсіндіре алады. Осымен байланысты стайкинг жағдайында молекулааралық өзараәрекеттесу магниттік құраушыға ие болуы мүмкін. Сұйық кристалды молекулалар ансамблінің тәртібін модельдеу кезінде молекулааралық өзараәрекеттесудің мүмкін болатын потенциалдың түрі ұсынылды. Сұйық кристалдар молекулаларының реттілігінің табиғаты әр түрлі табиғатқа ие, бірақ бір реттілік шамасы бойынша молекулааралық өзара әрекеттесулермен анықталатындығы көрсетілді.

Агельменев М.Е.

Межмолекулярные взаимодействия в жидких кристаллах.

Проведен анализ возможных механизмов осуществления ориентационной упорядоченности в мезофазе жидких кристаллов. Показано, что бензольные кольца в структуре играют основную роль в существовании мезофазы. Фан-Флековский парамагнетизм, обусловленный кольцевыми токами в бензольных кольцах, по-видимому, является одной из причин такой упорядоченности. По-видимому, это объясняет высокую степень упорядоченности жидких кристаллов при воздействии магнитного поля. В связи с этим, межмолекулярное взаимодействие в случае стайкинга может иметь и магнитную составляющую. Предложен вид возможного потенциала межмолекулярного взаимодействия при проведении моделирования поведения ансамбля жидкокристаллических молекул. Показано, что природа упорядоченности молекул жидких кристаллов определяется межмолекулярными взаимодействиями различной природы, но по величине одного порядка.

Завгородний А.В., Аймуханов А.К., Зейниденов А.К., Аюбекова А.Е.

Магнит өрісінің CuPc нанокұрылымының вольтамперлік сипаттамаларына әсері.

Жұмыста нанокұрылымды мыс фталоцианинінде (CuPc) заряд тасымалдағыштарды тасымалдау процесінде

спин күйлерінің ролін зерттеу нәтижелері ұсынылған. Термиялық тозаңдану әдісімен алынған қабықша α -фаза құрылысына ие екендігі және CuPc нанотаспалары n -фазасында орналасатындығы көрсетілген. CuPc нанокұрылымының вольт-амперлік сипаттамаларына (ВАХ) сыртқы магнит өрісінің әсері зерттелді. Магнит өрісіне енгізу кезінде қысқа тұйықталу тоқ мәнінің азаюы биполяронның пайда болу процесінде полярондардың «спинді бұғаттау» механизмімен байланысты болатыны көрсетілген. Нанотаспаларда «спинді бұғаттаудың» әсері күштірек байқалатыны көрсетілген.

Завгородний А.В., Аймуханов А.К., Зейниденов А.К., Аюбекова А.Е.

Влияние магнитного поля на вольтамперные характеристики наноструктур CuPc.

В работе представлены результаты исследования роли спиновых состояний в процессе переноса носителей заряда в наноструктурах фталоцианина меди (CuPc). Показано, что пленка, полученная методом термического напыления, имеет структуру α -фазы, наноленты CuPc находятся в η -фазе. Исследовано влияние внешнего магнитного поля на вольтамперные характеристики (ВАХ) наноструктур CuPc. Показано, что уменьшение значения тока короткого замыкания при наложении внешнего магнитного поля связано с механизмом «спиновой блокировки» полярон в процессе образования биполярона. Показано, что в нанолентах эффект «спиновой блокировки» проявляется сильнее.

Копбалина К.Б., Маженов Н.А., Бимбетова Г.М.

Мультимолекулярная кабықшақтардың құрылымы мен электронды өтулерді кванттық-химиялық есептеу.

Флуоресценцияның динамикалық және статикалық өшулері оттегі молекулаларымен өзара әрекеттесуі кезінде жүретіндігі белгілі. Оттегі мен антрацен кешенінің ең қарапайым үлгілерінен - оттегінің бір молекуласынан және антрацен молекуласының құрылатын кешен ұсынылады. Кванттық-химиялық есептеулер Gaussian 98 бағдарламалық пакетінің көмегімен жүргізілген. Антрацен мен оттегі молекулаларының кешені үшін негізгі электрондық күйдің тепе-тең геометриясы алынды. Берілген кешен үшін электрондық жұтылу спектрі есептелген. Антрацен мен оттегінің бұл кешені – фотоорнықты емес екендігі анықталған.

Копбалина К.Б., Маженов Н.А., Бимбетова Г.М.

Квантово-химические расчеты структуры и электронных переходов мультимолекулярных пленок.

Динамическое и статическое тушения флуоресценции происходит при контакте взаимодействия молекул кислорода. Из наиболее простых моделей комплекса кислорода и антрацена предлагается комплекс, состоящий из одной молекулы кислорода и антрацена. Квантово-химические расчеты выполнены с помощью программного пакета Gaussian 98. Получена равновесная геометрия основного электронного состояния для комплекса молекул кислорода с антрацена. Рассчитан электронный спектр поглощения для данного комплекса. Установлено, данный комплекс кислорода с антраценом не фотоустойчив.

Нариманов Р.К., Нариманова Г.Н.

Сфераны орап ағып өту есебін шешуде толық көп торлы әдісті қолдану.

Тұтқырлы ағыстың сфераны орап ағып өтудің классикалық есебінің сандық шешімі мысалында тура есептеумен салыстырғанда көп торлы әдісті қолдану тиімділігін анықтау жүргізілді. Әр түрлі айырымдық сұлбалар қарастырылды. Құйын теңдеуі үшін тордан торға өту үшін 9 нүктелі үлгіні пайдалану қажеттілігі көрсетілген. Рейнольдстің әр түрлі сандары үшін үйкеліс кедергісінің коэффициенті есептелген. Көп торлы әдісті пайдалану кезінде Рейнольдс санына шектеу қою қажеттілігі ескерілген.

Нариманов Р.К., Нариманова Г.Н.

Применение полного многосеточного метода при решении задачи обтекания сферы.

На примере численного решения классической задачи обтекания сферы вязким потоком проведено определение эффективности применения многосеточного метода по сравнению с прямым расчетом. Рассмотрены различные разностные схемы. Показано, что для перехода от сетки к сетке для уравнения вихря необходимо использовать 9-точечный шаблон. Для различных чисел Рейнольдса был рассчитан коэффициент сопротивления трению. Отмечено ограничение на число Рейнольдса при использовании многосеточного метода.

Сабденов К.О., Сакипов К.Е.

Жылу желілер қабырғалары мен құбырларынан қоршаған ортаға жылу беру коэффициентін есептеу.

Цилиндрлік беттерден жылу беру коэффициентін анықтаудың қарапайым жартылай аналитикалық тәсілі ұсынылады. Тәсіл идеясы жылу толқыны және процестің автотомельдік сипаты туралы түсінігіне негізделген, бұл өз кезекте аналитикалық формуланы алуға мүмкіндік береді. Жылу беру коэффициентінің төмендеуіне физикалық түсінік берілді. Жылу тарату туралы есептің сандық шешімі мен жуықталған шешімді салыстыруымен аналитикалық формуланың жоғары дәлдігі көрсетілген. Жоғары дәлдікпен көп уақытта құбырдан қоршаған суық кеңістікке жылу тарату автотомельді процесс деп санауға болады.

Сабденов К.О., Сакипов К.Е.

Расчет коэффициента теплоотдачи от стен и труб тепловых сетей в окружающую среду.

Предлагается простой полуаналитический способ определения коэффициента теплоотдачи от цилиндрических поверхностей. Идея способа основана на представлении о тепловой волне и автомодельном характере процесса, что позволяет получить аналитическую формулу. Дано физическое объяснение снижения коэффициента теплоотдачи. Сравнением приближенного решения с численным решением задачи о распространении тепла показана высокая точность аналитической формулы. Распространение тепла от трубы в холодное окружающее пространство при больших временах с высокой точностью можно считать автомодельным процессом.

Ершина А.К., Ершин Ш.А.

Екі роторлы Бидарье-2 атты жел энергетикалық құрылғысының жоғары тиімділігі туралы.

Мақалада аномальдық жоғары пайдалы әсер коэффициентіне ие Бидарье-2 жел генераторының конструкциялық ерекшеліктері қарастырылған. Бидарье-2 жел турбинасының НВІ роторының негізгі конструкциясы көрсетілген. Екі роторға ие Бидарье-2 жел турбинасының конструкциясы қазіргі заманғы жел қондырғыларымен салыстырғанда әлдеқайда жоғары тиімділікке ие. Бидарье-2 жел турбинасының қуатын есептеу кезінде жел қозғалтқыштың айналу моменті ескерілген. Бидарье-2 жел қозғалтқыштың көмегімен жел энергиясын пайдалы энергияға айналдыру мүмкіндігін зерттеу нәтижелері оның бірегейлігін дәлелдеді.

Ершина А.К., Ершин Ш.А.

О высокой эффективности двухроторного ветроэнергетического устройства Бидарье-2.

В статье рассматриваются конструктивные особенности ветрогенератора Бидарье-2 с аномально высоким коэффициентом полезного действия. Показана базовая конструкция ротора НВІ ветротурбины Бидарье-2. Благодаря конструкции с двумя роторами ветротурбина Бидарье-2 обладает гораздо большей эффективностью, чем все современные ветроэнергетические устройства. При расчете мощности Бидарье-2 учитывался момент вращения ветродвигателя. Изучение возможности преобразования ветровой энергии в полезную с помощью ветродвигателя Бидарье-2, подтверждают его уникальность.

Сакипова С.Е., Танашева Н.К.

Айналмалы цилиндрлерден құрылатын желтурбинаның аэродинамикасын модельдеу.

Жұмыс Қазақстандағы баламалы энергетиканың, оның ішінде жел энергетикасының дамыту келешектеріне арналған. Мақалада ANSYS FLUENT бағдарламалық кешенінде үш қалақшалы жел турбинасының орап ағып өту аэродинамикасына компьютерлік модельдеуді қолдану мүмкіндіктері қарастырылған. Өсьтік симметриялық жағдайда есепті шешу үшін бастапқы теңдеулер жүйесі және шекаралық шарттар келтірілген. ANSYS MESH бағдарламасының көмегімен есептелінетін доменді және жел турбинасының үш-өлшемді CAD-моделін құру нәтижелері көрсетілген. Ағынның әр түрлі жылдамдықтары кезінде желтурбинаның виртуалды моделі үшін маңдайлық кедергінің аэродинамикалық күшінің сандық мәндеріне талдау жүргізілді.

Сакипова С.Е., Танашева Н.К.

Моделирование аэродинамики ветротурбины с вращающимися цилиндрами.

Работа посвящена перспективам развития альтернативной энергетики в Казахстане, в частности, ветроэнергетики. В статье обсуждаются возможности применения компьютерного моделирования аэродинамики обтекания трехлопастной ветротурбины в программном комплексе ANSYS FLUENT. Приведена система исходных уравнений и граничные условия для решения задачи в осесимметричной постановке. Показаны результаты построения расчетного домена и 3-х мерной сеточной CAD-модели ветротурбины с использованием подпрограммы ANSYS MESH. Проведен анализ численных значений аэродинамической силы лобового сопротивления для виртуальной модели ветротурбины при различных скоростях потока.

Мерзадинова Г.Т., Сакипов К.Е., Шарифов Д.М., Мирзо А., Бекешев А.З.

Материалдардың жылу өткізгіштігі мен температура өткізгіштік коэффициенттерін анықтауға арналған лазерлік фотоакустикалық әдіс.

Мақалада материалдардың термофизикалық қасиеттерін анықтау үшін микрофонды детектрлеу сұлбасына ие лазерлік фотоакустикалық әдісінің зерттеу нәтижелері келтірілген. Материалдардың термофизикалық қасиеттерін анықтаудың лазерлік фотоакустикалық әдісінің басқа қолданыстағы әдістерді толықтыратындығы көрсетілген. Розенцвейг-Гершо іргелі теориясына негізделген фотоакустикалық әдісті қолданудың сипатты ерекшеліктері қарастырылды. Бір өлшемді және үш қабатты фотоакустикалық ұяшықта қатты күйдегі материалдардың температура өткізгіштік коэффициентін анықтау есебінің математикалық моделі құрастырылды. Ұсынылған фотоакустикалық әдісті құрылымдары біркелкі емес, көп қабатты, композициялық, ұнтақтәрізді, наноматериалдар және басқа құрылымдары күрделі болатын материалдардың қасиеттерін зерттеуге тиімді қолданылуы мүмкін.

Мерзадинова Г.Т., Сакинов К.Е., Шарифов Д.М., Мирзо А., Бекешев А.З.

Лазерный фотоакустический метод для определения коэффициентов теплопроводности и температуропроводности материалов.

В статье приведены результаты исследований лазерного фотоакустического метода для определения теплофизических свойств материалов с микрофонной схемой детектирования. Было показано, что фотоакустический метод определения теплофизических свойств материалов дополняет другие существующие методы. Рассмотрены характерные особенности применения фотоакустического метода, основанного на фундаментальной теории Розенцвейга-Гершо. Разработана математическая модель задачи определения температуропроводности твердотельных материалов в одномерной и трехслойной фотоакустической ячейке. Предложенный фотоакустический метод может быть успешно применен для исследования сложных по структуре материалов, таких как структурно-неоднородные, многослойные, композиционные, порошкообразные, наноматериалы и др.

Юров В.М., Олешко В.С.

Машиналардың металл бөлшектерінің контактілік потенциалдар айырмасына қоршаған ортаның әсері.

Берілген жұмыста машиналардың металл бөлшектерінің электронының шығу жұмысы мен контактілік потенциалдар айырмасына қоршаған ортаның әсері қарастырылған. Кельвин-Зисман әдісімен Al, Ti және Ni үлгілеріндегі контактілік потенциалдар айырмасын әр түрлі температура, қысым және ауаның салыстырмалы ылғалдылығы, сондай-ақ қоршаған ортаның тепе-тең емес және тепе-тең жағдайларында өлшеуді қамтитын тәжірибелік зерттеулер жүргізілді. Контакттік потенциалдар айырмасын өлшеу «Поверхность-11» құрылғысында жүргізілді. Атмосфералық параметрлер НАМА EWS-800 сандық метеорологиялық станциясы көмегімен өлшенді. Металдардың контактілік потенциалдар айырмасын өлшеу нәтижелері математикалық статистика әдістерімен өңделді. Эксперименттік зерттеулердің нәтижелері контактілік потенциалдар айырмасы және металды үлгілерден электронның шығу жұмысының қоршаған ортаның температурасының өзгеруіне тікелей әсерін көрсетті, олар орташа корреляциялық тәуелділікке ие. Атмосфералық қысым мен ауаның салыстырмалы ылғалдылығы зерттелетін металдардың контактілік потенциалдар айырмасы мен металды үлгілерден электрондардың шығу жұмысына әлсіз әсерін тигізетіндігі анықталды, олардың әсерін ескермеуге болады. Қоршаған ортаның тепе-тең емес және тепе-тең жағдайларының металдардың контактілік потенциалдар айырмасы және металды үлгілерден электрондардың шығу жұмысына әсері зерттелді. Қоршаған ортаның тепе-тең емес жағдайында контактілік потенциалдар айырмасы төмендейтінін (электронның шығу жұмысы артатынын) анықтайтын нәтижелер алынды, сонымен қатар өлшеу нәтижелерінің орташа квадраттық ауытқуының артатыны анықталды. Жоғарыда келтірілген зерттеулер негізінде металдардың контактілік потенциалдар айырмасын зертханалық жағдайларда өлшеу ұсынылады.

Юров В.М., Олешко В.С.

Влияние окружающей среды на контактную разность потенциалов металлических деталей машин.

В настоящей работе рассмотрено влияние параметров окружающей среды на работу выхода электронов и контактную разность потенциалов металлических деталей машин. Проведены экспериментальные исследования, включающие измерения контактной разности потенциалов на образцах из Al, Ti и Ni способом Кельвина-Зисмана, при различных параметрах: температуре, давлении и относительной влажности воздуха, а также в неравновесных и равновесных условиях окружающей среды. Измерения контактной разности потенциалов проводились прибором «Поверхность-11». Параметры атмосферы измерялись цифровой метеорологической станцией НАМА EWS-800. Полученные результаты измерений контактной разности потенциалов металлов обрабатывались методами математической статистики. Полученные результаты экспериментальных исследований показали прямое влияние изменение температуры окружающей среды на контактную разность потенциалов и работу выхода электронов металлических образцов, имеющее среднюю корреляционную зависимость. Обнаружено, что атмосферное давление и относительная влажность воздуха оказывает слабое влияние на контактную разность потенциалов и работу выхода электронов исследуемых металлов, их влиянием можно пренебречь. Исследовано влияние на контактную разность потенциалов и работу выхода электронов металлических образцов равновесных и неравновесных параметров окружающей среды. Получены результаты, подтверждающие уменьшение контактной разности потенциалов (увеличение работы выхода электронов) металлов, а также увеличение среднего квадратического отклонения результатов измерений при неравновесных условиях окружающей среды. На основании проведенных исследований рекомендуется измерение контактной разности потенциалов металлов проводить в лабораторных условиях.

Нариманова Г.Н., Инкина М.А.

Ретрансляциялауға не өздігінен бапталатын желі негізінде мәліметтерді гетерогенді жеткізу жүйесі.

Мақалада мәліметтерді жеткізудің сымсыз технологиясының құрылымдық ерекшеліктері қарастырылады. Клиент-сервер архитектурасы негізінде мәліметтерді жеткізу алгоритмі құрастырылды. Берілген алгоритм оңтайлы маршрутты автоматты түрде іздеумен ретрансляция мүмкіндігін қамтиды. Өте көп кедергілер

жағдайында мәліметтерді қашықтықтан жинау және жеткізудің жоғары тиімділігін қамтамасыз ететін мәліметтерді гетерогенді жеткізу жүйесі ұсынылған. Мәліметтерді жеткізу жүйесі мәліметтерді берудің оңтайлы бағытын автоматты түрде таңдауға мүмкіндік береді.

Нариманова Г.Н., Инкина М.А.

Система гетерогенной передачи данных на основе самонастраивающейся сети с ретрансляцией.

В статье рассматриваются особенности структуры беспроводных технологий передачи данных. На основе архитектуры клиент-сервер разработан алгоритм передачи данных. Данный алгоритм включает возможность ретрансляции с автоматическим поиском оптимального маршрута. Предложена система гетерогенной передачи данных, обеспечивающая высокую эффективность дистанционного сбора и передачи данных в условиях большого количества помех. Система передачи данных позволяет автоматический выбор оптимального маршрута передачи данных.

Есенбаева Г. А., Есбаева Д. Н., Макажанова Т. Х.

Пластиналардың иілу моделі үшін есептеу әдістері туралы.

Мақала үлкен қолданбалы маңызы бар және ғылым мен техниканың әр түрлі салаларында кездесетін пластиналардың иілу есептерін зерттеуге арналған. Мақалада есептеу әдістерінің құрылымы келтірілген, олардың негізгі құраушылары көрсетілген, екі параллель жақтары бойынша топсалы және басқа екі жақталарда еркін шекаралық шарттары бар тікбұрышты пластиналарды есептеудің классикалық тәсілі сипатталған. Тригонометриялық қатарлар әдісінің математикалық аппараты пластиналарды есептеу үшін қажетті көлемде ұсынылған. Тік бұрышты пластинаның иілу есебін Леви әдісімен есептеудің дербес жағдайлары келтірілген. Бұл мақала негізінен механиктерге, физиктерге, инженерлерге және техникалық мамандықтардың мамандарына бағдарланған.

Есенбаева Г.А., Есбаева Д.Н., Макажанова Т.Х.

О методах расчета для модели изгиба пластин.

Статья посвящена исследованию задач изгиба пластин, которые имеют большое прикладное значение и встречаются повсеместно в самых различных отраслях науки и техники. В статье представлена структура методов расчета, выделены их основные компоненты, охарактеризован классический подход расчёта прямоугольных пластин, шарнирно опертых по двум параллельным сторонам и с произвольными граничными условиями на каждой из двух других сторон. Математический аппарат метода тригонометрических рядов представлен в необходимом для расчёта пластин объеме. Приведены частные случаи расчета изгиба прямоугольной пластины методом Леви. Данная статья ориентирована, главным образом, на механиков, физиков, инженеров и специалистов технических специальностей.

Есбаев А.Н., Есенбаева Г.А., Рамазанов М.И.

Жылуөткізгіштіктің айтарлықтай жүктелген тендеуі үшін модельді зерттеу.

Жылуөткізгіштіктің айтарлықтай жүктелген тендеуі үшін зерттелетін есеп күшті тоқты аппараттардың электр доғасындағы жылуфизикалық процестерді математикалық модельдеумен байланысты. Мұндай құбылыстарды эксперименттік түрде зерттеу олардың тез аққыштығы салдарынан қиынға соғады және бірқатар жағдайларда тек математикалық модель олардың динамикасы туралы нақты ақпарат бере алады. Жүктелген қосылғышта туындының реттілігі жүктеменің қозғалысыз нүктесі кезінде және жүктеме нүктесі айналымы жылдамдықпен қозғалған жағдайда жылуөткізгіштіктің тендеуінің дифференциалдық бөлігінің реттілігінен кем, тең және артық болғанда математикалық модельдің зерттеуі жүргізілген. Мақала негізінен жүктелген дифференциалдық тендеулердің практикалық салдарымен айналысатын ғылыми зерттеушілерге бағдарланған.

Есбаев А.Н., Есенбаева Г.А., Рамазанов М.И.

Исследование модели для существенно нагруженного уравнения теплопроводности.

Исследуемая задача для существенно нагруженного уравнения теплопроводности связана с математическим моделированием теплофизических процессов в электрической дуге сильноточных отключающих аппаратов. Экспериментальные исследования таких явлений затруднены вследствие их быстротечности, и в ряде случаев лишь математическая модель способна дать адекватную информацию об их динамике. Исследование математической модели проведено, когда порядок производной в нагруженном слагаемом меньше, равен и выше порядка дифференциальной части уравнения теплопроводности, при неподвижной точке нагрузки и в случае, когда точка нагрузки движется с переменной скоростью. Статья ориентирована, в основном, на научных исследователей, занимающихся практическими приложениями нагруженных дифференциальных уравнений.

Васенин И.М., Нариманов Р.К., Шрагер Л.А., Перчаткина Е.В.

Кіші өлшемді газ көпіршіктері бар екі фазалық сұйық ағынын модельдеу.

Еркін және мәжбүр конвекцияны ескеруімен ауырлық күш өрісінде кіші өлшемді көпіршіктері бар газ-сұйықтық орта қозғалысының моделі ұсынылған. Модельде көпіршіктердің біркелкі емес концентрациясы болған жағдайда ауырлық күштің өрісінде еркін конвекцияны шарттайтын процестер автоматты түрде ескерілген. Өзара енетін континуумдарға ие екі фазалық ортаны сипаттаумен салыстырғанда бұл модель туындыларда кіші параметрлерден құрылмайды. Екі фазалық ағын байланыс резервуарларында судың озонизация есебіне ұқсас есеп салдарында қарастырылған. Сығылған газ модельдермен ұқсастық есептеулер үшін жақсы дамыған сандық шешу сұлбаларын үшін пайдалануға мүмкіндік береді.

Васенин И.М., Нариманов Р.К., Шрагер Л.А., Перчаткина Е.В.

Моделирование двухфазного течения жидкости с пузырьками газа малых размеров.

Предложена модель движения газожидкостной среды с пузырьками малых размеров в поле сил тяжести с учетом свободной и вынужденной конвекции. В модели автоматически учитываются процессы, обуславливающие свободную конвекцию в поле силы тяжести при наличии неоднородной концентрации пузырьков. В отличие от описания двухфазной среды взаимопроникающими континуумами модель не содержит малых параметров при производных. Двухфазное течение рассмотрено в приложении к задачам, подобным задаче озонирования воды в контактных резервуарах. Аналогия с моделями сжимаемого газа позволяет использовать для расчетов хорошо разработанные численные схемы решения.

Потапов А.А.

«Фракталды радиофизика және фракталды радиоэлектроника» іргелі бағытын құру және дамыту: «фракталды радиожүйелерді жобалау» 1 бөлім. Теория және негізгі ғылыми бағыттар.

Мақаланың бірінші бөлімінде автордың 40 жыл ішінде құрастырған және әзірлеген текстуралар, фракталдар, бөлшек операторлар және бейсызықты динамика әдістері негізінде жаңа ақпараттық технологияларда ғылыми бағыттары ұсынылған. Зерттеу «Фракталды радиофизика және фракталды радиоэлектроника: фракталды радиожүйелерді жобалау» іргелі ғылыми бағыты аясында жүргізіледі. Аталған бағыт РҒА В.А.Котельников атындағы радиотехника мен электроника институтында 1979 жылдан қазіргі уақытқа дейін автормен құрылып, бастамашылдық етілген.

Потапов А.А.

Создание и развитие фундаментального направления «фрактальная радиофизика и фрактальная радиоэлектроника: проектирование фрактальных радиосистем» Часть 1. Теория и основные научные направления.

В первой части статьи представлены созданные и разработанные автором за 40 лет научные направления в новых информационных технологиях на основе текстур, фракталов, дробных операторов и методов нелинейной динамики. Исследование проводится в рамках фундаментального научного направления «Фрактальная радиофизика и фрактальная радиоэлектроника: проектирование фрактальных радиосистем», инициированного и разрабатываемого автором в ИРЭ им. В. А. Котельникова РАН с 1979 года по настоящее время.

Потапов А.А.

«Фракталды радиофизика және фракталды радиоэлектроника: фракталды радиожүйелерді жобалау» іргелі бағытын құру және дамыту 2 бөлім. Таңдаулы нәтижелер және келешектік бағыттар.

Мақаланың екінші бөлімінде 40 жыл ішінде автор мен оның басшылығындағы ұжыммен алынған текстуралар, фракталдар, бөлшек операторлар және бейсызықты динамика әдістері негізінде жаңа ақпараттық технологияларды құру бойынша негізгі нәтижелер ұсынылған. Жоғарыда аталған ұғымдардың радиолокацияның ғылыми айналымға енгізуі авторға «іріктеу топологиясы» ~ «фракталды сигнатура» жалпылама ұғымымен біріктірілген жаңа өлшемдік және топологиялық (энергиялық емес!) белгілер немесе инварианттарды әлемде алғаш рет ұсынып, қолдануға мүмкіндік берді.

Потапов А.А.

Создание и развитие фундаментального направления «фрактальная радиофизика и фрактальная радиоэлектроника: проектирование фрактальных радиосистем» часть 2. Избранные результаты и перспективные направления.

Во второй части статьи представлены полученные за 40 лет автором и коллективом под его руководством основные результаты по созданию новых информационных технологий на основе текстур, фракталов, дробных операторов и методов нелинейной динамики. Введение в научный обиход радиолокации вышеупомянутых понятий позволило автору впервые в мире предложить, а затем и применить новые размерностные и топологические (а не энергетические!) признаки или инварианты, которые объединены под обобщенным понятием «топология выборки» ~ «фрактальная сигнатура».

**INFORMATION
ABOUT AUTHORS**

**АВТОРЛАР ТУРАЛЫ
МӘЛІМЕТТЕР**

**СВЕДЕНИЯ
ОБ АВТОРАХ**

- Agelmenev, M.E.** – Doctor of chem.sciences, Professor, Physical-Technical Faculty, E.A. Buketov Karaganda State University, Karaganda, Kazakhstan
- Aimukhanov, A.K.** – PhD, Associate Professor, Physical-Technical Faculty, E.A. Buketov Karaganda State University, Karaganda, Kazakhstan
- Astanov, S.Kh.** – Doctor of phys.-math. sciences, Professor, Physics Department, Bukhara Engineering-Technological Institute, Bukhara, Uzbekistan
- Ayubekova, A.Ye.** – Master student, Physical-Technical Faculty, E.A. Buketov Karaganda State University, Karaganda, Kazakhstan
- Baltabekov, A.S.** - Candidate of phys.-math.sciences, Docent, Physical-Technical faculty, E.A. Buketov Karaganda State University, Karaganda, Kazakhstan
- Bekeshev, A.Z.** - Candidate of phys.-math.sciences, Head of the Nanotechnology Laboratory, K. Zhubanov Aktobe Regional National University, Aktobe, Kazakhstan
- Bimbetova, G.M.** - Master, Lecturer, Department of General and Theoretical Physics L.N. Gumilyov Eurasian National University, Nur-Sultan, Kazakhstan
- Guchenko, S.A.** – PhD student, Physical-Technical faculty, E.A. Buketov Karaganda State University, Karaganda, Kazakhstan
- Guseinov, N.R.** - Master of Science, National Nanotechnology Laboratory of Open Type, al-Farabi Kazakh National university, Almaty, Kazakhstan
- Hayitov, D.E.** - Master, Assistant of Physics Department, Bukhara Engineering – Technological Institute, Bukhara, Uzbekistan
- Ibrayev, N.Kh.** – Doctor of phys.-math.sciences, Professor, Director of the Institute of Molecular Nanophotonics, E.A. Buketov Karaganda State University, Karaganda, Kazakhstan
- Inkina, M.A.** - Design engineer, EleTeam Limited, Tomsk, Russia
- Kambarova, Zh.T.** – PhD, Docent, Physical-Technical faculty, E.A. Buketov Karaganda State University, Karaganda, Kazakhstan
- Kasimova, G.K.** - PhD student, Bukhara Engineering-Technological Institute, Bukhara, Uzbekistan
- Kopbalina, K.B.** – Master of Science, Senior Lecturer, Department of Physics, Karaganda State Technical University, Karaganda, Kazakhstan,
- Kudabayeva, M.A.** - Master of Science, Senior Lecturer of the Department of Solid State Physics and Nonlinear Physics, 1st year doctoral student, al-Farabi Kazakh National University, Almaty, Kazakhstan
- Kumekov, S.E.** - Doctor of phys.-math.sciences, Professor, Department of Engineering Physics, Kazakh National Research Technical University named after K.I.Satpaev, Almaty, Kazakhstan
- Laurinas, V.Ch.** - Candidate of phys.-math.sciences, Assoc. Professor, Physical-Technical faculty, E.A. Buketov Karaganda State University, Karaganda, Kazakhstan
- Makazhanova, T.Kh.** - Candidate of phys.-math.sciences, Docent, E.A. Buketov Karaganda State University, Karaganda, Kazakhstan
- Mazhenov, N.A.** - Candidate of phys.-math.sciences, Professor, Department of Physics, Karaganda State Technical University, Karaganda, Kazakhstan
- Merzadinova, G.T.** - Doctor of Technical Sciences, Professor, Vice-Rector of Research Work, L.N.Gumilyov Eurasian National University, Nur-Sultan, Kazakhstan
- Mirzhonova, N.N.** – Master, Assistant of Physics Department, Bukhara Engineering - Technological Institute, Bukhara, Uzbekistan
- Mirzo, A.** - Assistant, Researcher, Research Institute, Tajik National University, Dushanbe, Tajikistan
- Myrzabekova, M.M.** - Master of Science, 1st year doctoral student, National Nanotechnology Laboratory of Open Type, al-Farabi Kazakh National University, Almaty, Kazakhstan
- Narimanov, R.K.** – Candidate of phys.-math.sciences, Assoc. Professor, Physico-technical faculty, Tomsk State University, Tomsk, Russia
- Narimanova, G.N.** – Candidate of phys.-math. sciences, Assoc. Professor, Dean of the Faculty of Innovative Technologies, Tomsk State University of Control Systems and Radioelectronics, Tomsk, Russia
- Nemkayeva, R.R.** - Master of Science, Engineer, National Nanotechnology Laboratory of Open Type, al-Farabi Kazakh National university, Almaty, Kazakhstan

- Oleshko, V.S.** - Candidate of Technical Sciences, Assoc. Professor, Professor of the Moscow Aviation Institute (National Research University), Moscow, Russia
- Perchatkina, E.V.** - Laboratory assistant, Physics and Engineering Faculty, Tomsk State University, Tomsk, Russia
- Potapov, A.A.** – Doctor of phys.-math. sciences, Professor, Academician, Head of the Chinese-Russian laboratory of informational technologies and signals fractal processing of JNU-IREE RAS, JiNan University (JNU), Guangzhou, China, V.A. Kotelnikov Institute of Radio Engineering and Electronics, RAS, Moscow, Russia
- Ramazanov, M.I.** - Doctor of phys.-math.science, Professor, E.A. Buketov Karaganda State University, Karaganda, Kazakhstan
- Ryaguzov, A.P.** - Candidate of phys.-math.science, Head of laboratory of optical and electrical methods of analysis, National Nanotechnology Laboratory of Open Type, al-Farabi Kazakh National university, Almaty, Kazakhstan
- Sabdenov, K.O.** – Doctor of Technical Sciences, Assoc. Professor, Heat Power Engineering Department, L.N. Gumilyov Eurasian National University, Nur-Sultan, Kazakhstan
- Saitova, N.K.** – Master, Lecturer, Department of Engineering Physics, Kazakh National Research Technical University named after K.I.Satpaev, Almaty, Kazakhstan
- Sakipov, K.E.** - Candidate of Technical Sciences, Assoc. Professor, Head of the Heat Power Engineering Department, L.N. Gumilyov Eurasian National University, Nur-Sultan, Kazakhstan
- Sakipova, S.E.** – Candidate of phys.-math.science, Professor, Physical-Technical Faculty, E.A. Buketov Karaganda State University, Karaganda, Kazakhstan
- Saulebekov, A.O.** – Doctor of phys.-math.science, Professor, M.V. Lomonosov Moscow State University, Kazakhstan branch, Nur-Sultan, Kazakhstan
- Saulebekova, D.A.** – Master student, M.V. Lomonosov Moscow State University, Kazakhstan branch, Nur-Sultan, Kazakhstan
- Seidualy, Kh.B.** – 4th year student, Physical-Technical faculty, E.A. Buketov Karaganda State University, Karaganda, Kazakhstan
- Seliverstova, E.V.** - PhD, Senior Lecturer, Researcher, Institute of Molecular Nanophotonics, E.A. Buketov Karaganda State University, Karaganda, Kazakhstan
- Sharifov, J.M.** – Candidate of phys.-math.science, Power Engineering Department, L.N. Gumilyov Eurasian National University, Nur-Sultan, Kazakhstan
- Sharipov, M.Z.** - Doctor of phys.-math.science, Head of Physics Department, Bukhara Engineering - Technological Institute, Bukhara, Uzbekistan
- Shrager, L.A.** – Master, Head of the University Laboratory, Physics and Engineering Faculty, Tomsk State University, Tomsk, Russia
- Tanasheva, N.K.** – PhD, Senior Researcher, Institute of Applied Mathematics, Ministry of Education and Science of Republic Kazakhstan, Karaganda, Kazakhstan
- Vasenin, I. M.** - Doctor of Physical and Mathematical Sciences, Professor, Tomsk State University, Tomsk, Russia
- Vassilyeva, K.I.** - 4th year student, Physical-Technical faculty, E.A. Buketov Karaganda State University, Karaganda, Kazakhstan
- Vénos, D.** - PhD, Researcher, Nuclear Physics Institute, Czech Academy of Sciences, Řež, Czech Republic
- Yershina, Sh.A.** – Doctor of techn.science, Professor, al-Farabi Kazakh National University, Almaty, Kazakhstan
- Yershina, A.K.** – Doctor of phys.-math.science, Professor, Kazakh National Women’s Teacher Training University, Almaty, Kazakhstan
- Yesbayev, A.N.** - PhD student, L.N. Gumilyov Eurasian National University, Nur-Sultan, Kazakhstan
- Yesbayeva, D.N.** - translator and web-developer, «Shanghai Factory-Amigo EC Technology Co., Ltd», Shanghai, China
- Yessenbayeva, G.A.** - Candidate of phys.-math.science, Docent, E.A. Buketov Karaganda State University, Karaganda, Kazakhstan
- Yurov, V.M.** - Candidate of phys.-math.science, Professor, Director of the Scientific Research Center, E.A. Buketov Karaganda State University, Karaganda, Kazakhstan
- Zavgorodniy, A.V.** – PhD student, Physical-Technical Faculty, E.A. Buketov Karaganda State University, Karaganda, Kazakhstan
- Zeinidenov, A.K.** – PhD, Associate Professor, Head of the Department of Radiophysics and Electronics, E.A. Buketov Karaganda State University, Karaganda, Kazakhstan
- Zhumabekov, A.Zh.** – PhD student, Physical-Technical Faculty, E.A. Buketov Karaganda State University, Karaganda, Kazakhstan

About «Eurasian Physical Technical Journal»

ISSN 1811-1165 Key title: Eurasian physical technical journal (Print)

Abbreviated key title: Eurasian phys. tech. j. (Print)

ISSN 2413-2179 Key title: Eurasian physical technical journal (Online)

Abbreviated key title: Eurasian phys. tech. j. (Online)

“Eurasian Physical Technical Journal” (Eurasian phys. tech. j.) is a peer-reviewed open access international scientific journal publishing original research results on actual problems of Technical Physics, Energy, Engineering and other related fields.

Since 2004 “Eurasian phys. tech. j.” is publishing in English. Periodicity is 2 issues per year.

E.A. Buketov Karaganda State University is the main organizer and financial sponsor of EAPhTJ. The efforts of the international highly qualified Editorial Board consisting prominent physicists from 12 countries allow provide EAPhTJ international level.

Since 2008 EAPhTJ has been included in the list of publications recommended by the Ministry of Science Education and Science of the Republic of Kazakhstan for the publication of the main results of the master's and PhD doctoral dissertations on the Physical and Mathematical sciences.

Based on the decision of the Content Selection & Advisory Board (CSAB) of May 8, 2019, the Eurasian Physical Technical Journal has been inducted into Scopus data base on three scientific areas: Energy, Materials Science, Engineering.

Publication Ethics and Malpractice Statement

Submission of an article to the Eurasian phys. tech. j. implies that the paper described has not been published previously, that it is not under consideration for publication elsewhere, that its publication is approved by all authors and tacitly or explicitly by the responsible authorities where the paper was carried out, and that, if accepted, it will not be published elsewhere in the same form, in English or in any other language, including electronically without the written consent of the copyright holder. In particular, translations into English of papers already published in another language are not accepted.

For information on Ethics in publishing and Ethical guidelines for journal publication see <http://www.elsevier.com/publishingethics> and <http://www.elsevier.com/journal-authors/ethics>.

The Eurasian phys. tech. j. follows the Code of Conduct of the Committee on Publication Ethics (COPE), and follows the COPE Flowcharts for Resolving Cases of Suspected Misconduct (http://publicationethics.org/files/u2/New_Code.pdf).

To verify originality, your article may be checked by the originality detection service Cross Check <http://www.elsevier.com/editors/plagdetect>.

Authors are responsible for the content of their publications. No other forms of scientific misconduct are allowed, such as plagiarism, falsification, fraudulent data, incorrect interpretation of other works, incorrect citations, etc. Authors are obliged to participate in peer review process and be ready to provide corrections, clarifications, retractions and apologies when needed. All authors of a paper should have significantly contributed to the research.

Reviewers should provide objective judgments and should point out relevant published works which are not yet cited. Reviewed articles should be treated confidentially. The reviewers will be chosen in such a way that there is no conflict of interests with respect to the research, the authors and/or the research funders.

Editors have complete responsibility and authority to reject or accept a paper, and they will only accept a paper when reasonably certain. They will preserve anonymity of reviewers and

promote publication of corrections, clarifications, retractions and apologies when needed.
The acceptance of a paper automatically implies the copyright transfer to the Eurasian phys. tech. j.
All submitted papers will be sent for reviewing to leading experts in the given area.
The Editorial Board of the Eurasian phys. tech. j. will monitor and safeguard publishing ethics.
The editors reserve the right to accept or reject manuscripts.

GUIDELINES FOR AUTHORS

Research articles, survey papers and short notes are accepted for exclusive publication in the «**Eurasian phys. tech. j.**» in English. The manuscripts and short notes must contain original results of investigation in the following scientific areas of Physics:

ENERGY.

- **Thermophysics.**
- **Hydrodynamics.**

MATERIALS SCIENCE.

ENGINEERING.

- **Devices and methods of experiment.**
- **Modeling of the nonlinear physical - technical processes.**
- **Ecological Aspects of New Technologies.**

All publishing manuscripts and short notes must have been recommended by a member of the editor board or by the organization (University), where the work was performed. The author who submitted an article for publication will be considered as a corresponding author.

The paper, short note or review paper shall include an abstract of the contents, not exceeding 200 words and keywords (no more than 10). The abstract must not coincide with the introduction or conclusive part of the work and must not contain references, abbreviations and other unknown words.

All articles should have list of keywords or terms (3 to 10) for indexing purposes.

The text of a paper must not exceed 8-12 pages including tables, figures (no more than 6) and references. A short note must not exceed 4-5 pages including no more than 2 figures. A review paper must not be more than 20 pages (including no more than 10 figures).

The text should be divided on structural parts: **Introduction, Theoretical part, Experimental technique, Results and Discussion, Conclusion**, etc.

Printed copies shall be on good quality paper of International size A4. All texts must be printed in Microsoft Word. It is preferable to use the Times fonts. The text must be printed in 12 point letters, 1.5 intervals. There shall be a margin of 30 mm at the left-hand edge, of 15 mm at the fore edge, of 30 mm at the head of the page and of 30 mm at the tail. All pages must be numbered.

Acknowledgments may be shown at the end of the article text, before **REFERENCES**.

All references must be numbered in the text (for example, [1], [2-4]) and listed in numerical order.

Equations in your paper have to be written using the Microsoft Equation Editor or the MathType (<http://www.mathtype.com>) for (Insert | Object | Create New | Microsoft Equation or MathType Equation).

Tables must be inserted into the text.

Figures should be prepared in a digital form suitable for direct reproduction. Figures shall be submitted on the separate sheets and not included into the text.

The following files must be submitted via e-mail:

- Article text (*.doc);
- Figures (fig1.jpg, fig2.pcx);
- Figure captions (*.txt, *.doc).

